

**On the Interaction of Chemically Conditioned Water with Steel
Heating Surfaces during Saturated Pool Boiling
- An Experimental Thermotechnical Approach**

Dissertation

zur Erlangung des akademischen Grades

Doktor-Ingenieur (Dr.-Ing.)

vorgelegt der

Fakultät für Maschinenbau und Schiffstechnik

der Universität Rostock

von

Holger Topp

geb. am 14. August 1980 in Rostock

Rostock, 14. September 2010

Als Dissertation genehmigt von der
Fakultät für Maschinenbau und Schiffstechnik der Universität Rostock

Tag der Einreichung: 14. September 2010
Tag der Verteidigung: 10. Dezember 2010

Gutachter:

Prof. Dr.-Ing. habil. Dieter Steinbrecht, Universität Rostock
Prof. Dr.-Ing. Dietmar Hein, Technische Universität München
Dr. rer. nat. Wolfgang Hater, BK Giuliani GmbH, Düsseldorf

Abstract

The heat transfer coefficients during the boiling of water at steel heating surfaces are subject to irreversible negative temporal changes. The interaction of the heating surface with boiling water can lead to a drop in efficiency as well as boiler malfunctions or breakdowns, which inevitably entail expensive and time-consuming measures.

In this work, the influence of the responsible physicochemical processes on the steel surface is investigated under saturated pool boiling conditions via thermotechnical measurements in a special apparatus using chemically conditioned water. For this purpose an oxide layer, whose surface structure, composition and thickness vary with the respective kind of treatment, is generated on single horizontal carbon-steel tube heating surfaces under specified conditions.

In contrast to classic inorganic feed water agents, due to their surface activity, alternative film-forming amine-based corrosion inhibitors feature a theoretical improvement potential regarding the nucleate boiling heat transfer as the relevant operational mode in most technical applications. However, scientific evidence on their behaviour in shell boilers is rather rare.

The impact of a corresponding treatment program, comprising inorganic and organic feed water agents, on the heating surface is examined thermotechnically and is further characterised by means of analytical methods. In a long-term test, significantly higher heat transmission coefficients (k) can be observed for the film-forming amine treated tubes as compared to the classic trisodium phosphate conditioning.

The influence of a chemical sample pretreatment on the reproducibility of the initial boiling behaviour and the time response of the heat transmission coefficients during operation is characterised. A modified etching procedure is worked out, which provides improvements compared to the literature. The type of preparation indicates an effect regarding the departure from nucleate boiling.

Furthermore, the impact of the surface structure on the nucleate pool boiling exponent (n) in the generally accepted dependency ($k \sim \dot{q}^n$) is characterised by experiment. In contrast to the literature, n is clearly affected by the surface morphology as modified by sample preparation and, where applicable, by the feed water treatment during operation and can be employed to characterise the heating surface properties thermotechnically.

Investigations on the effect of exemplary inorganic and organic feed water agents on the critical heat flux density and multilayer adsorption during stand-by and down-time are carried out.

Meinen Eltern

*People love chopping wood.
In this activity one immediately sees results.*

Albert Einstein

Vorwort

Die vorliegende Dissertation wurde in der Zeit von Januar 2007 bis Juli 2010 an der Fakultät für Maschinenbau und Schiffstechnik der Universität Rostock am Lehrstuhl Umwelttechnik unter der wissenschaftlichen Leitung von Herrn Prof. Dr.-Ing. habil. Dieter Steinbrecht angefertigt.

An erster Stelle danke ich Herrn Prof. Dr.-Ing. habil. Dieter Steinbrecht für die freundliche Aufnahme in seinen Arbeitskreis, die interessante Themenstellung sowie die stete Bereitschaft zu anregenden Diskussionen. Mein Dank gilt Herrn Prof. Steinbrecht ebenfalls für die fortwährende Unterstützung, für die mir gewährten Freiheiten in der Bearbeitung der Thematik und das mir entgegengebrachte Vertrauen.

Herrn Prof. Dr.-Ing. Dietmar Hein vielen Dank für das Interesse an meiner Arbeit und die Bereitschaft, das Zweitgutachten zu erstellen.

Sehr bedanke ich mich bei unserem Kooperationspartner, der BK Giuliani GmbH, für die Finanzierung des Forschungsprojektes und die äußerst freundliche, offene und kompetente Zusammenarbeit.

Für das Gutachten meiner Arbeit, die rege Kommunikation und Unterstützung sowie die „gemeinen“ nicht-technischen Fragen möchte ich Herrn Dr. Wolfgang Hater sehr danken. Auch danke ich André de Bache, Christian zum Kolk und Michael Urschey für die freundliche und freundschaftliche Zusammenarbeit.

Mein Dank geht an alle Mitarbeiter der Lehrstühle Umwelttechnik und Verfahrenstechnik/Biotechnologie für ihre Hilfsbereitschaft und die Unterstützung während meiner wissenschaftlichen Tätigkeit.

Ich danke Herrn Prof. Dr.-Ing. habil. Detlef Behrend und seinen Mitarbeitern für die wissenschaftliche Unterstützung bei der Konfokal- und Rasterelektronenmikroskopie am Institut für Biomedizinische Technik in Warnemünde.

Ich wage es nicht mir vorzustellen, was aus der vorliegenden Schrift ohne meine fleißigen Korrektoren Friedrich, Ester, Franziska und Anke geworden wäre, die sich hartnäckig durch die zähen Formulierungen und Fehler quälten.

Mein größter Dank für ihre außeruniversitäre Unterstützung, den Beistand und Freude während meiner Promotionszeit geht an meine Familie, meine Freunde und ganz besonders an meine liebe Freundin Anke und unsere Tochter Svenja für ihr Verständnis, Motivation und Rückhalt.

Ohne Euch wäre diese Arbeit nicht zustande gekommen.

Contents

1	Introduction and motivation	1
2	Boiling processes in shell boilers	5
2.1	Specifics of an impressed heat flux density	8
2.2	Properties of the heat transferring surface	10
3	Corrosion processes in the water-steam-cycle	13
3.1	Passivating oxide layers	14
3.2	Classic inorganic feed water treatment	17
3.3	Treatment with film-forming amines	19
4	Approaching a complex physicochemical issue	23
4.1	Current state of research	23
4.1.1	Numerical simulation	23
4.1.2	Experiment	25
4.1.3	Conclusion	26
5	Experimental determination of the heat transfer coefficient	27
5.1	Test setup and specimens	27
5.1.1	Apparatus	27
5.1.2	Tube samples	29
5.2	Measuring system	30
5.2.1	Determination of the outer tube surface temperature	31
5.2.2	Determination of the heat transfer coefficient	33
5.2.3	Determination of the heat transmission coefficient	34
5.3	Method of comparing the experimental data	37
5.3.1	Standardisation of the heat transmission coefficient	37
5.3.2	Influence of the exponent on the comparability	40
5.3.3	Time response of the heat transmission coefficient	41
5.3.4	Statistical evaluation	43

6	Design of investigations	44
6.1	Nucleate boiling	45
6.1.1	Effect of continuous nucleation	46
6.1.2	Conclusion	48
6.2	Convective boiling	49
6.3	Reproducibility of the initial boiling behaviour	50
6.3.1	Impact of the heating rate	50
6.3.2	Influence of the pretreatment	51
6.4	Investigated feed water treatments	53
6.4.1	Conditioning with solid alkalising agents	53
6.4.2	Organic all-volatile treatment	55
6.4.3	Film-forming amine treatment	56
	Dosing and sampling, analytics	57
	Treatment of bare steel heating surfaces	59
	Change from a classic to the film-forming amine treatment	60
6.5	Surface analyses	60
6.6	Critical operating conditions	62
6.6.1	Critical heat flux density during nucleate pool boiling	62
6.6.2	Suppression of nucleation by an organic film	63
7	Results and discussion	66
7.1	Trisodium phosphate treatment	66
7.1.1	Start conditions	66
7.1.2	Conclusion	74
7.1.3	Time response of k during operation	76
	Nucleate pool boiling	77
7.1.4	Conclusion	87
7.1.5	Surface properties after trisodium phosphate treatment	87
7.1.6	Conclusion	93
7.2	Trisodium phosphate and hydrazine	93
7.3	Organic all-volatile treatment	100
7.4	Film-forming amine treatment	100
7.4.1	Treatment of metallic-blank tube samples	100
7.4.2	Switch from trisodium phosphate to film-forming amine	106
7.4.3	Conclusion	112

7.4.4	Changeover from trisodium phosphate and hydrazine to film-forming amine	114
7.5	Burn-out phenomena	115
7.5.1	Burn-out I	115
7.5.2	Burn-out III	117
7.5.3	Conclusion	118
8	Conclusion and preview	120
9	Bibliography	124
	Appendix	131
A	Computational determination of the heat transmission coefficient	133
A.1	Iteration procedure and convergence	133
A.2	Evaluation routine (Matlab-code)	137
B	Photometric test calibration	141
C	Nucleate boiling curves from the nucleation site investigations	143
D	Organic all-volatile treatment	147
E	Video recordings (Optical data carrier)	151
F	Reduction of the heat transmission coefficients during Cetamine conditioning	155
G	Selected microsection/CLSM pictures	156
H	Changeover from phosphate and hydrazine treatment to FA	163
I	Further burn-out III test results	167
J	Estimation of the savings potential under film-forming amine treatment	171

List of Figures

1.1	Water-side and flue-gas-side view of the damaged fire-tube inside an amine treated 3-pass fire-tube smoke boiler.	4
2.1	Nukiyama diagram for saturated boiling at atmospherical pressures.	5
2.2	Influence of the wall superheat ΔT on the minimum nuclei radius r_{min} for boiling water at steel heating surfaces.	7
2.3	Qualitative Nukiyama diagram for an impressed heat flux density.	9
2.4	SEM photograph of a metallic-blank cold-drawn surface (a) and a typical oxide layer generated under test conditions (b).	11
3.1	Zoomed-in photograph of magnetite crystals.	14
3.2	Ion species in the system iron/water.	15
3.3	Two-ply character of the magnetite layer.	16
3.4	Generally accepted arrangement of film forming amines on a solid metal surface.	20
3.5	Experimentally determined surface tension of film-forming amine conditioned deionised water at an atmospherical pressure.	21
4.1	Literature values for the thermal conductivity of magnetite and hematite.	25
5.1	Sectional view and schematic arrangement of the test setup.	28
5.2	Cross-sectional view of a heated tube wall with an inner thermal insulation (grey).	31
5.3	Qualitative temperature profile radial to the tube heating surface during convective pool boiling.	35
5.4	Model of the actual electric resistance configuration as caused by the oxide layer development.	36
5.5	Band of boiling curves as a result of impressing fixed electrical currents (see chapter 6).	37
5.6	Development of exemplary boiling curves at $p_s = 15 \text{ bar}$	38
5.7	Normalisation of k to the reduced heat transmission coefficient C_{red} by regression and extrapolation.	39

5.8	Regression of $k(\dot{q})$ using the fixed exponent \bar{n} resulting in a rotation around a characteristic pivot.	40
5.9	Exemplary development of C_{red} at $p_s = 15 \text{ bar}$	42
6.1	Time response of the exemplary tube A226 during PO_4 treatment and permanent nucleation at $p_s = 15 \text{ bar}$	47
6.2	Time response of C_{red} under permanent nucleation compared to layer generation without tube heating at $p_s = 15 \text{ bar}$	48
6.3	Schematic depiction of the inner vessel processes during convective pool boiling.	50
6.4	Influence of the film-forming amine concentration on the saturation temperature of steam at atmospheric pressure.	57
6.5	Nitrogen-supported dosing system for the organic product.	58
6.6	Qualitative depiction of a cold start-up using the test-setup.	65
7.1	Reproducibility of the initial nucleate boiling behaviour versus equation 7.1 for charge 1, unmodified etchant.	67
7.2	Reproducibility of the initial nucleate boiling behaviour versus equation 7.1 for charge 1, modified etchant.	68
7.3	Reproducibility of the initial nucleate boiling behaviour versus equation 7.1 for charge 2, unmodified etchant.	69
7.4	Reproducibility of the initial nucleate boiling behaviour versus equation 7.1 for charge 2, modified etchant.	70
7.5	Influence of the pretreatment and charge on the initial boiling behaviour at $p_s = 2 \text{ bar}$	72
7.6	Qualitative comparison of the observed active nuclei number on the respective tube surfaces at $p_s = 2 \text{ bar}$	72
7.7	Comparison of the experimentally determined boiling curves exponent with equation 2.7.f	73
7.8	Reproducibility of the initial convective boiling behaviour versus equation 7.1 for charge 2, modified etchant.	73
7.9	Impact of the dimension tolerances according DIN EN 10305-1 on k for $p_s = (2, 15) \text{ bar}$	75
7.10	Time behaviour of the boiling curves exponent n during trisodium phosphate treatment at $p_s = 15 \text{ bar}$	76
7.11	Exemplary development of the boiling curves under nucleate pool boiling conditions at $p_s = 15 \text{ bar}$	77

7.12	Time response of the reduced nucleate boiling heat transmission coefficient C_{red} at $p_s = 15 \text{ bar}$ during PO_4 treatment.	78
7.13	Experimental data and boiling curves at $p_s = 15 \text{ bar}$ during nucleate pool boiling at the start and for steady state k	79
7.14	Time response of C_{red} , obtained at $p_s = 10 \text{ bar}$ during PO_4 treatment at 15 bar	79
7.15	Experimental data and boiling curves at 10 bar during nucleate pool boiling at the start and for steady state k	80
7.16	Time response of C_{red} , obtained at $p_s = 5 \text{ bar}$ during PO_4 treatment at 15 bar	80
7.17	Experimental data and boiling curves at 5 bar during nucleate pool boiling at the start and for steady state k	81
7.18	Time response of C_{red} , obtained at $p_s = 2 \text{ bar}$ during PO_4 treatment at 15 bar	82
7.19	Experimental data and boiling curves at 2 bar during nucleate pool boiling at the start and for steady state k	82
7.20	Time response of the reduced nucleate pool boiling heat transmission coefficient C_{red} during PO_4 treatment according to equation 7.5.	84
7.21	Reproducibility of the time response of k during trisodium phosphate treatment using equation 7.5.	85
7.22	Time response of C_{red} during convective boiling at $p_s = 2 \text{ bar}$ under trisodium phosphate treatment.	86
7.23	Reproducibility of the convective heat transmission coefficient $k(\dot{q}, \tau)$ at $p_s = 2 \text{ bar}$ during trisodium phosphate treatment at $p_s = 15 \text{ bar}$	87
7.24	Visual impression of an exemplary tube prior to installation and after achieving steady state conditions of k during PO_4 treatment.	88
7.25	Comparison of the surface structure (AFM-3D height image): delivery condition and steady state tube after PO_4 treatment.	89
7.26	CLSM picture (top) and roughness profile (bottom) of an exemplary steady state tube sample after 320 h of PO_4 treatment.	90
7.27	Apparent layer thickness $\delta(\tau)$ after PO_4 operation at $p_s = 15 \text{ bar}$, calculated using equation 5.17.	91
7.28	CLSM picture of an epitactic-like oxide layer, found on an exemplary $PO_{4,\infty}$ tube.	92
7.29	CLSM picture of the topotactic-like oxide layer on an exemplary $PO_{4,\infty}$ tube.	92

7.30	Start values and steady state of $k(\dot{q})$ during $PO_4 + N_2H_4$ treatment at $p_s = 15 \text{ bar}$	94
7.31	Time behaviour of the nucleate boiling exponent n during $PO_4 + N_2H_4$ treatment at $p_s = 15 \text{ bar}$	95
7.32	Time response of C_{red} at $p_s = 15 \text{ bar}$ during $PO_4 + N_2H_4$ treatment.	95
7.33	Time response of C_{red} at $p_s = 15 \text{ bar}$ during $PO_4 + N_2H_4$ operation compared to PO_4 treatment.	96
7.34	CLSM-results of an exemplary $PO_4 + N_2H_4$ treated tube sample compared to the pure PO_4 conditioning at the steady state of k	97
7.35	Mean boiling curve at $p_s = 2 \text{ bar}$ at the end of $PO_4 + N_2H_4$ operation.	98
7.36	CLSM view of exemplary polished tube samples after more than 250 h of $PO_4 + N_2H_4$ conditioning at $p_s = 15 \text{ bar}$	99
7.37	Initial nucleate boiling curve for <i>Cetamine</i> treatment compared to PO_4 at $p_s = 15 \text{ bar}$	101
7.38	Development of the nucleate boiling exponent at $p_s = 15 \text{ bar}$ under the influence of the film-forming amine.	102
7.39	Development of the nucleate boiling C_{red} under <i>Cetamine</i> treatment at $p_s = 15 \text{ bar}$, reduced by $\bar{n} = 0.63$	103
7.40	Steady state boiling curves for $Cetamine_\infty$ and $PO_{4,\infty}$ conditioning at $p_s = 15 \text{ bar}$	103
7.41	Steady state boiling curve for $Cetamine_\infty$ conditioning at $p_s = 2 \text{ bar}$ compared to $PO_{4,0}$ and $PO_{4,\infty}$	105
7.42	Freeze frames of the nucleate boiling behaviour for $Cetamine_0$ compared to $PO_{4,0}$	105
7.43	CLSM-results of an exemplary <i>Cetamine</i> treated tube sample compared to PO_4 conditioning at the steady state of k	106
7.44	CLSM view of an exemplary polished tube sample after 400 h of <i>Cetamine</i> operation.	106
7.45	Boiling behaviour at $p_s = 15 \text{ bar}$ immediately after treatment switch from $PO_{4,\infty}$ to <i>Cetamine</i>	107
7.46	Development of n during <i>Cetamine</i> treatment at $p_s = 15 \text{ bar}$ after the changeover from pure phosphate conditioning.	108
7.47	Development of C_{red} after the changeover from $PO_{4,\infty}$ to <i>Cetamine</i> conditioning at $p_s = 15 \text{ bar}$	109
7.48	Comparison of the CLSM view and surface profile of exemplary $PO_{4,\infty}$, $Cetamine_\infty$ and $PO_{4,\infty} \rightarrow Cetamine_\infty$ treated tube surfaces.	110

7.49	Saturation of nuclei at high thermal loads during $PO_4 \rightarrow Cetamine$ treatment at $p_s = 15 \text{ bar}$	111
7.50	Development of the boiling curve of two test samples at $p_s = 2 \text{ bar}$ after switching from $PO_{4,\infty}$ to <i>Cetamine</i> conditioning.	112
7.51	Net enhancement of k for <i>Cetamine</i> operation relative to the steady state of PO_4 conditioning at $p_s = 15 \text{ bar}$	113
7.52	Critical heat flux densities and highest attainable values of \dot{q} at $p_s = 2 \text{ bar}$	116
7.53	Influence of the pretreatment on the experimentally acquired critical heat flux densities at $p_s = 2 \text{ bar}$	117
7.54	Cold start-up results for the steady state <i>Cetamine</i> treated tube A160.	118
7.55	Hot stand-by results for the steady state <i>Cetamine</i> treated tube A160.	119

List of Tables

3.1	TRD 611 rules for the pH-value and the electric conductivity of the boiler water β in shell boilers up to 68 <i>bar</i> which are operated with salt-free feed water.	17
6.1	Impressed electrical currents I and desired heat flux densities \dot{q} originating from preliminary tests.	45
6.2	Test configuration: investigated tube charge and specimen preparation. . .	52
6.3	Parameters for the trisodium phosphate treatment.	54
6.4	Typical boiler water and steam parameters at (25 °C) during film forming amine treatment.	60
6.5	Nomenclature for the assayed treatments. (The arrow marks a changeover from the reference to the organic treatment after reaching steady state of the surface during reference treatment.)	61
6.6	Investigated system conditions for the burn-out III tests.	64
7.1	Coefficients and statistical accuracy of equation 7.1 applied to the different combinations (charge, etchant).	71
7.2	Determined (rounded) time constants for the investigated pressures during nucleate pool boiling and average value $\bar{\kappa}$	83
7.3	Coefficients for equation 7.5.	83
7.4	Principal data describing the impact of $(PO_4 + N_2H_4)_\infty \rightarrow Cetamine$ treatment on the heat transfer at $p_s = 15 \text{ bar}$	114
7.5	Results of the burn-out I tests on metallic-blank and steady state tube samples.	115

Nomenclature & indexes

Symbol	Dimension	Denotation
a, c	K^{-1}	empirical prefactors
b, f, y		empirical factors
d	m	diameter
k	$W/(m^2K)$	heat transmission coefficient
l	m	length
m		exponent of the pressure
\dot{m}	kg/s	mass flow
n		exponent of the heat flux density
p	bar	pressure
p^*		reduced pressure
\dot{q}, \dot{q}_A	W/m^2	heat flux density
r	m	radius
s	m	wall thickness
t	s	time constant of condenser discharge process
u	V	present voltage
x, x', z		counting variables
$[x]$	$ppm, mg/l$	concentration of species x
A	m^2	area
C	K^{-1}	constant, axis intercept

\dot{C}	W/K	heat capacity flow
E		extinction
I	A	electric current
\dot{Q}	W	heat flux, heating power
R	Ω	electric resistance
S_X	dimension of X	mean standard deviation of X
T	K	absolute temperature
U	V	voltage
V	m^3	volume
X	various	determined physical quantity

Greek symbols

Symbol	Dimension	Denotation
α	$W/(m^2K)$	heat transfer coefficient
β	$\mu S/cm$	specific electric conductivity
γ	N/m	surface tension of the boiling water
Γ	K^{-1}	prefactor
δ	m	(layer) thickness
Δh_v	J/kg	mass-specific latent heat at the respective saturation pressure
ε	%	relative error
ζ, κ	h	time constants
λ	$W/(m \cdot K)$	heat conductivity
ξ	Ω/m	specific electric resistance

ρ'	kg/m^3	mass density of the boiling water at the present saturation pressure
ρ''	kg/m^3	mass density of the saturated steam at the present saturation pressure
σ	%	relative mean deviation
τ	h	(treatment) time, period
ϑ	$^{\circ}C$	temperature (Celsius-scale)
ψ		factor describing the pressure dependency of the exponent
Φ		operation characteristic (acc. Bosniakovic)

Indexes

Index	Denotation
<i>ambi</i>	ambient
<i>A</i>	area related
<i>calc</i>	calculated
<i>cross</i>	cross-sectional
<i>exp</i>	experimental
<i>guess</i>	guessed value
<i>i</i>	inner, inside
<i>in</i>	inlet
<i>liq</i>	liquid
<i>L</i>	layer
<i>m</i>	mean, average
<i>max</i>	maximum

<i>min</i>	minimum
<i>o</i>	outer, outside
<i>out</i>	oulet
<i>red</i>	reduced
<i>s</i>	saturation
<i>steam</i>	steam
<i>tot</i>	total, overall
<i>v</i>	volume related

Abbreviations

Abbreviation	Denotation
<i>aA</i>	alkalising amine
<i>AFM</i>	atomic force microscope
<i>AVT</i>	all-volatile treatment
<i>CHA</i>	cyclohexylamine
<i>CLSM</i>	confocal laser scanning microscopy
<i>FA</i>	film-forming amine
<i>DEHA</i>	diethylhydroxylamine
<i>K_R</i>	geometry constant
<i>MEA</i>	monoethanolamine
<i>NBR</i>	nitrile butadiene rubber
<i>NO_x</i>	nitrogen oxide
<i>ODA</i>	octadecylamine
<i>PTFE</i>	polytetrafluorethylene

pH	negative decade logarithm of the hydronium ion concentration
pK_s	negative decade logarithm of the acid dissociating constant K_s
R	$C_xH_{x'}$ (alkyl moiety)
SEM	scanning electron microscope
sys	system
treatm.	treatment

1 Introduction and motivation

The phase change of water in boiler applications is one of the key processes to provide thermal and electric energy from various primary energy sources. Its availability, its high specific heat capacity and its non-toxicity to the environment¹ makes water the number one choice for many technical working cycles.

According to their basic construction and operation, steam- and hot water boilers can be divided into two main groups: flow boilers and shell boilers.

Flow boilers usually consist of numerous tubes of moderate diameter. Water flows inside these tubes while it is being heated continuously. Here, circulation of the water is established by natural (and/or forced) convection with an integrated drum as phase separator (drum boilers, Sulzer arrangement). Natural circulation is complemented by circulation pumps. Another principle to achieve even higher power densities can be applied by pumping the water through the pipes without phase separation (once through boilers, Benson arrangement). Flow boilers are used mainly in large scale power plants for power generation at high (or supercritical) pressures.^[1]

Shell boilers, on the other hand, realise pool boiling (or boiling in an indefinitely extended vessel). The mostly tubular heating surfaces are fully submerged in the surrounding liquid. While the water is boiling on the tube's outer side, heating takes place from the inside by burning fuel or by hot flue gases flowing inside. Mass transport from the heated surface into the bulk liquid inside a shell boiler is exclusively provided by natural convection. Systematically inherent, their operating pressure is limited to approximately 25 *bar* for technically relevant steam output (30 *bar* in special applications),^[1] as large surfaces are subjected to the system pressure.

Although shell boilers have been replaced by flow boilers in large-scale power plants, they prevail in industrial application, where mostly horizontal heating tubes are installed. The secondary loop in pressurised-water reactors in nuclear power plants also feature a shell-boiler-like principle, which is designed for pressures up to 60 *bar* in a vertical tube bundle arrangement.

In power generation, flue gas heated shell boilers are often used for auxiliary or start-up purposes.^[1] Whenever robust operation behaviour outweighs the demand for high pressures

¹The climate relevance of water will not be discussed in this work.

or quick response, shell boilers are installed. Being complex constructions with fire and flue gas tube arrangements depending on the field of application, usually hot water or saturated steam is generated in fire-tube shell boilers. Furthermore, superheated steam can be produced using steam-carrying pipes (the steam is flowing through the pipe) located in the deflecting chamber(s). This principle is applied for instance in modern multi-pass fire-tube shell boilers.

Besides electrical power generation, hot water and steam are required for many other applications, like the paper industry, food industry and refinery purposes, where mostly shell boilers are used.

Since the majority of water and steam-touching materials in a steam generator are made from steel, complex iron corrosion and other irreversible conversion processes take place on unalloyed as well as stainless steels, influencing the heat transferring surface properties.^[2-6] Unrecognised or untreated corrosion can easily cause malfunctions and even destruction of boiler parts.^[7] Yet, corrosion not only threatens the operation mechanically (thermal tension), but also affects the boiling heat transfer. Foulings, like corrosion products, have an adverse effect on the heat transmission from the metallic surface through the fouling layer to the boiling water, since it is of thermally insulating character. Parts of the heat transferring surface exposed to high thermal loads and featuring foulings might be destroyed due to overheating (e.g. boiling crisis).

As a consequence, diverse measures have been established to counteract or even design the electro- and physicochemical corrosion phenomena incorporating the development of uniform passivating oxide layers to protect the heating surface from further corrosion.^[8,9] Despite being corrosion products as well, magnetite (Fe_3O_4) and hematite (Fe_2O_3) layers are considered most advantageous regarding surface passivation during start-ups and down-time, being able to withstand minor thermal tension.^[1,2] Chemical water treatment is the state-of-the-art instrument to develop and maintain the mentioned protective layers.

The impact of water conditionings on the heating surface structure, oxide layer thickness, surface morphology and porosity is considered oppositional:^[10,11]

While an additional heat transfer impeding (i.e. passivating) layer is built up on the heat transferring unit affecting convective heat transfer, the porosity of the oxidised surface has an enhancing effect regarding nucleation.

Besides classical inorganic conditionings (on the basis of phosphates, sulfates, hydroxides or ammonia), a rather new treatment attracts more and more interest recently: The organic feed water treatment with film-forming amines (FA).

These long-chain organic substances feature an amphiphilic character and a strong affinity

to metal surfaces where they, as their name suggests, form a more or less dense and compact film in a molecular dimension. This film theoretically prevents the electrolyte solution (boiler water) from contacting the inner boiler surface susceptible to corrosion and is assumed to be strongly driven by adsorption, ion interaction and Van der Waals forces.^[12–15] Furthermore, their alkaline character supports corrosion inhibition.

FA are considered surface active substances and have already been applied successfully since the 1950s in form of a very popular organic film-forming corrosion inhibitor on amine basis: octadecylamine (ODA). As often applied in pressurised-water reactors,^[16] a combined ODA/hydrazine treatment was run in several boiler facilities, providing a good system response regarding corrosion inhibition and dispersing corrosion products or scale. A decline of the condensing droplet diameter to 50 % was observed, while a turbine efficiency increase of 1.5 % over inorganic treatment resulted due to a more advantageous expansion progress.^[17,18]

Consequently, a potential of improving nucleate boiling heat transfer over typically inorganically conditioned boiler water can be assumed for diluted amine dispersions in the feed water. Positive effects of an organic treatment have been reported regarding the heat transfer during pool boiling.^[19]

Hypothetically, an enhanced boiling heat transfer and expansion progress in the turbine can help to increase part load efficiency.

Despite their positive capabilities, the propagation of film-forming agents is decelerated by conventional instructions and regulations as well as the fear of the formation of low-molecular acids (i.e. acetic acid) and carboxylate ions (formate, acetate, propionate).^[20] Worries about an increase in the electrical conductivity of the conditioned water or a decrease of the critical heat flux density during nucleate boiling are possibly also of relevance although there are many positive operational reports available on the effect of film-forming amines on the heater surface properties.^[21–24]

Yet, scientific evidence regarding the thermotechnical behaviour of film-forming amines in steam boilers is rare. In the past, malfunctions and breakdowns of amine-treated steam generators led to speculations whether those alternative corrosion inhibitors might have at least a proportionate share on the respective causes.^[25,26]

Former tests at the Chair of Environmental Engineering in Rostock could already exclude measurable effects of two exemplary organic corrosion inhibitors on the critical heat flux density experimentally.^[27] However, a risk of suppression of nucleation by an organic film at lower pressures during down-time or stand-by was also identified (burn-out III).

Picture 1.1 demonstrates a capital damage of the waved fire-tube in an amine treated 3-pass fire-tube shell boiler.^[26] Such incidents are not unusual and represent a serious

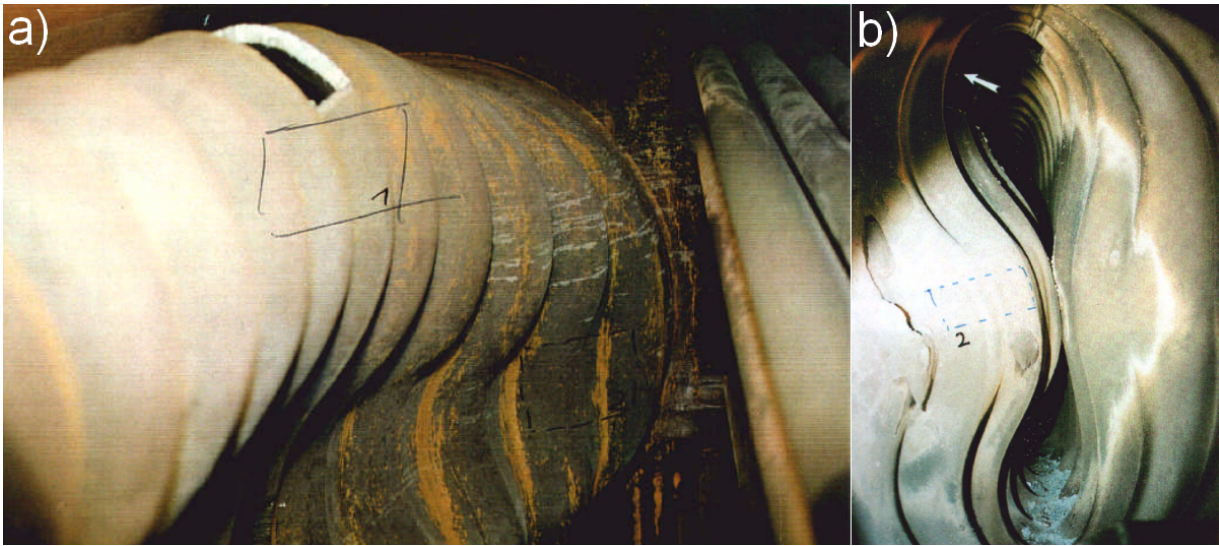


Figure 1.1: *Water-side (a) and flue-gas-side (b) view of the damaged fire-tube inside an amine treated 3-pass fire-tube smoke boiler. The tube assumably collapsed caused by suppressed nucleation.*^[26]

economical issue considering the cost for repair or even replacement of damaged boiler parts and resulting business interruption. Not to mention constructional damages or even injuries of personnel.

Also the use of state-of-the-art NO_x -reduced burners could verifiably be made responsible for diverse boiler breakdowns, although a water-side cause was assumed.^[27] Correspondingly, emission guided cutting-edge burner policy implies a threat to conventionally designed shell boilers.

The aim of this work is, therefore, to gain practical information on the interaction of inorganically as well as organically conditioned deionised water with the heat transferring surface under shell boiler conditions. A key focus is on the applied agents' impact on the heat transfer from steel heating surfaces to boiling water and the characterisation of their influence on the heating surface properties during pool boiling as well as their effect on critical operation modes.

Besides a scientific assessment of the actual behaviour of a variety of feed water agents, the derived information is supposed to help choosing an appropriate conditioning for the operation of shell boilers, not only from a plant-cycle chemical but a thermotechnical point of view.

2 Boiling processes in shell boilers

Considering saturated heat transfer from a fully submerged heating surface to a surrounding coolant, the transferred area-related thermal load (heat flux density) \dot{q} is directly proportional to the temperature difference ΔT between the heating surface (index w) and the saturated coolant (index s). A factor of proportionality is introduced as heat transfer coefficient α .

Newtons fundamental equation of heat transfer can be applied as follows, for the case where ΔT equals $T_w - T_s$:^[28]

$$\dot{q} = \alpha \cdot \Delta T \quad (2.1)$$

Given the dominating mechanisms of heat transfer in the boundary layer that is surrounding the heating surface, pool boiling of water can be divided into three distinct regions: *Free convection*, *nucleate boiling* and *film boiling*. Film boiling is furthermore divided into unstable and stable film boiling. Figure 2.1 depicts those regions schematically according to Nukiyama^[29] for an impressed wall (boundary layer) superheat ΔT at atmospherical pressures.

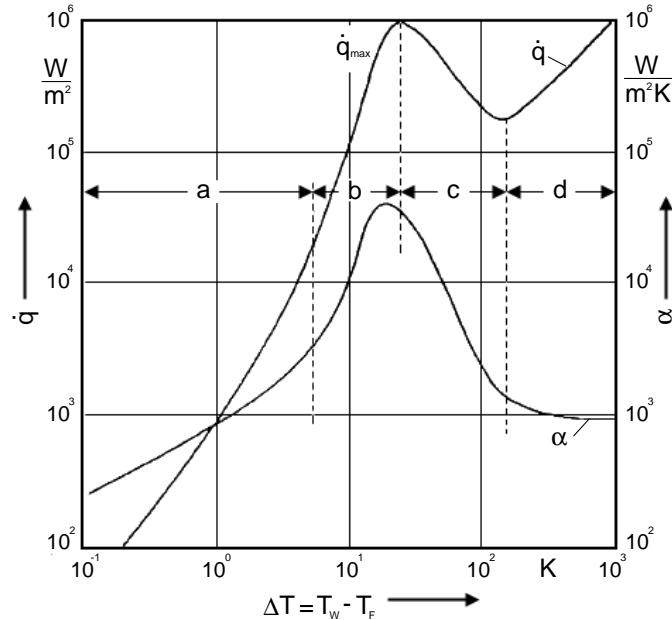


Figure 2.1: *Nukiyama diagram for saturated boiling at atmospherical pressures: a - convective boiling, b - nucleate boiling, c - unstable film boiling, d - stable film boiling.*^[29]

The boiling curves $\alpha(\Delta T)$ position and inclination in the Nukiyama diagram are determined by the heating surfaces properties, as material and structure, by the material/liquid combination and by the saturation pressure.

Convective boiling is characterised by a small boundary layer superheat ΔT (see figure 2.1 a). The critical conditions for bubble forming on the surface are not satisfied, yet. Superheated water is transported from the boundary layer to the free surface by buoyancy forces only and vaporises there.^[30–32] The corresponding heat transfer coefficient α between the heated surface and the boiling water is determined by local convective flow velocities only.^[31]

Industrial shell boiler applications usually imply *nucleate pool boiling* (see figure 2.1 b). Nucleate boiling is characterised by high-grade dynamic processes on the heating surface.^[33]

Once the superheat ΔT has reached a certain extent, nucleation sets in (ONB: onset of nucleate boiling). Nuclei (or nucleation sites), like cracks or grooves in the heater surface, containing non-condensed vapour or gas residues, are activated.^[29,30,34] The minimum superheat that is necessary to activate a nucleus of the radius of curvature r_{min} complies with following equation, which combines the mechanical equilibrium of a bubble and the Clausius-Clapeyron relation:^[31]

$$r_{min} = \frac{2\gamma \cdot T_s}{\rho'' \cdot \Delta h_v(T_s) \cdot \Delta T} \quad (2.2)$$

where γ is the surface tension between the boiling water and its saturated steam, the saturated steam mass density is ρ'' and the enthalpy of evaporation is $\Delta h_v(T_s)$. At such nucleation sites, whose distribution, radius of curvature, and shape differ significantly for technical surfaces, bubbles grow fed by evaporation from an adjacent microlayer between the bubble and the heated wall. When buoyancy forces surpass adhesive forces at the bubble foot, this bubble will depart removing heat from the heater surface.^[35]

As the saturation pressure and the wall superheat increase, more and more smaller nuclei become active. The influence of ΔT on the available radius of curvature of a nucleus is depicted simplified in figure 2.2 for atmospherical pressure.

This depiction is of rather scientific value as, considering shell boiling applications, unusually high pressures are implemented to demonstrate the trend of smaller available nuclei radii compared to atmospherical pressure. The respective areas are limited to $\Delta T = 25 \text{ K}$ for saturated boiling as, according to Michejew,^[34] film boiling occurs at such wall superheat at $p_s = 1 \text{ bar}$ (see film boiling described belows).

Nucleation is subject to hysteresis.^[11,30,31] Although literature states a value of $\Delta T \approx 7 \text{ K}$

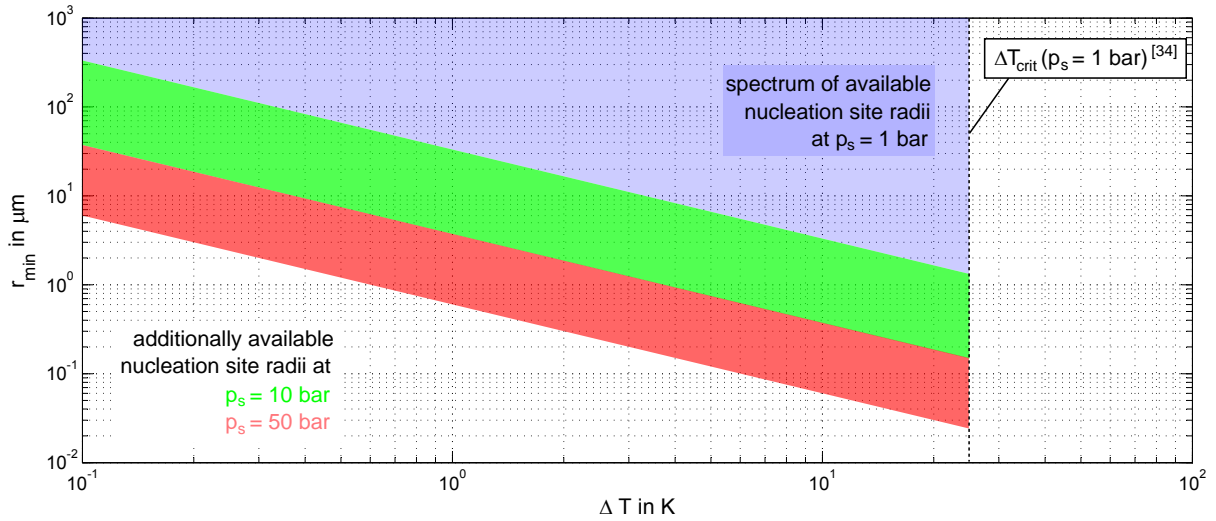


Figure 2.2: Influence of the wall superheat ΔT on the minimum nuclei radius r_{min} for boiling water at steel heating surfaces at different saturation pressures according to equation 2.2.

for nucleation to set in at atmospherical pressures, the necessary superheat for nucleation depends on the operational mode.^[11,31] If operation is carried out with an increasing superheat (or rising impressed heat flux, respectively) ONB sets in at higher values, as activation of nuclei requires additional energy. The resulting heat transfer coefficient rises corresponding to the region of convective boiling with some few bubbles on the heating surface that are not influencing convection significantly. Eventually, α increases more than proportionally to the superheat and meets the curve of nucleate boiling.

In turn, a decreasing superheat or heat flux results in stable nucleate boiling until the parameters do not comply with the critical conditions for nucleation anymore (see next section for more information).

Departed bubbles leave a trail behind which is generally assumed to induce an enhanced convective flow, inserting boiling (not superheated) water from the bulk liquid into the boundary layer, while evaporation directly cools the heater surface.^[36] Peng et al. demonstrated experimentally that interfacial evaporation and condensation at the bubble surface induce jet-like flows from the bubble to the bulk liquid, resulting in cooling without bubble departure from the surface.^[37] Providing large scale heat fluxes without noticeable increase in superheat, nucleate boiling is the desired operation in technical applications. During fully developed nucleate pool boiling even severe heat fluxes can be transferred securely. Compared to convective boiling, there is no longer any significant influence of convective flow on the heat transfer coefficient α when nucleate boiling is fully developed.^[38] For technical purposes, this boiling region is described by a simple power law $\alpha(\Delta T)$ providing

sufficient accuracy:^[30,31]

$$\alpha = (C_{\Delta T} \cdot \Delta T)^{1/(1-n)} \quad (2.3)$$

where $C_{\Delta T}$ and n are (pressure-dependent) quantities. The factor $C_{\Delta T}$ characterises thermal as well as micro geometric surface properties and the material-liquid combination, while n represents the influence of the boundary layer superheat ΔT on the heat transfer coefficient.

After exceeding a critical boundary layer superheat (depending on the properties of the fluid, heating surface and the operation point) or the maximum impressed heat flux density \dot{q}_{max} during nucleate boiling, the transferred heat flux drops dramatically to a minimum, when - according to the Leidenfrost phenomenon - a dense insulating vapour layer is formed between the bulk liquid and the heating surface. This condition is described by the expression *unstable film boiling* (see figure 2.1 c), since the developing film collapses in alternation. If the surface temperature of the heater is increased significantly to further raise the transferred heat flux (supported by thermal radiation) *stable film boiling* can be observed (see figure 2.1 d).

2.1 Specifics of an impressed heat flux density

The operation of fire-tube, heat recovery boilers and electrically heated systems means adjusting the heat flux to the system (e.g. by convection and radiation from the exhaust gas to the inner walls), unlike controlling the temperature difference as shown in the Nukiyama diagram (see figure 2.1). Here, a heat flux density is being impressed upon the surface.

Consequently, the boundary superheat ΔT is a result of the impressed heat flux density \dot{q} and linked with the heat transfer coefficient $\alpha(\dot{q})$. Therefore, assuming identical system parameters the effect of an increased \dot{q} is equivalent to increasing ΔT in figure 2.2. More and more radii of smaller size get activated as the heat flux density increases.

Thus, another power law derived from equation 2.3 is usually applied to determine the nucleate pool boiling heat transfer coefficients at a distinct operating pressure using the exact same exponent n as in equation 2.3:^[11,30]

$$\alpha = C_{\dot{q}} \cdot \dot{q}^n \quad (2.4)$$

Figure 2.3 qualitatively demonstrates the boiling regimes for an impressed heat flux density with respect to hysteresis of nucleation.

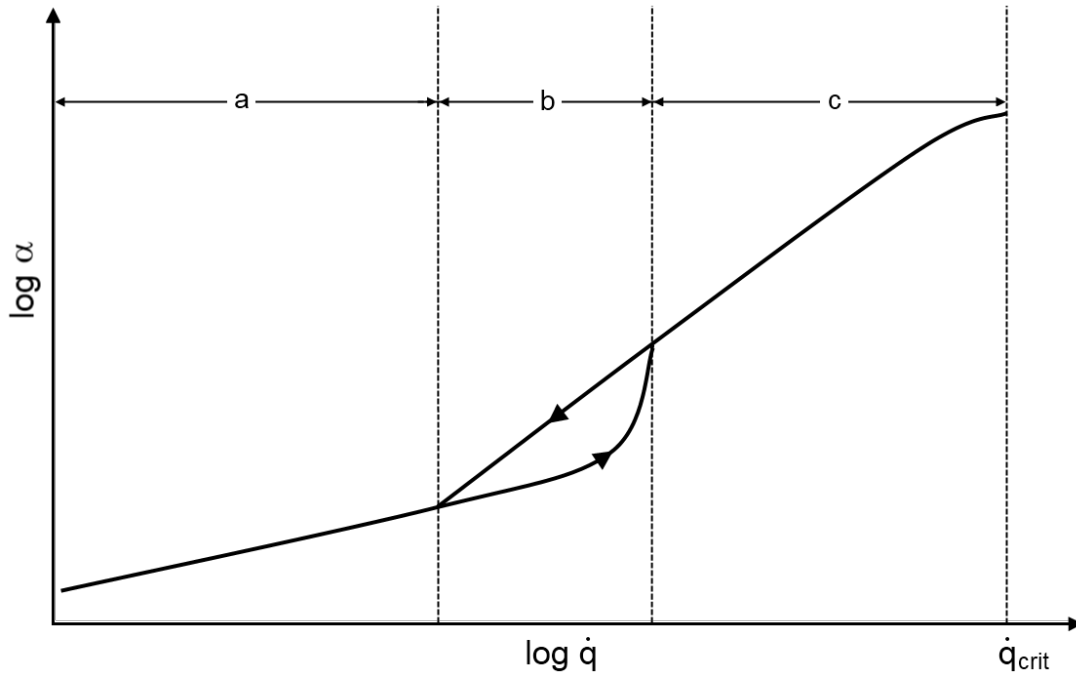


Figure 2.3: *Qualitative Nukiyama diagram for an impressed heat flux density: a - convective pool boiling, b - hysteresis of nucleation, c - nucleate pool boiling; \dot{q}_{crit} - burn-out I.*

Expression 2.4 is also known as *boiling curve*, which differs in $C_{\dot{q}}$ and n for the respective boiling regime (convective/nucleate boiling) and saturation pressure. Circumstance $\Delta T = f(\dot{q})$ involves forming of the above mentioned vapour layer after reaching the critical heat flux density \dot{q}_{crit} for nucleate boiling. Due to the fact that the heat transfer coefficient declines instantly (*boiling crisis, 1st kind*) this vapour film results in a surface temperature exceeding the melting point of the heater material (in systems with electrical heating). In systems heated by flue gas remarkable deformations followed by mechanical destruction of the tube surface will occur, after the material reached the flue gas temperature. This condition inevitably leads to the destruction of the heater (*burn-out I*). Thus, film boiling cannot be put into practice in systems with an impressed heat flux density and poses a serious threat to technical facilities. Unstable film boiling can already occur locally, when large vapour columns coagulate prior to departing from the surface. This unstable film collapses alternately until eventually a dense insulating film is formed leading to burn-out I. Burn-out II, also called dry-out is a phenomenon in flow boilers, which does not matter in this context.

A German-Dutch collaboration of the FDBR and Stoomwezen evinces that film boiling can occur already at heat flux densities $\dot{q} \approx 300 \cdot 10^3 \text{ W/m}^2$ in a compact boiling tube arrangement.^[39] This kind of film boiling phenomenon is induced by the piping arrange-

ment and bubble interaction formed on adjacent tube surfaces. Pool boiling demands an infinitely extended bulk liquid surrounding the heater to prevent disturbances of convective flow. This construction-caused phenomenon is not to be mistaken with the critical heat flux density in nucleate pool boiling on a single tube as depicted in diagram 2.3. The FDBR therefore recommends the design of shell boilers up to a maximum of $\dot{q} = 240 \cdot 10^3 \text{ W/m}^2$ in order to avoid damages. However, in some applications, values of $\dot{q} = 300 \cdot 10^3 \text{ W/m}^2$ can be achieved in fluidised bed combustion plants. Therefore, considering 10 % overhead, the technically interesting area of specific heat fluxes can be assumed to be $40 \cdot 10^3 \text{ W/m}^2 \leq \dot{q} \leq 330 \cdot 10^3 \text{ W/m}^2$.

Burn-out I can not only be induced by effects on the boilers water side but also on the exhaust gas side. Low-NO_x burners feature very transient flame characteristics. As a result, highly increased local heat fluxes from the exhaust gas to the inner walls can occur, possibly damaging the heat transferring unit.^[27]

Another boiling crisis, the so called *burn-out III* phenomenon, has been observed and characterised by Steinbrecht et al.^[27] being traced back to sorption processes of film-forming substances during transient operation. The theory is that a dense multimolecular film of organic agents is formed covering the heating surface during down-time or stand-by. Now, if suddenly a heat flux density would be impressed for example by switching on the burner(s) of a fire-tube shell boiler, the surface film impedes nucleation on the surface. As a consequence, the heating surfaces temperature will increase rapidly. If the time necessary for desorption of the film is longer than the time to reach the melting temperature of the heater material, burn-out III will occur.

Graßmann considers film-forming corrosion inhibitors to be a possible cause for boiler breakdown.^[26]

Mentioned burn-out processes are of enormous importance regarding the operation of steam generators with filming agents and have to be investigated to make statements on the applicability of film-forming corrosion inhibitors.^[27]

2.2 Properties of the heat transferring surface

Besides the system parameters pressure, temperature and heat flux density, caloric and geometric properties of the material have a significant effect on the boiling behaviour, including surface (micro-)geometry, material, the existence of foulings/layers and their morphology.^[2,31,33,40]

Accordingly, not only the heating surface arrangement/inclination but most importantly

the micro geometry of the surface and the shape of the nucleation sites considerably affect the wall superheat or heat flux density needed to activate the respective nucleus.^[30,31]

A wide range of cavities is available on technical surfaces mostly characterised by roughness parameters. Mean roughness R_m , root-mean-squared roughness R_q and average roughness height only approximate the surface structure for technical purposes. A quantitative characterisation of shape and *distribution* of surface cavities is not possible using such attributes.^[31] For example, if the boiler tubes are fabricated by drawing, resulting grooves (see figure 2.4: (a)) act as nucleation sites as well as cracks in oxide layers (see figure 2.4: b)). Latter defects are usually induced by thermal or mechanical tension.^[41]

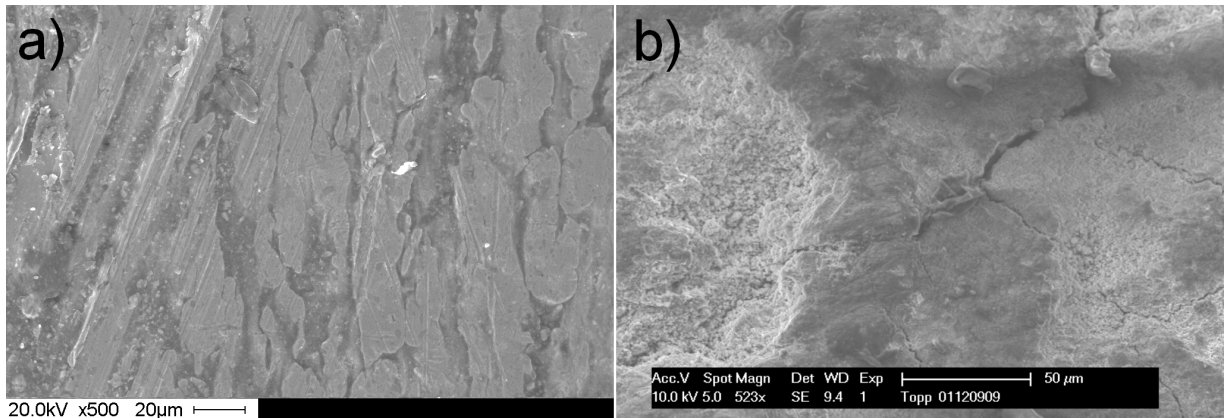


Figure 2.4: SEM photograph of a metallic-blank cold-drawn surface (a) and a typical oxide layer generated under test conditions (b).

Organic deposits, scale, corrosion products as well as oxide layers pose heat transfer resistances but also enhance nucleation by an increased mean roughness, as additional nuclei can be activated.^[33]

The VDI Wärmeatlas (VDI Heat-Atlas),^[31] for instance, states the following correlation for the heat transfer coefficient α incorporating the heating surface properties:

$$\frac{\alpha}{\alpha_0} = C_W \cdot F(p^*) \left(\frac{\dot{q}}{\dot{q}_0} \right)^n \quad (2.5)$$

with respect to a known data pair $\alpha_0(\dot{q}_0)$ at the desired reduced saturation pressure p^* . The factor $F(p^*)$ states the relative pressure dependency of α which is also determined empirically. Prefactor C_W depends also on the system pressure, the type of boiling liquid and surface morphology. Currently, a quantitative dependency for C_W cannot be given. The roughness term in C_W , however, correlates with the arithmetic mean roughness value

R_a as defined in DIN 4760.^[42] It is found with:

$$C_{W,R} = \left[\frac{R_a}{R_{a0}} \right]^{0.133} \quad (2.6)$$

where $R_{a0} = 0.4 \mu m$ for *copper* is used. For (pure) water, the pressure dependent exponent n is stated to follow the equation:^[30,31]

$$n(p^*) = 0.9 - 0.3 \cdot p^{*0.15}; \pm 0.1 \quad (2.7)$$

The influence of feed water agents or oxide layers/impurities on the heat transfer is not taken into account by equation 2.7. A corrosive feedback on the heat transferring surface by the liquid including possible additives is influencing the heat transfer during nucleate boiling via the thermal conductivity and surface structure of the oxidised surface. As the materials properties change from metallic to oxidised steel during the treatment period τ , the change of the heating surface must be implemented.

In order to compare the time response of the heat transfer in shell boilers under dissimilar chemical conditioning, the determination of the initial boiling behaviour is essential. Given the operation period τ , Steinbrecht suggests a statistically secured empirical equation for initial nucleate pool boiling of demineralised water at plain carbon steel (St 35) cold-drawn precision tubes and repeatedly identical test conditions (tube material, start-up heating rate):^[43]

$$\alpha(\tau = 0) = 5.63 \cdot \dot{q}^{0.7} \cdot \left(\frac{p_s}{p_0} \right)^{0.3} \quad (2.8)$$

This equation allows calculating the expected start value α as function of the heat flux density \dot{q} with a *fixed* exponent $n = 0.7$.

The mean deviation for the constant is stated with $\sigma = 12.6 \%$ and the maximum error of measured data is found within $\pm 25 \%$. The investigated range of saturation pressures is $1.1 \text{ bar} \leq p_s \leq 25.4 \text{ bar}$, $p_0 = 10 \text{ bar}$. Equation 2.8 represents the base situation which is to be checked for the actual test conditions in order to gain sustainable comparative conclusions.

In contrast to equation 2.7, correlation 2.8 does not suggest a pressure dependency of the boiling curves exponent n .

3 Corrosion processes in the water-steam-cycle

Although the formation of corrosion products found in the water-steam-cycle is certainly well understood and specified, corrosion induced boiler defects occur frequently due to the complexity and individuality of the boiler equipment.^[44,45] Constructional particularities and operational modi have to be taken into account selecting an appropriate feed water treatment. Eddy waters and vortex areas can easily lead to enrichment of acid and lye resulting in corrosion. Dynamics of start-up and alternating load operation put stress on particular boiler parts. Cracks can develop even further supported by local corrosion.

Corrosion in steam boilers is multifaceted: Stress corrosion cracking, sublayer corrosion and oxygen induced pitting corrosion - only to name some forms, which can be correlated with the individuality of the boiler system. Sometimes even improper operation can be presumed.^[46]

In the majority of steam boilers feed water conditioning is used to intervene in or design the corrosion processes. However, a complete corrosion inhibition cannot be provided by any of the known methods.

In most facilities an increase of the pH-level in the boiler water (by adjusting the feed water pH-value) is sufficient to reduce the electrochemical potential of steel in the water and thereby cut down the risk of corrosion by initiating formation of passivating layers.^[1,4] This operation type is called *alkaline operation*.

Depending on the dissolved species, there is another route in chemical feed water conditioning/surface passivating. Here, additional oxidising agents are dosed into the feed water. This operation is called *neutral operation*, as a significant pH-value increase is not carried out. If applicable, both conditionings are applied as *combined operation* when the pH-value is adjusted and oxygen is dosed to enhance formation of protective layers.

Before use, the water is treated thermally (degassing), chemically (precipitation) or/and by ion exchangers (condensate polishing). Make-up water is sometimes even sourced from reverse osmosis or de-ionisation plants to further reduce its electrolytic character and 'avoid' corrosion processes.

Besides operation with solid alkalising agents, the volatile alkalising agent ammonia is used (in high-pressure boilers). Since there is no alkalisation of the boiler water, this treatment is recommended for salt-free feed water only. Volatile alkalisation is sometimes also applied in

a combined treatment with additional oxygen dosing to support development of passivating oxide layers in a combined treatment.

3.1 Passivating oxide layers

Oxide layers, such as magnetite and hematite layers, are of enormous interest since - being compact and firmly adhering - they provide a passivating effect regarding corrosion.^[9,47] Magnetite (Fe_3O_4) as the desired species, belongs to the spinel group. It consists of wustite (FeO) and hematite (Fe_2O_3) in the crystal type $Fe^{II}(Fe^{III})_2O_4$.^[45] Magnetite provides a Mohs hardness of 5.5 – 6.5 and a mass density of 5.1 – 5.2 g/cm^3 . Besides being advantageous regarding surface passivation, it withstands certain thermal stress during operation and alternating pressures. At lower pressures, magnetite is often accompanied or even substituted by hematite, while the former is the prevailing species in high-pressure flow boilers.

Depiction 3.1 shows an exemplary microscopic photograph of magnetite crystals as a structure generated in a high pressure test loop.^[48]

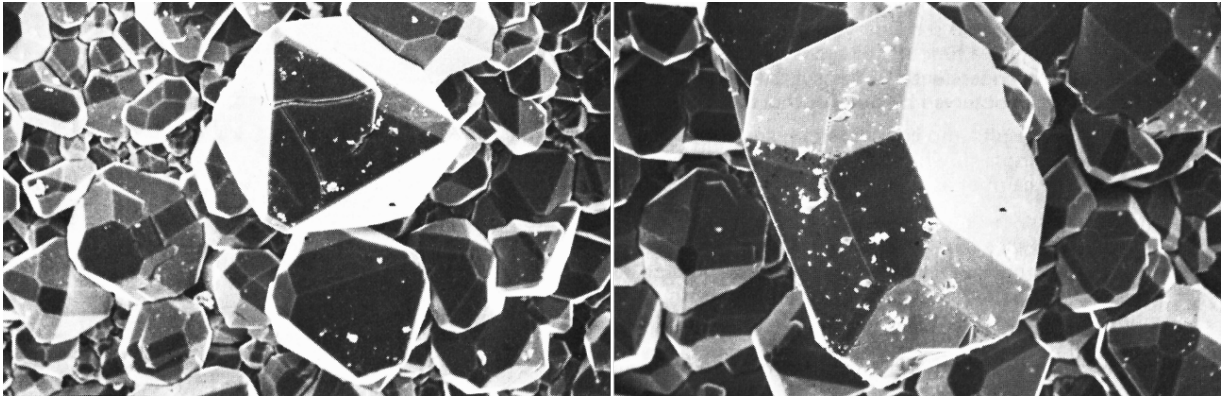


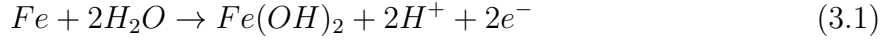
Figure 3.1: *Zoomed-in photograph of magnetite crystals.*^[48]

Damages due to material overheating or an efficiency drop caused by heat-transmission-impairing layers lead to regulations for periodic chemical (or mechanical) cleaning. Boiler manufacturers recommend diverse cleaning measures to ensure safe operation, whenever a critical area-related layer mass (e.g. 500 g/m^2) is “detected” in high pressure cycles, for instance. Detection usually means cutting the pipe material, followed by a surface analysis when output losses indicate such an influence.

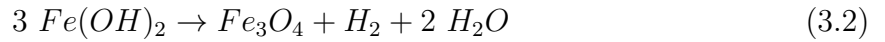
Passivating magnetite or hematite layers are only formed under special circumstances and can be preserved with respect to those conditions.^[47–49]

Magnetite is generated on steam and water touching steel components at temperatures above 180 °C (approx. 10 bar saturation pressure) in significant quantities.^[48] Oxygen

is unessential, since the oxidation capacity of water satisfies the magnetite generation from insoluble iron hydroxide ($Fe(OH)_2$) at the mentioned temperatures and sufficient quantities of hydroxide ions.^[47] The first temperature- and pH-value-dependent step in magnetite generation is the oxidation of iron to iron(II) hydroxide:



Since formation of Fe_3O_4 implies production of hydrogen, its detection can be used to observe the layers development. Above approximately 200 °C there is practically no iron hydroxide detectable at all, because the so called Schikorr reaction prevails:^[47-49]



The chemical conversion from dissolved iron hydroxide to magnetite is a very complex process. A simplified depiction of possible species in the system water/iron is found in the scheme 3.2 according to Bohnsack.^[50]

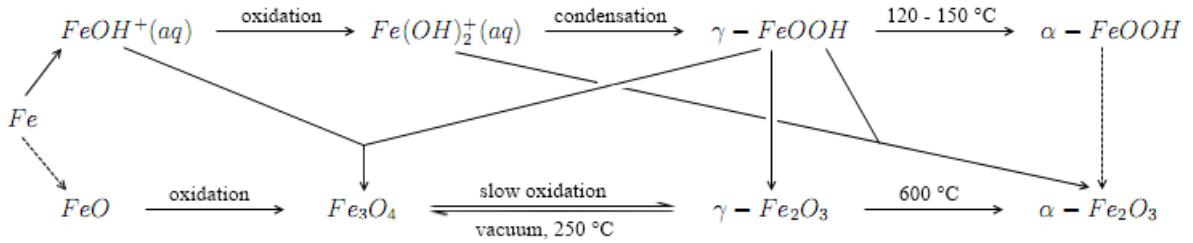
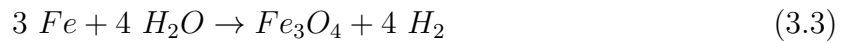


Figure 3.2: Ion species in the system iron/water according to Bohnsack.^[48]

A far more detailed description of the occurring reactions can be found in the literature.^[48,50] To simplify matters, magnetite generation is described by the following global reaction equation:



The strongly temperature dependent iron oxidation and corresponding layer growth is a finite process, which is controlled by ion diffusion. While in the early days of corrosion science magnetite was considered to be coating the base material, today topotactic and epitactic sublayers are distinguished, as depicted in figure 3.3.^[33,45,51]

Compared to the topotactic layer, which is quite compact and dense, the epitactic layer is porous and loose. Its coarse surface features a wide nucleation site spectrum able to enhance nucleation during nucleate pool boiling.^[33] When, with respect to the needed superheat, bubbles cannot be formed (convective boiling), the magnetite bilayer represents a resistance to the heat transfer. Under nucleate boiling conditions, both, enhancing and

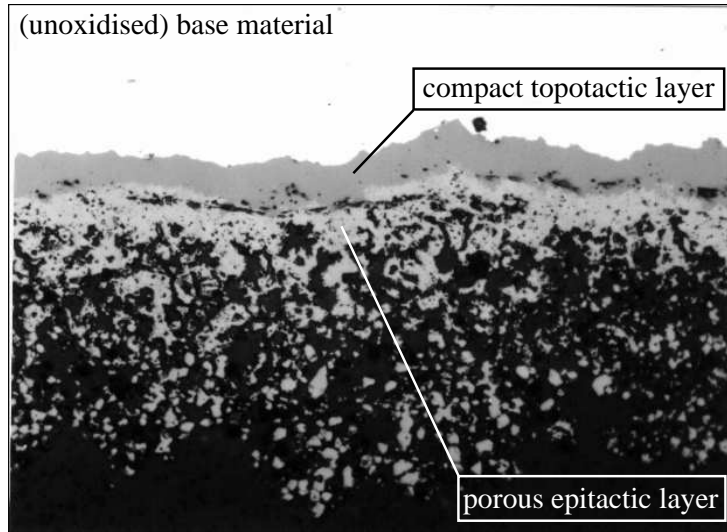


Figure 3.3: *Two-ply character of the magnetite layer: A typical exemplary structure on the inner surface of an evaporator tube (high-pressure flow boiler).*^[51]

impeding factors, occur simultaneously.

Hömig and other researchers report the overall magnetite layer thickness δ at operating temperatures above 200 – 300 °C to follow the function:^[47,51]

$$\delta^2 = \zeta \cdot \tau \quad (3.4)$$

with the operating time τ and a time constant ζ (data sourced from measurements). At even higher temperatures (beyond 570 °C), the magnetite layer development is considered “finished” after $\approx 50 h$ on stainless steel. On carbon and mild steel wustite is the dominating species at such high temperatures providing only small protection.^[52] In either case, corrosion does not come to a halt, but oxidation and transport of corrosion products from the surface are assumed in balance.^[47]

Below 200 °C the layer growth on steel surfaces can be described using a logarithmic law, which is characterised by rapid initial corrosion and a slower progression.^[47] During layer formation, dissolution and generation processes increasingly form an equilibrium, since ion diffusion, that is necessary for the corrosion process, is strongly impeded by the layer itself.

Steinbrecht et al. suggest an exponential approach to model the time dependence of layer formation indicated by thermotechnical measurement during convective and nucleate pool boiling. A thermotechnically verified steady state of the oxide layer during pool boiling can be expected within a time scale of several hundred hours depending on operational conditions at pressures up to 40 bar.

A feedback of oxidation on the nucleation characteristic was assumed as well.^[11,33]

Homogeneous and compact oxide layers, regarding their surface structure and morphology, are generally considered more advantageous over porous surfaces from a physicochemical point of view. They are estimated to provide a more efficient corrosion protection by a smaller absolute surface area and a more compact structure. Mentioned homogeneity, however, might be adverse in respect to nucleation, as only part of the cavity spectrum can be activated at a pressure under usual heat flux densities. The smaller the major fraction of cavities, the higher the boundary superheat has to become to eventually activate this cavity. This aspect is discussed later in this work (see section 7.4.2).

3.2 Classic inorganic feed water treatment

Corrosion induced malfunctions or damages can be avoided by maintaining protective passivating oxide layers and a defined water quality. The salt content directly determines anodic iron dissolution, while particles and organic substances are known to decrease the critical heat flux density. In order to ensure safe operation, the technical rule TRD 611 prescribes appropriate parameters for feed and boiler water quality by pH-value and electric conductivity β in shell boilers up to 68 bar (see table 3.1).^[9] In order to meet the

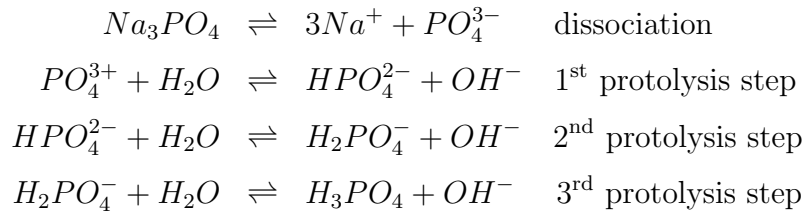
Table 3.1: *TRD 611 rules for the pH-value and the electric conductivity of the boiler water β in shell boilers up to 68 bar which are operated with salt-free feed water.*

Quantity	Dimension	Guidance level	Monitoring
β (25 °C) without strongly acidic sampling cation exchanger	$\mu S/cm$	< 50	continuous
β (25 °C) after strongly acidic sampling cation exchanger	$\mu S/cm$	< 150	discontinuous
pH-value (25 °C)	-	9.5 to 10.5	discontinuous, if necessary via auxiliary quantities

stated demands, solid and/or volatile alkalising agents are applied in shell boilers to attain the desired pH-value. As a solid alkalising agent trisodium phosphate (Na_3PO_4) is recommended instead of sodium or potassium hydroxide. In 1999 more than 70 % of the drum boilers and the majority of shell boilers have been operated with Na_3PO_4 .^[53] It exclusively

shifts the pH-value in the boiler water. The vapour phase is generally not affected. However, depending on the design and operation of the shell boiler, a sudden increased steam demand or system pressure drop (and respectively increased steam production) might lead to *carry-over* of non-volatile salts and deposits.

Na_3PO_4 concentrations of 7.5 – 15 mg/l are needed to adjust the pH-level in the boiler water to 9.5 - 10.5. Trisodium phosphate dissociates in water, i.e. the phosphate ion is subject to protolysis (in the following the reaction paths of sodium are neglected).



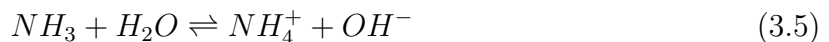
Three protolysis reactions are possible depending on the pK_s value (describing the acid dissociating strength), with products from hydrogen phosphate to phosphorous acid. All three reactions are leading to an increase of the pH-level in the water.

Besides alkalisation, sodium phosphate binds polyvalent scaling cations like Ca^{2+} or Mg^{2+} , which can be blown-down.²

Other solid alkalisating agents, like sodium- or lithium hydroxide, are dosed where applicable, if the desired pH-value cannot be maintained using Na_3PO_4 with respect to the maximum electric conductivity.

If pitting corrosion by oxygen is an issue in the boiler, highly volatile oxygen scavengers like hydrazine (N_2H_4) or organic equivalents like morpholine (C_4H_9NO) and diethylhydroxylamine, DEHA ($C_4H_{11}NO$) are added to the feed water neutralising oxygen. Such agents belong to the reducing agents, further impeding corrosion on the treated surfaces (see section 6).

Whenever high pressures are required, for example in flow boilers, usually the AVT (all-volatile treatment) using ammonia (NH_3) is the treatment of choice.



As mostly numerous parameters (pH-level of the boiler water and the condensate, direct and degassed electric conductivity of the water and the steam) have to be controlled in order to meet the requirements of turbine manufacturers or the limiting values in the

²Mentioned ions are not present in relevant quantities using salt-free water.

guidelines, proper instrumentation is important and dosing is often complex. Appropriate locations for the measurement have to be chosen and auxiliary quantities are often used, as the type of the applied inorganic feed water agents depend on the water quality, on the boiler setup and operation.

3.3 Treatment with film-forming amines

Ammonia derivatives suggest themselves as additives to the feed water, since they offer an alkaline character. But as ammonia is highly volatile, water quality has to be maintained high. If the quality decreases, alkalisation is also necessary for the boiler water, which cannot be provided properly by ammonia especially in shell boilers, where the steam/liquid ratio is relatively low. Most organic products on the basis of film-forming amines provide a composition of film-forming and alkalising amines of different volatility, alkalising the water as well as the steam part in a boiler. This effect can be substantiated as those fractions are detected in the condensate.^[13,23,24]

Long chain hydrocarbons with one or more amino groups have been developed and already applied successfully as film forming amines (FA) in different boiler types. Formulations used in the water-steam-cycle can be assigned to the substance class of oligoalkylamino fatty amines. They follow a general composition:^[15]



For monoamines (e.g. octadecylamine) factor $z = 0$, since there is no secondary amino group.

Mentioned amines feature an amphiphilic character consisting of a polar (amino group) and a non-polar (R^1 or $R^2 = C_xH_x$) molecular part. The former aspires to the polar water molecules, while the non-polar hydrocarbon chain opposes this behaviour. Because of the long hydrocarbon chain, fatty amines alone are hardly soluble in water. Additional substances are added in order to provide dispersion.

Film-forming amines accumulate on all kinds of interfaces and interphases and feature a strong affinity to steel surfaces.^[15] In contrast to the inorganic boiler water treatment, the dosing and analytics of film-forming amines is rather simple, as the detection of an excess of film-forming amines in the boiler water or the condensate indicates a complete corrosion inhibiting surface film (assumption).

The actual molecular arrangement on the boiler surfaces, however, is still being discussed. Frahne talks about uncoordinated (chaotic) adsorption immediately after dosing.^[12] With

proceeding time, lateral intermolecular forces as well as convection/flow are assumed to help forming a homogeneous layer on all boiler parts.

In contrast to washing tensides of comparable structure, the orientation of the film-forming amine molecules is assumed to be with their amino group towards the steel surface.^[13] The alkyl chain points into the water against its intrinsic preference, as figure 3.4 demonstrates for an exemplary mono- (ODA) and a diamine (oleylpropylenediamine). As the actual arrangement (angle between surface and amine molecule) is unclear, it is depicted simplified only.

The explanation for this behaviour is quite theoretical and not verified. Steel has a negative electrical potential in water. On the other hand nitrogen is a comparably electronegative element, inducing the dipole character of the amino group amplified by the so-called “+I effect” (electron-pushing effect) of the hydrocarbon chain, which further contributes to the polarity. Accordingly, the hydrogen atoms in the amino group are polarised positive. Consequently, an interaction between the steel and the amino group can be considered responsible in the first place.

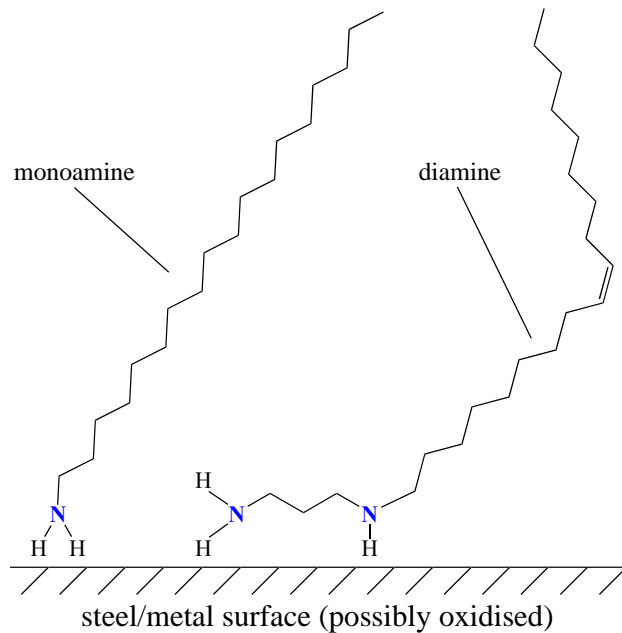


Figure 3.4: Generally accepted arrangement of film forming amines on a solid metal surface.

An electrostatic effect between the positively polarised hydrogen atoms and the negatively charged surface caused by anodic iron dissolution is possible. Such a scenario is applicable for an electric bilayer as found at metallic-blank surfaces. However, this is rather unsound in shell boilers, where an oxidised surface can be assumed.^[14] As ion diffusion is impaired by the oxidised surface, an electric double layer of sufficient potential is probably not present.

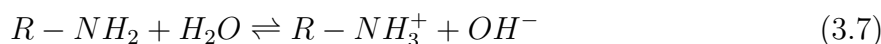
Another feasible explanation would be an interaction between the hydrogen atoms of the hydrophilic head group and the oxygen atoms in the oxide layer corresponding to hydrogen bonds. Furthermore, nitrogen carries an unbound electron pair, which might coordinate into the free d-orbital of the iron atoms.^[54]

Consequently, the mentioned theories comply with the general opinion that adsorption and

the corresponding corrosion inhibitory effect increases with the number of amino groups in the molecule. Di- and polyamines presumably “adsorb” to the surface in a more compact way. (Adsorption is not strictly correct as physical and chemical forces cause the molecule to spread on surfaces.)

As a conclusion, film-forming amine corrosion inhibitors of mentioned composition basically feature two distinct functional effects: On the one hand, the organic surface film can be assumed to prevent dissolved corrosion relevant ions from contacting the steel surface to some extent. On the other hand, a chemical inhibition is caused by the alkaline character of the film forming molecules influencing the electro-chemical potential of steel in water locally and thereby decreasing the rate of anodic iron dissolution. Small fractions of the FA component as well as the alkalisng amines form alkylammonium cations and hydroxide ions in water.

The following equation demonstrates this reaction in a simplified manner for the terminal amino group:



As film-forming amines belong to the group of surface active agents, they are not only able to disperse corrosion products and other particles, but might also enhance evaporation by decreasing the surface tension of the boiling water (see equation 2.2).^[55]

Preliminary tests using the du-Noüy ring method at atmospherical pressures and three temperatures show a reciprocal relation between the volume fraction of amine in the water and its surface tension as depicted in figure 3.5 exemplarily for the film-forming amine in *Cetamine*[®] V211.^[56]

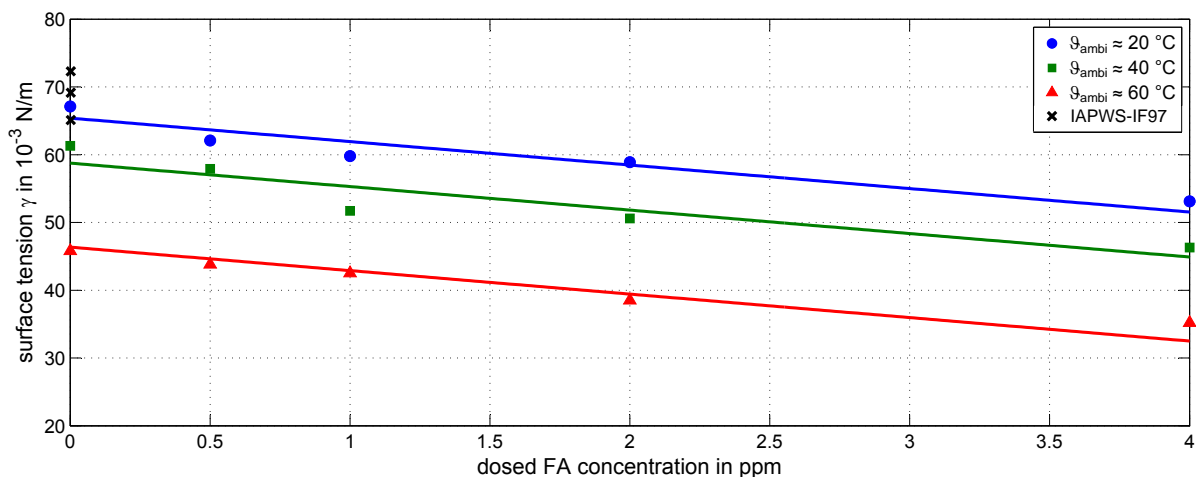


Figure 3.5: Experimentally determined surface tension of deionised water treated with the film-forming amine in *Cetamine*[®] V211 at an atmospherical pressure.

Although there is a slight disagreement between the experiment and literature data for pure

water,^[57] the effect of film-forming amines on the surface tension of water is significant. This behaviour can be assumed to influence nucleation and bubble departure under pool boiling conditions.^[55] A decrease in bubble departure diameter and an increase in bubble departure frequency is imaginable as observed by Steinbrecht et al.^[27]

4 Approaching a complex physicochemical issue

The individuality of steam generator equipment puts the regulations for water quality to a test, as corrosion rates and oxide layer properties highly depend on constructive aspects among many others.^[26] Even for two similar facilities, occurring corrosion products hardly match regarding their surface structure, thickness or composition connected with an individual transport and sedimentation of corrosion products.^[58] Consequently, prediction of corrosion processes and their effects on the heat transfer requires thorough investigation. Diverse ways are imaginable to converge a physicochemical context as investigated in this work.

4.1 Current state of research

4.1.1 Numerical simulation

Very popular today is the use of numerical tools to simulate the expected occurring physical processes mathematically in order to save time and experimental costs. Physical processes are therefore described mathematically by processing analytical or algebraic correlations for the physical quantities of interest.

Until today, a comprehensive and summary theory allowing prediction of the heat transfer coefficient during nucleate pool boiling at an accuracy necessary for technical purposes is still lacking.^[31] Currently, most correlations apply the similarity theory complemented by empirical constants that are modified to fit experimental data.^[59]

Yagov critically examines the feasibility of a theoretical numerical prediction of the nucleate boiling heat transfer.^[60] In conclusion, the author states that today strict numerical solutions cannot be applied for practical prediction of boiling processes as they are able to simulate particular internal processes in boiling but not the entire phenomenon, as required for technical purposes. Yagov does not see a change in this situation for the near future.

A lot of effort has already been spent by numerous work groups to numerically predict, for example, the onset of nucleate boiling, the heat transfer coefficient or the critical heat flux density during pool boiling.^[61–63] However, the necessary (simplifying) assumptions to even predict the heat flux transferred to the steam during nucleate pool boiling with an

exactly known number of nucleation sites are numerous. Validation results, mostly sourced from *artificial nucleation sites* experiments, show respectable agreement.^[64] Cylindrical, conical, and reentrant cavities are usually the reference. However, finding such a type of defined cavities on technical surfaces is rather unsound.

The surface conditions play a major role in the predictability of nucleate boiling processes. Untreated oxidised or machined metallic-blank metal surfaces, as found in the majority of steam boilers, cannot be predicted satisfactorily regarding their initial boiling characteristics, let alone their time behaviour during realistic operation under feed water treatment.^[30,43]

The first contact of a heat transferring surface with boiling water has a formative impact on all future nucleation processes during the onset of nucleate boiling. One and the same nucleus (nucleation site) will exclusively be reactivated whenever the critical conditions for nucleate boiling are satisfied.^[65] Steinbrecht et al. also assume a feedback of this first contact on the oxide layer development.^[33] Such influences have to be taken into consideration in any physically based model. Surface roughness and nucleation site density is of enormous importance when dealing with nucleate boiling phenomena.

Thermal conduction in multiple layers is a well known problem accessing a wide range of works on the necessary physical layer properties.^[31] Thus, theoretically the problem of thermal conduction through developing layers, for instance, can be solved analytically, whenever the respective physical properties are known. Although there are a lot of thermodynamic data of various materials, only few publications are available on, for instance, the thermal conductivity of magnetite or hematite and other corrosion products in steam generators.^[66–69] Published experimental data differ noticeably due to different origin of the experimentally analysed substances supporting the statements made on boiler individuality.

Manahan investigated iron oxide (magnetite) flakes from a pressurised water reactor regarding their thermal expansion and thermal conductivity.^[58] The uncertainty of the data reported is about 50 to 100 % for the three examined samples. Further studies were carried out regarding the effect of impurities on the thermal resistance of oxide layers. Remarkable effects were observed. Impurities are inevitable in steam generators due to differences in quality of steel, water and conditioning used. Thus, density, porosity and thermal conductivity of investigated oxide species differ from boiler to boiler. Figure 4.1 shows data from different researchers.^[58,70,71]

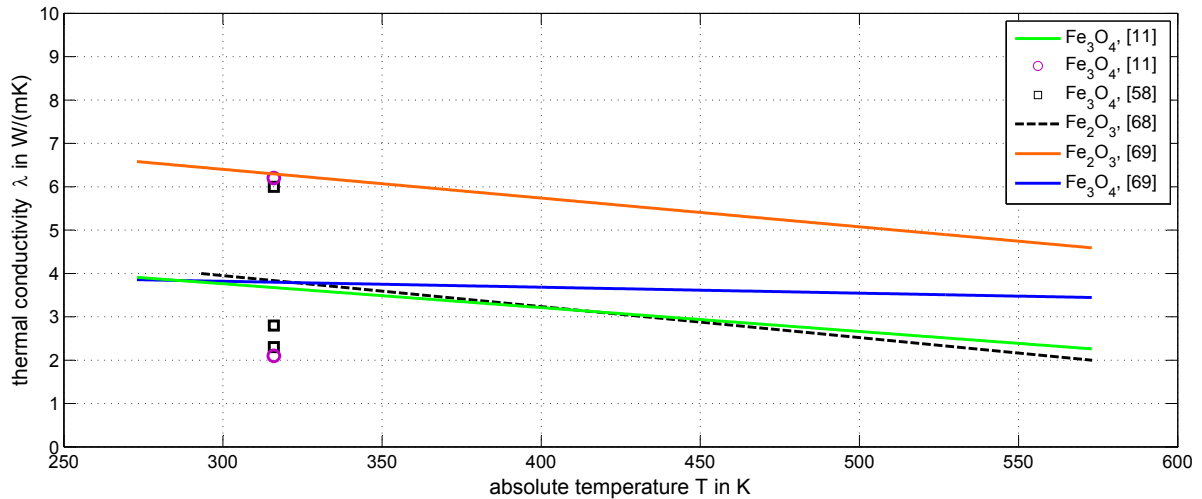


Figure 4.1: Literature values for the thermal conductivity of magnetite and hematite.

The layer composition might also vary significantly from hematite (Fe_2O_3) to magnetite (Fe_3O_4) or even iron hydroxide at lower saturation pressures. Complex reaction paths of crucial species like Fe^{2+}/Fe^{3+} and others as well as their corresponding counter ions during corrosion handicap numerical simulation.^[48] Chemical and flow processes as found in steam boilers often interact with each other, which induce changes in the pH-level, for instance. Large systems of coupled equations result and corresponding computing power has to be high.

4.1.2 Experiment

Since the layer composition and surface properties are hard to predict in shell boilers, experimental work under shell boiler conditions is favourable as it provides practical data. Experimental data is indispensable in order to predict physical or chemical processes in steam generators.

Realistic shell-boiler-like conditions can be established experimentally using a pressurised vessel equipped with a heat transferring surface and a manageable arrangement of temperature sensors. Since the surface properties of the heat transferring unit determine the boiling characteristics, a thermotechnical experimental arrangement of an electrically heated unit in a pressurised vessel accompanied by precise temperature measurement enables the characterisation of technically relevant heat exchanger surface properties.^[10,11,27,32,33]

Consequently, if water quality is maintained high and, besides corrosion, no further surface processes (e.g. scale) are taking place, the heat transmission from the heating surface to the boiling water is *exclusively* determined by steel oxidation. Given this condition and a steady state operation, such facility allows an experimental characterisation of the surface

properties via a thermotechnical approach.

Apart from surface modifications, the heat transfer during pool boiling is determined by the impressed heat flux, the operation pressure, and the inclination of the transferring unit.^[72]

As the basic case, in this work horizontal heat transferring surfaces are investigated.

Due to the fact, that corrosion is a process difficult to reproduce, a statistic approach is required. Considering an experimental approach, this might result in a remarkable expenditure of time.^[33,65]

4.1.3 Conclusion

Some of the coupled processes and conditions, that have to be simulated to gain information on heat transfer and layer development during pool boiling, are the following:

- local fluid velocity
- local temperature distribution near the heating wall (boundary layer)
- nucleation on metallic-blank surfaces with random nuclei arrangement
- temperature and pressure dependent bubble growth and departure from the surface
- species distribution, source and sink of (dissolved) ions
- chemical reactions (e.g. Schikorr), kinetics of solution and dissolution of the occurring species^[47,50]
- surface occupancy of film forming substances (mono-/multilayer arrangement)
- resulting oxide layer growth, feedback of bubble growth/fluid velocity

The stated list implies the knowledge of the corresponding boundary conditions. Considering the amount of chemical species, their reaction paths and coupled equations in an appropriate reaction mechanism, a numerical approach of long-term corrosion and thermo- or fluid dynamics on the corresponding processes is rather unpromising. Local particle velocities have to be calculated coupled with chemical interactions and bubble forming.

The charm of an experimental approach, in turn, is the straightforward access to crucial practical information including relevant physical quantities by Nukiyama^[29] (boiling) curves regardless of the composition and type the layers consist of. Therefore, an experimental thermotechnical approach is chosen to generate data not available until today, providing information on the interaction of conditioned water on steel heating surfaces and consequently on the linkage between corrosion processes and heat transfer in shell boilers.

5 Experimental determination of the heat transfer coefficient

Corrosion products on the heating surfaces as well as scaling salts or filming agents represent heat transfer resistances. The required boundary layer superheat for an onset of nucleate boiling is influenced significantly by surface morphology as well as by interaction of bubble nucleation and surface development.^[30,73]

Surfactants, like film-forming amines, are not only able to affect the bubble departure diameter and the bubble frequency, influencing the heat transfer during nucleate boiling but also the surface properties of a heating surface by dispersion.^[13,19,27] In the following paragraphs, the equipment used and algorithms applied for the experimental determination of the heat transfer coefficient α as well as the heat transmission coefficient k during the pool boiling of conditioned water are described.

The presented experimental setup has already been used in several works in a similar arrangement and the method has been validated by Steinbrecht et al.^[19,25,27,32,33,74,75] Therefore, an additional comparison of the experimentally obtained heat transfer coefficients with literature data and further evaluation for sources of error is renounced, as already described in detail by Steinbrecht.^[11]

5.1 Test setup and specimens

5.1.1 Apparatus

For the investigations of pool boiling phenomena two devices identical in construction are used. These facilities allow observations at system pressures up to $p_s = 40 \text{ bar}$ (limited by glass sight funnels for optional visual access). A directly resistance-heated seamless precision tube represents the heating surface, which is fully submerged in the boiling water.

Scheme 5.1 depicts the configuration of the apparatus including a detailed illustration of its internals. For the determination of the heat transmission coefficient the electrical current through the test tube (3), the inner tube temperature (11) and the saturation

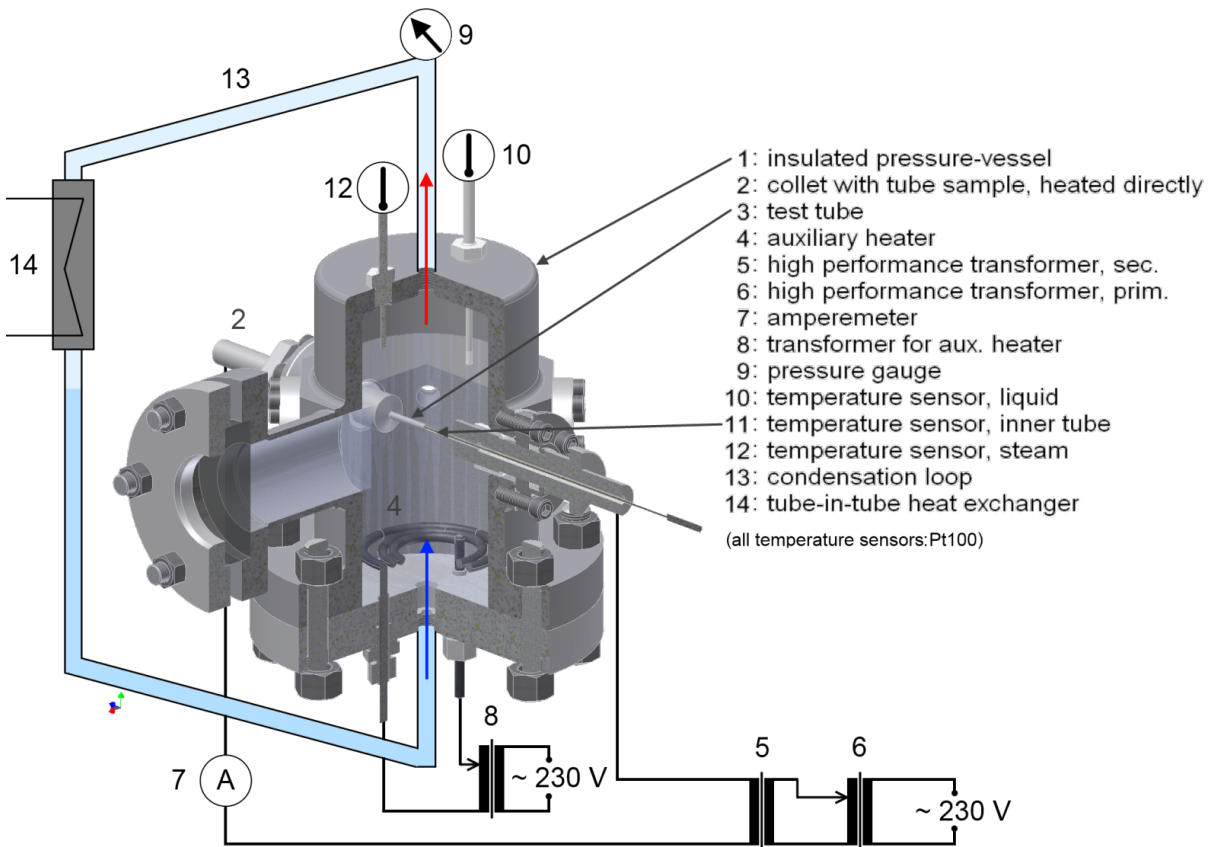


Figure 5.1: *Sectional view and schematic arrangement of the test setup.*

temperature of the steam (12) are required. These physical quantities, in turn, are evaluated by a numerical calculation (see section 5.2). The data acquisition is provided by a PC-supported data logger (LINSEIS LSB36 III). Both, steam and water temperature, are measured by Pt100-sensors of the type 1/5 DIN B (0 °C), while a calibrated Pt100-sensor (type DIN B) is applied for the inner tube temperature. The amperage through the test tube is measured by an inductive method using current transducers of class 0.5 quality. As, according to former works,^[11,33,43] the random error width of experimental data can be assumed large compared to the systematic error, further discussion of the systematic influence on the experiment is renounced due to the stated high quality acquisition. Both test facilities are operated fully independently, as they are equipped with a separate high performance transformer each, providing a maximum current of $I = 1550 \text{ A}$ at a low-potential voltage of up to $U = 5.0 \text{ V}$. Thus, heat flux densities up to $\dot{q} = 2 \cdot 10^6 \text{ W/m}^2$ (depending on the setup and operational conditions) can be impressed continuously variable with the use of the applied tube material described in section 5.1.2. The presented setup allows the assessment of convective boiling as well as nucleate boiling conditions. In certain conditions the critical heat flux density in nucleate pool boiling can be exceeded

(result: burn-out I, see section 7.5), depending on the electric properties of the steel.

The autoclaves feature a total volume of approximately 5 l each. In addition to the tube heating, an auxiliary heater is integrated into both vessels for stand-by and maintaining/adjusting the desired operating point.

A circular condensation loop serves as an external heat exchanger and ensures recirculation of volatile feed water agents. Two separate pipe-in-pipe heat exchangers are installed in parallel to grant steady state conditions during high heat flux impression. In turn, a detachable insulation, prevents significant heat losses to the environment at low thermal loads.

Furthermore, several optical accesses for visual observations optionally complement the facility and provide the ability to obtain digital video recordings of internal processes. Both vessels are equipped with diverse sampling points in the water and vapour phase.

Since parallel investigations can be carried out simultaneously, one vessel is used for inorganic operation (see section 6), while the other one is operated with the organic feed water agents to prevent contamination and cross-effects.

5.1.2 Tube samples

In the described test grid a directly electrically heated segment of a seamless steel tube represents the heat transferring surface. The applied tubes are DIN EN 10305-1 certified cold-drawn precision pipes. Made from St 35 BK (1.0308), the geometry of all investigated tubes is $d_a \times s = 6.00 \times 1.00 \text{ mm}$ consistently.

As integrated into the connectors by soldering with a silver hard solder, each specimen features a heated length of approximately 75-80 mm. The experimental determination of the released heat flux and the heat transmission coefficient is uninfluenced by the actual heated length (see section 5.2). However, fringe effects by soldering residues etc. can be avoided by positioning the inner tube sensor in the middle of the heated length, remote from the thermal impact of any deposits.

Extensive preliminary tests show, that pipes from one and the same fabricating process (melting and drawing) have to be used in order to exclude the influence of material and geometry tolerances on the reproducibility of the heat transmission behaviour (see sections 6 and 7).

Whenever a tube sample is referred to in the text: The names of the specimens follow a subsequent pattern. An identity number of the respective vessel (A1 or A2) is complemented by the consecutive number of the specimen. For example, A205 refers to the tube 05 being tested in apparatus number 2.

5.2 Measuring system

Assuming an impressed electrical heat flux density \dot{q}_A transferred from a tubular heating surface to surrounding coolant yields:

$$\dot{q}_A = \frac{\dot{Q}}{A} = \alpha \cdot \Delta\vartheta \quad (5.1)$$

Here, $\Delta\vartheta$ is the empirical temperature difference between the outer heating surface ϑ_o and the saturation temperature of the steam $\vartheta_s(p_s)$ and α is the heat transfer coefficient. The absolute thermal load is \dot{Q} and the outer tube surface is A . Knowing the heat flux density \dot{q}_A and the mentioned temperature difference, the determination of a steady state α can be carried out.

The temperatures of the saturated steam ϑ_s and the bulk liquid ϑ_l can be measured accurately by an appropriate high-quality sensor (here Pt100, 1/5 DIN B (0 °C)). A reliable and sufficiently precise measurement of the outer tube temperature ϑ_o via a physical sensor is impossible. By being located on the heated outer surface or even nearby, a sensor would have a dramatic impact on the processes within the boundary layer and on the heat transfer due to its sheer size. The local heat release as well as the surface properties would get compromised by such a sensor on the heating surface, since the micro geometry determines the distribution and the arrangement of the nuclei during nucleate boiling. In this case, nucleation, development and departure of the bubble would *not be representative* for the physical processes on a real tube surface.

The heating surface's outer temperature ϑ_o must therefore be determined based on the measured inner tube temperature ϑ_i combined with the temperature dependency of the steels heat conductivity. This method is only valid, if the heat is transferred exclusively across the outer tube surface. Transfer across the inner face must be prevented by appropriate means (i.e. by a ceramic thermal insulation closing the physical gap between the temperature sensor and the inner tube). Consequently, there is not any higher temperature than the inner tube wall temperature, measured precisely by a resistance thermo sensor (Pt100, DIN B, calibrated). Even though the idea of a homogeneous outer surface temperature is unsound due to large local temperature gradients in the material (during nucleate boiling) and the boundary layer, determination of a representative steady state average inner heater temperature allows to determine a technically relevant temperature on the outer surface. The impact of any gradients $d\vartheta_o/dt$ are, literally smoothed by the material heat capacity using an inner tube wall temperature measurement.

In case electric heating is applied for tube heating in an experimental scale to simulate

the heat flux throughout the wall, this method is sufficiently accurate for steady state conditions applying a current measurement, as long as a fair length of the tube is being heated. That means, homogeneity of the mean tube temperature can be assumed for the entire heated tube length. Furthermore, any significant heat transfer to the inside tube needs to be excluded by the mentioned inner thermal insulation.

The current supplying parts of the setup must be electrically insulated from the vessel walls to prevent electric bypass and erroneous determination of the thermal load. For this purpose an electric resistance of $R > 10^6 \Omega$ is considered sufficient as verified by a resistance measurement before and during the experiment.

The three-dimensional problem of heat transfer from a tubular heating surface to boiling water in the described setup can be reduced by the tube length, if the described pre-conditions are met. A precise temperature and electrical current measurement enable the determination of the heat transfer coefficient between the outer tube wall and the boiling liquid as well as the heat flux density.

5.2.1 Determination of the outer tube surface temperature

In the following, a tube section of the length l with an inner radius r_i and an outer radius r_o is assumed, in which heat sources with a volume-related heat flux \dot{q}_v are distributed homogeneously. If the inner tube surface is thermally insulated and convective heat transfer is prevented, heat is only transferred across the outer surface of the tube, which is essential for the described method. Assuming homogeneous heating, an infinitesimal circular layer with a thickness of dr is considered at the radius r , restricted by isothermal faces (see figure 5.2).

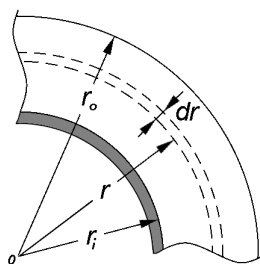


Figure 5.2: *Cross-sectional view of a heated tube wall with an inner thermal insulation (grey).*

Assuming steady state heat transfer, Fourier's law applies for the heat flux crossing the isothermal interface of the infinitesimal thin section of the tube wall with the length l :^[28]

$$\frac{\dot{Q}}{2\pi r \cdot l} = \dot{q}_A = -\lambda \cdot \frac{d\vartheta}{dr} \quad (5.2)$$

The volume-related heat flux \dot{q}_v is related with the area-specific heat flux \dot{q}_A , the heat flux density, as follows:

$$\dot{q}_v = \dot{q}_A \cdot \frac{2r}{r^2 - r_i^2} \quad (5.3)$$

Considering countless homogeneously distributed heat sources \dot{q}_v inside the tube wall volume V yields the following equation for a 1-dimensional temperature gradient $d\vartheta/dr$:

$$\frac{d\vartheta}{dr} = -\dot{q}_v \cdot \frac{r^2 - r_i^2}{2\lambda r} \quad (5.4)$$

The separation of variables yields:

$$d\vartheta = \frac{\dot{q}_v \cdot r_i^2}{2\lambda} \frac{dr}{r} - \frac{\dot{q}_v \cdot r}{2\lambda} dr \quad (5.5)$$

Evaluation of equation 5.5 shows a temperature gradient of zero for $r = r_i$. This is fundamental for the experimental determination of the heat transfer coefficient. There is no temperature higher than the inner tube temperature ϑ_i , which can be measured. The temperature gradient $d\vartheta/dr$ becomes zero at $r = r_i$ for an infinitely long tube allowing calculation of the outer tube wall temperature. In the experimental setup, a thermal insulation prevents the heat transfer across the inner tube surface.

Integration of equation 5.5 results in:

$$\vartheta = \frac{\dot{q}_v \cdot r_i^2}{2\lambda} \ln r - \frac{\dot{q}_v \cdot r^2}{4\lambda} + C \quad (5.6)$$

where C is an integration constant.

This constant C can be obtained via the boundary conditions for the measured inner tube temperature. Here, $r = r_i$ and $\vartheta = \vartheta_i$:

$$C = \vartheta_i - \frac{\dot{q}_v \cdot r_i^2}{2\lambda} \ln r_i + \frac{\dot{q}_v \cdot r_i^2}{4\lambda} \quad (5.7)$$

The introduction of equation 5.7 in 5.6 yields:

$$\vartheta = \frac{\dot{q}_v \cdot r_i^2}{2\lambda} \ln r - \frac{\dot{q}_v \cdot r^2}{4\lambda} + \vartheta_i - \frac{\dot{q}_v \cdot r_i^2}{2\lambda} \ln r_i + \frac{\dot{q}_v \cdot r_i^2}{4\lambda} \quad (5.8)$$

Having subsumed and introduced the respective variables at the outer face of the tube $r = r_o$ and $\vartheta = \vartheta_o$, the difference between the inner tube temperature ϑ_i and the outer

tube surface temperature ϑ_o can be evaluated:

$$\vartheta_i - \vartheta_o = \frac{\dot{q}_v \cdot r_i^2}{4\lambda} \left[\left(\frac{r_o}{r_i} \right)^2 - 2 \ln \frac{r_o}{r_i} - 1 \right] \quad (5.9)$$

Substitution of the volume specific by the area specific power yields:

$$\vartheta_i - \vartheta_o = \frac{\dot{q}_A}{\lambda} \cdot \frac{2r_a}{r_o^2 - r_i^2} \cdot \frac{r_i^2}{4} \left[\left(\frac{r_o}{r_i} \right)^2 - 2 \ln \frac{r_o}{r_i} - 1 \right] \quad (5.10)$$

Since the majority of terms in equation 5.10 depends only on constant geometric variables, these terms can be concentrated in a constant (geometry constant, K_R). Here, a developing oxide layer does not influence the measurement, as, using the geometry of the bare steel tube and the thermal conductivity of the mentioned, the outer steel temperature rather than the oxide surface temperature is being determined.

Then, the simplified equation for the outer wall temperature is:

$$\vartheta_i - \vartheta_o = \frac{\dot{q}_A}{\lambda} \cdot K_R \quad (5.11)$$

5.2.2 Determination of the heat transfer coefficient

If equation 5.1 is complemented by expression 5.11, it can be applied for the desired heat transfer coefficient in the case of a metallic-blank surface:

$$\alpha = \frac{\dot{q}_A}{\vartheta_i - \frac{\dot{q}_A}{\lambda} \cdot K_R - \vartheta_s} \quad (5.12)$$

Introducing the rating equation for electric resistances,^[76] \dot{q} is found with:

$$\dot{q} = \frac{\xi(\vartheta_m) \cdot \frac{l}{A_{cross}} \cdot I^2}{A_s} \quad (5.13)$$

The specific electric resistance ξ and the heat conductivity λ are dependent of the local/mean wall temperature $\xi(\vartheta_m)$, $\lambda(\vartheta_m)$; with the average wall temperature ϑ_m :^[34]

$$\vartheta_m = \frac{\vartheta_i - \vartheta_o}{\ln \left(\frac{\vartheta_i}{\vartheta_o} \right)} \quad (5.14)$$

According to equation 5.12 and given the temperature dependence of ξ and λ , the presented method represents an implicit approach to α . The solution is carried out in an iterative way. The iteration routine, proof of convergence and evaluation can be found in the appendix A.

An advantage of the presented method is its independence of the heated tube length, since the electric resistance as well as the heat flux density are determined by it. The tube length is eliminated mathematically. Possible disparities of single tubes during the assembly process do not affect the method's accuracy.

5.2.3 Determination of the heat transmission coefficient

In the case of a developing or already built-up layer of finite thermal conductivity, the heat transfer coefficient α turns into a heat transmission coefficient k . This heat transmission coefficient is of major importance compared to the heat transfer coefficient from the oxidised surface to the water, as it describes both, the heat transfer and the heat conduction in the layer.^[11]

The value of k can be determined the identical way without further knowledge of the layer properties. The in-line heat transfer resistance of the layer on the heating surface causes an increase of the inner tube temperature compared to the metallic-blank sample. This increased value of ϑ_i is measured by the sensor for inner tube wall temperature.

Picture 5.3 shows a schematic intersection view of the test tube with the inner temperature sensor and a qualitative temperature profile between the inner tube wall and the boiling water under convective pool boiling conditions: *a)* demonstrates the first contact of the bare steel tube with boiling water, *b)* depicts the system after a certain layer generation. For the statements on the temporal impact of the layers thickness on the heat transfer, the convective part of boiling is used. In a steady state, the surface temperature on the outside of the layer ϑ_{oL} equals the surface temperature ϑ_o of the metallic-blank tube, since the stationary convective heat transfer remains uninfluenced by the surface type and morphology.^[11]

This yields:

$$k = \frac{\dot{q}}{\vartheta_i - \frac{\dot{q}}{\lambda} \cdot K_R - \vartheta_s} \quad (5.15)$$

The heat transmission coefficient becomes:

$$k = \left(\frac{1}{\alpha} + \frac{\delta}{\lambda_L} \right)^{-1} \quad (5.16)$$

with the layer thickness δ and the average heat conductivity of the layer λ_{Lm} . The fraction δ/λ_L is named *fouling coefficient* and describes the growing layer. The heat transmission coefficient k becomes α for $\delta/\lambda_L = 0$.

The convective boiling heat transmission coefficient is influenced by the heat transfer impeding character of the oxide layer only. In theory, the time discrete value $k(\tau)$ can be

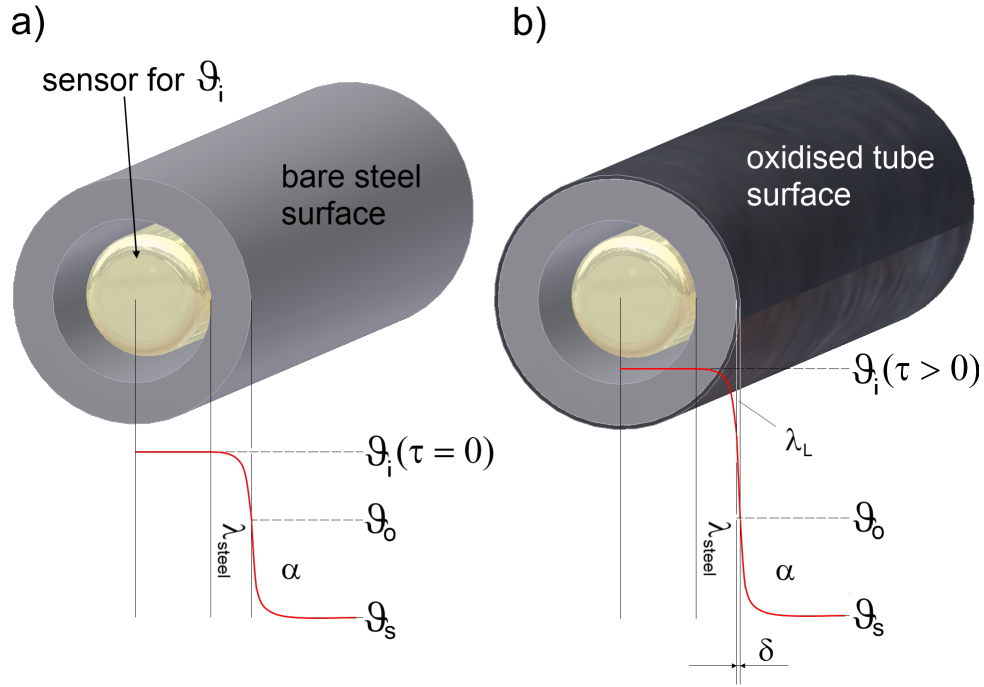


Figure 5.3: *Qualitative temperature profile radial to the tube heating surface during convective pool boiling, (a): metallic-blank surface, (b): existing magnetite layer.*

compared with the initial heat transfer coefficient $k(\tau = 0) = \alpha$ in order to calculate the developing layer thickness δ .

According to equation 5.16, the size of k is determined by the convective heat transfer coefficient α and by the heat conductivity λ . As steady state heat transfer during convective pool boiling remains unaffected by layer generation,^[33] the temperature of the outer metallic-blank surface $\vartheta_o(\tau = 0)$ at the start of layer generation equals the layer surface temperature $\vartheta_{oL}(\tau > 0)$ during oxide layer development.

Thus, assuming a constant thermal conductivity of the oxide layer, its thickness δ can theoretically be calculated by the following expression:

$$\delta(\tau) = \lambda_L \left(\frac{1}{k(\tau)} - \frac{1}{\alpha} \right) \quad (5.17)$$

The values of k and α are obtained based on experimentally determined quantities. The mean layer temperature, as it is needed to calculate the layer's thermal conductivity, is derived from the iterative determination of the outer tube wall temperature. Consequently, the validity of equation 5.17 has to be verified by other means, like microscopic methods. The thermal conductivity λ_L is also a function of the (average) layer temperature, porosity and composition, crystal orientation and sample density.^[11,58,69,71] The layer temperature,

in turn, correlates with the impressed heat flux density \dot{q} . Given the scattering of literature values, $\lambda_L(\vartheta)$ is assumed comparable for the expected species magnetite and hematite.

Since the layer porosity plays an important role for the process of nucleation, calculated δ by using existing literature values for λ_L is assumed to reflect an apparent quantity only.^[11] The oxide layer's duality cannot be apprehended by mentioned convective boiling experiment.

Neither the actual (summary) thermal conductivity of the assumably porous layer nor its thickness are known for sure. Thus, analytical methods have to be applied in order to gain information on the true layer thickness. As a consequence, retrograde calculation of the true thermal conductivity is imaginable and, given the assumed porosity, must be expected lower than stated in the literature.^[11,33,58,69,71]

The presented method is valid for a small layer thickness only, as, derived from the previous algorithm, the geometry of the electrically heated steel surface (conductor) are assumed to maintain unaltered during operation. This is unsound, since, in the case of magnetite, an oxide layer, which is formed on the surface, consists of an epitactic and a topotactic sublayer. Given the accordance between thermal and electric conductivity, magnetite is a rather poor electrical conductor.^[77,78] Consequently, if a layer is present, the actual heater resistance comprises a metallic conductor of a reduced diameter, compared to its original unoxidised surface, and both oxide sublayers of an increased electrical resistance, connected in parallel. See figure 5.4 for a simplified model of the actual arrangement.

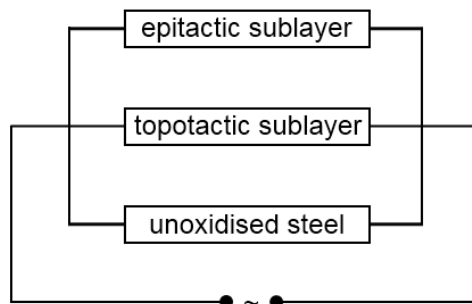


Figure 5.4: *Model of the actual electric resistance configuration as caused by the oxide layer development.*

With respect to this model, if an oxide layer is present, an apparent outer wall temperature is calculated, which differs from the actual value. The thermal conductivity is affected, analogously. Given a measured oxide layer thickness of $\delta \ll 30 \mu m$, as discussed in chapter 7, the influence of the layer on the accuracy of the method is considered negligible, if compared to the expected spreading width of experimental data.^[11]

5.3 Method of comparing the experimental data

5.3.1 Standardisation of the heat transmission coefficient

Comparison of the discrete heat transmission coefficients k under the influence of different conditionings or after certain periods during the same treatment is difficult to establish, because the respective heat flux densities are determined not only by the impressed electric current (see section 5) but also by the operating pressure, oxide layer development and random influences, every experiment is subject to.

Figure 5.5 depicts an exemplary band of boiling curves at $p_s = (2, 5, 10, 15) \text{ bar}$ to demonstrate the pressure influence on the heat flux density as one factor.

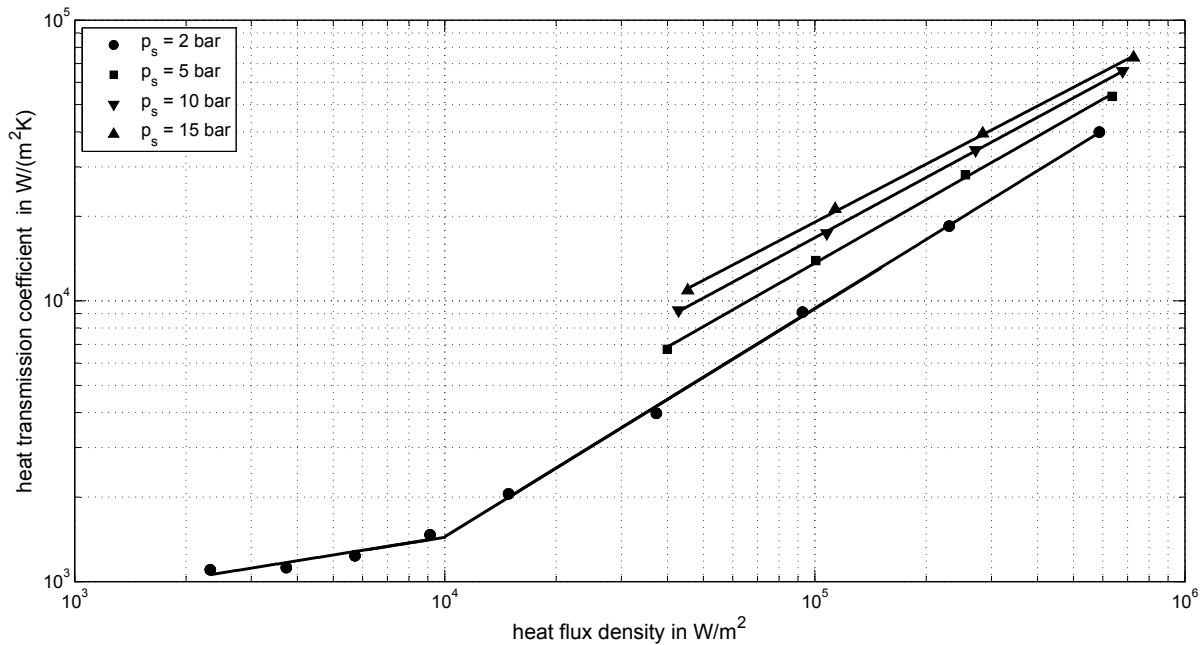


Figure 5.5: Band of boiling curves as a result of impressing fixed electrical currents (see chapter 6).

According to figure 5.5, the saturation pressure (saturation temperature) influences the electrical resistance, being a function of the tube wall temperature. With rising saturation temperature, the tube wall temperature increases correspondingly, resulting in a comparably higher specific electric resistance. Given this resistance, a lower amperage satisfies for a similar heat flux density.

Referring to Steinbrecht and Schlünder, slightest differences in the surface properties and corresponding heat transfer conditions result in a considerable spreading width, even if the very same tube material, pretreatment and preheating gradient $dT/d\tau$ are applied.^[11,30] Consequently, the heat transfer behaviour differs from sample to sample even worsening

the problem of aiming at an certain operation point. This issue is affecting every data set $k(\dot{q})$: The heat flux density is determined by the actual heat transmission coefficient from the tube to the coolant k , obtained for the applied fixed amperages (see section 6).

Diagram 5.6 shows the time response $k(\dot{q}, \tau)$ at a saturation pressure of $p_s = 15 \text{ bar}$.

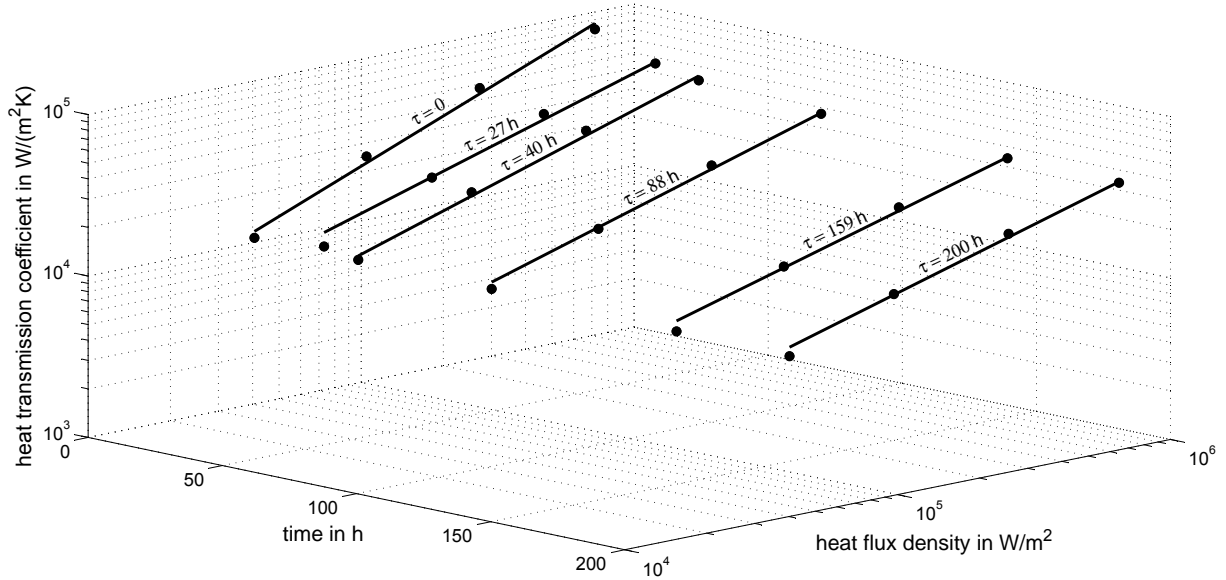


Figure 5.6: *Development of exemplary boiling curves at $p_s = 15 \text{ bar}$.*

However, the resulting operation points \dot{q} as well as the corresponding heat transmission coefficients k belong to the identical time and pressure discrete boiling behaviour, unless the boiling region is exceeded (see chapter 6 for the precautions). The very boiling characteristics then can be modelled by a boiling curve, regardless of the actually impressed heat flux density. Therefore, the experimental data $k_i(\dot{q}_i)$ undergoes a power-law regression $k(\dot{q}) = C \cdot \dot{q}^n$ for every distinct measuring time τ and pressure stage. As a result, each boiling curve contains two random erroneous coefficients (C , n) for the respective boiling regime. Consequently, the presented boiling curves in figure 5.6 are difficult to compare, because the exponents $n = f(\tau)$ of the consequent curves differ.

In order to establish comparability, *only one* characteristic coefficient C_{red} , which is representative for the investigated treatment time, saturation pressure, type of treatment and boiling region, is gained by a normalisation procedure of z data pairs $k(\dot{q})$ using a fixed average exponent $\bar{n}(p_s)$:^[11]

$$C_{red}(\tau, p) = C|_{\tau, p} = \frac{1}{z} \sum_{i=1}^z \frac{k_i}{\dot{q}_i^{\bar{n}}} \quad (5.18)$$

That is to say, the resulting reduced heat transmission coefficient C_{red} represents a standardised heat transmission coefficient for $\dot{q} = 1 \text{ W/m}^2$. Derived from regression, C_{red} can

be considered a projection of the boiling curve along its slope onto the $(k - \tau)$ -plane. The dimension of C_{red} follows equation 2.4 with $[C_{red}] = 1 K^{-1}$.³

The proposed mathematical expression allows a quanti by evaluating the reduced heat transmission coefficients $C_{red}(\tau, p)$ with respect to the following conditions:

- The exponent $\bar{n}(p)$ remains approximately constant during the treatment for the respective boiling regime.
- The measurements are carried out at similar heat flux densities.

Since this reduction includes an extrapolation of $k(\dot{q})$ to the axis intercept $k(\dot{q} = 1 W/m^2)$, a simplified demonstration (see figure 5.7) can be achieved for the same data set. For each examined boiling region the presented method gains one characteristic time, pressure and feed water treatment dependent coefficient C_{red} reduced by the influence of the heat flux density.

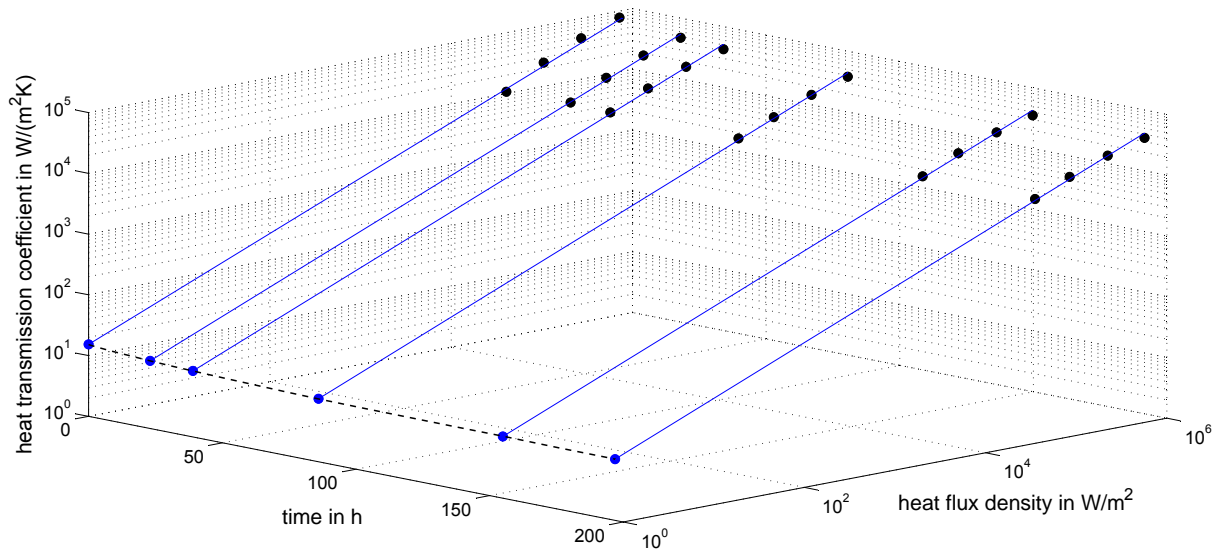


Figure 5.7: Normalisation of k to the reduced heat transmission coefficient C_{red} by regression and extrapolation.

³Whenever stated in the text, the quantity C_{red} will appear without a dimension for clarity reasons.

5.3.2 Influence of the exponent on the comparability

The boiling curves exponent $n(p)$, which is sourced from the regression, might be subject to temporal changes caused by modifications of the nucleation characteristics for different kinds of water treatment or during the identical conditioning ($n = f(p, \text{treatment})$). In the previous section, for instance, a fixed exponent was introduced. Calculation of C_{red} allows re-calculation of k only for an exponent featuring neglectable change during operation. However, in the case of a (steady) chronological change $dn(p)/d\tau$ due to surface processes affecting nucleation characteristics, fixation of n is conditional. It is still advantageous in regard to obtain comparability of normalised heat transfer levels under different types of feed water treatment.

Figure 5.8 demonstrates the result of using a fixed \bar{n} different from the result of unmodified regression. The achievement is a rotation of the boiling curve around a fixed pivotal point

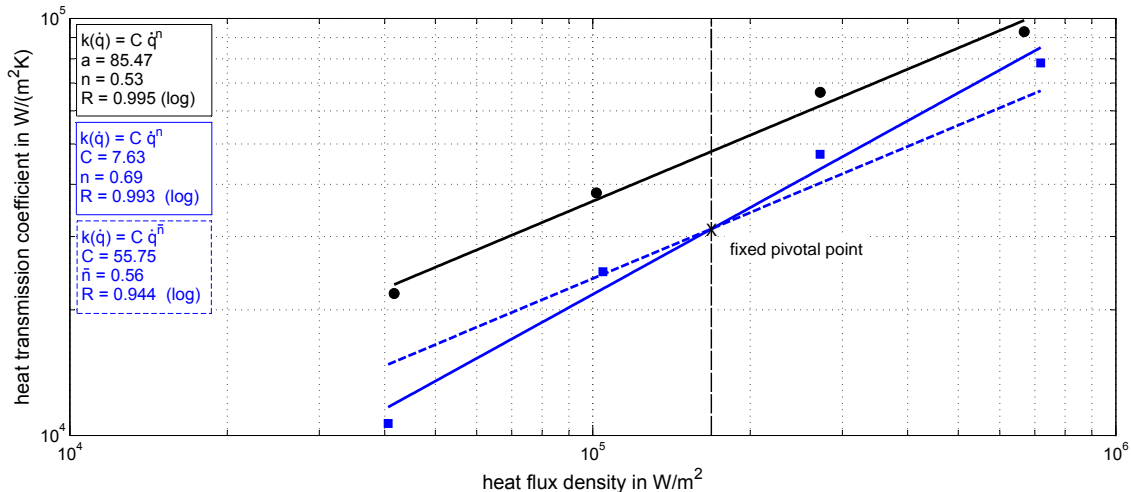


Figure 5.8: Regression of $k(\dot{q})$ using a fixed exponent \bar{n} resulting in a rotation around a characteristic pivot. Improved comparability of C_{red} is achieved by parallelisation of the boiling curves at different τ .

at $\dot{q} \approx 160 \cdot 10^3 \text{ W/m}^2$ that is typical for the series of predetermined heat flux densities and relevant for technical applications.

After reduction with a fixed exponent, the resulting C_{red} is thereby normalised to the according reference. Rotation at a fixed \dot{q} helps to establish comparability of C_{red} with actually different exponents. Apart from violating the remaining heat flux densities and the respective heat transmission coefficients the benefit of this procedure is an improved general comparability of C_{red} by 'parallelisation' of the boiling curves.

However, an accurate re-calculation of k by using the modified regression equation, is obviously impossible using a fixed exponent, which is different from the actual exponent

from regression. In order to compare the discrete differences between the boiling curves of distinct water treatments the respective statistically firm boiling curves have to be used.

5.3.3 Time response of the heat transmission coefficient

In order to identify the impact of a certain treatment on the heat transfer, the time necessary to gain thermotechnical steady state conditions of the heat transmission coefficient is of interest, after the desired treatment was initiated. When oxidation processes on the heating surface are the only cause for a decline in k , as it is the case in this study, the mentioned period is an indication for the interaction rate of surface and coolant. Thus, the kinetics of surface modification can be determined via parallel thermotechnical determination of k .

An exponential decay function is used (see figure 5.9) to describe the development of $C_{red}(\tau)$ providing good agreement:^[11]

$$C_{red}(\tau) = C_{\infty} + \Delta C \cdot \exp\left(-\frac{\tau}{\kappa}\right) \quad (5.19)$$

With τ as the treatment period, C_{∞} as the steady state boundary value of C_{red} and κ as the time constant, the systems time response on the feed water treatment can be modelled.

With respect to the expected scattering for $C_{red}(\tau)$ of about ± 25 %, as stated by Steinbrecht for demineralised water,^[33] a convention regarding an appropriate abort criterion is needed to mark a stationary state. In this case an analogy to electric capacitors is used. Discharging of capacitors with an in-line shunt is classified by the period $x \cdot t$, necessary to achieve a certain capacitor voltage compared to the direct voltage as multiple of the Euler number e .^[79] Here, t is the time constant of discharge.

As long as there are no additional requests, a discharge process is considered complete after $1 \cdot t$, when a voltage ratio $u(t)/U_{max} = 36.8$ % is reached.

Further characteristic discharge points are:

$$\begin{aligned} u(3 \cdot t)/U_{max} &= 4.98 \%, \\ u(4 \cdot t)/U_{max} &= 1.83 \% \text{ and} \\ u(5 \cdot t)/U_{max} &= 0.67 \% \end{aligned}$$

A period of $5 \cdot t$ equals a discharge of 99.3 %. For simplification reasons, a 99 % decrease of C_{red} regarding the boundary value C_{∞} is chosen as abort criterion. Thermotechnically

indicated steady state of the tubes properties can be assumed for:

$$C_{red}(\tau) = C_{\infty} + 0.01 \cdot \Delta C \quad (5.20)$$

The time τ_{99} necessary to achieve such stationarity is calculated accordingly:

$$\tau_{99} = -\kappa \cdot \ln(0.01) \quad (5.21)$$

As the distinct types of water treatment feature dissimilar chemical water qualities, their effect on the values of τ_{99} can be expected different, too. Development of the reduced heat transmission coefficient and τ_{99} of a phosphate treated tube are displayed as an example in diagram 5.9. Development of the exponent n determines a change in the

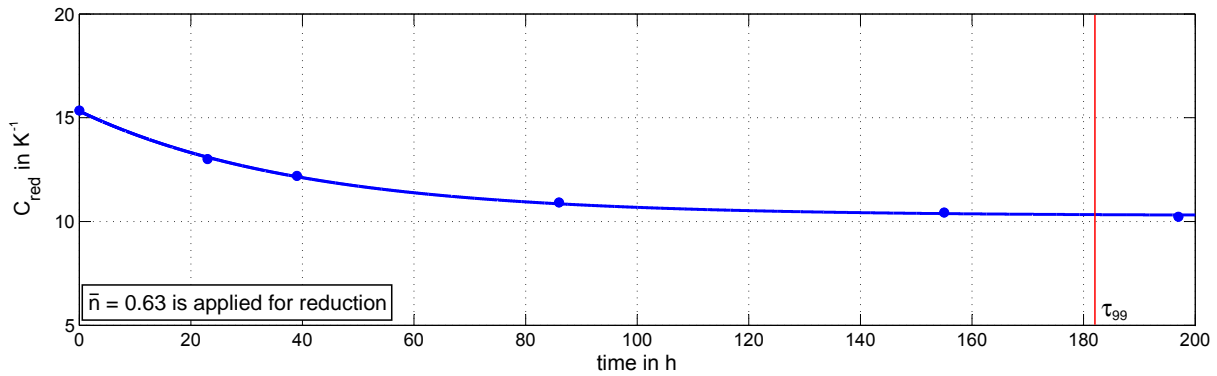


Figure 5.9: Exemplary development of C_{red} at $p_s = 15$ bar. Approximation by the exponential decay in equation 5.19 yields the time scale τ_{99} necessary to achieve a steady state of heat transfer.

boiling characteristics and can be considered proportionally responsible for the decline of the heat transmission coefficient. Corresponding to this, if there is a noticeable change in the exponent during treatment, it is assumed to follow the similar asymptotic behaviour as for C_{red} . Therefore, if applicable, an identical time constant κ is used to describe its exponential development during operation.

5.3.4 Statistical evaluation

As experimental data are subject to random influences, a certain statistical evaluation is necessary. The characteristic standard instrument, used to describe the significance of the regression/models used in this work, is the relative mean deviation σ .

When the experimentally determined values X_i in a random sample of N values are independently *normally distributed* around their average \bar{X} , which represents the expectation value $X := \bar{X}$, their mean standard deviation S_X is defined as follows:^[80]

$$S_X = \sqrt{\frac{1}{N-1} \sum_{i=1}^N (X_i - \bar{X})^2} \quad (5.22)$$

When measurements are carried out at different locations/operation points j , which belong to the same random sample, these values can have different averages. Finding a global expectation value can be difficult. To establish comparability for these values, a relative mean deviation σ is derived, using the deviation of X_i relative to the respective average \bar{X}_j :

$$\sigma = \sqrt{\frac{1}{N-1} \sum_{i=1}^N \left(\frac{X_i}{\bar{X}_j} - 1 \right)^2} \quad (5.23)$$

The true value of the quantity X is assumably located inside the boundaries $\pm\sigma$, which contain 68.3 % of the values from the random sample. This relative mean deviation σ will be used to describe the significance of experimental data in this work. If applicable, σ is complemented by the maximum deviation ε_{max} , which is of minor statistical relevance.

Whenever the result of a regression model X_{calc} is chosen as the expectation value, depending on the quality of the model, this expectation value might differ from the experimental average value. If there is not any better model at hand, the experimentally obtained values X_i are consequently not normally distributed around the calculated value X_{calc} anymore. In this case, the relative mean deviation σ is used nevertheless, in order to provide an instrument of comparability. As a result of this, the determined value of σ is expected larger for $X := X_{calc}$ than for $X := \bar{X}$, because it is acentric compared to \bar{X} .

6 Design of investigations

In the following, the influence of classical inorganic and organic feed water agents on the heat transfer under pool boiling conditions is being investigated. Therefore, different scenarios have to be assayed in order to simulate practically relevant conditions. While under inorganic treatment the heat transferring surfaces are conditioned starting from a bare steel surface, two dissimilar scenarios are simulated using film-forming amines. At a first instance, the long-term heat transfer behaviour of metallic-blank specimens will be studied simulating the operation of a new shell boiler. Secondly, a turnover from an inorganically operated shell boiler to the film-forming amine treatment will simulate a treatment switch.

The saturation pressure, at which the impact of conditioned feed water is investigated, is chosen as $p_s = 15 \text{ bar}$ ($\vartheta_s = 198.29 \text{ }^\circ\text{C}$). This is a typical pressure stage in industrial shell boiler applications and complies with the requirements of the Schikorr reaction, $\vartheta_s > 180 \text{ }^\circ\text{C}$ (regardless of the applied conditioning).^[27]

As time and pressure discrete boiling curves of the type $k(\dot{q}) = C \cdot \dot{q}^n$ need to be calculated from measured data, criteria for the number and type of operation point need to be defined for the measurement.

While an additional layer of iron oxide tends to impair the heat transfer during convective boiling as a heat transmission resistance, its surface morphology (roughness) improves nucleation by offering a wide range of nucleation sites.^[33,65] Although both, heat transport impeding and promoting effects, occur simultaneously during the experiment, the distinct boiling regions (see section 2) can be assayed to distinguish between benefit and handicap of the bare steel surface and a possible layer.^[32]

Each boiling curve $k = f(\dot{q})$ comprises infinitely many data sets and the more data introduced in the regression, the better the significance of the model. However, since one boiling curve is considered characteristic for the entire investigated boiling regime, the assayed heat flux densities can be reduced to a manageable number and characteristic location, where the requirements for significance can be fulfilled on the one hand and following conditions on the other hand:

1. In order to avoid a significant impact of any surface processes (e.g. corrosion) during the measurement, only a few operating points are held for a shortest possible period.
2. The operating points \dot{q} must be sufficiently apart from the borders to the adjacent boiling region.
3. Measurements are carried out with descending thermal loads in order to prevent hysteresis of nucleation. (Relevant only for pressures where both, convective and nucleate boiling, can be put into practice.)

Hence, a maximum number of nine chosen representative operation points is investigated at the respective saturation pressure and treatment period τ .

As discussed before, an impression of the very same heat fluxes at different pressures and/or treatment periods is impaired by developing thermal and/or electric heater properties during oxide generation. A real-time evaluation of the heat flux density and according operation cannot be provided by the setup used. As an alternative, fixed electrical currents are applied instead, which are evaluated for the calculation of \dot{q} . Preliminary tests at $p_s = 2 \text{ bar}$ during phosphate treatment provide the corresponding amperages for the desired thermal loads. Table 6.1 shows the impressed electric currents and corresponding heat flux densities. Regardless of the investigated treatment or saturation pressure applied

Table 6.1: *Impressed electrical currents I and desired heat flux densities \dot{q} originating from preliminary tests.*

$I \text{ (A)}$	51	65	82	104	132	210	333	530	841
$\dot{q} \text{ (} 10^3 \text{ W/m}^2\text{)}$	3	4	6	10	16	40	100	251	631

during the measurement, these fixed amperages are used assuming small variations in the corresponding heat flux densities.

6.1 Nucleate boiling

During nucleate pool boiling each measurement consists of at least four different operating points, which are applied in descending order:

$$I = 841 \text{ A} \rightarrow 530 \text{ A} \rightarrow 333 \text{ A} \rightarrow 210 \text{ A}$$

At saturation pressures higher than 2 bar additional smaller amperages are impressed if necessary, since convective boiling can not be established.

As described in section 5.3, normalisation of the determined heat transmission coefficients to C_{red} is sensitive to the number (and location) of \dot{q} . Consequently, all measurements under the treatment type comprise the same amount of operating points and values of \dot{q} to remain comparability.

6.1.1 Effect of continuous nucleation

In order to identify a feedback of bubble generation on the developing oxide layer and the according boiling heat transfer, a single long-term trial at a fixed operation point is carried out under trisodium phosphate conditions (A226). Alongside the determination of the respective heat transmission coefficient on a regular basis, data of the boiling curves exponent is gathered to detect surface modifications/change in boiling behaviour by discontinuously determining boiling curves. If there is significant influence on the time response, permanent impression of a 'fixed' heat flux density must be considered.

The test is carried out starting from a metallic-blank tube at $p_s = 15 \text{ bar}$. Data collection is set to every 300 s continuously at a fixed electric current of $I = 510 \text{ A}$ resulting in a heat flux density of $\dot{q} \approx 250 \cdot 10^3 \text{ W/m}^2$. This heat flux density is situated in the upper range of technical application in shell boilers promising the clearest influence on the surface properties and heat transfer, if any.

On a daily basis, the test is stopped for a brief period of time, in which the boiling curves are determined at $p_s = (2, 5, 10, 15) \text{ bar}$. Afterwards the pH-value is checked and, if necessary, adjusted by dosing further trisodium phosphate, before the desired heat flux density is impressed again. Here, the evaluated data of the electrical current and previously achieved heat flux density were used to readjust the amperage to a value, which expectedly yields the desired \dot{q} .

A significant impact on the boiling curves exponent or reduced heat transmission coefficient could not be detected under permanent nucleation compared to tests without continuous tube heating.

Therefore, under the described system conditions from a thermotechnical point of view, permanent nucleation can be considered uninfluential regarding the nucleation site distribution and nuclei availability during nucleate pool boiling. Standardisation of k to C_{red} is carried out using the mean exponent $\bar{n} = 0.63$, gained during trisodium phosphate treatment (abbrev.: PO_4) at $p_s = 15 \text{ bar}$ (see section 7.1). Picture 6.1 shows the time response $C_{red}(\tau)$ of tube A226 during PO_4 treatment at $p_s = 15 \text{ bar}$. Sampling and dosing moments are implemented in the diagram, when the boiling curves were determined as well.

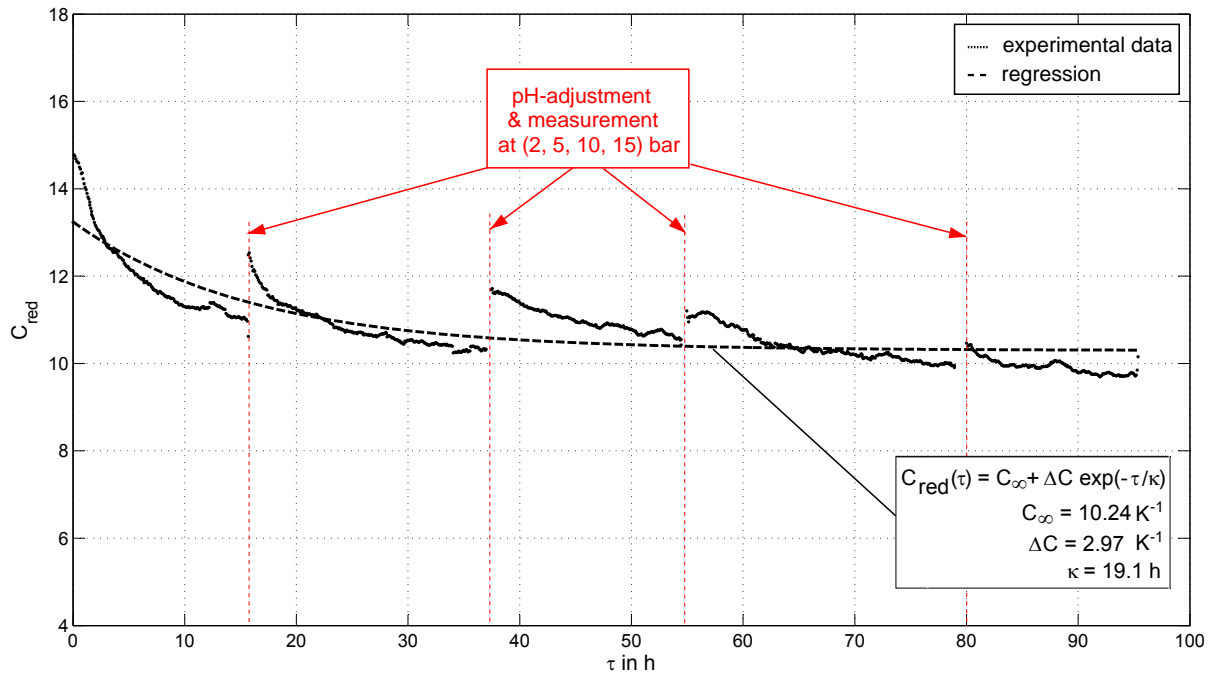


Figure 6.1: *Time response of the exemplary tube A226 during PO_4 treatment and permanent nucleation at $p_s = 15$ bar.*

According to depiction 6.1, there is a considerable change in the heat transmission coefficients (here reduced to C_{red} , see section 5.3) between the end of continuous nucleation and immediately after restart of tube heating. It takes several hours of further operation until the original values are restored. The reason for such a behaviour is unclear. The obtained boiling curves gathered between the tests do not show any significance regarding an overall change in the heat transfer behaviour. Although the used conditioned feed water is of low electric conductivity, it contains dissolved gases, like oxygen and carbon dioxide. Those gas residues are possibly able to act as nuclei if adsorbed to the tube walls. As the water is degassed repeatedly after the dosing, this effect is expected small.

Thus, it is assumable, that pausing permanent bubble generation or pH-value adjustment has a temporal impact on the heat transfer after restart. Neither of both situations is typical for industrial shell boilers: Here, pH-measurement and adjustment are carried out quasi-continuously, while the same operation point is usually maintained constant for several hours.

The results of regression for the experimentally obtained values of C_{red} at $p_s = 15$ bar using the fixed mean exponent during the treatment compared to the time response without permanent tube heating is presented in figure 6.2. That means, while on the surface of tube sample A226 a permanent nucleation took place during the entire test period, the reference values of C_{red} have been determined by impressing heat flux densities only during

discontinuous measurements. Between the test sessions, the system pressure is maintained constant by the auxiliary heater only. Found deviation between permanent tube heating and using the auxiliary heater is within the relative mean deviation of C_{red} as determined for the latter case.

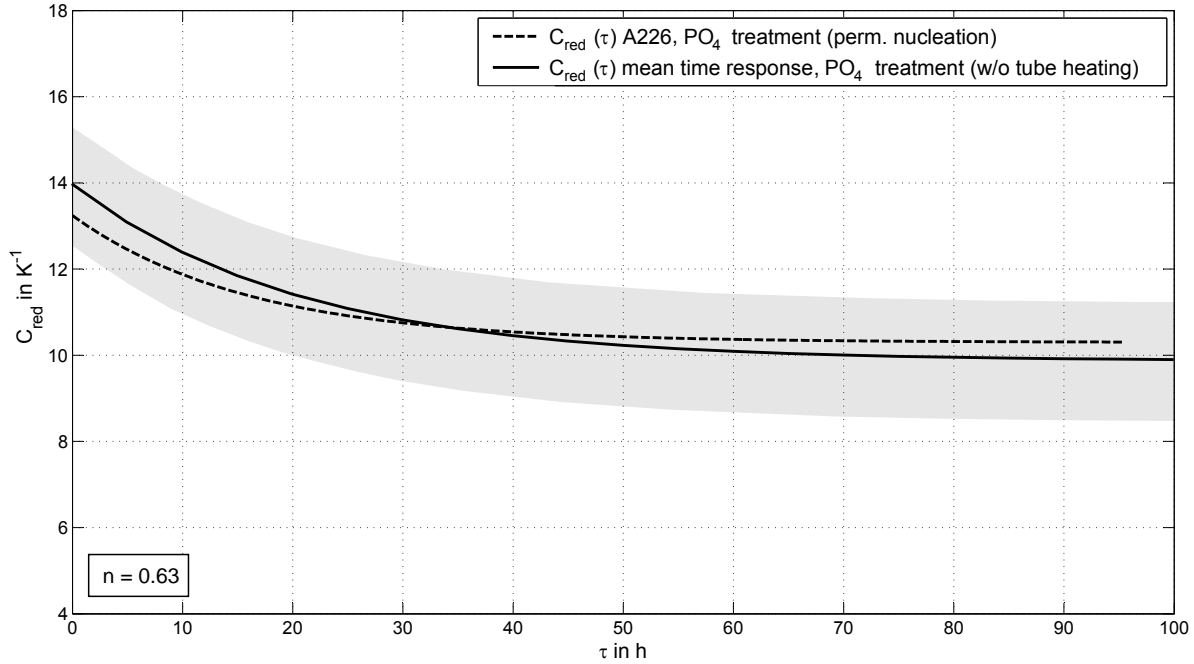


Figure 6.2: *Time response of the exemplary tube A226 during PO_4 treatment with permanent nucleation compared to layer generation without tube heating at $p_s = 15$ bar (the tinted area represents the mean deviation).*

6.1.2 Conclusion

Under the PO_4 treatment, permanent nucleation caused by impression of a moderate heat flux density has a negligible effect on the heat transmission behaviour. Neither the overall decline in the heat transmission coefficient nor the time scale τ_{99} differs significantly to data without the tube heating. A temporary improvement in the heat transmission coefficient after an operational downtime is observable after discontinuous pH-value adjustment only, which is not applied in real shell boilers. As a consequence, for technical purposes the found differences are considered negligible.

Bubble forming does not measurably influence the exponent of the discontinuously determined boiling curves during the long-term trials neither. A feedback of a nucleation on the layer properties cannot be observed from a thermotechnical point of view. All tests in this work are therefore carried out without a permanent tube heating. Measurements take place discontinuously during the entire operational period.

6.2 Convective boiling

The region of convective boiling can only be put into practice at very low heat fluxes and saturation pressures. The higher the boundary layer superheat and the pressure get, the smaller nuclei can be activated and bubbles are formed on the surface interfering with natural convection. Some few bubbles usually do not interfere with convective boiling as long as the typical loops of superheated liquid caused by free convection can develop. As soon as bubble generation and departure cause turbulences, the critical conditions for convective boiling are violated. Therefore, the following small amperages are impressed in descending order:

$$I = 132 A \rightarrow 104 A \rightarrow 82 A \rightarrow 65 A \rightarrow 51 A$$

Per definition, pool boiling requires an infinitely large bulk liquid surrounding the heating surface. In this case interactions between the vessel borders and the heat transferring surface can be excluded. Preliminary tests with short-term visual access show bubble forming on the vessel walls during convective boiling tests. Unsteady operation, such as cooling down from a higher pressure stage, cannot be avoided entirely in order to comply with upper condition 1 in section 6. For the sake of short cooling periods the condensation loop and the heat exchanger are applied as explained in section 5.1. During the cooling process the thermally insulated wall material is superheated with respect to the boiling liquid. Given described superheat, nucleation occurs on the vessel walls cooling the material. Those bubble induce flow, which is disturbing formation of the mentioned convective loops and thereby causes increased convective heat transfer from the tube to the coolant.

In order to prevent mentioned undesirable nucleation and corresponding turbulence during convective boiling a (small) negative temperature gradient must be assured from the bulk liquid through the vessel walls to the environment by closing the condensation loop during the measurement. Given sufficient time to reach the thermal equilibrium, the heat is then transmitted via the vessel material to the surrounding without nucleation. Figure 6.3 demonstrates the inner processes and corresponding schematic temperature distribution with active and inactive external cooling in the condensation loop. As the actual flow field is unclear, the purpose of figure 6.3 is a schematic illustration only.

Preliminary measurements during convective boiling indicate the rotation axis of the fluid

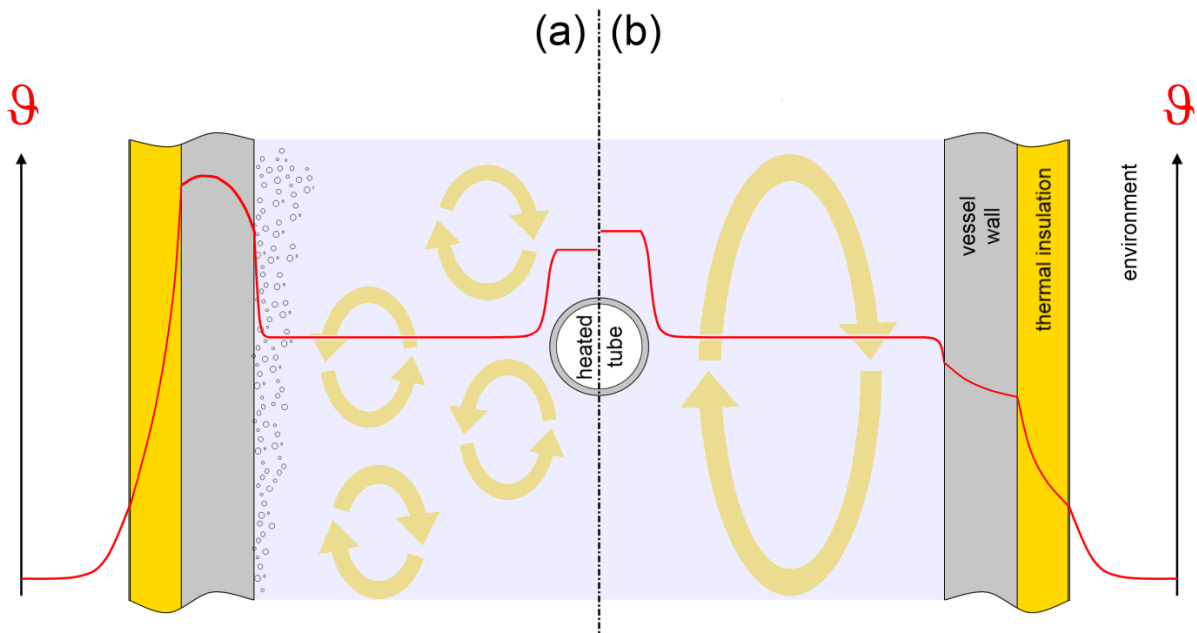


Figure 6.3: *Schematic depiction of the inner vessel processes with open (a) and closed (b) condensation loop during convective pool boiling. The qualitative temperature trend is coloured red.*

flow to be congruent with the tube axis by logging the inner tube wall temperature while changing the sensor position. A significant temperature gradient along the tubes heated length cannot be detected. Thus, the applied single position measurement of the inner tube wall temperature is valid to determine the heat transmission coefficient under convective pool boiling conditions.

6.3 Reproducibility of the initial boiling behaviour

Confronting the impact of different feed water treatments on the surface properties and heat transmission requires strictly defined reference conditions. Under similar or even identical circumstances and specimen preparation, neither the initial heat transfer during nucleate boiling nor ensuing corrosion processes are accurately reproducible.^[43] A defined system start-up, careful cleaning and preparation of the heating surfaces are indispensable.^[30] Reproducibility is only achievable using statistical data administration and experimental support values.

6.3.1 Impact of the heating rate

According to Steinbrecht, a heating rate lower than $dT/d\tau \approx 60 \text{ K}/\text{min}$ hampers experimental determination of actual starting conditions due to beginning corrosion.^[43] Since

Steinbrecht et al. used unconditioned demineralised water, the effort to minimise the statistical spread of the starting conditions in this work is expected even harder, as any feed water alkalisation is supposedly accelerating oxidative conversion processes. Therefore, the highest possible heating rate of more than $dT/d\tau \approx 100 \text{ K/min}$ is applied in an identical procedure for all tests.

6.3.2 Influence of the pretreatment

VGB directive R 513 recommends a series of cleaning measures prior to the first boiler start-up in order to remove fabrication residues and deposits. Boil out, (diverse) chemical cleaning and blow out of the cleansing solution are the basic procedures.^[81]

Based on this directive, that also applies for shell boilers, all specimens undergo a defined pickling process before getting in first contact with the conditioned feed water. After the tube sample is soldered into the current conductors, it is therefore:

1. Cleaned with acetone,
2. pickled with an acidic etchant solution,
3. flushed with tap water,
4. neutralised with a 10 % soda solution,
5. flushed with deionised water and
6. flushed with 2-propanol before it is
7. dried in a furnace at $\vartheta = 105 \text{ }^\circ\text{C}$ for 20 min.

The described pretreatment has two distinct purposes: Firstly, any contaminants from fabrication or transport are removed. Grease and oil are known to induce comparably smaller values of \dot{q}_{crit} . Secondly, all possible corrosion products built up during transport and storage are removed from the surface, which is thereby 'activated' regarding any expected surface process incorporating oxidation.

Preliminary experiments with mentioned pretreated tube specimens show, that different tube charges of the same tube quality (*St 35 BK*) treated with the pickling solution (immersion process for a period of 3 min: 50 vol-% *HCl*(32 %), 10 vol-% *HNO₃*(65 %), 40 vol-% deionised water) affect the observed nucleate boiling heat transfer coefficients remarkably compared to merely 2-propanol cleaned samples. Depending on the charge, the pickling process apparently 'creates' additional nuclei on the pretreated tube surface by

removing oxidation products, improving the heat transfer. The influence of the parameters *tube charge* and *pretreatment* is therefore investigated using two different providers (named *charge 1* and *charge 2*) and two distinct pretreatments (see table 6.2).

In addition, the etchant solution is changed to smaller acid concentrations and the etching period enhanced (modified etchant) in order to reduce the influence of time error during the pretreatment but maintaining a similar cleaning effect. Some additional tests are carried out using 2-propanol treated specimens for comparing the initial boiling characteristics and burn-out I behaviour to the pretreated tube samples. Table 6.2 shows the investigated combinations.

Table 6.2: *Test configuration: investigated tube charge and specimen preparation.*

Tube charge	Etchant title, pickling period & etchant composition
charge 1	unmodified etchant, 3 <i>min</i> 50 vol-% <i>HCl</i> (32 %), 10 vol-% <i>HNO</i> ₃ (65 %), 40 vol-% deionised water
	modified etchant, 6 <i>min</i> 25 vol-% <i>HCl</i> (32 %), 5 vol-% <i>HNO</i> ₃ (65 %), 70 vol-% deionised water
charge 2	unmodified etchant procedure, 3 <i>min</i> 50 vol-% <i>HCl</i> (32 %), 10 vol-% <i>HNO</i> ₃ (65 %), 40 vol-% deionised water
	modified etchant, 6 <i>min</i> 25 vol-% <i>HCl</i> (32 %), 5 vol-% <i>HNO</i> ₃ (65 %), 70 vol-% deionised water
	no etching, 2-propanol cleaned

Charge 2 is sourced from the same melting and drawing process. Regardless of the provider, the samples used are cold-drawn seamless precision tubes as specified by DIN EN 10305-1 (DIN 2391) made of plain carbon steel.^[82] The outer diameter of 6.00 *mm* is verified by sample survey using a micrometer screw before and after pretreatment. There is no evidence of a significant material removal by any of the applied preparations that would jeopardise the determination method of the heat transmission coefficient as described in

section 5.2.

Investigations are carried out also for the region of convective boiling. Evidentially, the nucleation site offer (being determined by charge and etchant) does not have any significant effect on the heat transport during convective boiling. Reproducibility evaluations are therefore only worked out for *charge 2, modified etchant* as described in section 7.1.1.

6.4 Investigated feed water treatments

A variety of typical inorganic additives and exemplary organic feed water agents is chosen to identify differences in the interaction between the tube heater surface and the boiling liquid. These conditionings are chosen to give an overview on surface-coolant interaction, as they cover the usual range of possible alkaline treatment types, from solid alkalising over partially volatile treatment to the all volatile treatment.

The demineralised feed water is provided by the thermal power plant KNG Rostock and conforms to the limit values of VGB directive R 450.^[83]

6.4.1 Conditioning with solid alkalising agents

While already many industrial shell boilers are operated using an alternative conditioning, the recommended treatment for shell boilers is usually the operation with solid alkalising agents.^[9] If necessary, alkalisation can be complemented by oxygen scavengers. Trisodium phosphate (Na_3PO_4) is the most applied solid alkalising feed water additive in shell boiling applications. Working with high-quality feed water the agent's ability of binding polyvalent cations does not apply. It acts solely as alkalising agent.

Within this work, Na_3PO_4 is applied in two variations:

1. Na_3PO_4 is the only chemical that is dosed into the feed water; short: ' PO_4 '.
2. The influence of Na_3PO_4 as alkalising agent and hydrazine (N_2H_4) as additional oxygen scavenger is studied; short: ' $PO_4 + N_2H_4$ '.

Table 6.3 lists the applied additives including their corresponding control factors for dosing. The sampling is carried out at $p_s = 15 \text{ bar}$ from the liquid and the vapour phase using stainless steel capillaries to cool the probe. The parameters of interest are the pH-value in the boiler water at $25 \text{ }^\circ\text{C}$ (measured using a pH-meter), its maximum direct electrical conductivity β (determined via conductivity electrode) and, if applicable, the hydrazine excess $[N_2H_4]$ in the condensate (determined via photometric test). The ortho-phosphate

concentration is also determined via photometric test and held $[PO_4^{3-}] < 20 \text{ ppm}$. If any of the stated parameters cannot be satisfied a complete water change is applied immediately.

Table 6.3: *Parameters for the trisodium phosphate treatment.*

Applied additive	pH-value (25 °C)	β (25 °C) in $\mu S/cm$	$[N_2H_4]$ in ppm
Na_3PO_4	$10.0 \leq pH \leq 10.5$	< 1500	
$Na_3PO_4 + N_2H_4$	$10.0 \leq pH \leq 10.5$	< 1500	0.2 – 0.5

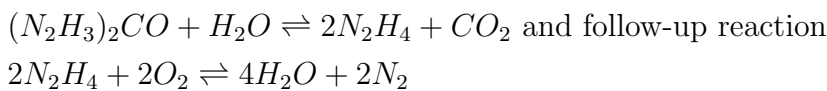
The layer generation is carried out at 15 bar. During pure phosphate treatment discontinuous measurements are carried out at $p_s = (2, 5, 10) \text{ bar}$, in order to gain information on the pressure dependency of k as discussed in section 7.

Trisodium phosphate and hydrazine

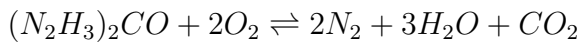
The hydrazine treatment ($PO_4 + N_2H_4$) is performed with the use of trisodium phosphate and carbohydrazide ($(N_2H_3)_2CO$), which reacts to hydrazine under boiler conditions. The main reason to apply hydrazine, is the neutralisation of oxygen. A surface passivation is also induced to a certain extent by its reducing character. Ferric oxide (Fe_2O_3 , hematite) is reduced to ferrous oxide (FeO , wustite), slowing down / impeding iron oxidation.^[84]

Depending on the system parameters, carbohydrazide is assumed to bind oxygen via two different reaction paths.^[84]

- Indirect path: Under an elevated temperature of $\vartheta > 135 \text{ °C}$, carbohydrazide reacts to hydrazine and binds oxygen to produce water, nitrogen and carbon dioxide.



- Direct path: At lower temperatures ($\vartheta < 135 \text{ °C}$), where hydrazine shows only little reactivity with oxygen, carbohydrazide binds dissolved oxygen without forming hydrazine at all.



As a consequence of carbohydrazide application, carbon dioxide and nitrogen are formed. The less oxygen in the boiler water to be scavenged, the smaller the amount of carbohydrazide, carbon dioxide and nitrogen as products in the steam phase. Such gaseous residues jeopardise the saturation temperature measurement: At the presence of gaseous components, the system pressure is not only generated by steam, but also by the partial pressure of mentioned products. Degassing is therefore carried out.

The dosing of carbohydrazide is carried out as follows:

The pH-value of demineralised feed water is adjusted by Na_3PO_4 to $10.0 \leq pH \leq 10.5$ and introduced into the vessel after the assembly of the test tube. It is then heated up by means of the auxiliary and the tube heating to a superatmospherical pressure, when thermal degassing of the unconditioned feed water is carried out to reduce the needed amount of carbohydrazide. Then the feed water agent is dosed into the system while preheating to the desired saturation pressure.

Sampling is carried out at $p_s = 15 \text{ bar}$ from the liquid and the vapour phase using stainless steel capillaries to cool the probe. While the pH-value of the boiler water sample is determined with a pH-sensor, the determination of the hydrazine concentration in the steam phase is carried out using a photometric test. The corresponding calibration curve can be found in the appendix B.

Preliminary tests indicate small leakages in the steam section of the setup (valves, piping interfaces, etc.), which cannot be eliminated completely and are intensified by pressure changes. Consequently, volatile components are removed gradually from the facilities. The according loss of hydrazine has to be compensated by redosing carbohydrazide. A fixed dosage is therefore applied daily, as continuous dosing cannot be carried out using the described setup. Additional measurements at $p_s = 2 \text{ bar}$ are carried out only after reaching steady state of k for investigations of convective boiling.

6.4.2 Organic all-volatile treatment

The all-volatile treatment (AVT) is also a state-of-the-art feed water conditioning. Here, the applied agents are readily soluble in the steam phase. Ammonia, for example, is one of the most commonly applied AVT chemicals in high-pressure flow boilers and often used along with hydrazine as oxygen scavenger.

In contrast to the inorganic ammonia treatment an amine based oxygen scavenger of high volatility, diethylhydroxylamine (DEHA), is employed together with an alkalisng amine to create organic AVT conditions. A combined product Ferrolix[®]8342 (BKG Water Solutions)⁴ is applied consisting of DEHA, cyclohexylamine (CHA) and monoethanolamine (MEA). Both latter formulations have a strictly alkalisng character. This treatment is investigated under the following parameters of the condensate:

- A pH-value: $9.0 \leq pH_{cond}(25 \text{ }^\circ\text{C}) \leq 9.5$ (adjusted by CHA and MEA)
- and a detectable DEHA excess.

⁴Ferrolix[®] is a registered brand name of BK Giulini GmbH

The DEHA concentration $[DEHA]$ is determined using a colorimetric test based on the reduction behaviour of di-ethylhydroxylamine on Fe^{3+} ions and detection of Fe^{2+} ions for $0 \leq [DEHA] \leq 0.3 \text{ ppm}$. The pH-measurement in the condensate is carried out using a pH-meter at room temperature, followed by cleaning the equipment with 2-propanol and deionised water.

After the system is filled with deionised water, it is heated up to a saturation pressure of $p_s = 2 \text{ bar}$ as quickly as possible, where thermal degassing is carried out. Afterwards the system is fed with a dilute aqueous solution of Ferrolix[®]8342 achieving the stated parameters. As the components of the mentioned product are mostly volatile, fractions of the chemicals are removed through unpreventable leakages in the steam section leading to both, a drop of the pH-value and the DEHA concentration in the condensate.

Thus, a fixed volume of 0.5 ml Ferrolix[®]8342 is dosed, whenever the pH-level or DEHA excess in the condensate fail to comply the stated parameters. Sampling is carried out at $p_s = 15 \text{ bar}$ from the liquid and the vapour phase using stainless steel capillaries to cool the probe. The time response of the heat transmission coefficient is also strictly determined at $p_s = 15 \text{ bar}$ to maintain continuous steady state conditions during the treatment.

6.4.3 Film-forming amine treatment

Film-forming amines are an alternative to the classic feed water treatment, whenever the latter is unable to provide satisfactory results. The applied organic product in this work is the corrosion inhibitor Cetamine[®]V211⁵ (BKG Water Solutions). This product consists of a film-forming diamine (oleylaminopropyleneamine) and alkalisng amines (cyclohexylamine, alcanolamine) of different volatility. Consequently, this product promises protection of the water and steam touching steel surfaces in a steam generator. Volatile components are recycled via the condensation loop (see section 5.1) so that a steady state circulation can be assured.

The following two different scenarios are of interest regarding the effect of film forming amines in shell boilers:

1. Treatment of metallic-blank tube surfaces. In short: '*Cetamine*'.
2. Change of the conditioning from classical inorganic trisodium phosphate feed water conditioning to the organic FA treatment after steady state conditions of the heat transmission coefficients. In short: ' $PO_{4,\infty} \rightarrow \textit{Cetamine}$ '.

⁵Cetamine[®] is a registered brand name of BK Giulini GmbH

The first scenario simulates the start of operation in a new or chemically cleaned shell boiler under film-forming amine treatment. The second case simulates changing the treatment in a so far phosphate conditioned shell boiler without removal of the passivating oxide layer. Both scenarios are relevant for practice as sometimes film-forming amines are applied where conventional feed water treatment failed to provide satisfactory results.^[15]

Dosing and sampling, analytics

Concentration adjustment of the film-forming amine and sampling is carried out at the operation pressure of $p_s = 15 \text{ bar}$. Sampling is carried out from both, the vapour and the liquid phase. Therefore, stainless steel capillaries with a length of several meters are used to condense and cool the sample. Prior to sampling, these capillaries are flushed in order to prevent loss of film-forming amine to the capillary walls. Quick processing of the sample is essential, as adsorption of the amine to the vial walls is an intrinsic characteristic. As a consequence, sampling is carried out with PTFE vials.

The sorption rate of the film-forming amine is depending on the system pressure/saturation temperature and the surface type. Consequently, the development of a sorption equilibrium takes a certain amount of time. According to Hater, a period of at least 6 hours is necessary to provide steady state conditions.^[15] Whenever a sorption equilibrium can be assumed, an explicit excess of free film-forming amine in the condensate proves sufficient to consider all surfaces covered with the organic film. In order to prevent a possible accumulation, the amine concentration in the condensate is limited to $0.5 \leq [FA] \leq 1.0 \text{ ppm}$.

This dilute mixture of water and film-forming amine is not a real solution but a micro dispersion. As shown in figure 6.4, provided by BKG Water Solutions, the steam temperature remains unaffected by typical amine concentrations in the mentioned range.

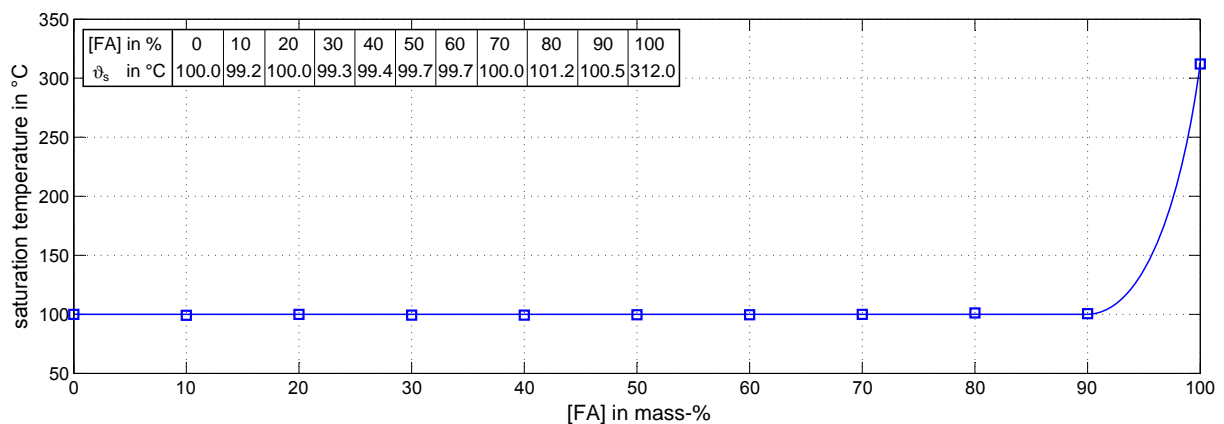


Figure 6.4: Influence of the film-forming amine concentration $[FA]$ on the saturation temperature of steam at atmospheric pressure.

The concentrations of free film-forming amine in the liquid and in the condensate are detected via a photometric test using a WTW PhotoLab Spektral NOVA 400 photometer. The applied test (A18, BK Giulini GmbH) is based on a molecular colour complex (rose-bengal) with the film-forming amine, that is formed in an acidic solution. The extinction as caused by the complex is determined at 560 nm wavelength and evaluated against a blind value. The photometric test is calibrated exclusively for a concentration range of $0 \leq [FA] \leq 4 \text{ ppm}$ film forming diamine. The calibration curve can be found in the appendix B.

Besides feed water pumps, a specifically designed dosing system (see figure 6.5) is used to dose small volumes of organic product Cetamine[®]V211 or a cleansing solution (1 % cyclohexylamine in deionised water), supported by a nitrogen overpressure. This high-

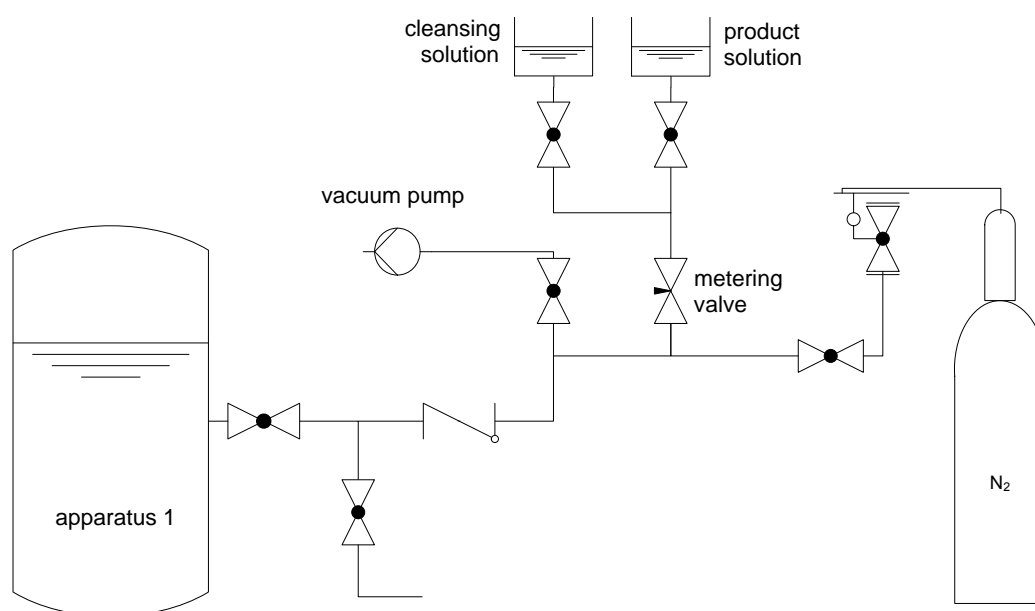


Figure 6.5: *N₂-supported dosing system for the organic product / cleansing solution. Standard parts have not been denoted.*

pressure dosing system is applied as follows:

Before dosing, it must be taken care that any corrosion relevant gases (e.g. oxygen, carbon dioxide) are removed from the piping. Therefore, the system is flushed with nitrogen for several times and repeatedly evacuated using a vacuum pump. Then the pipes are flushed with the product solution to prevent concentration losses due to 'adsorption' to the inner walls. Afterwards, the system is evacuated again to transfer the desired volume of a product parent solution into the system via a metering valve. The valve is closed after the desired amount of product has entered the piping and a slight overpressure to the operating pressure is used from the nitrogen bottle to transfer the charge into the autoclave after

the ball valve at the vessel has been opened. Reverse flow is counteracted by the check valve.

An insertion of nitrogen cannot be entirely avoided when using the described dosing method. Although nitrogen as an inert substance has no chemical effect on oxidation, any additional gases in the water-steam-cycle have to be excluded to its best discretion. Resulting partial pressure compromises an accurate determination of the saturation temperature. Thus, additional thermal degassing is necessary, while the remaining nitrogen in the pipe between the autoclave and the check valve is drained by opening the outlet valve.

As a consequence, the film-forming amine is removed from the vessel with every degassing process, sampling and by leakages, which has to be taken into account regarding the dosing amount.

After this procedure, the cleansing solution is used to remove film-forming amine residues from the dosing system. The described aqueous cleansing solution is also used after the end of each test run (tube change) by the use of a dummy to make sure that the system is clean before the next test run is initiated.

Treatment of bare steel heating surfaces

A metallic-blank and pretreated test tube, that has been dried in a furnace, is installed in the apparatus. An initial product volume of $V \approx 0.5 \dots 0.8 \text{ ml}$ Cetamine[®]V211 containing $[FA] \approx 1 \%$ is dosed into $V = 4.2 \text{ l}$ deionised feed water under constant stirring and is then pumped into the vessel after the assembly of the tube sample. Immediately afterwards the heating phase begins. After repeated degassing at superatmospheric pressure, this amount of product usually leads to a free film-forming amine concentration of $0.3 \dots 0.8 \text{ ppm}$ in the condensate.

At $p_s = 2 \text{ bar}$ the initial boiling heat transmission coefficients are determined immediately with decreasing heat flux densities comprising all thermal loads listed in table 6.1. Although discussed 'adsorption' of the film-forming amine requires certain time, at this point quick data acquisition is essential in order to keep the influence of starting corrosion small at low pressures $p_s < 15 \text{ bar}$.

Both, the auxiliary heater and the tube heating are used to further heat up the water to the desired operating pressure of $p_s = 15 \text{ bar}$, where the starting conditions are determined. Tube heating is switched off during long term operation. The system pressure is kept up only by the auxiliary heater. Dosing and sampling are carried out according to section 6.4.3, on a daily basis.

The usual observed boiler water quality during the experiment, expressed by the pH-value in the condensate pH_{cond} and in the boiler water pH_{liq} , and the direct electrical conductivity of the boiler water β_{liq} are listed in the following table 6.4.

Table 6.4: *Typical boiler water and steam parameters at (25 °C) during film forming amine treatment.*

Parameter	pH_{liq}	pH_{cond}	β_{liq}	$[\text{FA}]_{\text{liq}}$	$[\text{FA}]_{\text{cond}}$
Value	8.2 ... 8.8	9.0 ... 9.5	70 ... 120 $\mu\text{S}/\text{cm}$	0.05 ... 0.6 ppm	0.2 ... 1.2 ppm

Change from a classic to the film-forming amine treatment

After a thermotechnically verified steady state of the tube surface is generated in the autoclave under PO_4 ($\text{PO}_4 + \text{N}_2\text{H}_4$) conditions, the respective tube is transferred tempered into the organically treated vessel. The autoclave is filled with water corresponding to the previous section 6.4.3 in order to assure a free film-forming amine concentration of $[\text{FA}] = 0.3 \dots 0.8 \text{ ppm}$ in the condensate. Heating is provided by auxiliary and tube heating. The starting conditions are determined as soon as degassing is carried out and 2 bar saturation pressure is present. After the corresponding measurement is taken, the influence of the organic product on the layer is investigated at $p_s = 15 \text{ bar}$ discontinuously, accompanied by daily concentration measurement and dosing (if necessary).

The subsequent measurements are carried out at $p_s = 15 \text{ bar}$ throughout the entire treatment period. Furthermore, less frequent investigations are carried out at $p_s = 2 \text{ bar}$ in the benefit of mostly steady state treatment conditions at $p_s = 15 \text{ bar}$.

Nomenclature

An abbreviation nomenclature is introduced to describe the type of feed water treatment and the state of the tube sample (operation period) as shown in table 6.5. Each treatment (treatm.) abbreviation is accompanied by an additional index for the corresponding surface condition. Index “0” means start of the respective treatment, “ ∞ ” symbolises thermotechnically indicated steady state of the surface regarding the heat transmission.

6.5 Surface analyses

Conventional reference surface analyses are applied to validate the experimental thermotechnical cognitions. Different methods are imaginable for the characterisation of the

Table 6.5: *Nomenclature for the assayed treatments. (The arrow marks a changeover from the reference to the organic treatment after reaching steady state of the surface during reference treatment.)*

Abbreviation	Applied additive	Verified surface state
$PO_{4,0}$	Na_3PO_4	start of treatm., met.-blank surface
$PO_{4,\infty}$	Na_3PO_4	end of treatm., steady state surface
$(PO_4 + N_2H_4)_0$	$Na_3PO_4 + N_2H_4$	start of treatm., met.-blank surface
$(PO_4 + N_2H_4)_\infty$	$Na_3PO_4 + N_2H_4$	end of treatm., steady state surface
$(DEHA + aA)_0$	$C_4H_{11}NO + aA$	start of treatm., met.-blank surface
$(DEHA + aA)_\infty$	$C_4H_{11}NO + aA$	end of treatm., steady state surface
Cetamine ₀	V211	start of treatm., met.-blank surface
Cetamine _∞	V211	end of treatm., steady state surface
$PO_4 \rightarrow$ Cetamine ₀	V211	start of treatm., oxidated surface
$PO_4 \rightarrow$ Cetamine _∞	V211	end of treatm., steady state surface
$(PO_4 + N_2H_4) \rightarrow$ Cetamine ₀	V211	start of treatm., oxidated surface
$(PO_4 + N_2H_4) \rightarrow$ Cetamine _∞	V211	end of treatm., steady state surface

surface morphology: Scanning electron microscopy (SEM), atomic force microscopy (AFM) and confocal laser scanning microscopy (CLSM).

The latter one proves most convenient and is used, where applicable, complemented with AFM measurements in order to identify the surface properties of all assayed feed water treatments. Obtained surface profiles and visualisations are employed to verify the thermotechnical observations.

The heat transfer behaviour during nucleate boiling conditions is strongly controlled by the cavity size spectrum of the present potential nuclei. Since generally accepted surface roughness amplitude parameters, like the average roughness R_a or the root mean squared roughness R_q (also: R_{RMS}), provide only little information about the nucleation site spectrum or the size of nuclei,^[31] surface analyses in this work are used only to derive trends and to explain the observed boiling phenomena. As the mentioned analyses are rather time-consuming, not every investigated tube sample is subject to the surface investigations.

6.6 Critical operating conditions

6.6.1 Critical heat flux density during nucleate pool boiling

According to the VDI-Wärmeatlas the critical heat flux density \dot{q}_{crit} for plane and tubular heating surfaces during pool boiling can be calculated using following empirical equation:^[31]

$$\dot{q}_{crit} = f \cdot \Delta h_v \sqrt{\rho''} \sqrt[4]{g\gamma(\rho' - \rho'')} \quad (6.1)$$

using the enthalpy of evaporation Δh_v at the according saturation pressure p_s , the mass density of the saturated steam ρ'' and the boiling liquid ρ' , the gravity constant g and the surface tension γ between the boiling water and the saturated steam. Prefactor f is stated with 0.13 to 0.16 to suit experimental data.

The maximum value for the critical heat flux density can be found for a saturation pressure of approximately $p_s = 64 \text{ bar}$ with:

$$\dot{q}_{crit} \approx \begin{cases} 3.8 \cdot 10^6 \text{ W/m}^2, & (f = 0.13) \\ 4.8 \cdot 10^6 \text{ W/m}^2, & (f = 0.16) \end{cases}$$

Given the examined treatment pressure of $p_s = 15 \text{ bar}$, equation 6.1 calculates a critical heat flux density of $\dot{q}_{crit} \approx 3 \dots 3.6 \cdot 10^6 \text{ W/m}^2$. Such high heat fluxes cannot be achieved at elevated pressures by the utilised electrical equipment, because the electrical resistance of the tube rises with increasing system temperature. In order to reach the critical heat flux density for nucleate pool boiling, only low system pressures can be investigated. A pressure of $p_s = 2 \text{ bar}$ is chosen where \dot{q}_{crit} can be achieved and tightness of the apparatus can be assured. Consequently, the required heat flux densities for chemically pure water under $p_s = 2 \text{ bar}$ are expected according equation 6.1:

$$\dot{q}_{crit} \approx \begin{cases} 1.4 \cdot 10^6 \text{ W/m}^2, & (f = 0.13) \\ 1.8 \cdot 10^6 \text{ W/m}^2, & (f = 0.16) \end{cases}$$

This spectrum of thermal loads can securely be provided by the electrical gear and allows precise statements on the departure from nucleate pool boiling.

The critical heat flux density is determined experimentally by gradually increasing the electrical current into the tube sample and simultaneous data acquisition. Quasi-steady state conditions can be supported by means of the tube-in-tube heat exchanger described in section 5.1. At the moment of burn-out I the power supply is interrupted. At an acquisition frequency of approximately 14 Hz , the previously acquired data sets - comprising the inner tube temperature, amperage and saturation temperature - are used to calculate the critical heat flux density and heat transmission coefficient, respectively.

6.6.2 Suppression of nucleation by an organic film

A widely unacquainted phenomenon has been reported by Steinbrecht et al. during operation with film forming organics in steam boilers. Traced back to polymolecular adsorption processes during stand-by conditions the term burn-out III was introduced.^[27] Here, a multimolecular organic film is considered to impede nucleation (by plugging nuclei) when suddenly impressing high heat fluxes from stand-by or start-up. If the initiated desorption process (by increasing temperature) takes longer than reaching the heater materials melting temperature, a burn-out III can occur. Such critical operating conditions can result, for instance, from high-heat-flux start-ups of a boiler after a downtime of several hours at reduced or sub-atmospheric pressures.

Since start-up and stand-by conditions might be critical for boiler operation, the organic film-forming amine operation is assayed regarding the burn-out III by impressing large heat flux densities beyond the usual boiling parameters from stand-still or reduced pressure using the described test facilities. Prior to each test, the system is given a period of at least six hours to reach a sorption equilibrium. Two scenarios are investigated during *Cetamine* treatment for metallic-blank tubes and after conversion from inorganic phosphate to organic treatment:

- Hot stand by after $> 6 h$ at $2 bar$ saturation pressure and
- cold start-up after $> 6 h$ at ambient temperature (subpressure).

Considering the resulting saturation pressure at room temperature, the latter case requires an external pressure source to be connected to the vessels and to prevent air from entering the autoclave. A nitrogen bottle is used to provide a slight overpressure for the entire test period of two distinct heat flux densities each.

As typical heat flux densities in shell boilers are recommended to $\dot{q} \ll 330 \cdot 10^3 W/m^2$,^[39] two heat flux densities are applied, intentionally exceeding the application range: $\dot{q} \approx 400 \cdot 10^3 W/m^2$ by simulating a moderate thermal overload and $\dot{q} \approx 800 \cdot 10^3 W/m^2$, representing the worst-case. These \dot{q} -values are impressed under different film-forming amine concentrations in order to study the effect of a wide range of possible (over-) dosages. If a burn-out III cannot be observed for these values, the investigated feed water agent proofs safe for boiler application. Table 6.6 lists the investigated scenarios carried out on steady state tubes only (*Cetamine*_∞, *PO*_{4,∞} → *Cetamine*_∞).

The listed film-forming amine concentrations are dosed at $p_s = 2 bar$, wherein after this saturation pressure is held for a period of at least $6 h$, before the actual test is started

Table 6.6: *Investigated system conditions for the burn-out III tests.*

\dot{q} in $10^3 W/m^2$	[FA] in ppm (dosed concentration)
400	(0.5...)1.0; 10; 100
800	(0.5...)1.0; 10; 100

or the heating is switched off. Further 6 h are spent at ambient temperature prior to the cold start-up.

As mentioned before, an impression of a specific heat flux density is not possible, as the thermal load changes with rising tube temperature in the electric heater. As an alternative, fixed amperages are used instead, in expectation of a heat flux density nearby the desired value. These electrical currents are based on measurements under phosphate conditioning at 2 bar, which the resulting heat flux densities are already known for:

$$750 A \approx 400 \cdot 10^3 W/m^2$$

$$1000 A \approx 800 \cdot 10^3 W/m^2$$

These amperages are applied manually as quickly as possible. As the tube temperature increases, re-adjustment of the amperage might be necessary. Data acquisition rate is set to 14 Hz, considered sufficient to recognise smallest temporal effects, like a tube wall temperature overswing.

Figure 6.6 depicts three possible qualitative progressions of a cold start-up as an example of what a burn-out III might manifest.

After an electric current is impressed on the test tube, its mean wall temperature increases leading to a rising heat flux density. Both physical quantities develop asymptotically for a normal start-up (solid line in figure 6.6).

An already critical impact of an organic layer on the mean wall temperature by suppressing nucleation on the surface is demonstrated by the dashed line in the same figure. Desorption processes result in an overswing of mean wall temperature and heat flux density, respectively. Desorption sets in after the boundary layer reaches a certain superheat. When desorption of the organic film is “complete”, nucleation sets in (if the boundary layer temperature approaches the saturation temperature at the actual system pressure). Bubble formation on the surface leads to an enhanced heat transfer to the boiling or even subcooled water (subcooled boiling results in remarkably high heat transfer coefficients), which eventually decreases the wall temperature and the heat flux density to the desired

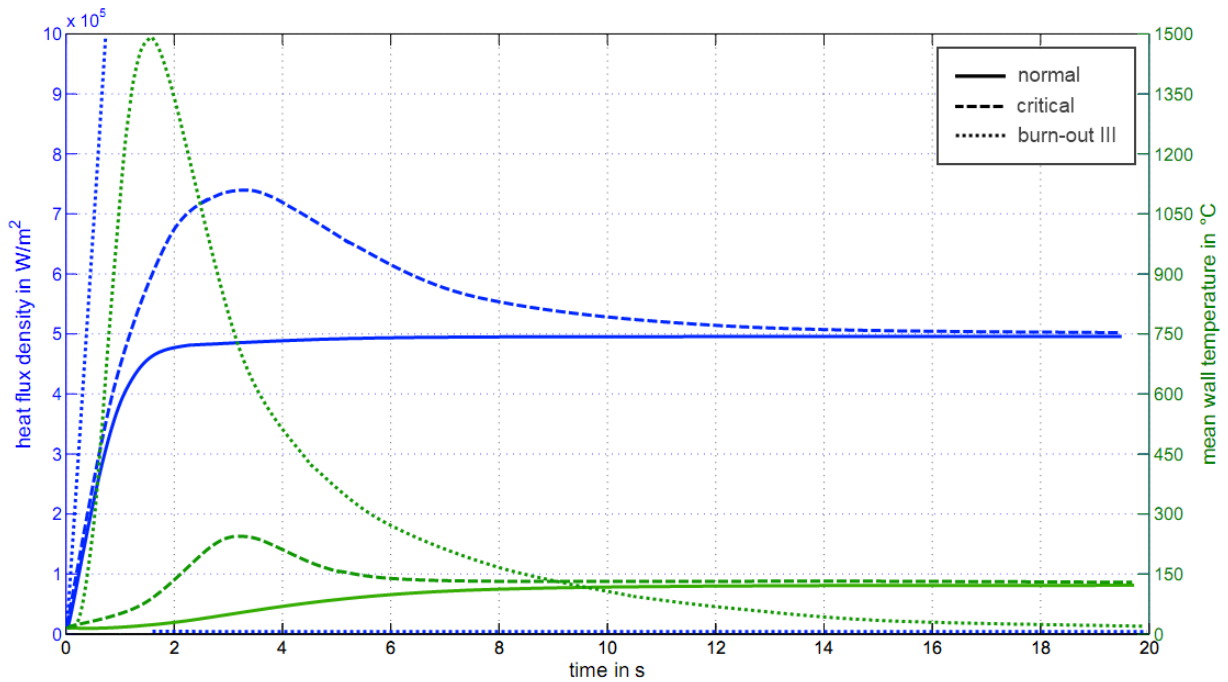


Figure 6.6: *Qualitative demonstration of a cold start-up using the electrical heating. The desired heat flux density is $\dot{q} = 500 \cdot 10^3 \text{ W/m}^2$.*

operation.

If desorption takes longer than the electrical heating to cause material temperatures higher than its melting point, a burn-out III occurs (dotted line in figure 6.6). Nucleation is prevented by a thick organic layer covering potentially available nuclei. The thermal load increases rapidly due to the high tube temperature. When the tube burns out, the power supply is interrupted and the heat flux density drops to zero.

7 Results and discussion

Since the saturation pressure in shell boilers is usually considerably higher than $p_s = 2 \text{ bar}$, this pressure is not discussed as intensely as $p_s = 15 \text{ bar}$, which is undoubtedly of major importance. Lower pressures are only discussed if necessary, like for reproducibility of the initial boiling behaviour, convective boiling or transition phenomena. Unless specified otherwise the typical phosphate treatment acts as reference for all investigated conditionings.

7.1 Trisodium phosphate treatment

7.1.1 Start conditions

The reproducibility of the initial boiling behaviour is essential for the comparison with any other treatment and/or treatment periods. Hence, a statistically firm study of $\alpha(\tau = 0)$ requires thorough and extensive repeated measurements and recurring identical pretreatment and measurement procedures.

In order to evaluate the reproducibility of the initial boiling behaviour regarding onset of nucleate boiling, more than 1000 value pairs $\alpha(\dot{q}, p_s)$ have been recorded for distinct tube charges and pretreatments described in section 6.3. The heat transfer coefficient is modelled as a function of the saturation pressure and the heat flux density for convective as well as nucleate boiling. Therefore, the known relation $\alpha = C \cdot \dot{q}^n$ is used, complemented by a non-dimensional pressure term p_{red}^m . Multivariate non-linear regression is applied on the following approach to fit the experimental data:

$$\alpha(\dot{q}, p_{red}) = \Gamma \cdot \dot{q}^{n(p_{red})} \cdot p_{red}^m \quad (7.1)$$

Here, Γ and m are pressure independent prefactors describing the influence of the charge, the pretreatment and the saturation pressure on the initial boiling heat transfer. A normalised saturation pressure $p_{red} = p_s/p_0$ is introduced, using a fixed reference pressure of $p_0 = 10 \text{ bar}$. A comparative visualisation of the calculated values α_{calc} via equation 7.1 with the experimentally gained data α_{exp} is used to demonstrate the significance of equation 7.1 and the reproducibility of α .

The pressure dependent boiling curves exponent $n(p_s)$ can be well approximated using an

exponential function of the saturation pressure p_s :

$$n(p_{red}) = n_0 + \Delta n \cdot \exp\left(-\frac{p_{red}}{\psi}\right) \quad (7.2)$$

Where n_0 is the asymptotic value for the exponent, Δn is the absolute decrease, and ψ is a factor, describing the pressure dependency.

Initial state *charge 1, unmodified etchant* is depicted in figure 7.1. Note: Logarithmic scaling results in asymmetric visualisation of σ and ε_{max} . Using equation 7.1, a mean

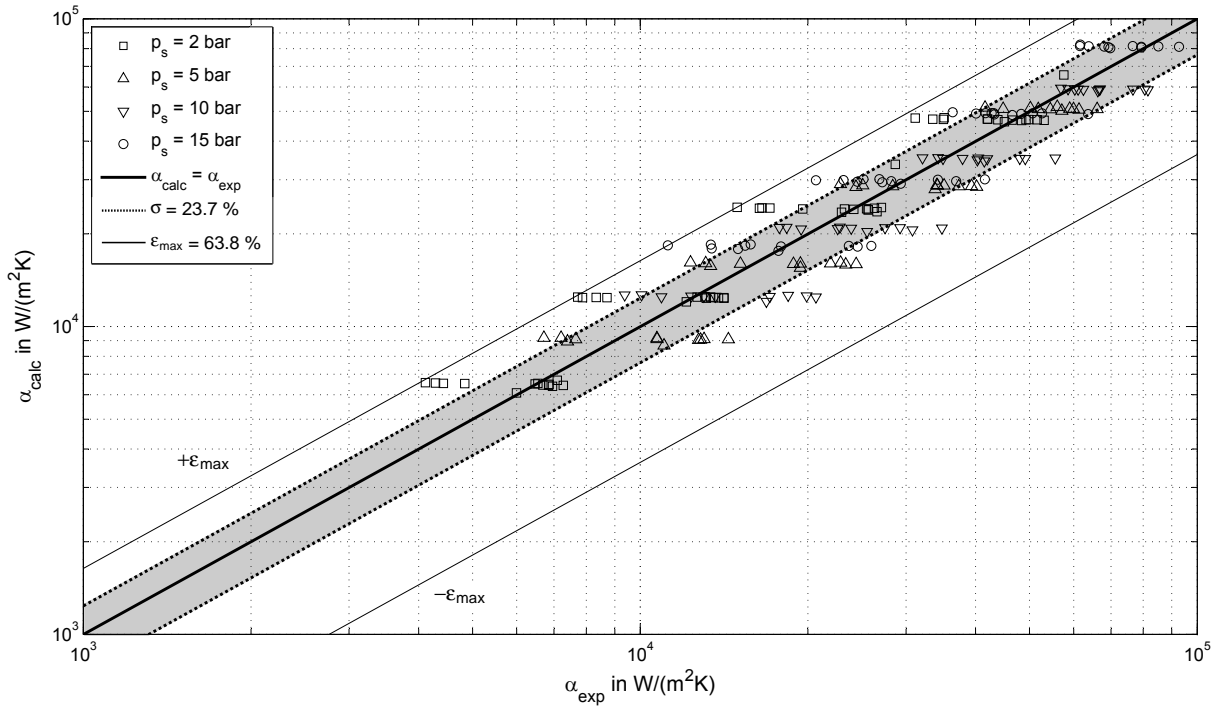


Figure 7.1: *Reproducibility of the initial nucleate boiling behaviour versus equation 7.1 for charge 1, unmodified etchant.*

deviation of $\sigma = 23.7 \%$ is achieved at a maximum scattering of $\varepsilon_{max} = 63.8 \%$. A fairly uniform location of the measured values around the graph of congruence demonstrates the quality of the chosen model. There are no obvious asymmetries in the data distribution.

A modification of the etchant to lower acid concentrations and an extended treatment period results in the experimental reproducibility presented in diagram 7.2 for *charge 1, modified etchant*. Here, the mean deviation increases to $\sigma = 26.4 \%$ compared to the unmodified pretreatment, while the maximum error is reduced by 10 % to $\varepsilon_{max} = 53.3 \%$. This combination still does not meet the demands for improved reproducibility.

Therefore, *charge 2* is introduced while maintaining the unmodified etching procedure. As it is sourced from the same melting and fabrication process, *charge 2* promises a more

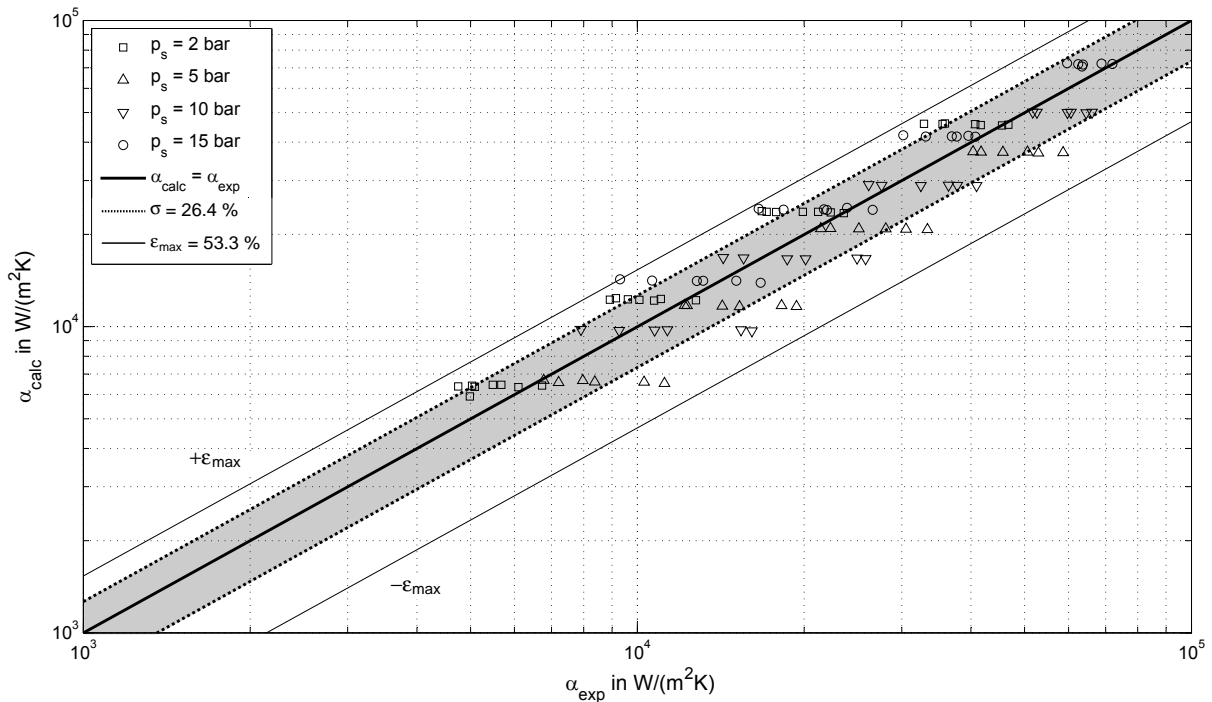


Figure 7.2: *Reproducibility of the initial nucleate boiling behaviour versus equation 7.1 for charge 1, modified etchant.*

consistent material quality/surface finish than *charge 1*. Accordingly, the experimental findings are presented in figure 7.3. *Charge 2* responds differently to the pretreatment compared to *charge 1*. The mean deviation of $\sigma = 17.6\%$ is cut-down significantly as well as the maximum error with $\varepsilon_{max} = 30.7\%$.

Finally, the modified etching procedure is applied to *charge 2* and provides further improvement. Depiction 7.4 shows experimental data versus calculation. The mean deviation $\sigma = 11.6\%$ is further reduced considerably by application of a modified etching procedure compared to the former method. The maximum error increases slightly to $\varepsilon_{max} = 33.3\%$ but is not of statistical relevance.

The reproducibility of the initial nucleate pool boiling heat transfer coefficients is improved using *charge 2, modified etchant* as compared to the initial combination. Given the differences in the boiling behaviour of the assayed combinations, the heat transfer of metallic-blank surfaces can only be calculated by means of experimental support values.

As a summary, table 7.1 lists the corresponding coefficients for all investigated combinations including the mean deviation σ and maximum error ε_{max} of α .

Picture 7.5 presents some chosen freeze frames of three exemplary tubes for an impressed electric current of $I = 186\text{ A}$ ($\dot{q} \approx 27 \cdot 10^3\text{ W/m}^2$) to visualise bubble formation on the investigated combinations (black and white pictures have been used for clarity reasons).

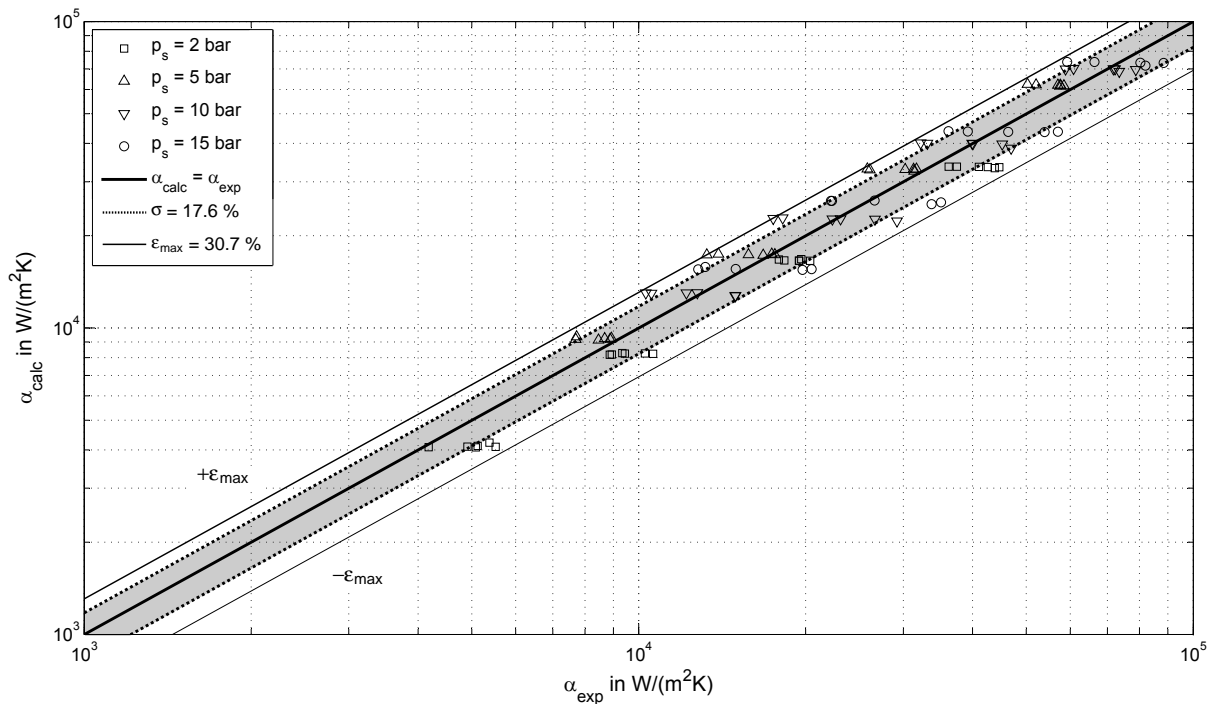


Figure 7.3: *Reproducibility of the initial nucleate boiling behaviour versus equation 7.1 for charge 2, unmodified etchant.*

Apparently, as recognisable by the number of active nuclei, both factors, etching procedure and tube charge, determine the heat transfer during nucleate boiling. Tubes from *charge 1* seem to react more intensely to the *unmodified etchant* despite identical quality, although the resulting heat transfer coefficients scatter significantly. A qualitative summary of the number of active nuclei for all assayed combinations is depicted in figure 7.6 on the basis of visual examination.

The corresponding mean boiling curves of all assayed combinations with their respective exponents, as obtained by an overall regression, are located in the appendix C. Furthermore, video recordings of the behaviour of the assayed tube pretreatments during the boiling process are carried out, which support the described cognitions (see optical data carrier in appendix E).

Assuming neglectable variations in the material composition of the investigated tube charges, the thermal properties of the heater material are not considered responsible for the observed differences in the heat transfer coefficient.^[11] The incongruity of the heat transfer coefficients must consequently be caused by the acidic pretreatment. Given identical water quality and test conditions, a modified nuclei radius spectrum on the surface is considered responsible for the observed active nucleation site density presented in the images. Literature states following generally accepted correlation for the expected heat

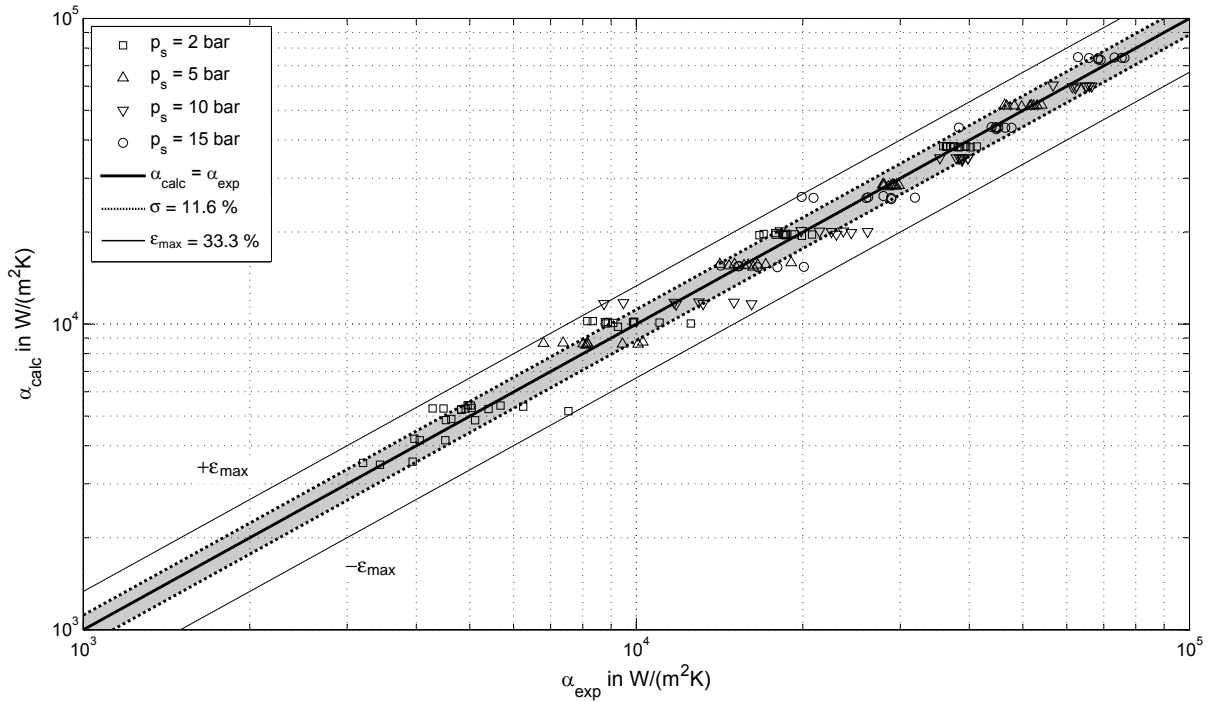


Figure 7.4: *Reproducibility of the initial nucleate boiling behaviour versus equation 7.1 for charge 2, modified etchant.*

transfer coefficient during nucleate pool boiling:^[31]

$$\frac{\alpha}{\alpha_0} = C_W \cdot F(p') \left(\frac{\dot{q}}{\dot{q}_0} \right)^n \quad (7.3)$$

α_0 and \dot{q}_0 are measured support values, $F(p')$ represents the pressure dependency of α with respect to the support values. The reduced pressure p' is in this case p/p_{crit} . C_W includes the relative influence of the (thermal and micro geometric/roughness) heating surface properties, whereas, in this case, exponent n is considered *pressure dependent only*.

It is shown, that the experimentally obtained exponent n differs with the type of pretreatment and tube charge and not only with pressure. Equation 7.3 does not incorporate this issue. A comparison of measured exponents and equation 2.7 is shown in picture 7.7.

A slightly steeper decrease of the experimental data with the pressure is evident (charge 2, modified etchant). All observed exponents are within the range of equation 2.7. Beside $p_s = 2 \text{ bar}$ the experimental exponent n is consistently lower than predicted by equation 2.7. Some investigated combinations, like *charge 1, unmodified etchant*, hardly even intersect with the statistically valid range of equation 2.7. As used for the investigations in this work, the relative mean deviation for *charge 2, modified etchant* is included into the

Table 7.1: *Coefficients and statistical accuracy of equation 7.1 applied to the different combinations (charge, etchant).*

Combination	Γ in K^{-1}	m	n_0	Δn	ψ	σ	ε_{max}
charge 1, unmodified etchant	33.48	1.39	0.53	0.30	0.43	23.7 %	63.8 %
charge 1, modified etchant	18.24	0.92	0.58	0.27	0.24	26.4 %	53.3 %
charge 2, unmodified etchant	20.87	1.64	0.48	0.33	0.99	17.6 %	30.7 %
charge 2, modified etchant	22.24	1.24	0.63	0.27	0.25	11.6 %	33.3 %

diagram for comparative reasons.

Exponent n describes the influence of the thermal load on the heat transfer coefficient. If the exponent is comparably lower than equation 2.7 predicts, α is determined less than expected by the heat flux density. This, in turn, means that assuming a comparable level of heat transfer (C_{red}), more nuclei are already active at smaller heat flux densities. The number of active nucleation sites does not increase as steeply as stated in the literature.^[31] Given equation 2.2 and bubble generation as the dominating heat transfer mechanism during nucleate boiling, the pretreated surface can be assumed to provide a sufficient fraction of larger cavities that can be activated at smaller heat flux densities or corresponding superheats.

Convective pool boiling

The region of free convective pool boiling is examined using the combination *charge 2, modified etchant*, as this pairing proves convenient for the reproducibility during nucleate boiling as well. The surface structure of *charge 2* as treated with the modified etchant is considered to have an insignificant effect on the heat transport during convective boiling.

A correlation is found in analogy to the nucleate boiling heat transfer. In this case, however, the statements refer exclusively to a saturation pressure of $p_s = 2 \text{ bar}$, as the only pressure where convection can be put into practice. The average exponent of the boiling curves is determined with $n = 0.31$ ranging from 0.19 to 0.41. Regression yields:

$$\alpha = 106.4 \cdot \dot{q}^{0.31} \quad (7.4)$$

with a relative mean deviation of $\sigma = 15.3 \%$ and maximum error of $\varepsilon_{max} = 31.9 \%$ for k (see figure 7.8).

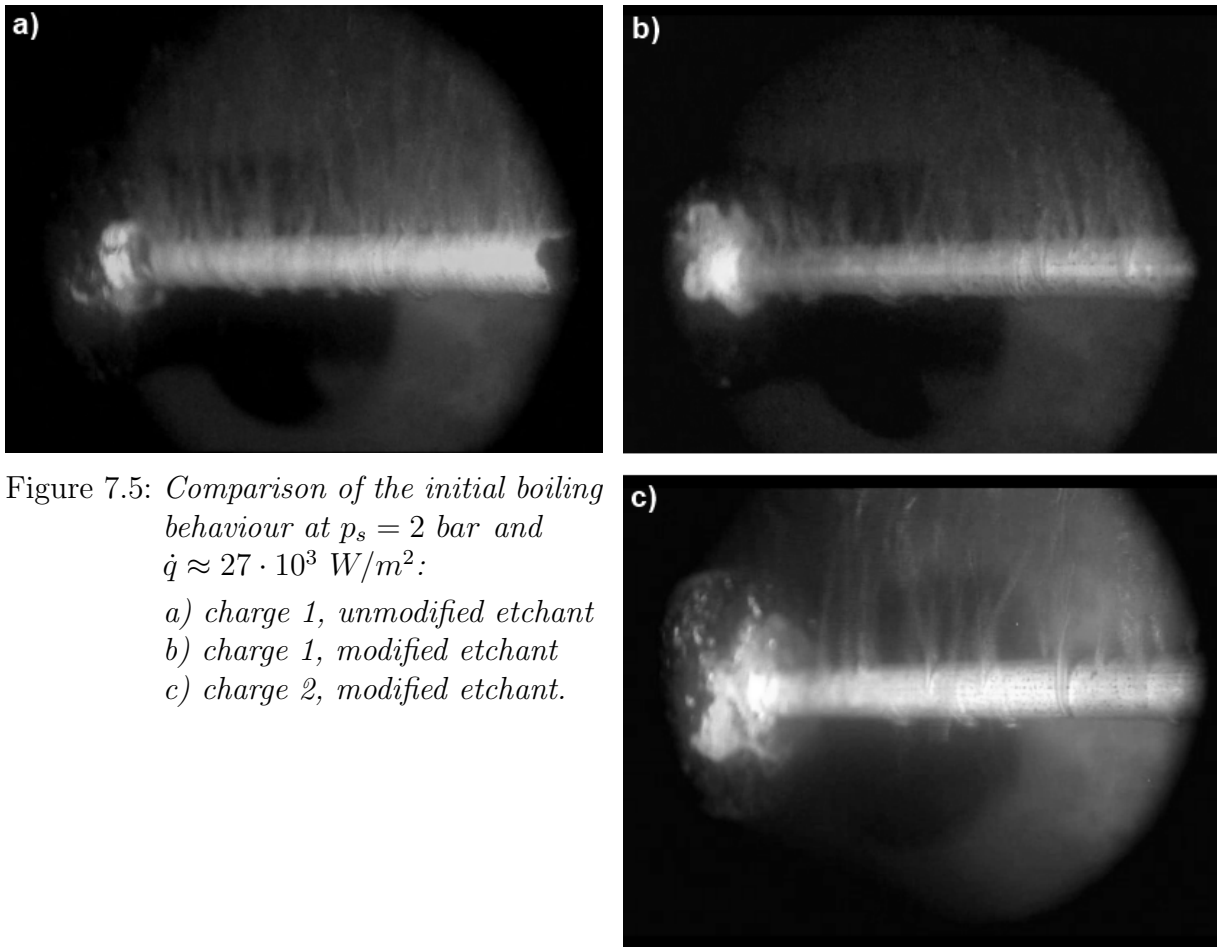


Figure 7.5: Comparison of the initial boiling behaviour at $p_s = 2 \text{ bar}$ and $\dot{q} \approx 27 \cdot 10^3 \text{ W/m}^2$:
 a) charge 1, unmodified etchant
 b) charge 1, modified etchant
 c) charge 2, modified etchant.

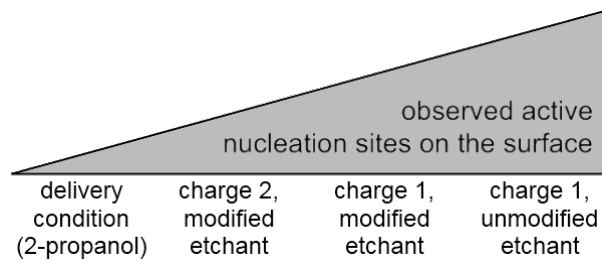


Figure 7.6: Qualitative comparison of the observed active nuclei number on the respective tube surfaces at $p_s = 2 \text{ bar}$.

Steinbrecht draws conclusions on the convective boiling heat transfer coefficient at pressures up to 25 bar using similar tube material and equipment (except for the tube diameter of 4.00 mm instead of 6.00 mm in this work) with well reproducible boiling curves.^[11]

As can be assumed, the reason for an earlier nucleation and increased heat transfer coefficients is the pretreatment/activation procedure by pickling described in section 6.3.

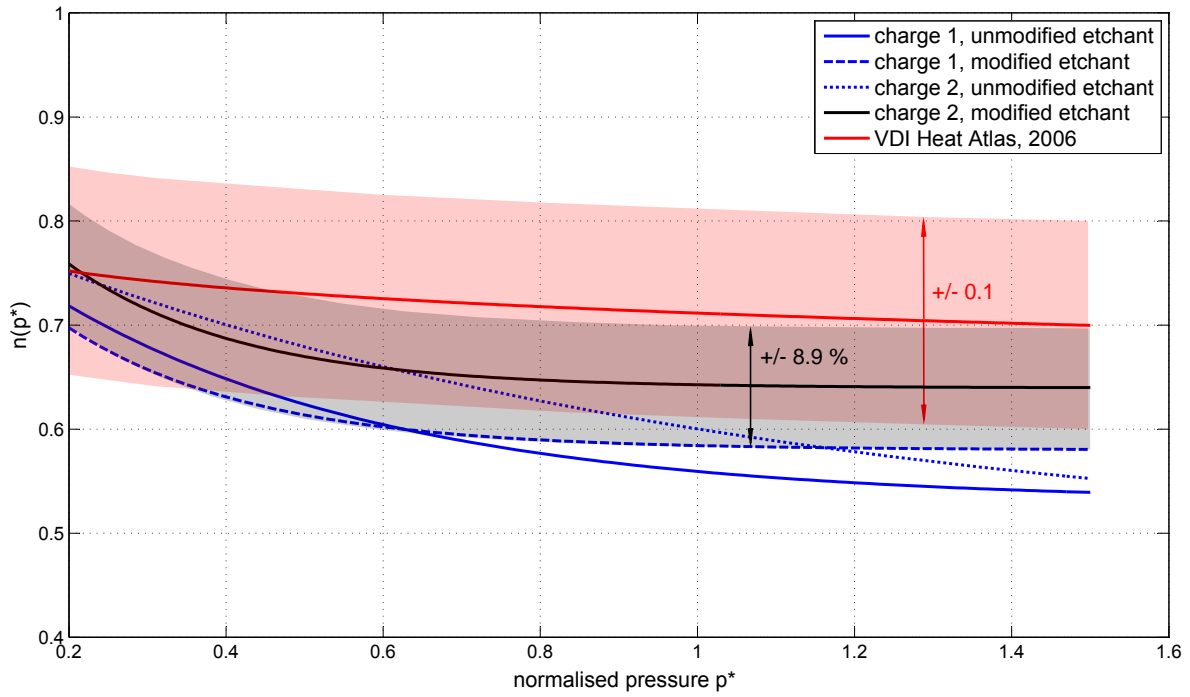


Figure 7.7: Comparison of the experimentally determined boiling curves exponent with equation 2.7 from the literature.^[31]

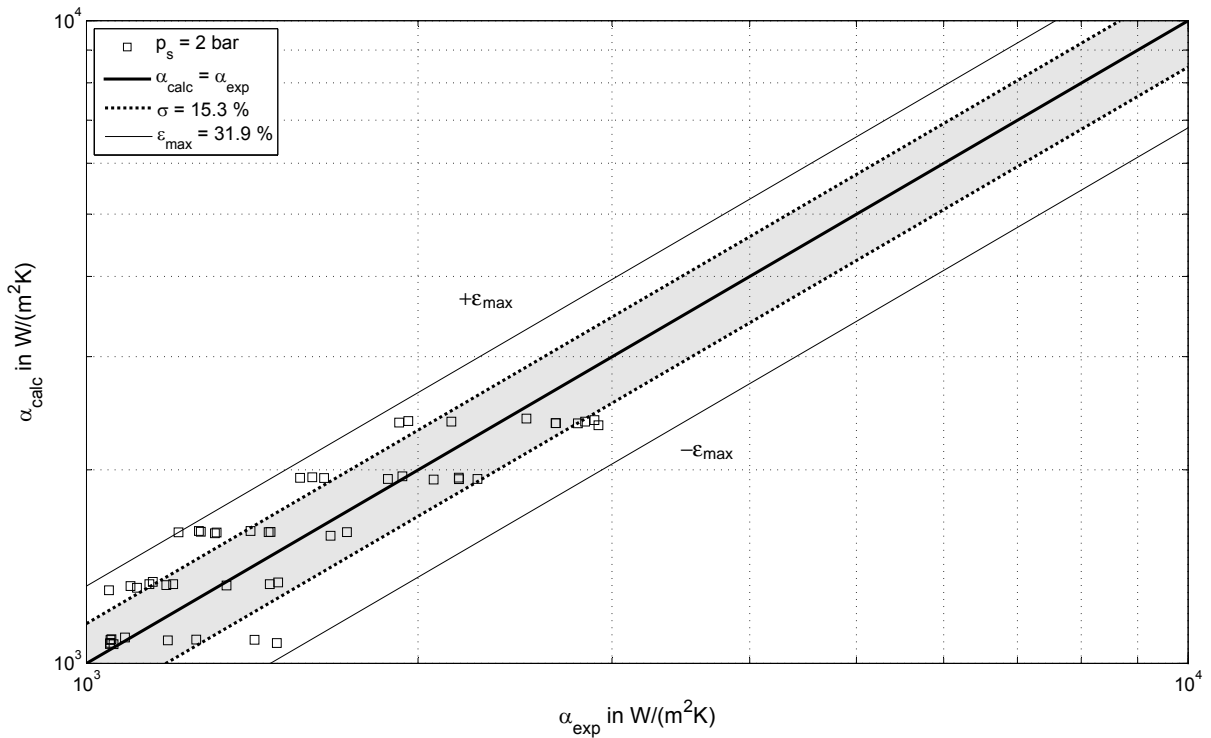


Figure 7.8: Reproducibility of the initial convective boiling behaviour versus equation 7.1 for charge 2, modified etchant.

The influence of pretreatment is supported by the experimental investigations on the effect of isopropanol on the initial heat transfer coefficients. *Charge 1, unmodified etchant* is therefore compared to *charge 2, 2-propanol* at elevated pressures. The results can be found in the appendix C.

7.1.2 Conclusion

Smallest variations in delivery quality and the type of pretreatment result in considerable differences of the initial nucleate pool boiling heat transfer.

The statistical spread can be reduced by means of specimens from the same melting and drawing process (*charge 2*) and an optimised chemical etching procedure (*modified etchant*). Enhanced heat transfer coefficients can be achieved with *charge 1, unmodified etchant* due to an increased number of active nuclei at comparable heat fluxes. However, scattering remains high. The combination of *charge 2* and the *modified etchant* provides the best reproducibility of α compared to the work of Steinbrecht^[43] or any other combination investigated in this work. In order to ensure the reproducibility of k during the operation with other conditionings, *charge 2, modified etchant* is used.

The exponent of the heat flux density under nucleate pool boiling conditions is influenced by the pretreatment and consequently by the micro geometric surface properties. This observation stands in contrast to the literature, where the exponent is stated to be only pressure dependent.

Remaining deviations of the initial heat transfer coefficients

- an attempt of interpretation

Despite intensive efforts, reproducibility of the initial heat transport conditions can only be achieved in statistical terms. The reasons are considered, among random influences every measurement is subject to, mostly of (micro-)geometric nature.

Besides morphological influences, test tubes of the described quality underlie fabrication tolerances according to DIN EN 10305-1 (DIN 2391).^[82] Those are defined for cold-drawn precision tubes with a maximum acceptable variation of the inner (Δd_i) and outer (Δd_o) tube diameter. The particular permitted tolerances in this case (6.00 mm x 1.00 mm) are:

$$\begin{aligned}\Delta d_o &= \pm 0.08 \text{ mm} \\ \Delta d_i &= \pm 0.15 \text{ mm}\end{aligned}$$

While the outer tube diameter can be checked easily, direct and practical measurements of the inner diameter or wall thickness are difficult. An unrecognised increased wall thickness

leads to a decreased heat flux density, as the electrically conducting cross-section rises with nearly unmodified surface area and vice versa. The influence of the maximum wall thickness tolerances is therefore investigated using the evaluation routine explained in section 5.2 by adjusting the temperature constant K_R .

For an exemplary series of measured data the effect of mentioned tolerances on heat flux density and heat transmission coefficient is calculated with respect to a minimum and maximum wall thickness in contrast to the nominal value. Since the specific heat flux rises with increasing system pressure / saturation temperature (electric current is constant), the most significant influences can be expected for high heat fluxes and elevated saturation pressures.

Figure 7.9 depicts the corresponding results for $p_s = (2, 15) \text{ bar}$. At high heat flux densities and $p_s = 15 \text{ bar}$, a variation of up to $\Delta k \pm 10 \%$ results assuming the worst case tolerance compared to the values for the nominal wall thickness. As the actual value of s is not quantified prior to the test, the corresponding uncertainty is assumed to have a proportionate share on the experimental variation of the heat transmission coefficient.

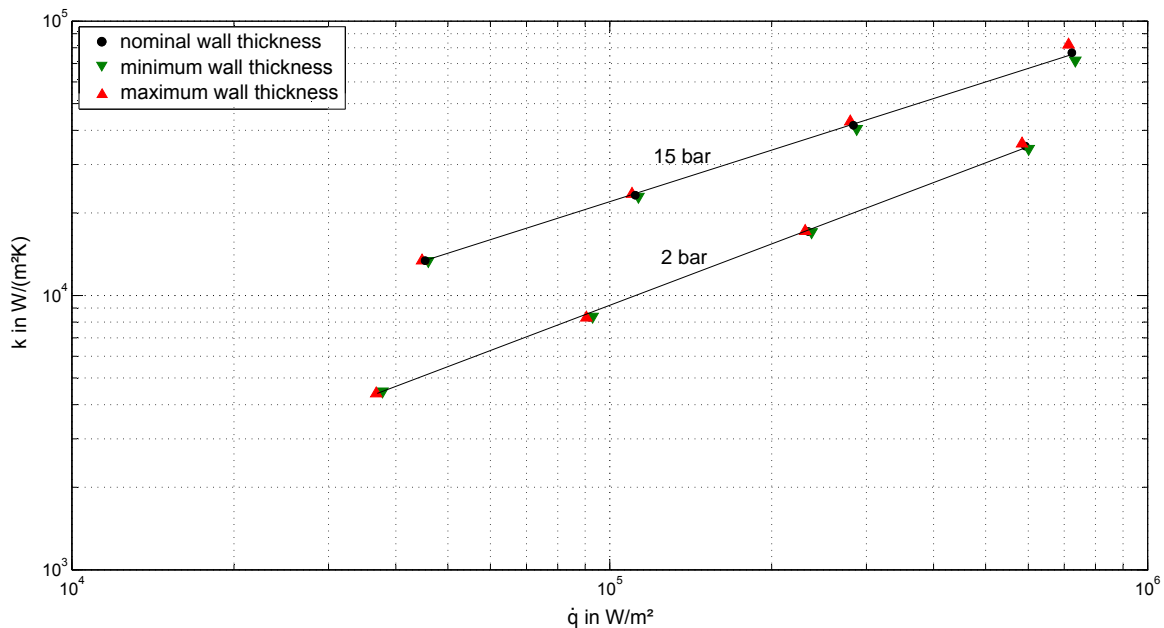


Figure 7.9: Impact of the dimension tolerances according DIN EN 10305-1 on k for $p_s = (2, 15) \text{ bar}$.

7.1.3 Time response of k during operation

An overall number of 741 data sets $k(\dot{q}, p_s, \tau)$ is evaluated regarding the effect of oxide layer generation on the heat transmission during the Na_3PO_4 treatment. The experimentally acquired heat transmission coefficient k shows a considerable decline during operation for all investigated pressures, boiling ranges and heat flux densities.

Apart from small temporal variations, a noticeable trend of the boiling curves exponent n can be observed neither for nucleate nor for convective pool boiling under inorganic PO_4 conditioning. As an example, the nucleate boiling exponent $n(\tau)$ at $p_s = 15 \text{ bar}$ is depicted in figure 7.10.

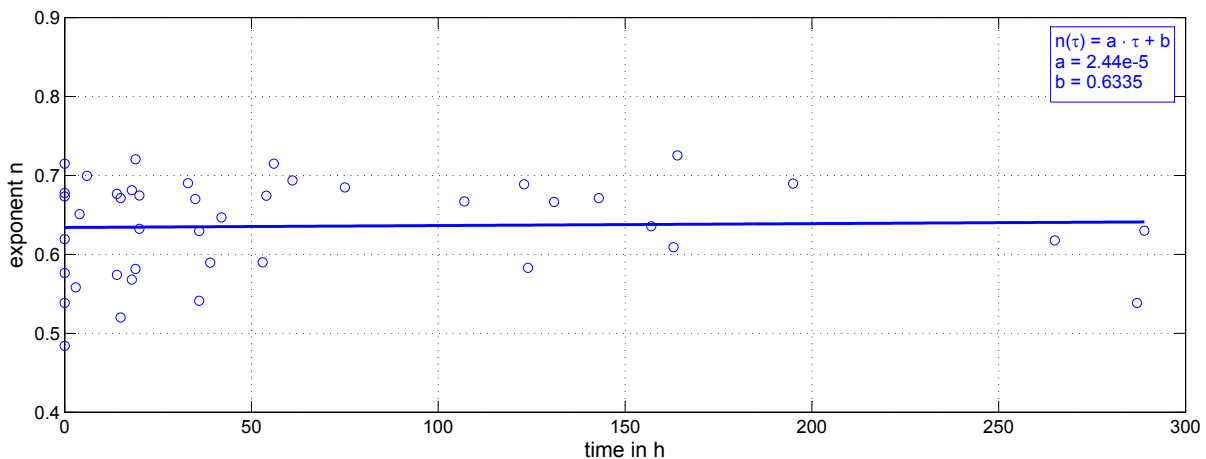


Figure 7.10: Time behaviour of the boiling curves exponent n during trisodium phosphate treatment at $p_s = 15 \text{ bar}$.

Scattering of n can be assumed a result of random influences on the heat transmission coefficient and consequently affecting the boiling curve. Regression is carried out using a linear approach. The slope of $dn/d\tau = 2.44 \cdot 10^{-5} \text{ h}^{-1}$ is neglectable. Analogous investigations on the time response of the exponent at $p_s = (2, 5, 10) \text{ bar}$ yield similar results.

As the exponent remains about constant during operation with Na_3PO_4 , according to section 5.3, a standardisation of k can be carried out according equation 5.18 using an average exponent $\bar{n}(p_{red})$ for the investigated pressure stage.

The corresponding pressure discrete exponent is valid for all determined boiling curves at the investigated pressure stage throughout the entire treatment period.

Nucleate pool boiling

Starting with the experiments for nucleate pool boiling at 15 *bar* and incorporating all investigated tube samples, an average exponent of $\bar{n}_{15} = 0.63$ is found. The discrete-time values vary from $n = 0.49$ to $n = 0.73$.

Picture 7.11 shows an exemplary boiling curve development $k(\dot{q}, \tau)$ at $p_s = 15$ *bar* during nucleate pool boiling under PO_4 conditions. Very characteristic is the asymptotic decline

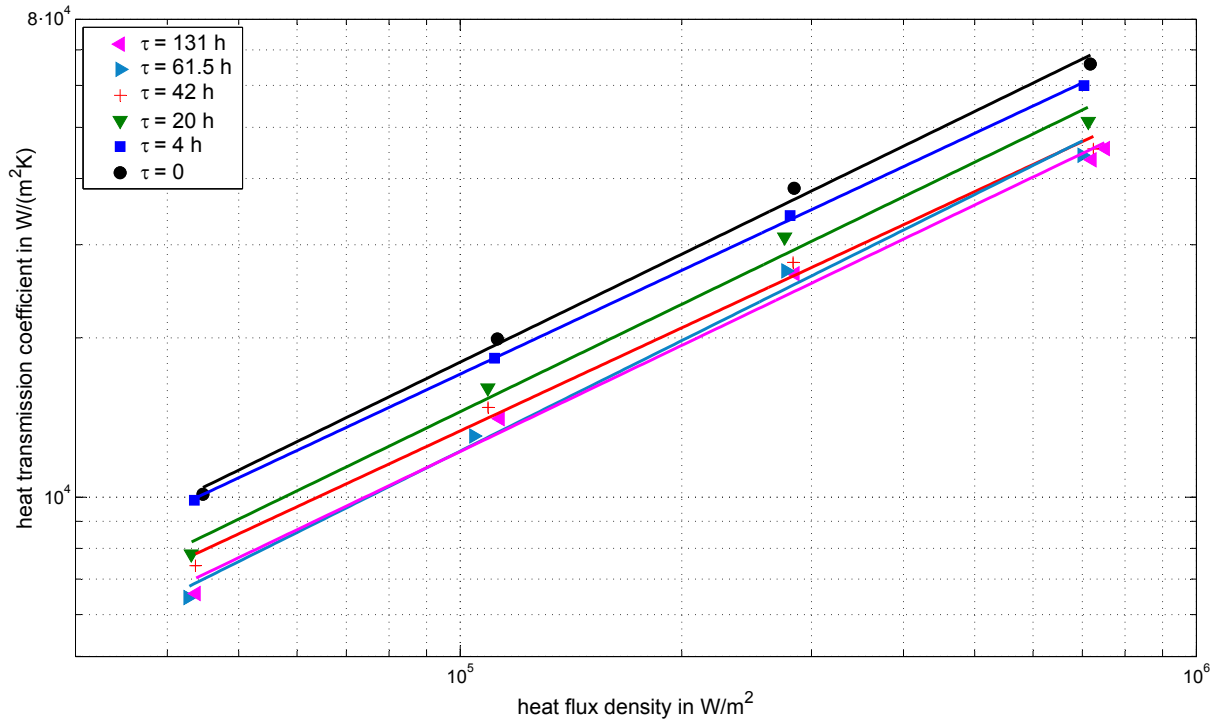


Figure 7.11: *Exemplary development of the boiling curves under nucleate pool boiling conditions at $p_s = 15$ bar.*

of k during operation as caused by the oxide layer generation, being a self impeding process. Data undergoes the reduction explained in section 5.3.

Multiple regression of the acquired data under nucleate boiling conditions and transformation from $k(\dot{q}, p_s, \tau)$ to $C_{red}(p_s, \tau)$ yields the time response of C_{red} at 15 *bar* (see figure 7.12).

The initial values of k determined during the studies of the starting conditions are included in the diagram. The exponential approximation is in good agreement with the measurement at a relative standard deviation of $\sigma = 10.1$ %. Using the corresponding time constant $\kappa = 20.8$ *h*, equation 5.21 calculates a treatment period of $\tau_{99} = 95.8$ *h* necessary to reach thermotechnical steady state of the heat transmission coefficient. Reduced heat transmission coefficient C_{red} shows a considerable overall decline of $\Delta C \approx 28$ %.

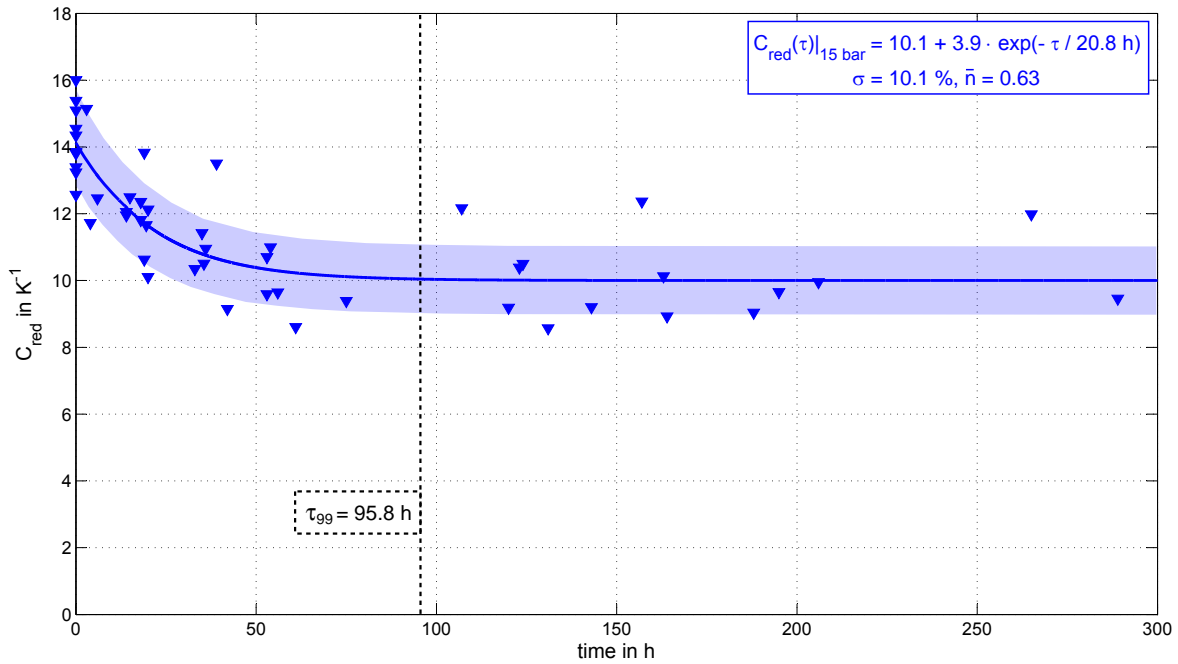


Figure 7.12: Time response of the reduced nucleate boiling heat transmission coefficient C_{red} at $p_s = 15$ bar during PO_4 treatment. The tinted area marks the relative mean deviation σ .

The absolute decline in k determined at 15 bar is depicted in figure 7.13 in comparison to boiling curves obtained by integrating equation 5.18 into 2.4 and non-linear regression. The relative mean deviation $\sigma = 13.5$ % is introduced to mark the statistical spread of experimental data.

The same mathematical procedure is carried out for $p_s = 10$ bar. An analogous asymptotic decline of k can be observed. Exponent n varies from 0.59 to 0.76 with an average of $\bar{n}_{10} = 0.65$. The time response is depicted in figure 7.14.

Experimental data can be approximated well by use of the exponential decay with a relative mean deviation of only $\sigma = 4.7$ %. A time constant of $\kappa = 20.3$ h is found by regression. Equation 5.21 yields a necessary treatment period of $\tau_{99} = 94.6$ h which is about the same as for 15 bar. During operation C_{red} decreases by $\Delta C \approx 28$ %.

Figure 7.15 shows the decrease of k between the start of treatment and steady state conditions.

The relative mean deviation for k compared to the regression is calculated to $\sigma = 8.4$ %.

Pictures 7.16 and 7.17 demonstrate the time response $C_{red}(\tau)$ and overall drop in k measured at $p_s = 5$ bar. The boiling curves exponent n for $p_s = 5$ bar varies from 0.59 to 0.82 with an average of $\bar{n}_5 = 0.67$.

Here, the reproducibility of the surface processes is rather poor. There is an intersection

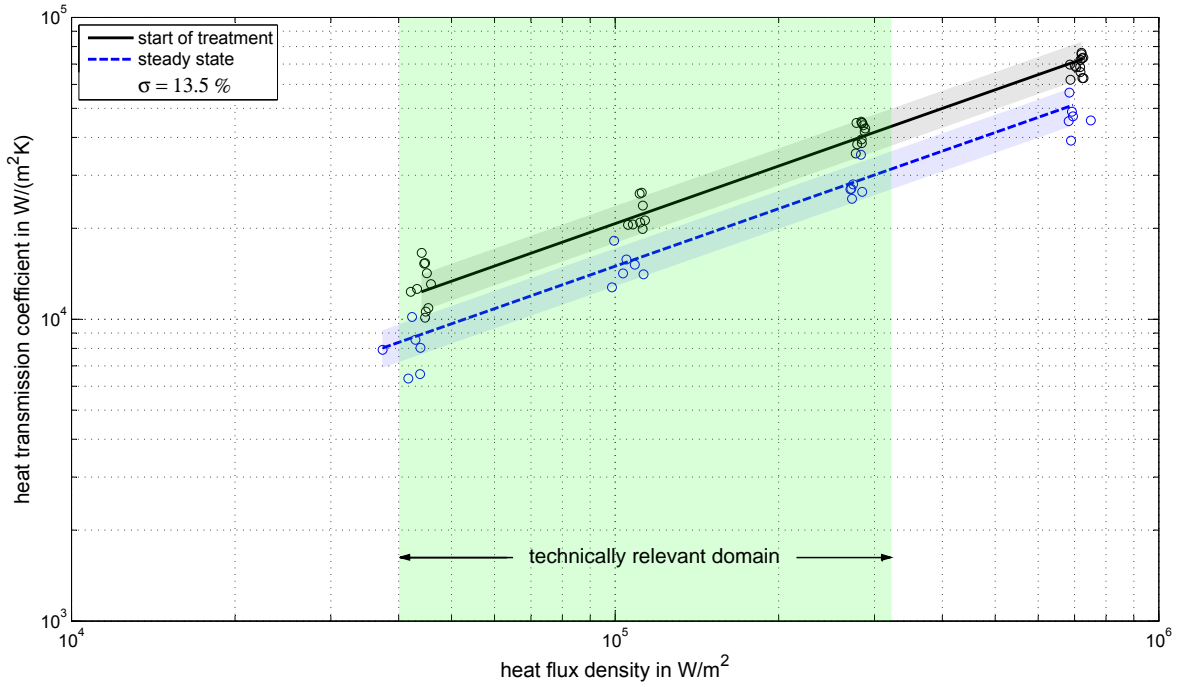


Figure 7.13: *Experimental data and boiling curves at $p_s = 15$ bar during nucleate pool boiling at the start and for steady state k .*

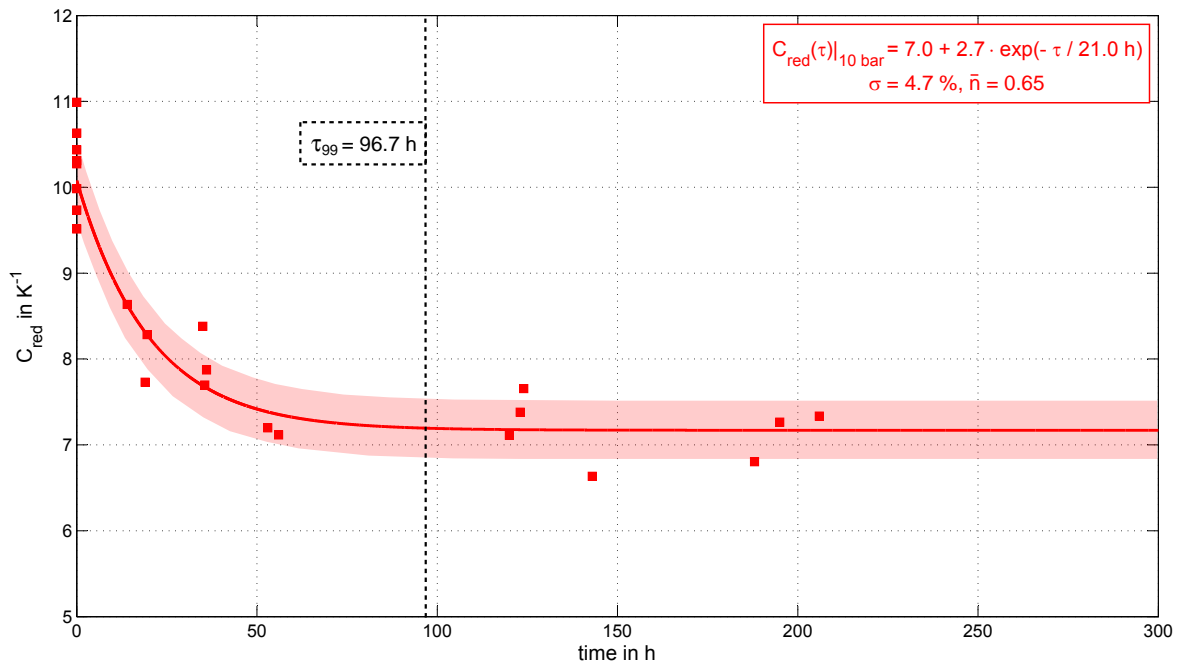


Figure 7.14: *Time response of C_{red} , obtained at $p_s = 10$ bar during PO_4 treatment at 15 bar.*

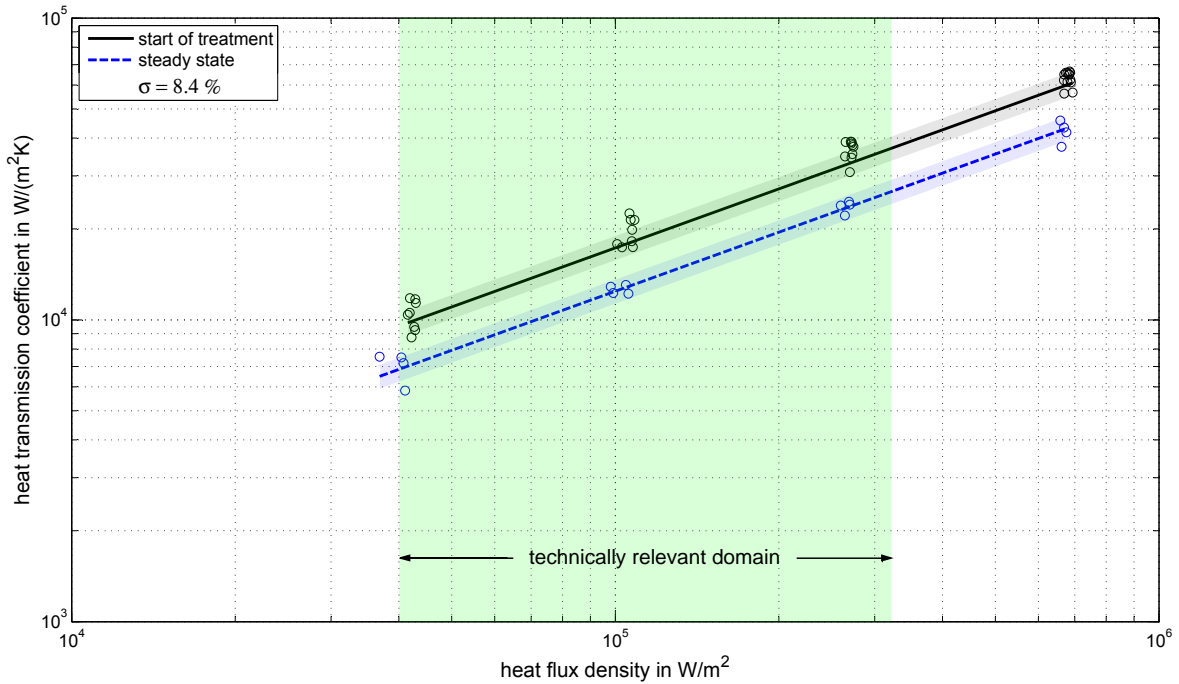


Figure 7.15: *Experimental data and boiling curves at 10 bar during nucleate pool boiling at the start and for steady state k.*

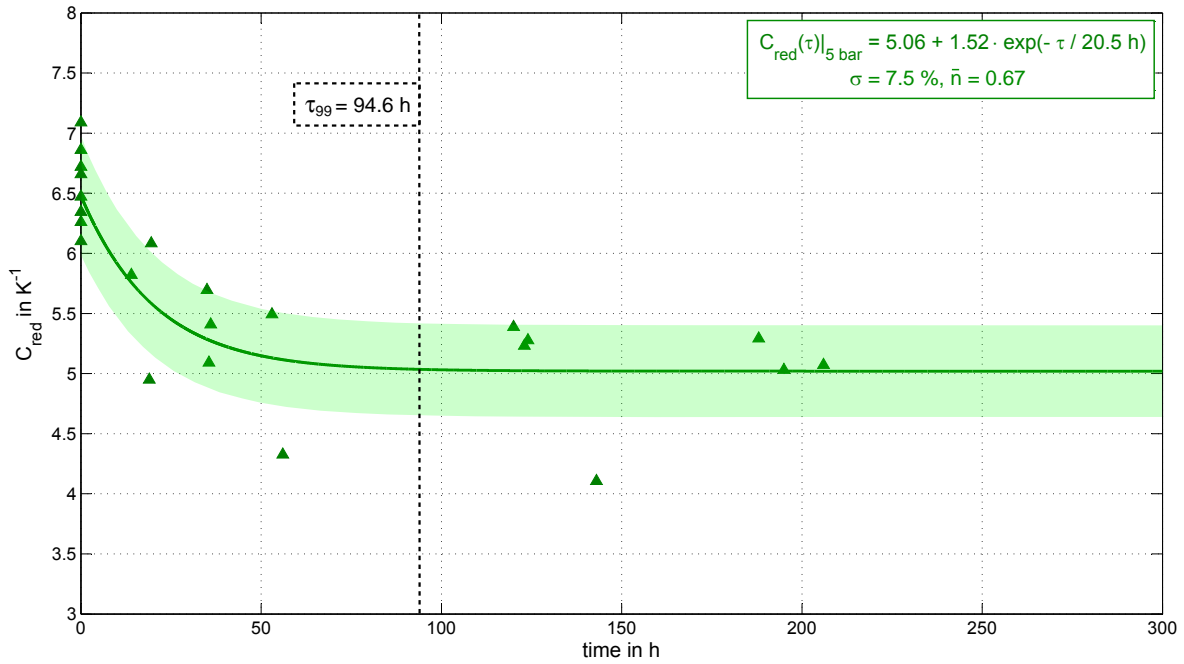


Figure 7.16: *Time response of C_{red} , obtained at $p_s = 5 \text{ bar}$ during PO_4 treatment at 15 bar.*

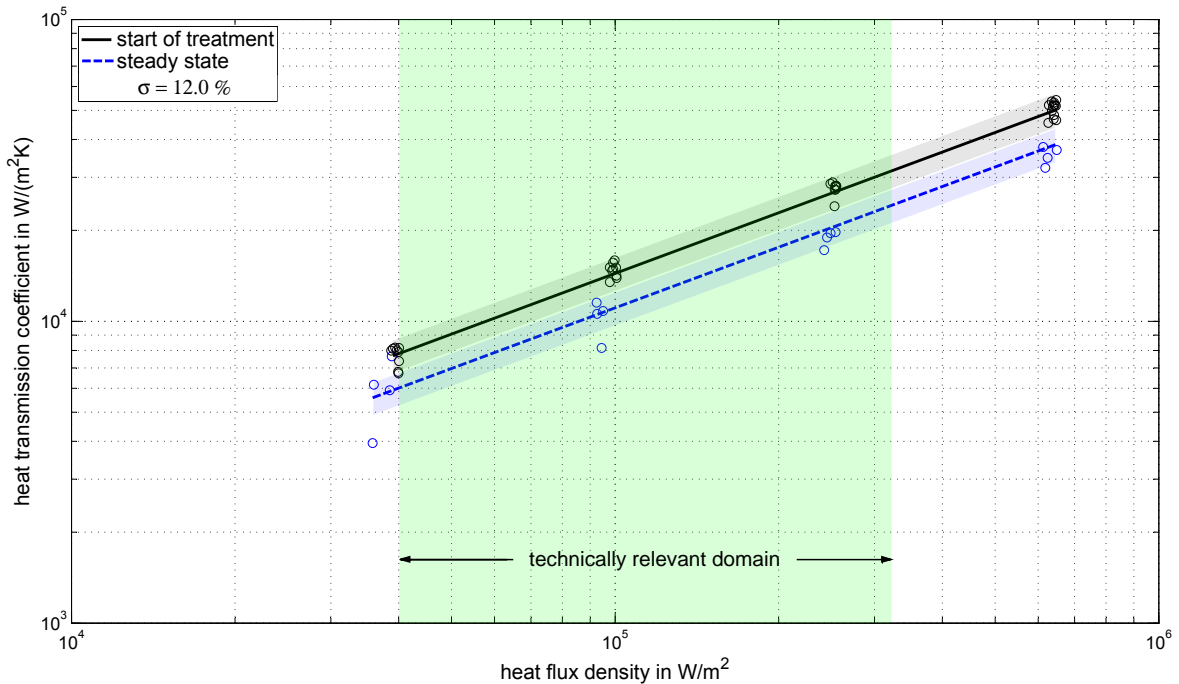


Figure 7.17: *Experimental data and boiling curves at 5 bar during nucleate pool boiling at the start and for steady state k .*

of σ in the beginning and at the end of the tests. The smaller corresponding values of k become with decreasing pressure, the clearer seems the influence of lacking reproducibility on differentiability. For $p_s = 5 \text{ bar}$ the drop in k is about 23 %.

The situation of reproducibility is worsening even more for nucleate boiling at $p_s = 2 \text{ bar}$ as presented in figures 7.18 and 7.19. Experimental values of n are within 0.66 to 0.86, with an average of $\bar{n}_2 = 0.76$.

Data scattering with $\sigma = 16.1 \%$ results in an obvious overlap of the mean deviations and impairs strict distinction between the starting conditions and the steady state of k . An overall decline in the heat transmission coefficient is determined with $\Delta k = 17 \%$. The relative decline of k correlates with the investigated pressure. So does the increase of the heat transmission coefficient. Both quantities develop asymptotically.

Layer generation takes place exclusively at $p_s = 15 \text{ bar}$. Consequently, when k is in thermotechnical steady state at $p_s = 15 \text{ bar}$, all additionally investigated lower pressure stages, $p_s = (2, 5, 10) \text{ bar}$, can be assumed to feature steady state values of k , too. Table 7.2 lists the values of κ during nucleate pool boiling at the investigated pressures. Although, there are differences in the time constants, an average time value $\bar{\kappa} = 20.5 \text{ h}$ is used for the entire investigated pressure range.

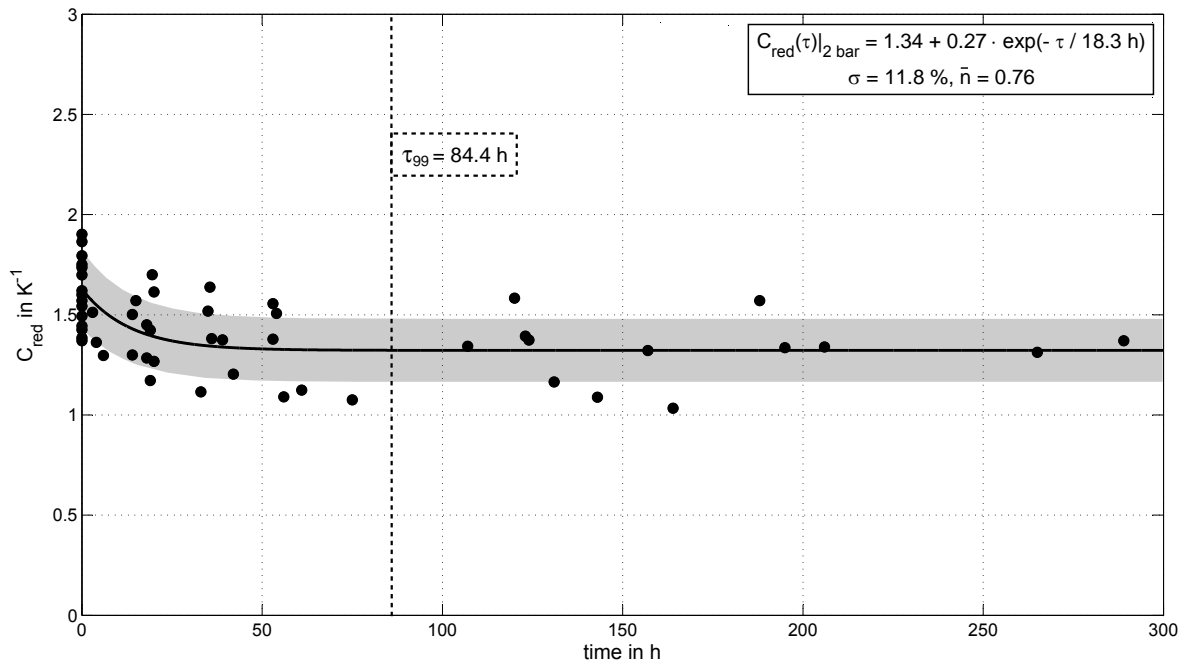


Figure 7.18: Time response of C_{red} , obtained at $p_s = 2$ bar during PO_4 treatment at 15 bar.

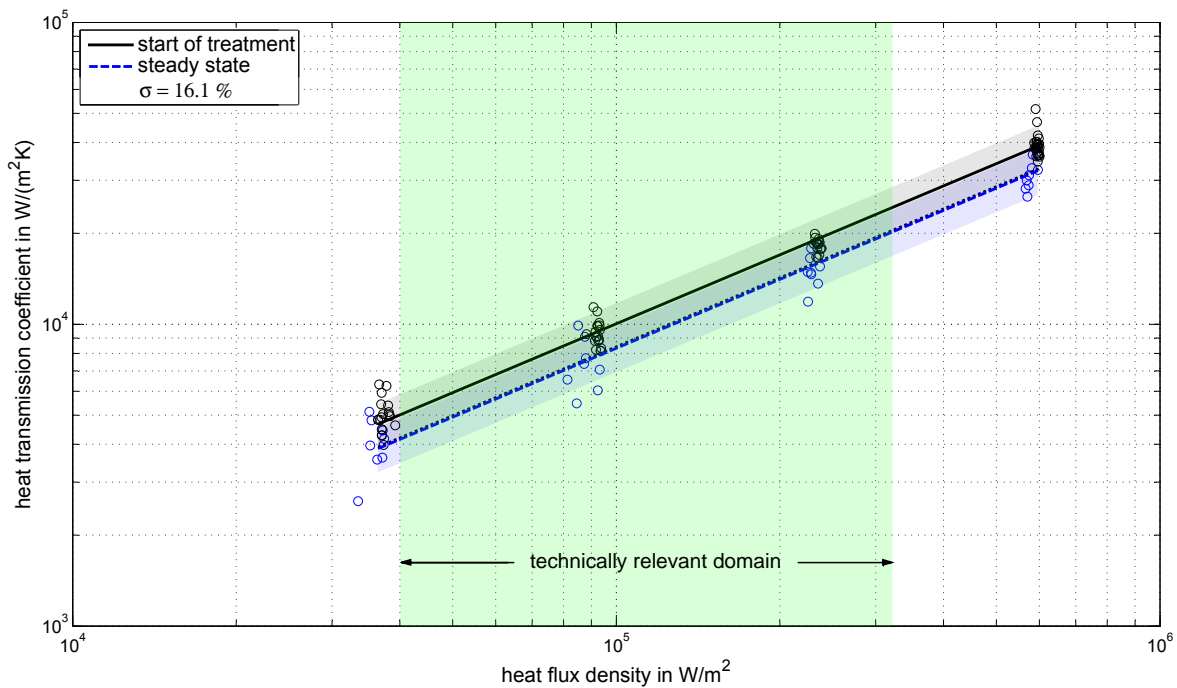


Figure 7.19: Experimental data and boiling curves at 2 bar during nucleate pool boiling at the start and for steady state k .

Table 7.2: *Determined (rounded) time constants for the investigated pressures during nucleate pool boiling and average value $\bar{\kappa}$.*

p_s in bar	2	5	10	15	$\bar{\kappa}$
κ in h	18.4	20.5	21.0	20.8	20.5

Use of $\bar{\kappa}$ enables correlation of C_{red} with the treatment period τ and the reduced saturation pressure p_{red} by multiple non-linear regression of equation 5.18 in order to gain *one* description of the type $C_{red}(\tau, p_{red})$:

$$\begin{aligned}
 C_{red}(\tau, p_s) &= C_0 + \Delta C \cdot \exp\left(-\frac{\tau}{\bar{\kappa}}\right) \\
 C_0 &= a \cdot (p_{red} + b)^y \\
 \Delta C &= c \cdot p_{red}
 \end{aligned} \tag{7.5}$$

Table 7.3 presents the coefficients and the statistical quality of equation 7.5, where an overall σ is determined for the entire pressure range. Figure 7.20 depicts the resulting curves.

Table 7.3: *Coefficients for equation 7.5.*

Coefficient	a	b	y	c
Value	8.49	-0.17	0.527	2.76

The following comprehensive empirical correlation 7.7 provides good reproducibility for the nucleate boiling heat transmission coefficient k_{nuc} :

$$\begin{aligned}
 k_{nuc}(\dot{q}, p_{red}, \tau) &= \left[8.49 \cdot (p_{red} - 0.17)^{0.527} + (2.76 \cdot p_{red}) \cdot \exp\left(-\frac{\tau}{20.54 \text{ h}}\right) \right] \dots \\
 \dots &\cdot \dot{q}^{(0.63+0.27 \cdot \exp(p_{red}/0.25))}
 \end{aligned} \tag{7.6}$$

$$\begin{aligned}
 [k_{nuc}] &= 1 \text{ W}/(\text{m}^2\text{K}) \\
 [\dot{q}] &= 1 \text{ W}/\text{m}^2 \\
 [\tau] &= 1 \text{ h}
 \end{aligned}$$

within the pressure range of $0.2 \leq p_{red} \leq 1.5$ and heat flux densities $40 \cdot 10^3 \text{ W}/\text{m}^2 \leq \dot{q} \leq 650 \cdot 10^3 \text{ W}/\text{m}^2$ for the trisodium phosphate treatment at $p_s = 15 \text{ bar}$ and pH-values of $10.0 \leq pH \leq 10.5$.

Despite the applied pretreatment and the measurement procedure carried out with the

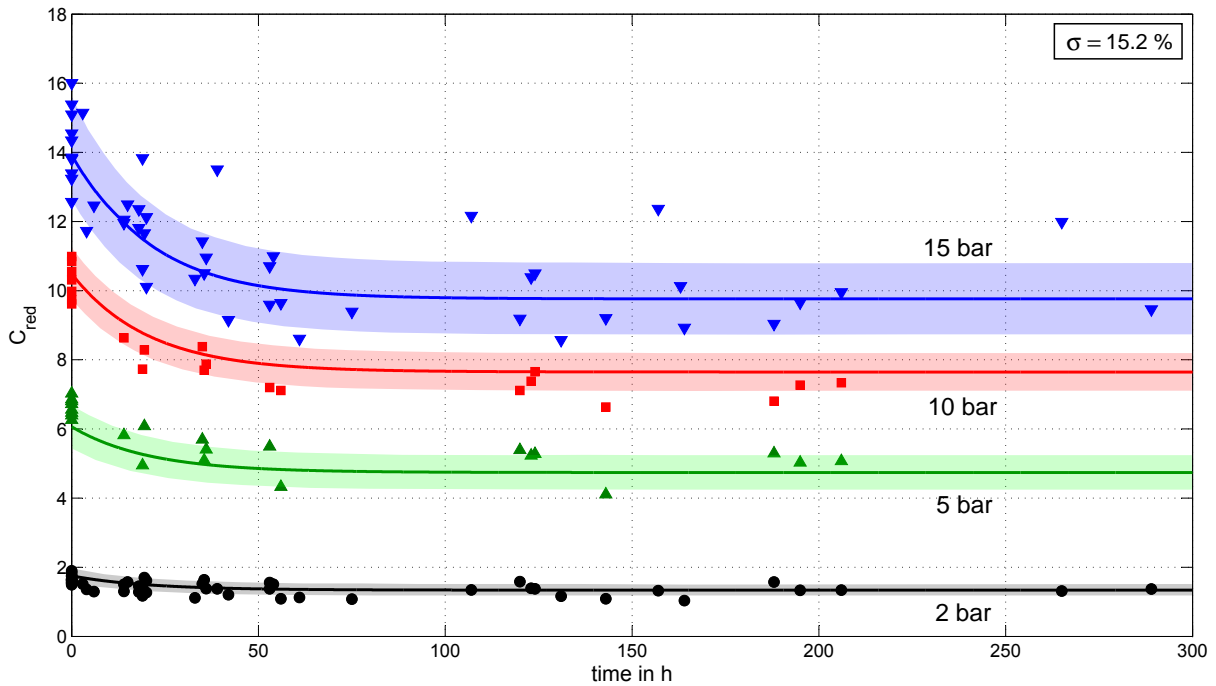


Figure 7.20: Time response of the reduced nucleate pool boiling heat transmission coefficient C_{red} during PO_4 treatment according to equation 7.5.

utmost care, a certain spread remains. The boiling curves $k(\dot{q}, p_s, \tau)$ can be calculated using equation 7.5 after implementing it into the known relation:

$$k = C_{red}(\tau, p_s) \cdot \dot{q}^{n(p^*)}$$

Picture 7.21 demonstrates the statistical significance of equation 7.5 with a relative mean deviation of $\sigma = 15.2\%$.

Convective pool boiling

The convective boiling heat transfer is only affected by the comparably low heat conductivity of the oxide layer, but not by the surface structure (see previous section on nucleate boiling). During trisodium phosphate treatment at $p_s = 15 \text{ bar}$, the convective boiling heat transmission coefficient determined at $p_s = 2 \text{ bar}$ shows similar asymptotic decline as for nucleate boiling conditions. Picture 7.22 presents the experimental data of C_{red} for convective pool boiling as function of the treatment period τ .

Regression yields a time constant of $\kappa = 19.5 \text{ h}$ and a total period $\tau_{99} = 89.7 \text{ h}$ necessary to gain steady state of k . The value of τ_{99} is insignificantly higher than for nucleate boiling at $p_s = 2 \text{ bar}$ and comparable to the mean time constant according to equation

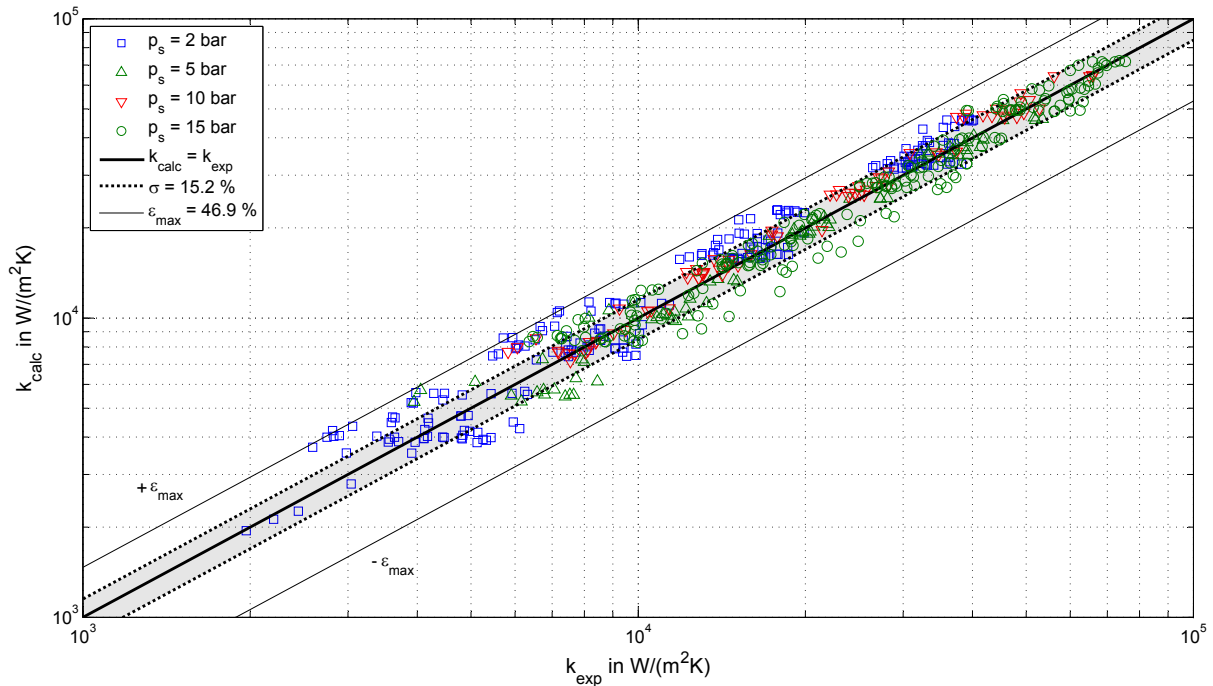


Figure 7.21: *Reproducibility of the time response of k during trisodium phosphate treatment using equation 7.5.*

7.5. Steinbrecht states the same time behaviour for nucleate and convective boiling at a constant operating pressure.^[11] As derived from the measured data, the time necessary to reach steady state conditions of k can be assumed equal for all investigated pressures. If convective boiling could be put into practice at pressures higher than 2 *bar* its time constant is probably similar to $\tau_{99} \approx 20$ *h* for trisodium phosphate treatment.

Although significantly affecting the convective heat transmission, a slight layer thickness increase does not necessarily manifest in an evident decrease of the nucleate boiling heat transmission coefficient. As accompanying the layer generation, an increased roughness enhances nucleate boiling heat transfer, while this advantage does not apply for free convection.^[33]

Compared to literature data^[11] at $p_s = 15$ *bar* for chemically pure water, the necessary treatment period during phosphate conditioning in this work is determined with less than 10 %. The cause can be assumed in the shifted pH-level of the boiler water, accelerating the oxidation process of iron to iron hydroxide and follow up passivating species (e.g. magnetite, hematite). The excess of hydroxide ions in the water is the driving force for ion diffusion and resulting iron conversion. A passivating oxide layer is assumed to develop quickly, preventing further corrosive attack.

A mean deviation of C_{red} with $\sigma = 9.9$ % is comparable to the spreading width of the nucleate boiling equivalent. The convective heat transmission coefficient can be calculated

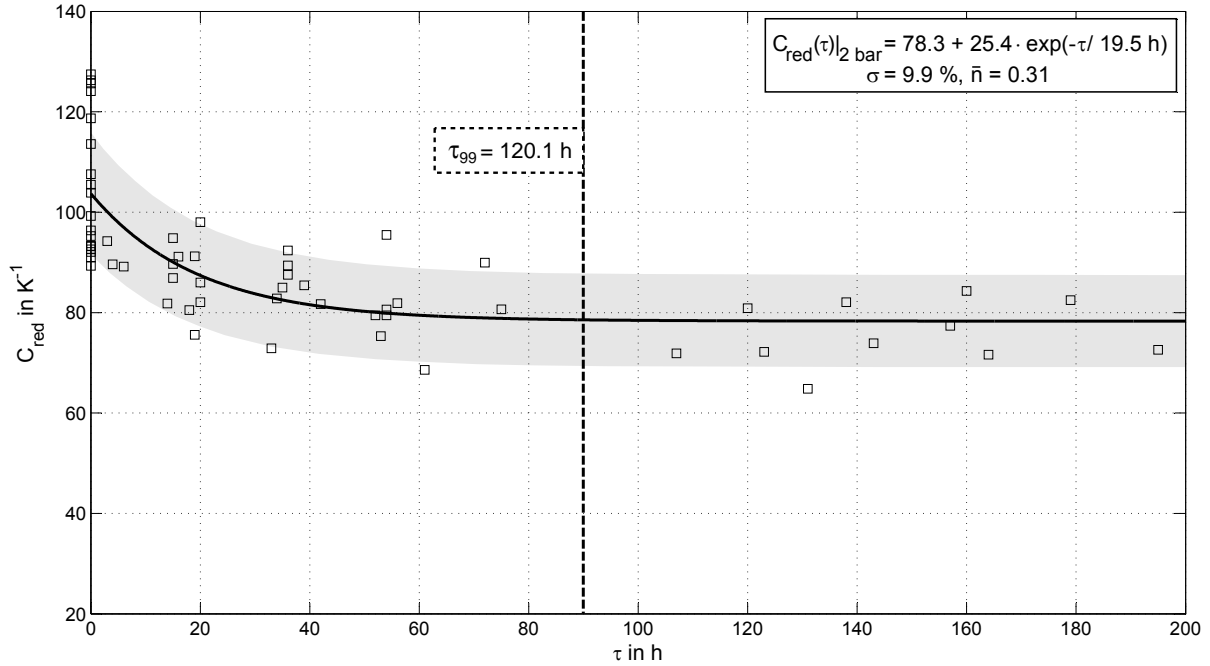


Figure 7.22: Time response of C_{red} during convective boiling at $p_s = 2$ bar under trisodium phosphate treatment.

implementing the average exponent $\bar{n} = 0.31$ into $k = C_{red} \cdot \dot{q}^{\bar{n}}$ with an accuracy of $\sigma = 11.7\%$ (see figure 7.23).

Correlation 7.8 can be used to describe the heat transmission coefficient $k_{conv}(\dot{q}, \tau)$ during convective boiling at $p_s = 2$ bar:

$$k_{conv}(\dot{q}, \tau) = \left[78.3 + 25.4 \cdot \exp\left(-\frac{\tau}{19.5 \text{ h}}\right) \right] \cdot \dot{q}^{0.31} \quad (7.7)$$

$$[k_{conv}] = 1 \text{ W}/(\text{m}^2\text{K})$$

$$[\dot{q}] = 1 \text{ W}/\text{m}^2$$

$$[\tau] = 1 \text{ h}$$

within the range of heat fluxes $3 \cdot 10^3 \text{ W}/\text{m}^2 \leq \dot{q} \leq 16 \cdot 10^3 \text{ W}/\text{m}^2$ at $p_s = 2$ bar for the trisodium phosphate treatment at a pressure stage of $p_s = 15$ bar and pH-values of $10.0 \leq \text{pH} \leq 10.5$, featuring a necessary treatment period $\tau_{99} \approx 90$ h comparable to nucleate pool boiling.

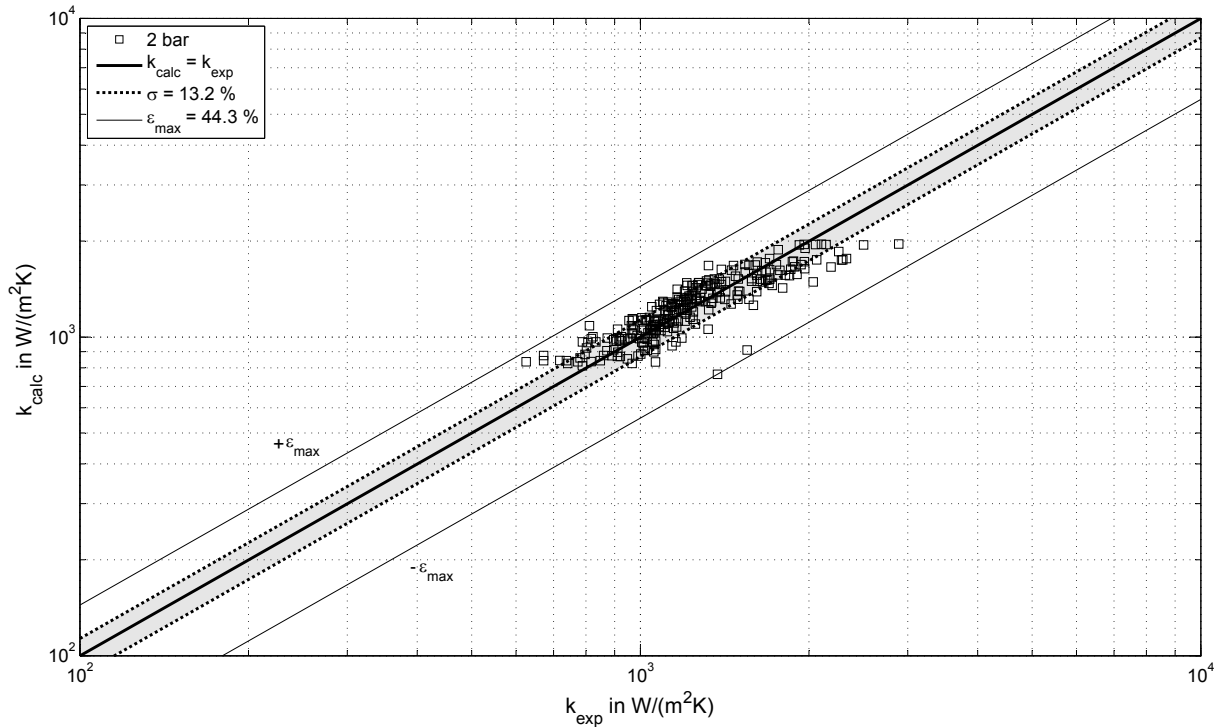


Figure 7.23: *Reproducibility of the convective heat transmission coefficient $k(\dot{q}, \tau)$ at $p_s = 2$ bar during trisodium phosphate treatment at $p_s = 15$ bar.*

7.1.4 Conclusion

As surface properties are assumed to be the main reason for the spreading width of k during nucleate boiling and given the fact that the surface roughness has a neglectable impact on convective heat transfer, a resulting relative mean deviation of $\sigma \approx 10\text{...}15\%$ for k_{calc}/k_{exp} appears to be an experimental limit for the reproducibility of the time response of k . A time and pressure dependency for the heat transmission coefficient $k(\dot{q}, p_{red}, \tau)$ is presented, as influenced by the described experimental trisodium phosphate conditions.

In the experimental scale, investigated in this work, the generation of a passivating oxide layer on the steel surface under trisodium phosphate treatment at $p_s = 15$ bar can be considered finished in thermotechnical terms after $\tau_{99} \approx 100$ h for nucleate boiling as the technically desired operation regime.

7.1.5 Surface properties after trisodium phosphate treatment

As the thermotechnical experiment theoretically allows statements on the heaters surface properties regarding structure, compactness and porosity (roughness) by evaluating the boiling curves orientation in the Nukiyama diagram, analytic methods are employed to

validate this theory.

During the trisodium phosphate treatment, an oxide layer is formed on the steel surface, affecting the boiling heat transport. Figure 7.24 gives a visual comparison of a test tube in a metallic-blank condition prior to installation and after achieving steady state conditions of k .

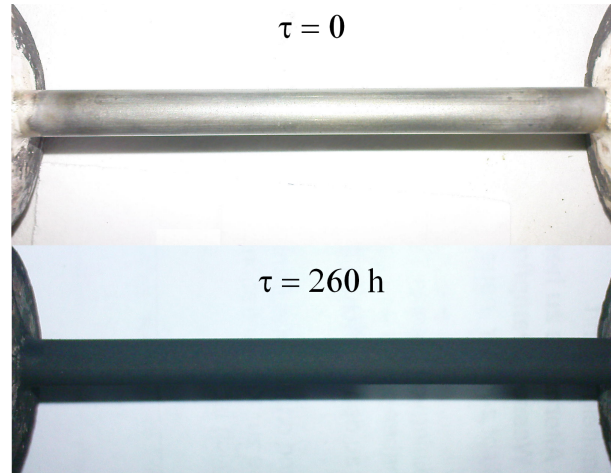


Figure 7.24: *Visual impression of an exemplary tube prior to installation and after achieving steady state conditions of k during PO_4 treatment.*

While drawing grooves are already visible to the naked eye on the metallic-blank sample (see figure 7.24, top), a typical dark oxide layer (see figure 7.24, bottom) can be found on the very same specimen after long-term operation under trisodium phosphate feed water conditioning, which is influencing the nucleation characteristics during nucleate pool boiling.

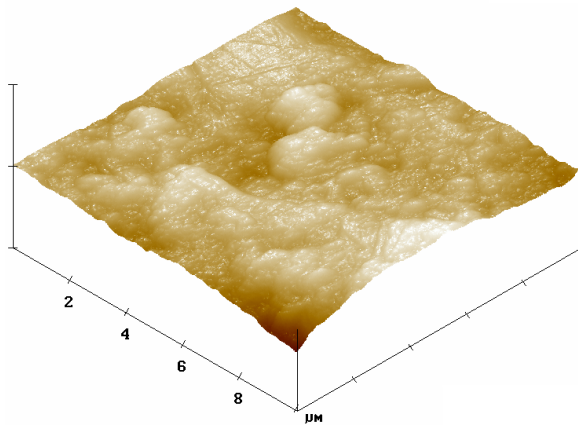
However, a systematic characterisation of the surface profile regarding changes in the nucleation site offer is difficult to establish, as the classic surface measurements only provide little information about the shape and distribution of nuclei. DIN 4760, for example, classifies form deviations in a 6-order pattern which superimpose themselves to form the actual surface profile:^[42]

1. straightness, flatness, roundness deviations (from tool guidance, etc.)
2. waviness (from vibrations of the machinery)
3. *grooves (resulting from the tooling, forward feed or infeed)*
4. *striae, sheds, summits (from fabrication)*
5. *roughnesses in the micro structure*
6. (crystal) lattice

In this context, the third, fourth and fifth order form deviations are of relevance.⁶

The surface analyses indicate a smooth fine-grit surface for the metallic-blank specimen, while the oxidised tube features an increased roughness and porosity. A comparison between the two mentioned conditions is demonstrated in picture 7.25 by means of atomic force microscopy (AFM).

Delivery condition, metallic-blank surface
AFM-3D height image



Phosphate treatment (PO_4), steady state specimen
AFM-3D height image

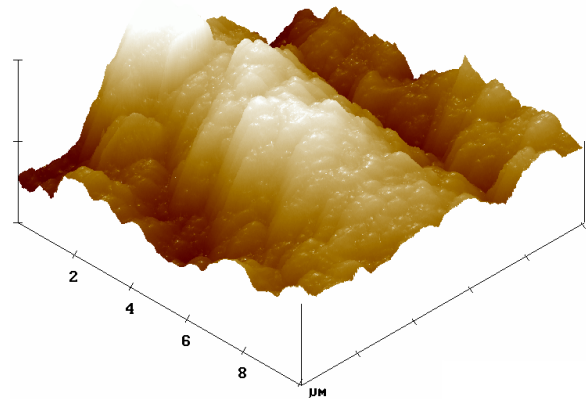


Figure 7.25: *Comparison of the surface structure (AFM-3D height image): delivery condition and steady state tube after PO_4 treatment.*

Figure 7.26 depicts the surface structure and roughness profile of an exemplary test tube after reaching thermotechnical stationarity.

Oxide crystals have grown orthogonally to the tube axis in form of lamellae featuring. These lamellae feature additional superimposed structures compared to the metallic-blank state, which is featuring drawing grooves at best. While, according to DIN 4760, these drawing grooves can be counted as third order form deviations, the oxide lamellae and crystals, the lamellae are made of, are located somewhere between the fourth order and the micro structure/framework of the material.

As derived from figures 7.25 and 7.26, the size of those lamellae is in the range of several micrometers. According to equation 2.2, those roughnesses clearly represent available nuclei that can be activated easily at moderate heat flux densities and low or medium saturation pressures as investigated in this work.

⁶Made classification is used predominantly for characterising machining-related deviations. To simplify matters, the oxide (crystal) growth and corresponding surface influence as well as storage and transport effects are tried to be classified according to this system.

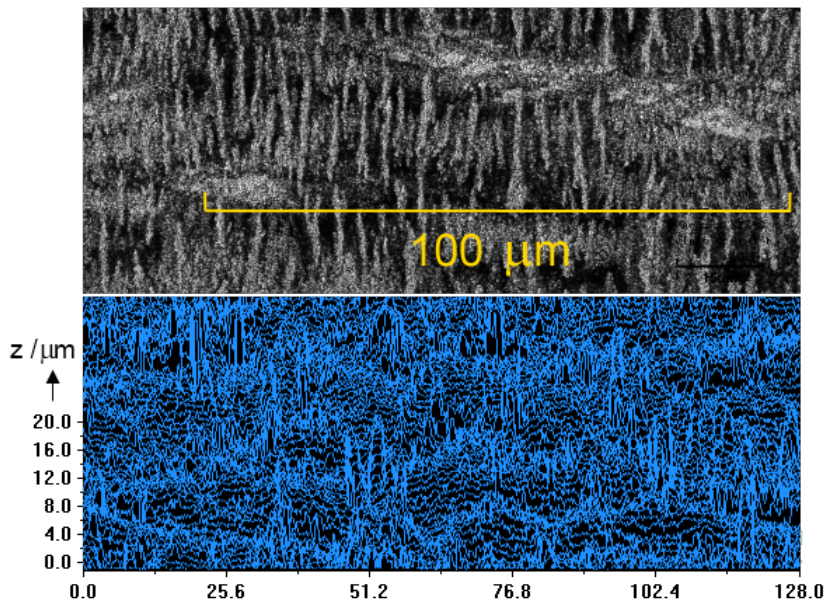


Figure 7.26: *CLSM picture (top) and roughness profile (bottom) of an exemplary steady state tube sample after 320 h of PO_4 treatment.*

So, although a heat transfer impeding oxide layer is formed on the steel surface, the increased roughness as generated during phosphate treatment provides an advantageous or at least compensating effect regarding nucleation. This analytical cognition substantiates the already thermotechnically gained information:

The assumed developing heat transport impeding oxide layer during trisodium phosphate treatment lowers the heat transmission coefficient under nucleate and convective pool boiling conditions at all investigated pressures. However, the increased roughness provides a sufficiently wide nucleation site spectrum to maintain a stable but pressure dependent boiling curve's exponent under nucleate pool boiling conditions.

Estimation of the oxide layer thickness

The convective part of the boiling curve is only influenced by the heat transfer impeding character of the oxide layer. Surface roughness and morphology, which are affecting nucleation, are rather irrelevant to the convective pool boiling heat transfer.^[11] In the following, an approach to determine the oxide layers effective thermal conductivity is presented.

The exponent n varies under convective boiling conditions due to random error (see previous section). For the benefit of comparability, a representative operation point \dot{q} and its corresponding heat transmission coefficient is employed. As shown in section 5.3, the use of a fixed exponent for the standardisation is valid for trendless variations of n . This procedure results in rotation of the boiling curve around a pivotal point $k_{pivot}(\dot{q}_{pivot})$. Mentioned

pivot is representative for the niveau of convective boiling. It can be calculated for each investigated tube sample and treatment period by linear interpolation and is furthermore used to determine the mean layer temperature ϑ_{Lm} :

$$\begin{aligned}\vartheta_{Lm} &= (\vartheta_o(\tau) + \vartheta_{Lo})/2 \\ \vartheta_{Lo} &= \vartheta_o(\tau = 0)\end{aligned}\quad (7.8)$$

According to Steinbrecht,^[11] the thermal conductivity of the oxide layer can be calculated using the following empirical equation, after ϑ_{Lm} is found:

$$\lambda_L = 3.91 - 5.5 \cdot 10^{-3} \cdot \vartheta_{Lm} \quad (7.9)$$

The values are between $3.22 \text{ W}/(\text{m} \cdot \text{K}) \leq \lambda_L \leq 3.23 \text{ W}/(\text{m} \cdot \text{K})$ with mean layer temperatures of $123.2 \text{ }^\circ\text{C} \leq \vartheta_{Lm}(\dot{q}_{pivot}) \leq 126.2 \text{ }^\circ\text{C}$. Employment of equation 5.17 yields layer thicknesses up to $\delta = 782 \text{ } \mu\text{m}$. Figure 7.27 demonstrates scattering of δ and regression using the same time constant $\kappa = 19.5 \text{ h}$ as for convective boiling C_{red} and best possible approximation with adjustable coefficients. The boundary value $\delta(\tau = 0) = 0$ is taken into account.

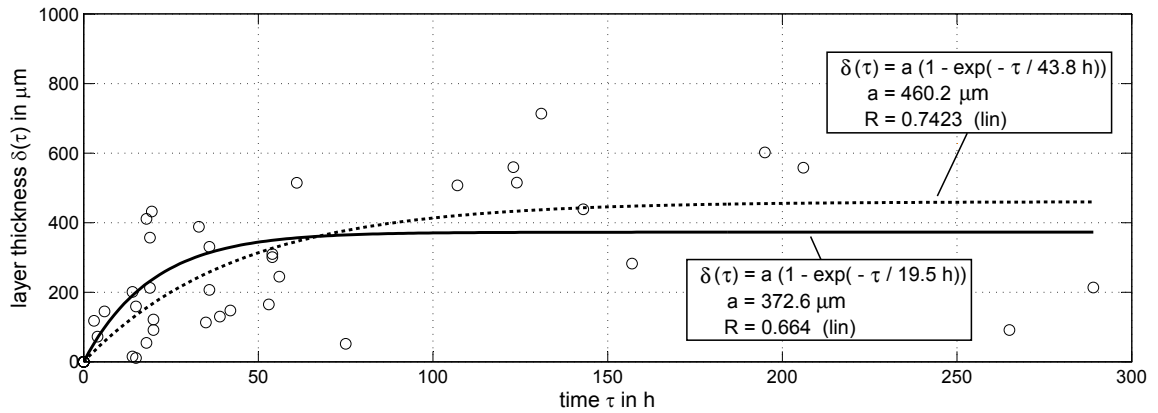


Figure 7.27: Apparent layer thickness $\delta(\tau)$ after PO_4 operation at $p_s = 15 \text{ bar}$, calculated using equation 5.17.

Using equation 7.9 for the thermal conductivity of compressed or non-porous oxides, the presented δ is comparably high. An asymptote of $\delta_\infty \approx 375.2 \text{ } \mu\text{m}$ is more than a third of the actual tube wall thickness. These values have to be checked and verified using conventional analytics. In this case polished microsection and microscopic measurement is chosen.

Analyses on two $PO_{4,\infty}$ samples are carried out by cutting the tube in half and embedding and polishing it. The axial center of the tube is assumed to be representative for the whole

surface as influences from the soldering can be avoided. Picture 7.28 shows the results of an exemplary tube sample using the CLSM method after reaching steady state of k . Some kind of porous epitactic sublayer can be found on the tube surface. Duality of the layer cannot be observed. Both investigated tubes feature very different sublayer arrangements

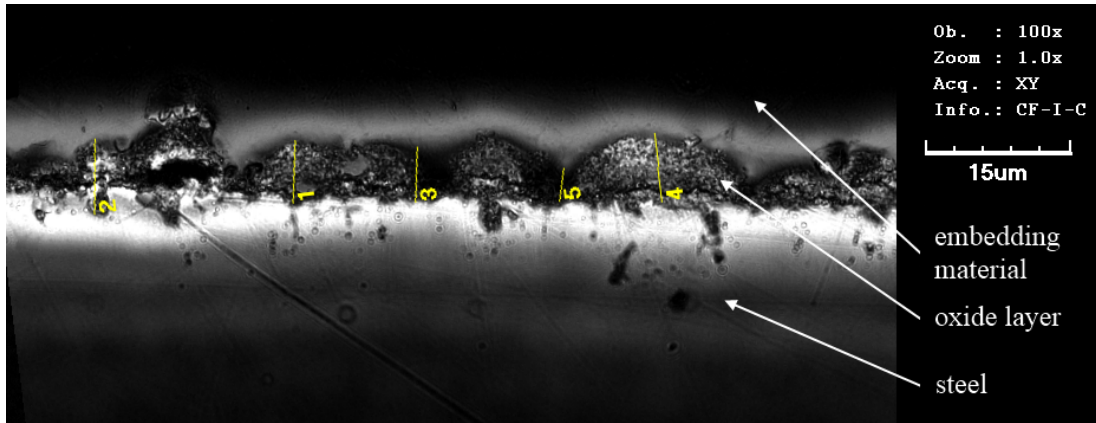


Figure 7.28: *CLSM picture of an epitactic-like oxide layer, found on an exemplary $PO_{4,\infty}$ tube.*

and appearance depending on the investigated spot. In some cases the presented epitactic-like sublayer is found, while at another location this kind of layer could not be verified. In such case, a sublayer of topotactic-like character and varying thickness is recognised as shown in picture 7.29. Both kinds of sublayers can be found on both samples to a certain extent.

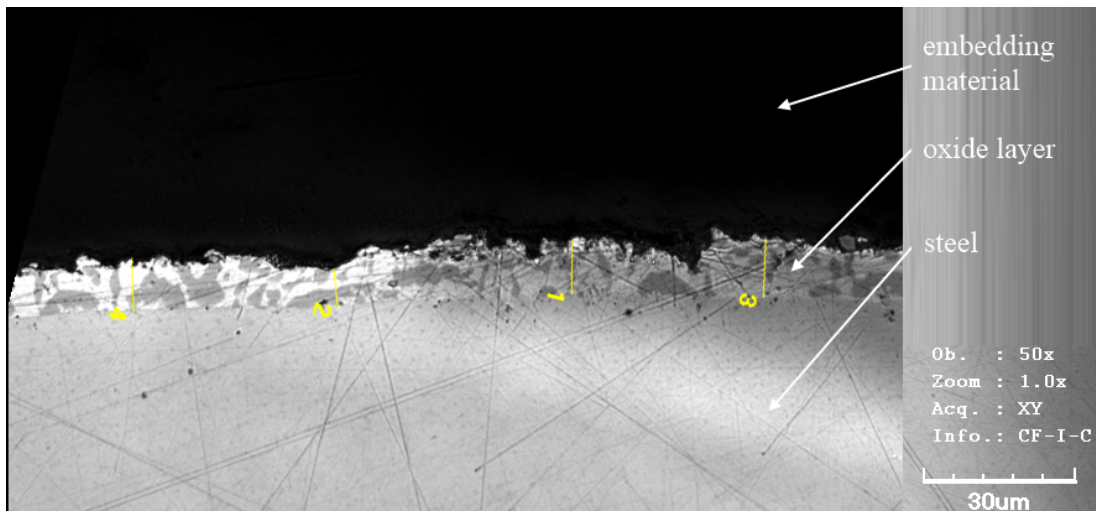


Figure 7.29: *CLSM picture of the topotactic-like oxide layer on an exemplary $PO_{4,\infty}$ tube.*

Determined layer thicknesses are in the range of $2.5 \mu\text{m} \leq \delta \leq 27.0 \mu\text{m}$ (26 locations on two specimens). Its distribution could not be correlated with the measured circumferential position.

Given a mean layer thickness of $\bar{\delta} \approx 15.2 \mu m$ ($\sigma = 39 \%$) and retrograde calculating the actual thermal conductivity according to:

$$\lambda_L = \frac{\bar{\delta}}{\left(\frac{1}{k} - \frac{1}{\alpha}\right)} \quad (7.10)$$

yields an average value of $\lambda_L \approx 0.11 W/(m \cdot K)$ at a mean temperature of $\vartheta_{Lm} = 124.8 \text{ }^\circ C$.

This analytically supported thermal conductivity, being derived from the thermotechnical experiment, is only 3.4 % compared to the values from literature.

7.1.6 Conclusion

Convective pool boiling heat transfer under trisodium phosphate treatment is subject to a remarkable negative alteration. The generated passivating oxide layer represents a verifiable heat transfer resistance.

Compared to the literature, thermotechnically and analytically determined thermal conductivities are considerably low. As porosity, density and crystal orientation influence the oxide layer during the experiment, a solely thermotechnical evaluation of the layer thickness is not possible. A significant inhomogeneity regarding the measured oxide layer thickness is found for the PO_4 treatment.

The experiment verifiably allows statements on the layer generation progress and the time necessary to reach a steady layer state. The presented cognitions on the morphology and surface roughness show very good agreement with the obtained CLSM profiles.

7.2 Trisodium phosphate and hydrazine

The thermotechnical experiment indicates a clear effect on the heat transmission behaviour during operation with hydrazine added to the pure Na_3PO_4 treatment as oxygen scavenger and passivating agent. Figure 7.30 presents the boiling curves $k(\dot{q})$ under $PO_4 + N_2H_4$ conditioning at 15 bar saturation pressure at the start of treatment and after reaching steady state of k .

During the treatment period, the boiling curves exponent at $p_s = 15 \text{ bar}$ varies between 0.58 and 0.81 (see figure 7.31). It increases slightly during operation, as demonstrated in figure 7.31. Given the value of $\tau_{99} = 191 \text{ h}$ for the development of C_{red} (see figure 7.32), the increase of n can be assumed to stop within the same period. An exponential decay approach is used to model the corresponding time response.

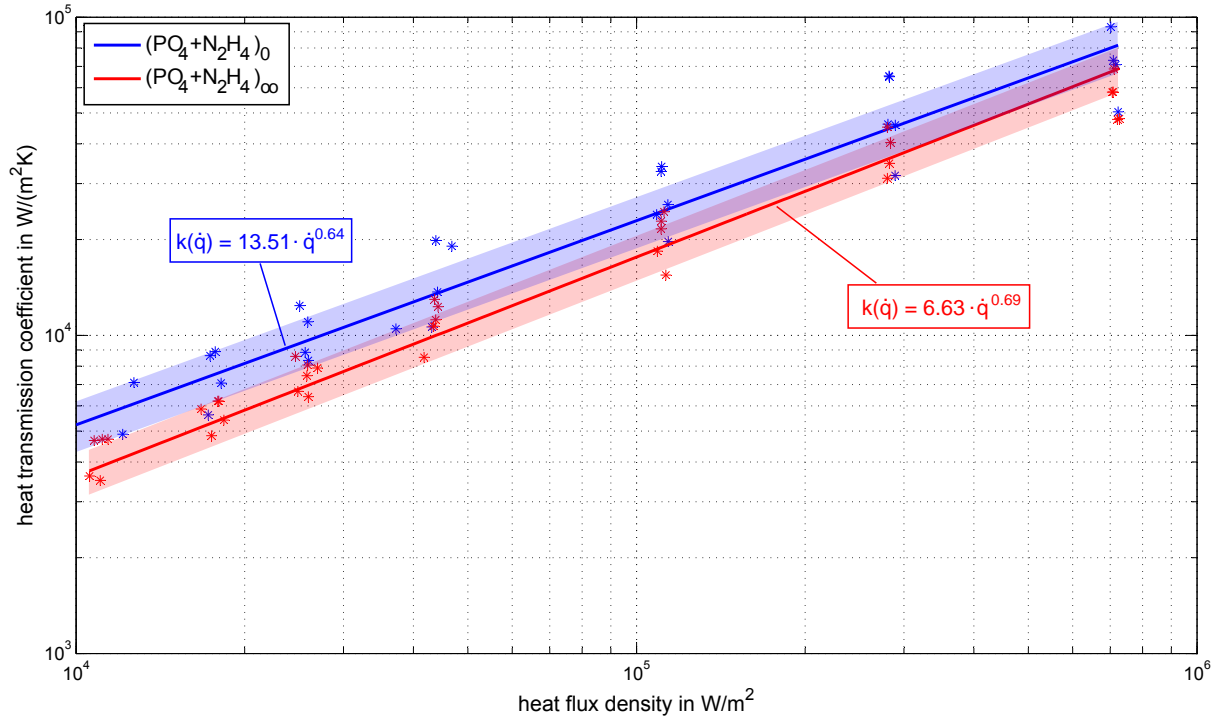


Figure 7.30: Start values and steady state of $k(\dot{q})$ during $PO_4 + N_2H_4$ treatment at $p_s = 15 \text{ bar}$.

Considering the spreading width, a clear reflection of the actual development cannot be derived. While in the beginning metallic-blank surfaces show an initial mean exponent of $n_{start} = 0.64$ (in comparison: $\bar{n}_{PO_4} = 0.63$), it is increased to $n_{steady} = 0.69$ when steady state for k is verified thermotechnically. While for metallic-blank tube surfaces the value of n is similar to the mean exponent of the pure phosphate treatment, its increase indicates a modification of the surface structure/nucleation site radii compared to the PO_4 conditioning. Presumably, a comparably lower surface roughness is present on $(PO_4 + N_2H_4)_\infty$ samples.

According to section 5.3, calculation of C_{red} can only provide comparability by using a fixed exponent. Therefore, the initial value of $\bar{n} = 0.64$ is used in order to compare the influence of hydrazine to the pure phosphate treatment, although a quantitative recalculation for k based on the obtained values C_{red} and \bar{n} is impossible. Reduction and multiple regression yields:

$$C_{red}(\tau) = 10.73 + 3.41 \cdot \exp\left(-\frac{\tau}{41.5 \text{ h}}\right) \quad (7.11)$$

with a relative mean deviation of $\sigma = 16.3 \%$ (for comparison: $\sigma = 15.2 \%$ for PO_4 treatment). The resulting time response of C_{red} is depicted in figure 7.32.

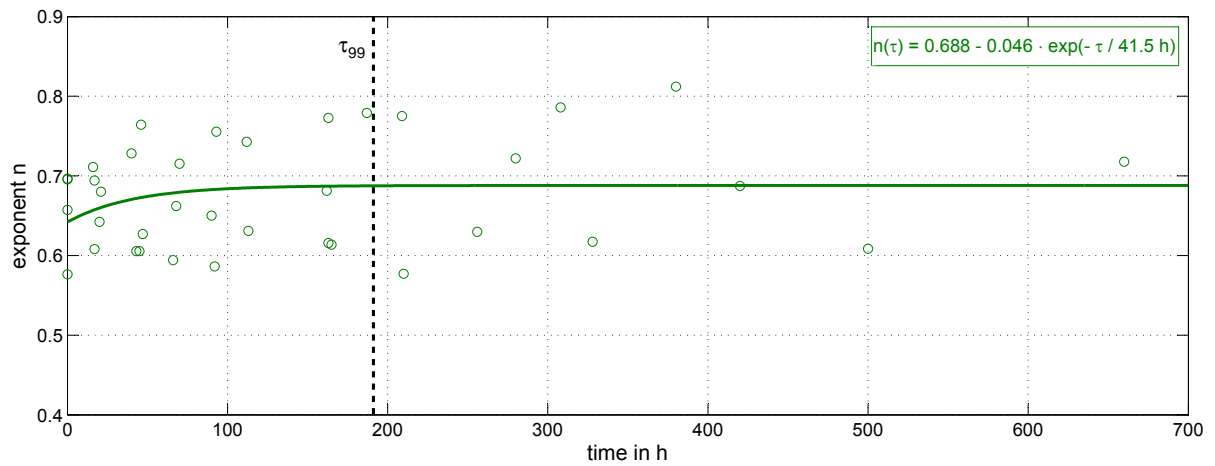


Figure 7.31: Time behaviour of the nucleate boiling exponent n during $PO_4 + N_2H_4$ treatment at $p_s = 15$ bar.

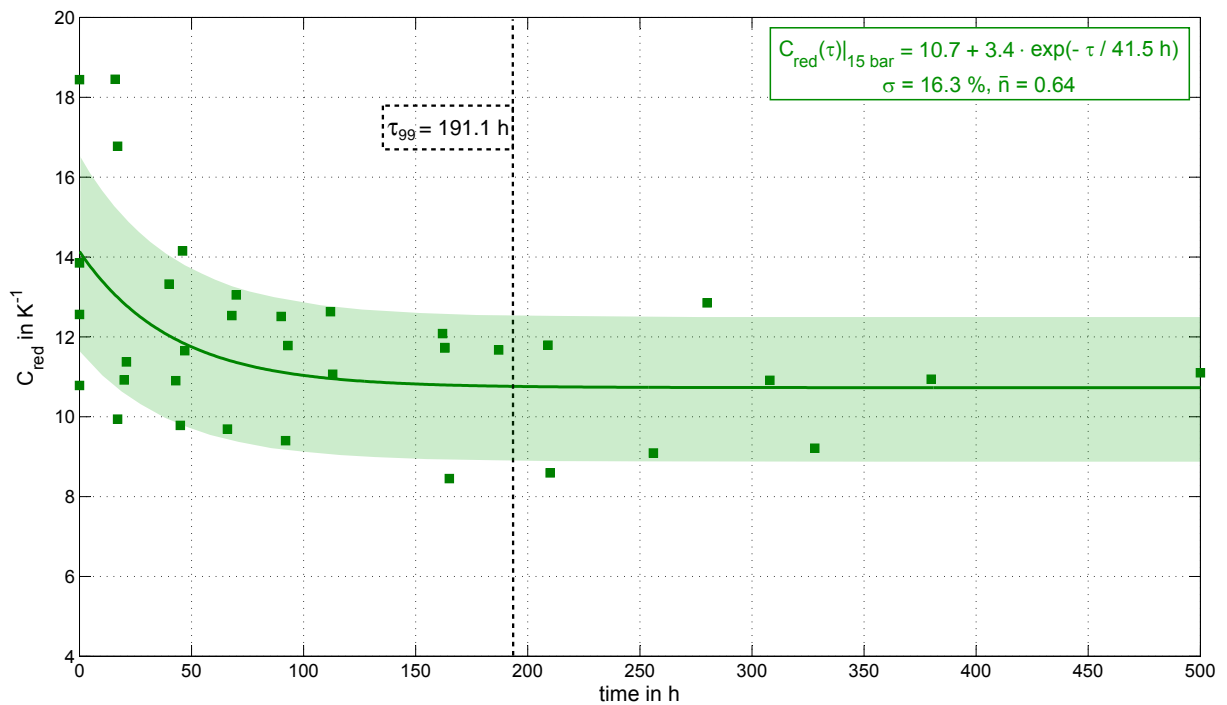


Figure 7.32: Time response of C_{red} at $p_s = 15$ bar during $PO_4 + N_2H_4$ treatment.

The niveau of C_{red} during $PO_4 + N_2H_4$ operation is quite similar to PO_4 , while the time response shows a necessary treatment period $\tau_{99} \approx 191 h$, which is twice as high as for pure phosphate. Such behaviour can be explained by the reducing effect of hydrazine that is impeding corrosion. Furthermore, oxygen residues maintaining inside the vessel after degassing under pure phosphate conditions accelerate build-up of corrosion products. Consequently, the oxidation rate is decreased during operation with hydrazine, resulting in a slower decline of the heat transmission coefficient k .

Picture 7.33 compares the graphs of C_{red} for $PO_4 + N_2H_4$ and PO_4 conditioning. The ini-

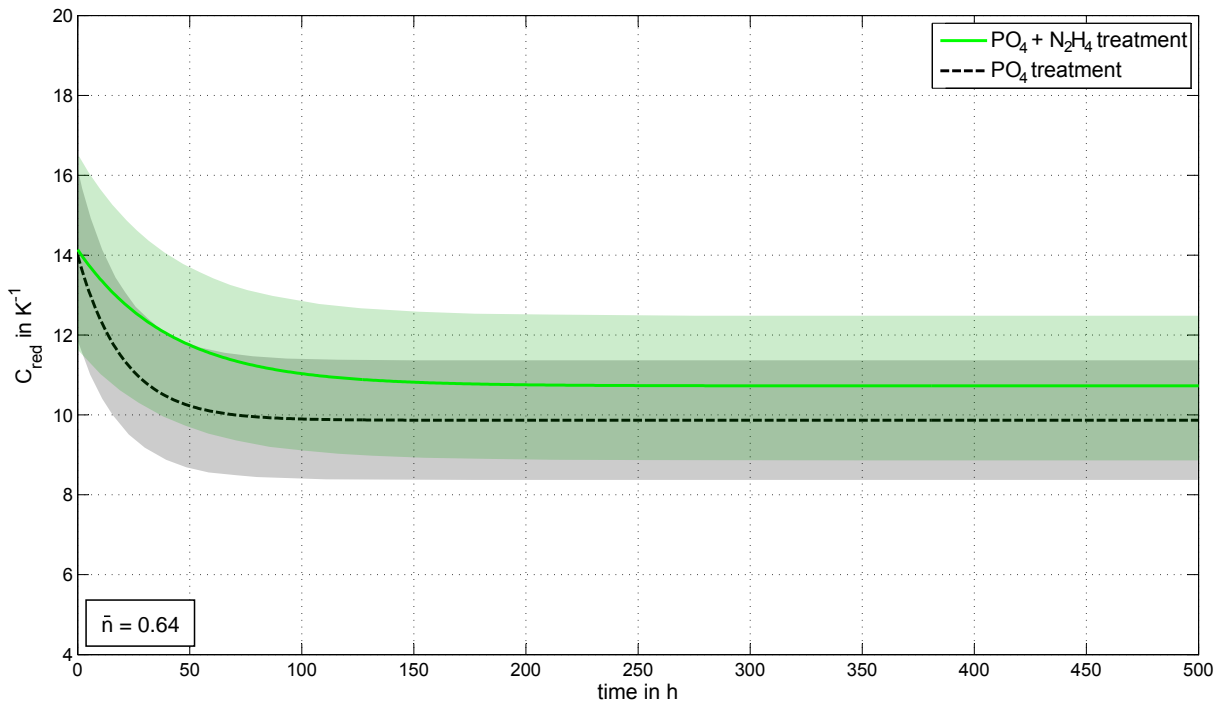


Figure 7.33: Time response of C_{red} at $p_s = 15 \text{ bar}$ during $PO_4 + N_2H_4$ operation compared to PO_4 treatment.

tial boiling behaviour of the $PO_4 + N_2H_4$ treatment agrees quite well with the data for pure phosphate. However, given a higher steady state exponent for $PO_4 + N_2H_4$, a smoother surface roughness can be assumed compared to the pure phosphate conditioning. Picture 7.34 demonstrates the expected differences in surface roughness after reaching steady state of k . Thus, as the exponent changes during phosphate and hydrazine treatment, calculation of $k(\dot{q}, \tau)$ by using C_{red} from equation 7.11 cannot be carried out, as $\bar{n} = 0.64$ taken as basis for reduction does not comply with the boiling curve for steady state. The use of the actual steady state exponent $n = 0.69$ combined with equation 7.11 overestimates the heat transmission coefficient at low and medium heat fluxes and underestimates it at high thermal loads (see section 5.3). Thus, standardisation of k to C_{red} only allows the qualitative comparison of the heat transmission behaviour in the case of developing

exponent. If the actual value of C_{red} is needed, $n(\tau)$ must be applied for reduction.

Applying the experimentally verified effect of the surface morphology on the exponent, at least from a thermotechnical view, hydrazine treated tubes feature a smoother surface than merely phosphate treated ones after reaching a thermotechnical steady state. This assumption can be substantiated by CLSM measurement as shown in figure 7.34.

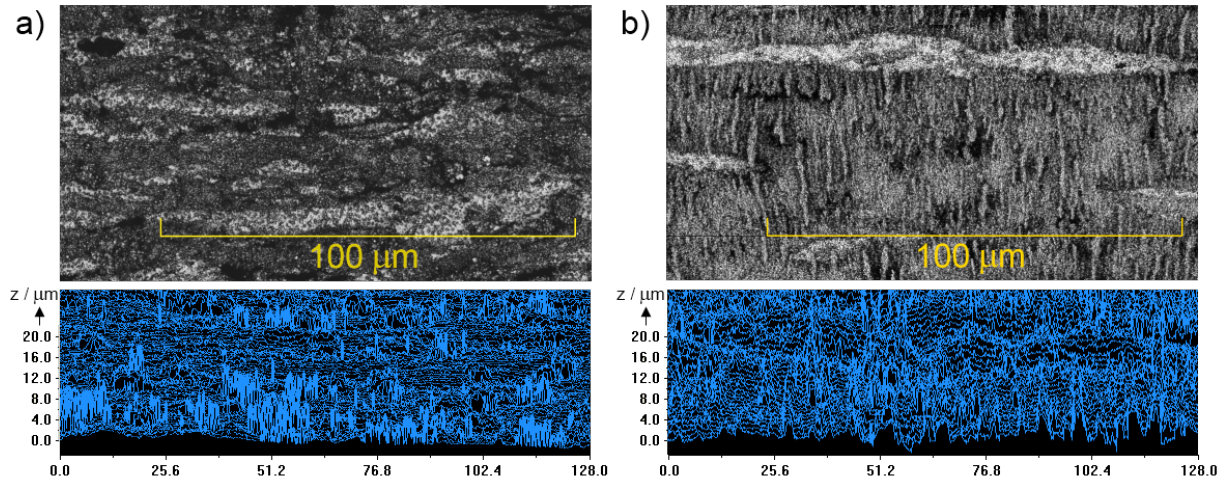


Figure 7.34: CLSM-results of an exemplary $PO_4 + N_2H_4$ treated tube sample (a) compared to the pure PO_4 conditioning (b) at the steady state of k .

The surface of the $PO_4 + N_2H_4$ operated tube sample is finer-grit than the PO_4 treated equivalent. Validating a slightly dissimilar boiling characteristics, which manifests in the mentioned exponent: Consequently, smaller nucleation site radii can be assumed on the surface. As a result, given similar system parameters, the influence of the heat flux density activating smaller nuclei is comparably stronger for the fine-grit $PO_4 + N_2H_4$ treated surface. However, a slightly higher oxide layer thickness of the PO_4 treated specimen is assumed to affect the corresponding heat transmission coefficient, which is lower compared to the additional hydrazine conditioning.

In addition to the investigations at $p_s = 15 \text{ bar}$, exemplary studies are carried out at 2 bar after reaching steady state conditions at 15 bar , including convective boiling. The experimental data are shown in picture 7.35.

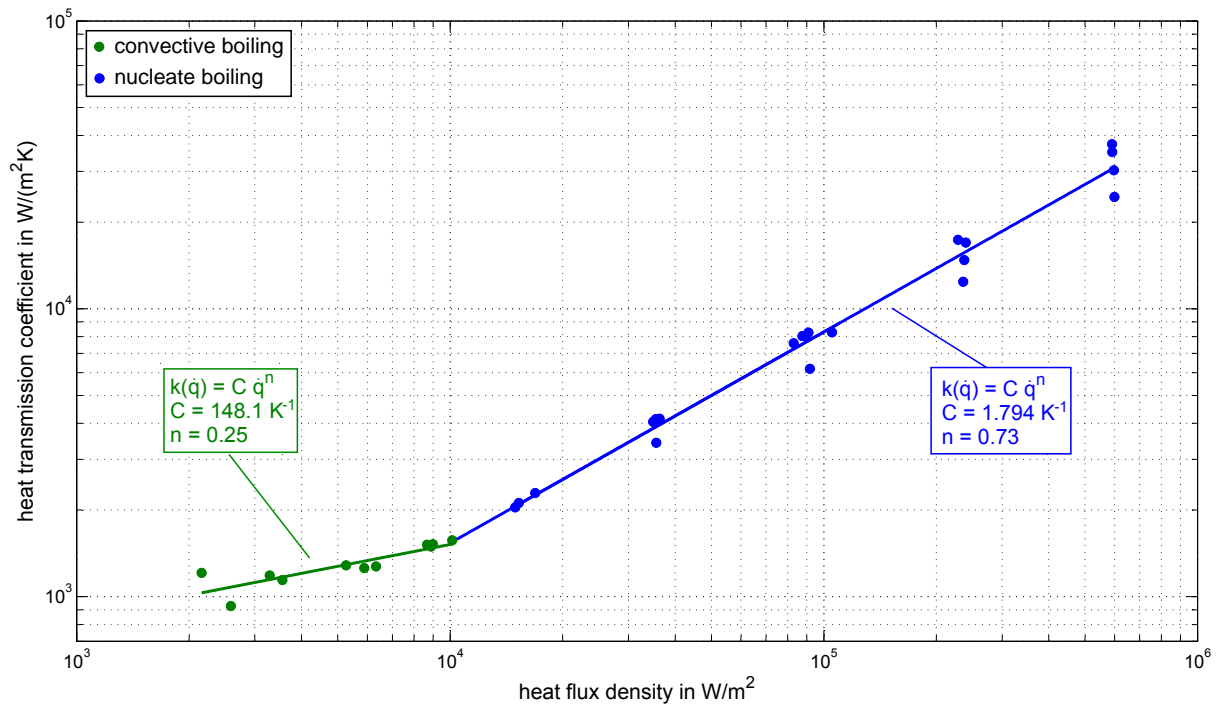


Figure 7.35: Mean boiling curve at $p_s = 2$ bar at the end of $PO_4 + N_2H_4$ operation.

The obtained average boiling curve equals those for pure PO_4 treatment, except for a slightly smaller exponent in both, nucleate and convective boiling:

$$\begin{aligned} \text{convective boiling} & \begin{cases} \bar{n}(PO_4 + N_2H_4) = 0.25 \\ \bar{n}(PO_4) = 0.31 \end{cases} \\ \text{nucleate boiling} & \begin{cases} \bar{n}(PO_4 + N_2H_4) = 0.73 \\ \bar{n}(PO_4) = 0.76 \end{cases} \end{aligned}$$

Differences in the convective boiling exponent are unspecific regarding the surface structure described by CLSM measurements. The value of n can be assumed to approach $\bar{n}(PO_4)$ with a larger assayed sample number. Differences of the nucleate boiling exponent have to be taken carefully considering the small amount of data. Hypothetically, this behaviour can be explained by a fill-up of available nuclei during the $PO_4 + N_2H_4$ treatment only concerning cavities formerly available at $p_s = 15$ bar, while the comparably larger radii spectrum at 2 bar remains unaffected. According to equation 2.2 and given nucleate boiling superheats of approximately $2 K \leq \Delta T \leq 10 K$, selectable radii are in the range of $2 \mu m \leq r_{min} \leq 2000 \mu m$.

With use of microsection analysis and CLSM microscopy, information on the oxide layer can be gathered. A compact oxide layer is found on the tube surfaces. Figure 7.36 depicts

the observations made on the tube surface of two exemplarily examined samples, which are comparable to the PO_4 treated ones regarding the thickness δ .

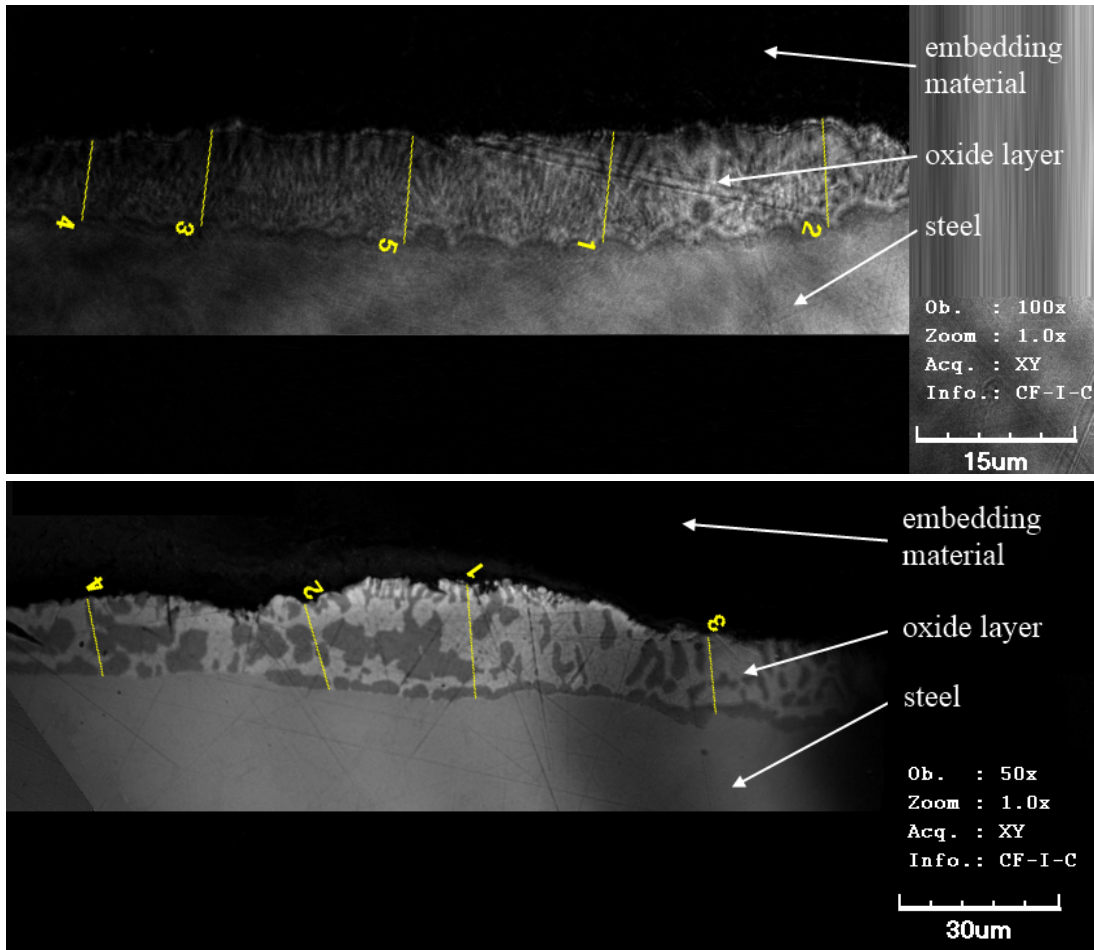


Figure 7.36: *CLSM view of exemplary polished tube samples after more than 250 h of $PO_4 + N_2H_4$ conditioning at $p_s = 15$ bar.*

Here, a bi-layer configuration cannot be recognised. At most of the studied locations, a compact and, regarding its visual appearance, rather homogeneous layer type is found. The measured thicknesses are between $6.7 \mu m \leq \delta \leq 24.9 \mu m$ (17 locations on two specimens) with an average value of $\bar{\delta} = 13.8 \mu m$ ($\sigma = 29.7 \%$). These values are similar to those found for the specimens, treated without an oxygen scavenger.

Although hydrazine has a remarkable effect on the oxidation rate, it leads to comparable results regarding oxide layer thickness and heat transmission niveau with respect to the treatment without the oxygen scavenger. Compared to pure trisodium phosphate conditioning, a slightly smoother surface can be recognised thermotechnically with a larger steady state exponent n , which is verified analytically. A temporal decline in the value of the nucleate boiling curve's exponent at $p_s = 15$ bar indicates a fill-up of formerly available

nuclei during the $PO_4 + N_2H_4$ treatment by iron oxide crystals. This behaviour does not significantly affect the nucleate boiling heat transmission coefficient at 2 *bar* saturation pressure.

7.3 Organic all-volatile treatment

The experimental long-term simulation of the heat transmission development under organic all-volatile feed water treatment ($DEHA + aA$) has been only of small success. Only very general statements are possible.

A summary including the obtained data can be found in the appendix D. As a preview, further investigations are suggested to be carried out in order to gain information on the layer development and corresponding impact on the heat transfer.

7.4 Film-forming amine treatment

A film-forming amine-based conditioning with Cetamine[®]V211 is studied regarding its temporal effect on the heat transport during pool boiling. Tests which are carried out on 16 tube samples yield a cumulative treatment period of more than 6000 *h*.

7.4.1 Treatment of metallic-blank tube samples

The initial pool boiling heat transfer coefficients differ significantly from those for inorganically treated tube samples as shown in figure 7.37 for a saturation pressure of 15 *bar*. The measured data for the reference treatment with Na_3PO_4 is omitted for clarity. In the following, the relative mean deviation is introduced instead.

An obvious difference in the boiling curves exponent due to the surface tension reducing effect of the film-forming amines is recognisable, leading to significantly higher heat transmission coefficients than for purely phosphate conditioned metallic-blank tube samples. Some of the k values are exceeding the $k = 100000 \text{ W}/(\text{m}^2\text{K})$ mark with a relative mean deviation of $\sigma = 21.8 \%$.

Since the surface properties of all investigated metallic-blank samples from *charge 2, modified etchant* are similar, any effect on the boiling curves exponent is considered to be caused by the surface tension lowering character of the film-forming amines. According to equation 2.2, additional nuclei become active as the surface tension drops at the interphase between the water and its steam. Mechanical equilibrium of the bubble induces smaller bubble (departure) diameters and possibly even higher departure frequencies.

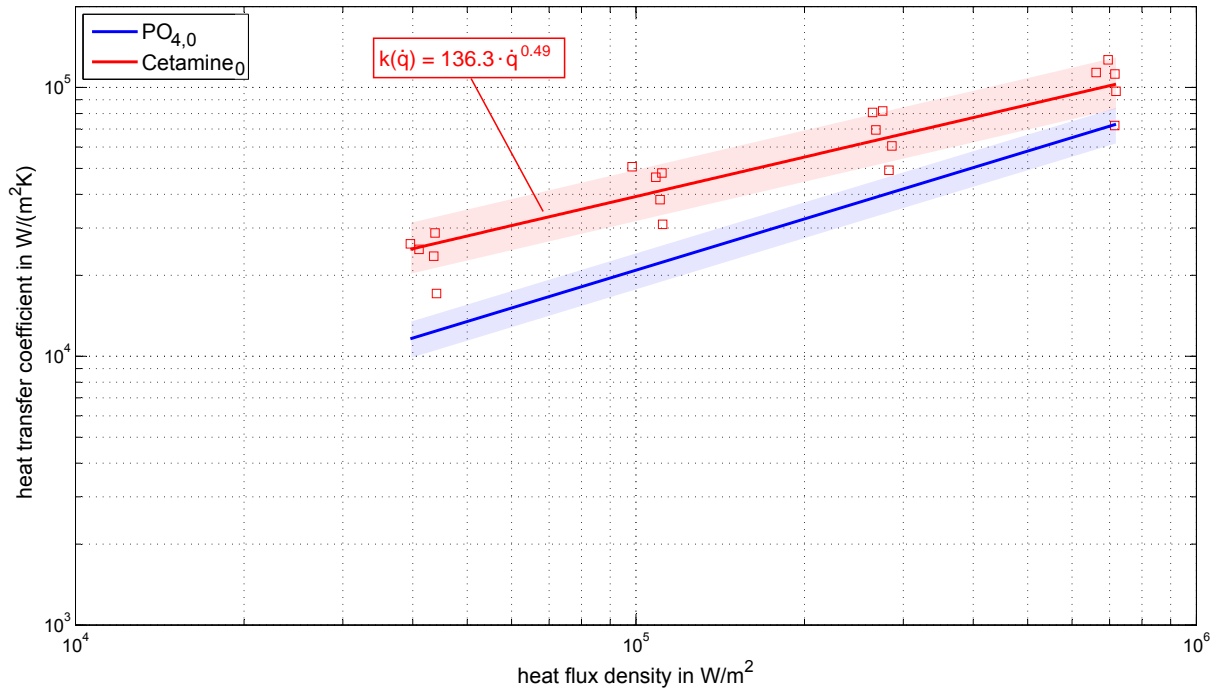


Figure 7.37: *Initial nucleate boiling curve for Cetamine treatment compared to PO_4 at $p_s = 15$ bar.*

The improvement of k compared to the inorganic treatment decreases with rising \dot{q} . This behaviour can be explained as follows: With rising \dot{q} the boundary layer superheat grows and thereby smaller nuclei radii are activated. The more nucleation sites are active, the less increase in the bubble number on the surface can be accomplished by lowering the surface tension.

Video recordings have been carried out comparing similar operation points regarding active nucleation site density. These show a clear improvement in the number of bubbles, departing the surface during film-forming amine treatment for metallic-blank surfaces (see appendix E).

At the beginning of the treatment, an average exponent of $\bar{n} = 0.49$ is found by regression, which is only decreasing slightly during operation but featuring a remarkable spread. Picture 7.38 demonstrates the development of n .

A linear model is used for regression, as a systematic exponential development could not be observed during operation. Considering the scattering of n , its temporal decline is neglected.

In the beginning of operation, the mean improvement of k over pure phosphate conditions is between $\Delta k = 125$ % at low heat fluxes ($\dot{q} = 40 \cdot 10^3$ W/m²) and $\Delta k = 40$ % at the highest measured heat flux density of $\dot{q} = 720 \cdot 10^3$ W/m².

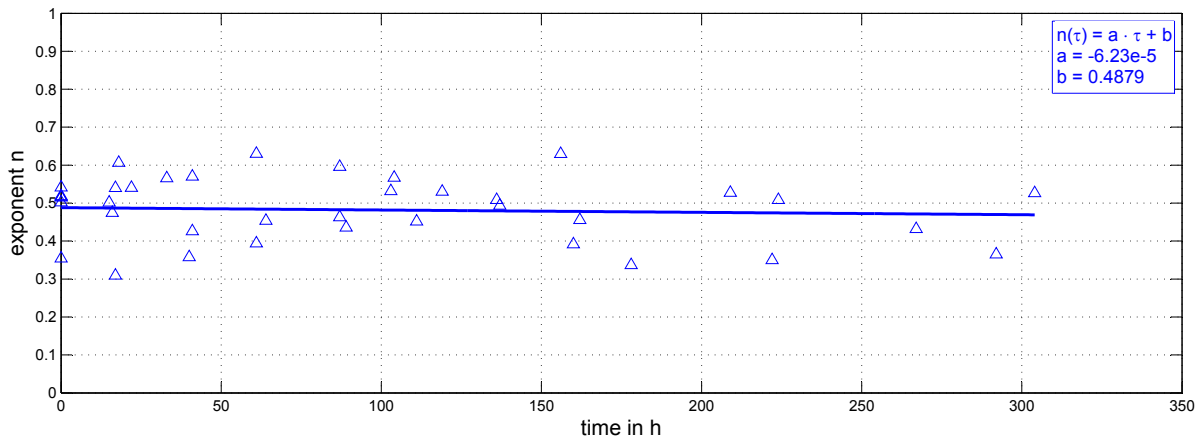


Figure 7.38: Development of the nucleate boiling exponent at $p_s = 15$ bar under the influence of the film-forming amine.

Using an average fixed boiling curve exponent $\bar{n} = 0.49$, a reduction of k to C_{red} is feasible (see section 5.3). However, since the comparability of C_{red} is sensitive to differences in the exponent, the value $\bar{n} = 0.63$ for the reference treatment PO_4 is applied to the experimental data. This procedure corresponds to standardisation of C_{red} to the trisodium phosphate treatment. The following diagram 7.39 compares the calculated standardised reduced heat transmission coefficients. (The use of $n = 0.49$ is also possible and would make reduction of the PO_4 data necessary. Comparison of the resulting values of C_{red} have a similar effect. Reduction with use of $n = 0.49$ as well as the time response are located in appendix F.)

A reduction and evaluation of the stated time behaviour of C_{red} yields a necessary treatment period $\tau_{99} = 78.9$ h, which is approximately 18 % shorter than for the pure phosphate treatment and even 60 % less than for $PO_4 + N_2H_4$ conditioning. After the treatment following nucleate boiling heat transmission coefficients are found experimentally in comparison to the PO_4 treatment (see picture 7.40).

As the free film-forming amine concentration in the boiler water is maintained constant and given the fact that the boiling curves exponent does not change significantly, the active nucleation site spectrum is not influenced from a thermotechnical point of view (i.e. by changes in the surface roughness).

Although film-forming amines are referred to as *corrosion inhibitors*, the decline in C_{red} indicates a modification of the surface, while remaining a similar nucleation characteristics. In this case, convective boiling and a comparison of the heat transmission coefficients at $p_s = 2$ bar help determine, whether a heat transfer impeding layer is formed and can be assumed to cause the described decline. Figure 7.41 shows the boiling curve at the end of *Cetamine* treatment vs. $PO_{4,0}$ and $PO_{4,\infty}$.

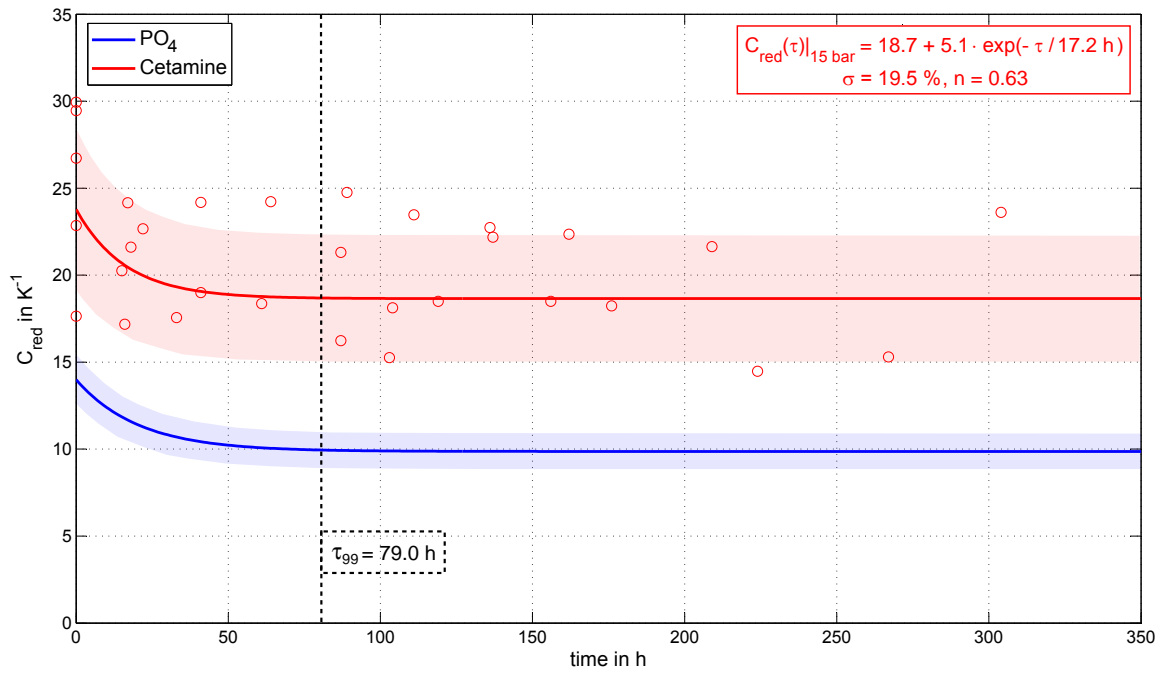


Figure 7.39: Development of the nucleate boiling C_{red} under Cetamine treatment at $p_s = 15$ bar, reduced by $\bar{n} = 0.63$.

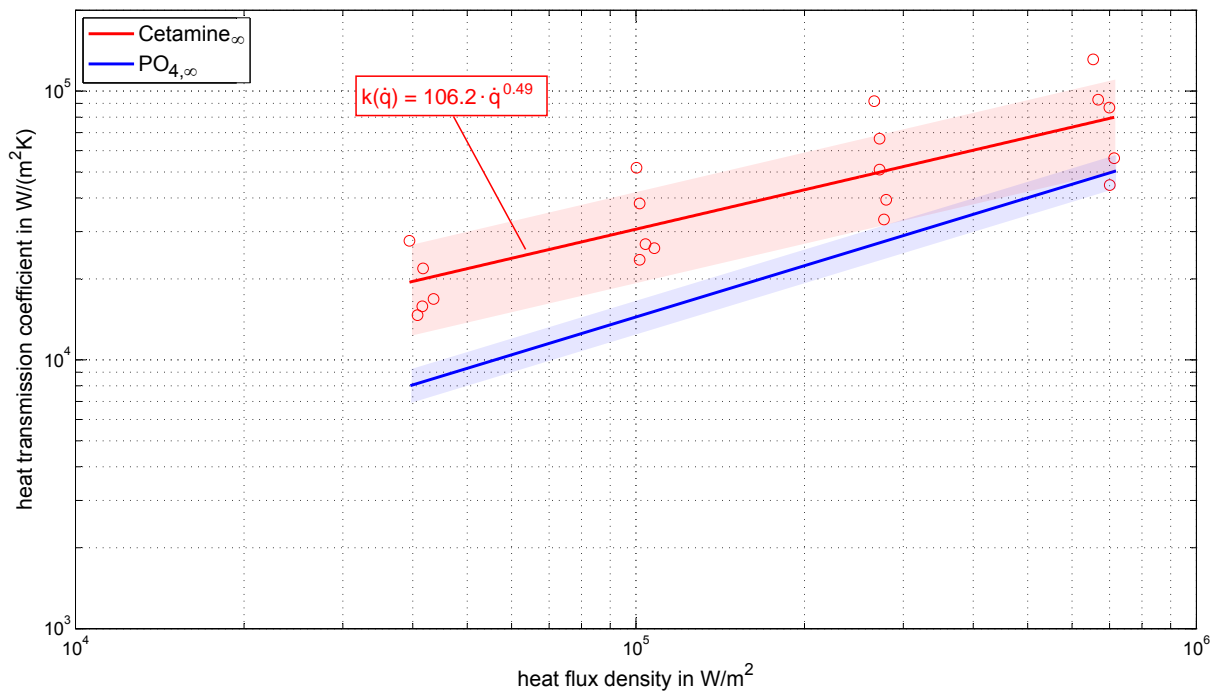


Figure 7.40: Steady state boiling curves for $Cetamine_{\infty}$ and $PO_{4,\infty}$ conditioning at $p_s = 15$ bar.

There is a significant difference $\Delta\dot{q}$ in the location of the onset of nucleate boiling between the film-forming amine and the inorganic treatment. In this case, an average $\Delta\dot{q} \approx 2800 \text{ W/m}^2$ is found, which the ONB occurs later during phosphate treatment. Hence, the necessary superheat, resulting from the impressed heat flux density, is lower for the amine treated system than for phosphate and for $PO_4 + N_2H_4$ (see also figure 7.35). The film-forming amine causes an earlier nucleation by activating comparably smaller radii.

The overall difference between the heat transmission coefficients under film-forming amine and phosphate treatment is less significant at $p_s = 2 \text{ bar}$ than at $p_s = 15 \text{ bar}$. Such behaviour was not expected, as the influence on the surface tension becomes less dominant with increasing system pressure. Consequently, the most significant increase in heat transfer could be expected at lowest saturation pressures. The steady state boiling curve for the film-forming amine is located approximately at a similar location as for $PO_{4,0}$ with a slightly smaller exponent. An overall improvement of k is found with $\Delta k \approx 70 \%$ at low heat flux densities ($40 \cdot 10^3 \text{ W/m}^2$) and $\Delta k \approx 40 \%$ at high values of $\dot{q} = 330 \cdot 10^3 \text{ W/m}^2$. Video recordings, however, show a significantly larger number of active nuclei on the tube surface during nucleate boiling at $p_s = 2 \text{ bar}$ for *Cetamine*₀ than for $PO_{4,0}$. Figure 7.42 shows the observed difference by black and white freeze frames at $I = 166 \text{ A}$, $\dot{q} \approx 21 \cdot 10^3 \text{ W/m}^2$.

Although there are no data on the initial convective boiling heat transmission under amine treatment, it can be assumed to equal phosphate conditions, because neither the saturation temperature nor the viscosity is influenced by the small amine concentrations used.

The surface properties are investigated using CLSM microscopy in order to characterise the surface roughness of *Cetamine* treated steady state samples compared to $PO_{4,\infty}$. Figure 7.43 shows the surface profile and visual on exemplary samples.

Surface morphology shows a comparably smoother roughness profile for the *Cetamine* treated tube sample. Although the surface is more homogeneous than after phosphate conditioning, the surface activity of the film-forming amine causes more intense nucleation. Determination of the available nuclei cannot be carried out, because the surface tension of the water-amine-dispersion is unknown. However, video recordings enable a study of the active nucleation site density at the beginning of *Cetamine* treatment and after reaching steady state of k , compared to the analogous conditions during PO_4 treatment. The mentioned videos are located in the appendix E, while chosen freeze frames can be found in the figures E.1, ff.

Furthermore, polished microsection is carried out to check for an oxide layer and (if present) determine its thickness. As picture 7.44 demonstrates, an oxide layer is formed on the

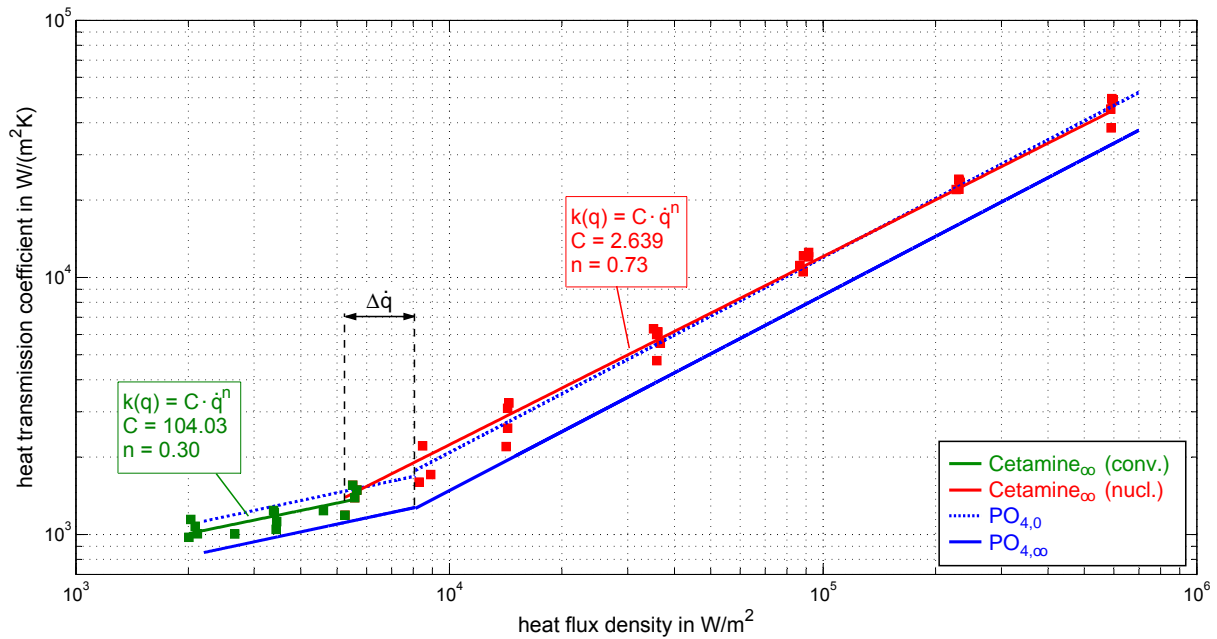


Figure 7.41: Steady state boiling curve for $Cetamine_{\infty}$ conditioning at $p_s = 2$ bar compared to $PO_{4,0}$ and $PO_{4,\infty}$.

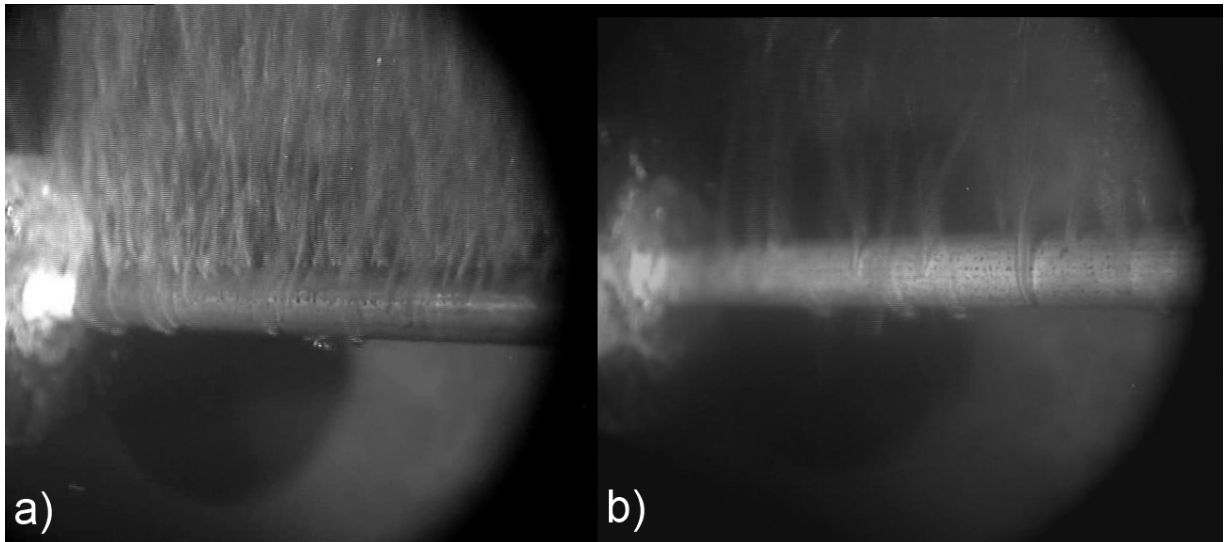


Figure 7.42: Freeze frames of the nucleate boiling behaviour for $Cetamine_0$ (a) compared to $PO_{4,0}$ (b) at $\dot{q} \approx 21 \cdot 10^4$ W/m^2 and $p_s = 2$ bar.

steel surface, which can be assumed to affect the steady state convective heat transmission coefficient. This coefficient is nominally located between the starting conditions of k and stationarity of convective boiling under PO_4 treatment. If the porosity of the oxide layer under $Cetamine$ conditioning compares to the PO_4 treatment, the layers thickness can be assumed smaller. This is the case for the examined sample with measured values

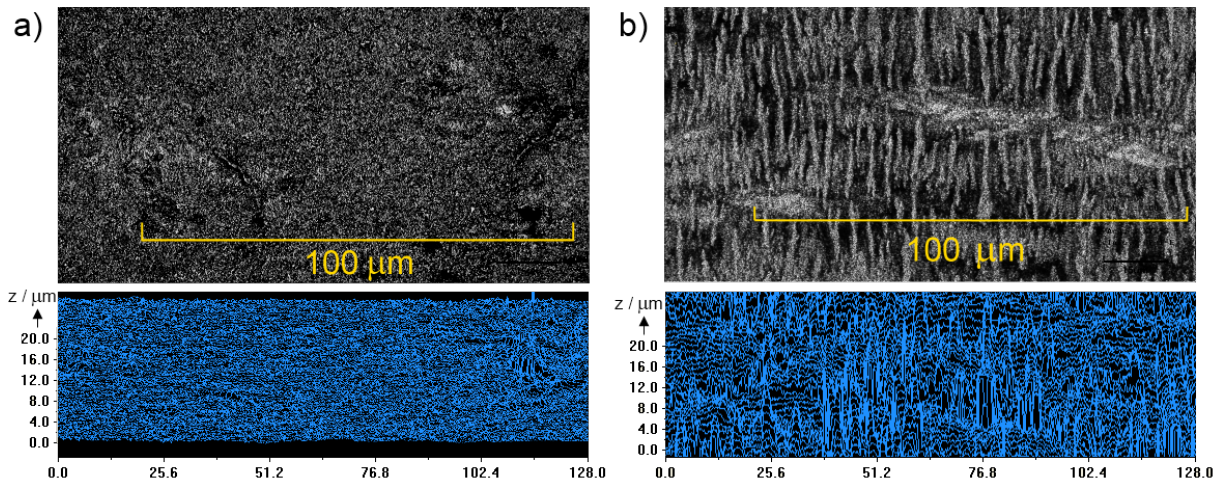


Figure 7.43: CLSM-results of an exemplary Cetamine treated tube sample (a) compared to PO_4 conditioning (b) at the steady state of k .

$1.6 \mu\text{m} \leq \delta \leq 7.3 \mu\text{m}$ (23 locations on two specimens) and an average of $\bar{\delta} \approx 5.9 \mu\text{m}$ ($\sigma = 26.5 \%$).

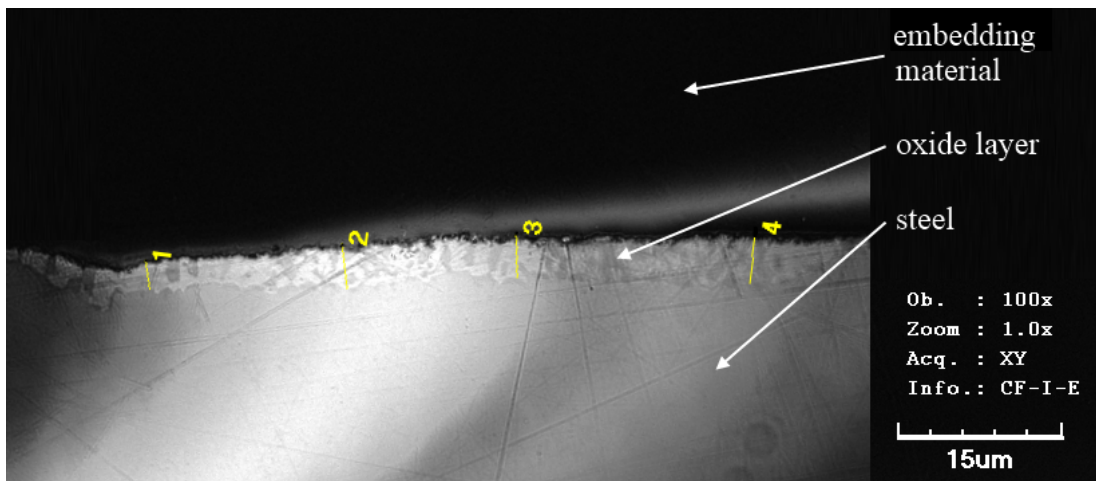


Figure 7.44: CLSM view of an exemplary polished tube sample after 400 h of Cetamine operation.

7.4.2 Switch from trisodium phosphate to film-forming amine

Whenever the chemical treatment in a boiler is switched, changes in the heater surface properties can be expected. In addition, changing from the inorganic trisodium phosphate to the organic film-forming amine might also bring out differences in the boiling behaviour, as an advantageous effect can be stated for metallic-blank heat transferring surfaces under surface tension lowering *Cetamine* treatment.

Several tube samples have been subjected to a changeover $PO_4 \rightarrow Cetamine$ resulting in a total treatment period of more than 1300 h . Immediately after the changeover is established and Cetamine-treated boiling water gets in contact with the formerly phosphate operated surface, a considerable increase in the heat transmission coefficient can be recognised. As immediately after start of amine operation, the surface is identical to the steady state of PO_4 treatment, the improvement of k , shown in figure 7.45 for $p_s = 15 \text{ bar}$, results exclusively from the surface lowering effect under *Cetamine* conditioning.

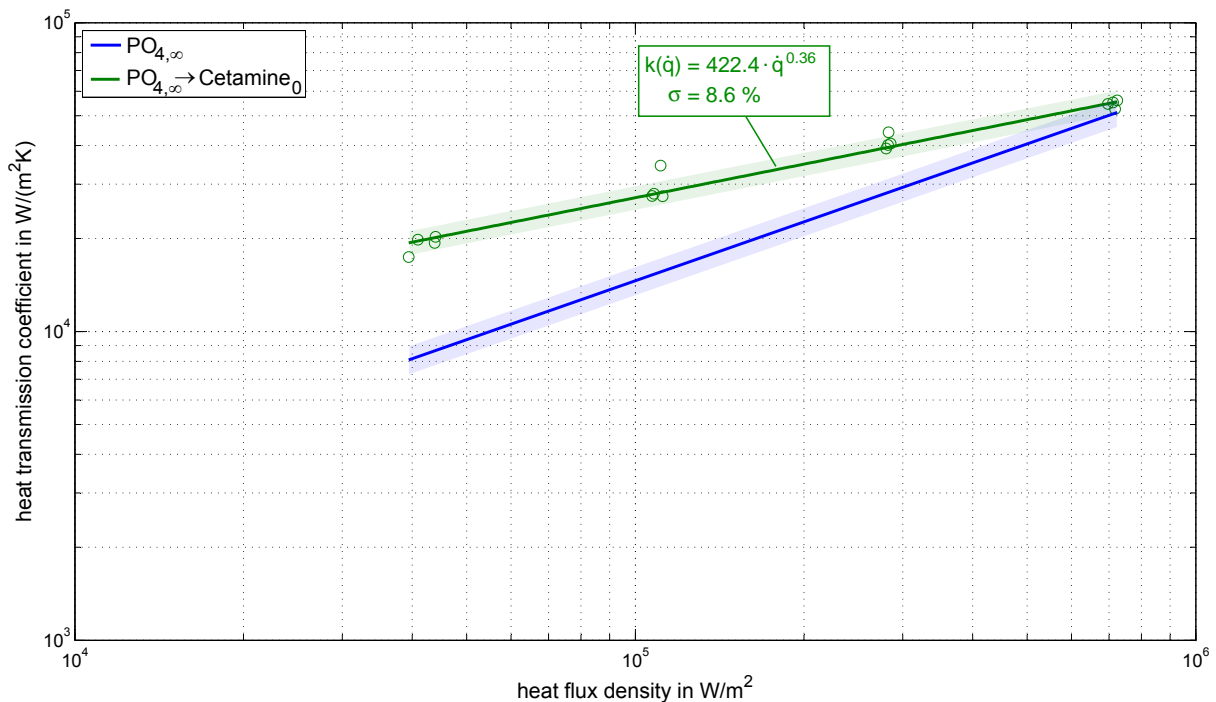


Figure 7.45: *Boiling behaviour at $p_s = 15 \text{ bar}$ immediately after treatment switch from $PO_{4,\infty}$ to *Cetamine*.*

The values of k at the highest measured heat flux density practically coincide for both treatments substantiating some kind of 'nucleation site saturation'. This means, that the surface active film-forming amine is unable to activate further nuclei, because at such high heat fluxes the number of active nucleation sites can already be assumed to be very close to its theoretical limit. The initial nucleate boiling k shows a relative mean deviation of comparably low $\sigma = 8.6 \%$.

For video recordings of the initial boiling behaviour immediately after switching from PO_4 to *Cetamine* supporting this thermotechnical statement see appendix E.1.

Including all experimental data,⁷ a significantly smaller exponent $n = 0.36$ is found for the

⁷If a specific tube sample had to be dispensed during the treatment due to malfunctions etc., the corresponding data were not integrated in the evaluation of the time response.

initial boiling curve after changeover to *Cetamine* compared to $n = 0.63$ for the trisodium phosphate treatment. The value of n is a function of the treatment period and drops down to $n = 0.49$ after reaching steady state conditions of k . Picture 7.46 shows the time dependency of the exponent.

Since the chemical parameters during $PO_{4,\infty} \rightarrow \textit{Cetamine}$ remain constant, a surface modification is considered responsible for the increase of n . The boundary value is found with $n = 0.49(0.485)$, which is rather close to the exponent of *Cetamine* conditioning of metallic-blank tube samples of $n = 0.49(0.488)$. Given a similar film-forming amine concentrations of $0.3 \text{ ppm} \leq [FA] \leq 0.8 \text{ ppm}$ for *Cetamine* and $PO_{4,\infty} \rightarrow \textit{Cetamine}$ treatment, a similar surface morphology can be assumed for the respective steady state samples. The exponent increase can be assumed to result from the dispersing character of film-forming amines being able to remove a certain amount of corrosion products even without any additional dispersants, like polyacrylates or polycarboxylates.

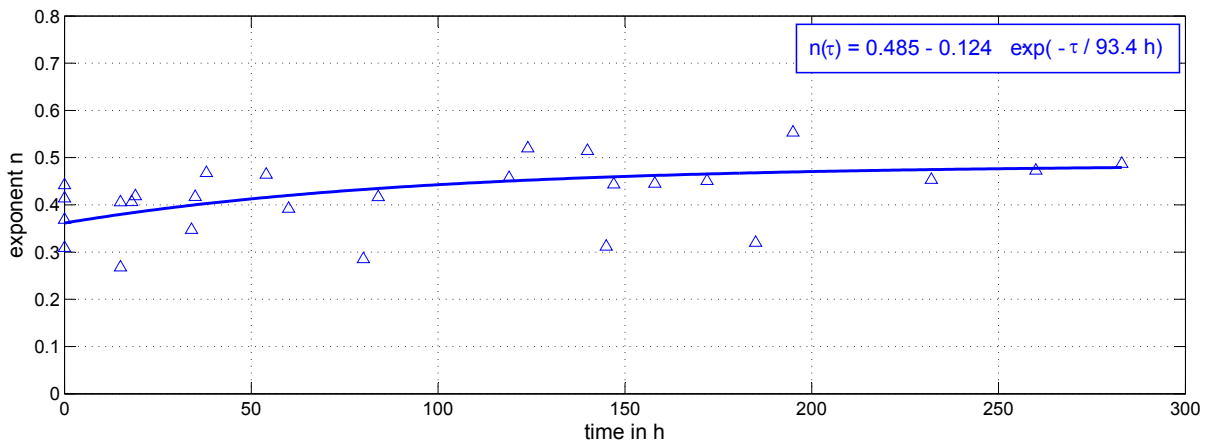


Figure 7.46: *Development of n during Cetamine treatment at $p_s = 15$ bar after the changeover from pure phosphate conditioning.*

The steady state exponent $n = 0.49$ is chosen for the reduction of k for comparability reasons. The corresponding time response of C_{red} is presented in picture 7.47. As caused by the statistical spread of experimental data for $\textit{Cetamine}_\infty$, there is a large intersection of the respective mean deviations of C_{red} under *Cetamine* ($\sigma = 17.8 \%$) and $PO_{4,\infty} \rightarrow \textit{Cetamine}$ ($\sigma = 6.1 \%$) conditioning. The relative mean deviation for the latter scenario indicates that the surface properties (surface morphology and structure) can be reproduced better on formerly phosphate treated surfaces than for metallic-blank start conditions.

The necessary treatment period under *Cetamine* conditions, until a steady state of C_{red} is evident after treatment switch from $PO_{4,\infty}$, is determined as $\tau_{99} = 430 \text{ h}$. This period is over twice as much time than needed for the $PO_4 + N_2H_4$ conditioning and even more

than five fold period, necessary for *Cetamine* treatment of bare steel surfaces. Such a comparable long treatment period indicates time-consuming surface modifications on the formerly phosphate treated samples. Obviously, the surface condition as generated during phosphate treatment takes the dispersion process a lot of time to generate a surface morphology similar to the state that would have been formed during *Cetamine* treatment when started from bare steel tubes. Considering the mentioned increase in the exponent n , the dispersing process, homogenising the tube surface, can be made responsible for the value of τ_{99} . The time response of C_{red} , calculated using the exponent during PO_4

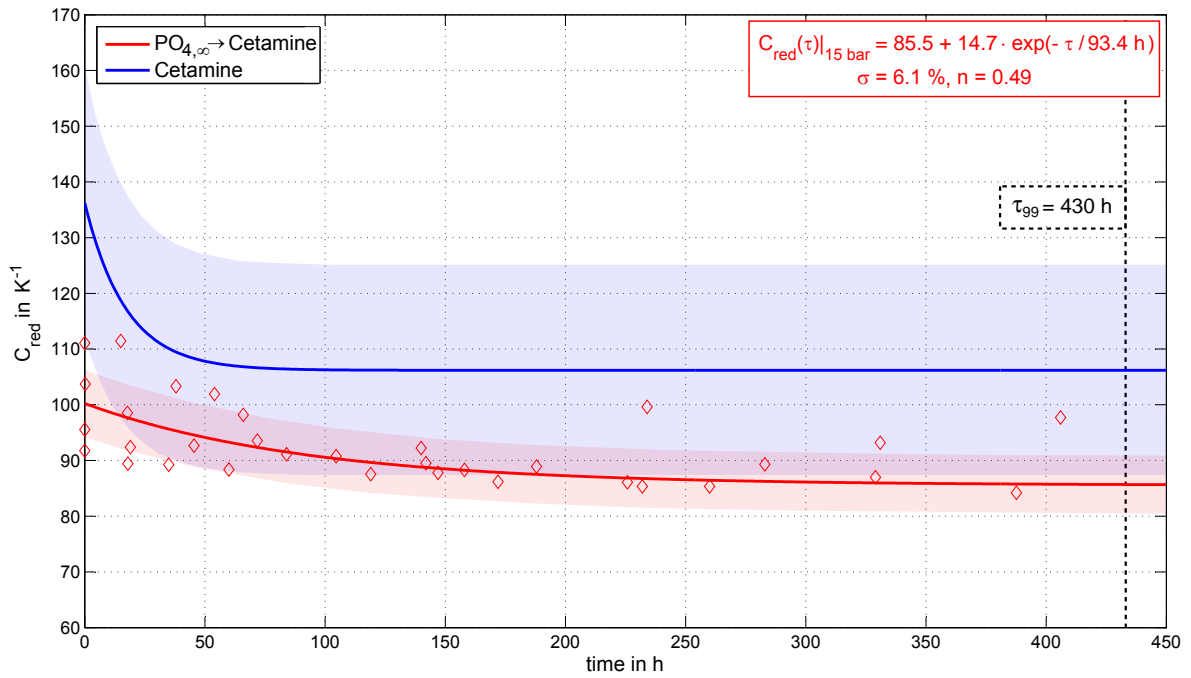


Figure 7.47: Development of C_{red} after the changeover from $PO_{4,\infty}$ to *Cetamine* conditioning at $p_s = 15$ bar.

treatment, compared to this condition is located in the appendix (see figure F.2).

Assuming the changes in the layer thickness being negligible, the mentioned surface modification is responsible for the development of n leads to a loss of available nucleation sites and the corresponding decline of low- and medium- \dot{q} heat transmission coefficients. This phenomenon is investigated using CLSM analytics after reaching steady state conditions, $PO_{4,\infty} \rightarrow Cetamine_{\infty}$.

Figure 7.48 shows clear differences in the surface structure of $PO_{4,\infty}$ and $Cetamine_{\infty}$. The surface roughness profile of the *Cetamine* treated tube sample features a significantly smoother finish than the PO_4 operated ones. Despite occasional inhomogeneities and remains from the phosphate treatment (grooves), the surface profiles of $PO_{4,\infty} \rightarrow$

$Cetamine_\infty$ are comparable to the $Cetamine_\infty$ regarding the substructure.

In addition to the surface characterisation, the oxide layer thickness is determined on polished samples by means of a CLSM measurement. The layer thickness is found with an average value of $\bar{\delta} = 15.8 \mu m$ (13 locations on two specimens) and a relative mean deviation of $\sigma = 20.1 \%$. An exemplary CLSM microsection view of a $PO_{4,\infty} \rightarrow Cetamine_\infty$ sample is found in the appendix G.

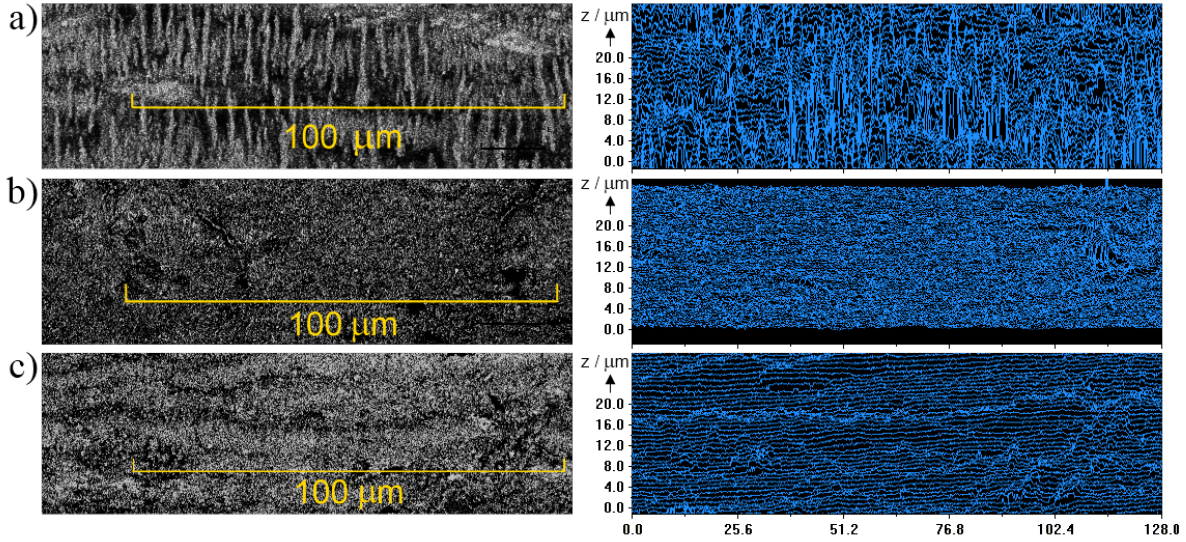


Figure 7.48: Comparison of the CLSM view and surface profile of exemplary $PO_{4,\infty}$ (a), $Cetamine_\infty$ (b) and $PO_{4,\infty} \rightarrow Cetamine_\infty$ (c) tube surfaces.

After the steady state of C_{red} is reached, the boiling curve of the following form agrees well with the experimental data at $p_s = 15 \text{ bar}$ within the technically relevant operation range $40 \cdot 10^3 \text{ W/m}^2 \leq \dot{q} \leq 330 \cdot 10^3 \text{ W/m}^2$ (see the black line in figure 7.49):

$$k(\dot{q}) = 88.9 \cdot \dot{q}^{0.49} \quad (7.12)$$

However, taking a closer look at the data around the modelled boiling curve at heat fluxes exceeding $\dot{q} = 200 \cdot 10^3 \text{ W/m}^2$ repeatedly provides k -values below the curve. Due to this cognition, smaller heat fluxes are taken into account, in order to gain certainty of the applied regression model. The following nucleate boiling operation points are included into the test program: $\dot{q} \approx (11 \cdot 10^3, 17 \cdot 10^3, 24 \cdot 10^3) \text{ W/m}^2$, which belong to the range of fully developed nucleate boiling at $p_s = 15 \text{ bar}$.

An interesting behaviour of the nucleate pool boiling heat transmission coefficients can be observed at $\dot{q} > 200 \cdot 10^3 \text{ W/m}^2$ as depicted in figure 7.49. Integrating the mentioned thermal loads and cancelling the regression at heat fluxes $\dot{q} \approx 300 \cdot 10^3 \text{ W/m}^2$ leads to

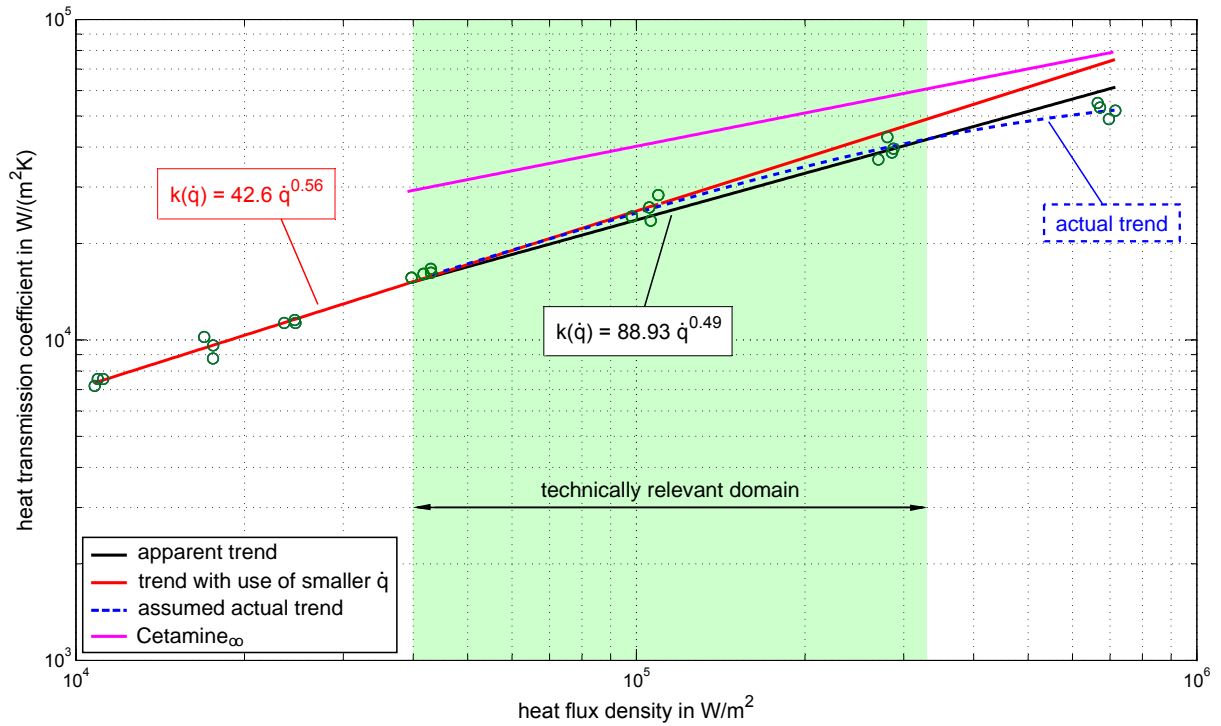


Figure 7.49: Saturation of nuclei at high thermal loads after the switch from PO_4 to *Cetamine* treatment at $p_s = 15$ bar compared to *Cetamine* $_{\infty}$.

a boiling curve power law, significantly different from the determined curve 7.12 for the technically relevant region (red line):

$$k(\dot{q}) = 42.6 \cdot \dot{q}^{0.56} \quad (7.13)$$

At elevated heat flux densities, an additional decline in the gradient $dk/d\dot{q}$ is present. The actual boiling behaviour is approximated by the dashed line. As a reference, the steady state boiling curve for *Cetamine* treatment is integrated in figure 7.49 as the solid purple line.

This phenomenon can be explained by a saturation of active nuclei on the surface. Apparently, the homogenised surface morphology, being responsible for the increase in the boiling curves exponent, causes an over proportional decrease in available nuclei, after a heat flux density of $\dot{q} > 200 \cdot 10^3 \text{ W/m}^2$ is reached. Not even a drop of the surface tension by the film-forming amine allows an activation of further nuclei beyond those that are already active on the surface. Formerly available nucleation sites in form of surfaces roughnesses have been dispersed during the *Cetamine* treatment of at least $\tau_{99} = 430 \text{ h}$, to an extent where only large boundary layer superheats at $p_s = 15 \text{ bar}$ are affected.

The analytically validated dispersion causes another thermotechnically verifiable phe-

nomenon. Convective boiling at $p_s = 2 \text{ bar}$ is not possible at all immediately after the switch from phosphate to *Cetamine* operation. With proceeding treatment and a corresponding increase in the nucleate boiling curves exponent, in some cases an onset of nucleation boiling (or better: onset of convective boiling with a decreasing thermal load) could be observed. The time response of an exemplary sample is depicted in figure 7.50 with a clear inflection point between the boiling regions after reaching the steady state of the heat transmission coefficient. The nucleate boiling exponent changes from $n = 0.61$

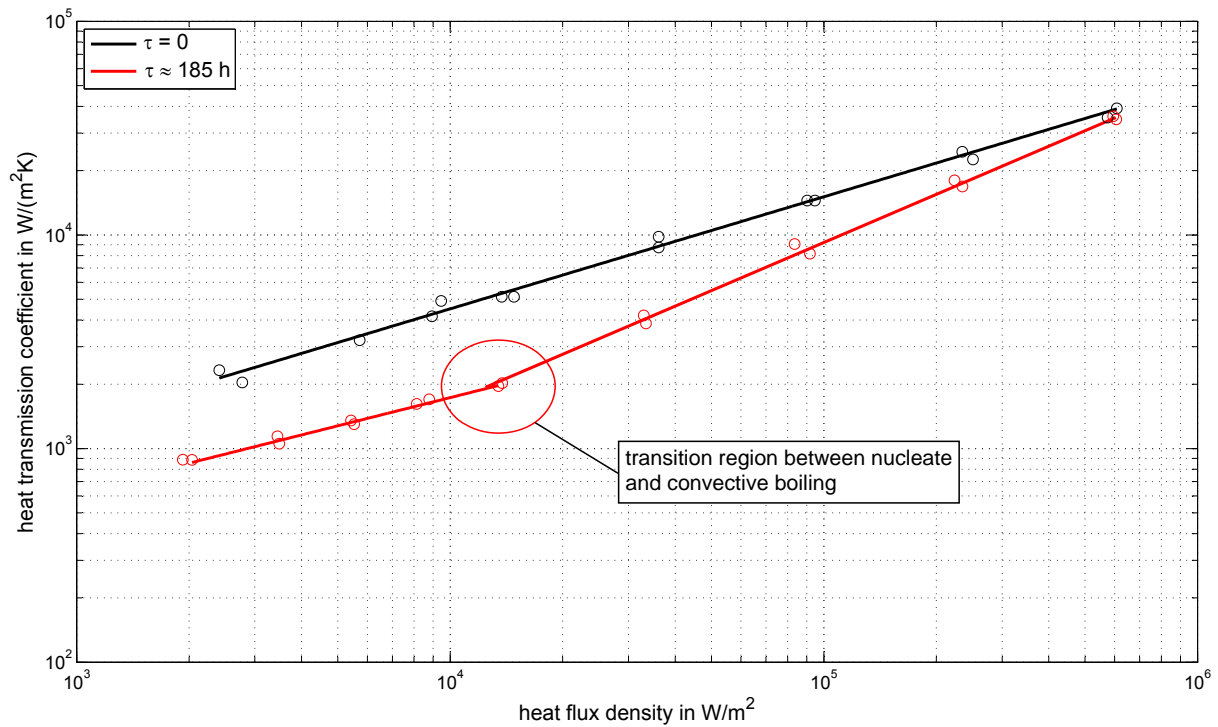


Figure 7.50: *Development of the boiling curve of two test samples at $p_s = 2 \text{ bar}$ after switching from $PO_{4,\infty}$ to Cetamine conditioning.*

to $n = 0.70$ during the treatment. While, in the beginning, convective boiling cannot be achieved by applying the smallest amperages, with proceeding operation and an increasing nucleate boiling exponent, convection sets in after $\tau > 180 \text{ h}$. Although, according to Steinbrecht^[33] nucleation can still be considered active with $n \gg 0.3$, free convection can be assumed the prevailing mechanism at low heat flux densities with an exponent $n = 0.44$.

7.4.3 Conclusion

The investigated film-forming amine treatment not only proves to provide a more homogeneous surface structure and smaller oxide layer thicknesses but also a significant increase

in the nucleate pool boiling heat transport. Metallic-blank as well as of formerly inorganically treated surfaces benefit from the surface tension lowering effect of the film-forming amine. While the boiling curves exponent can be considered constant during the treatment

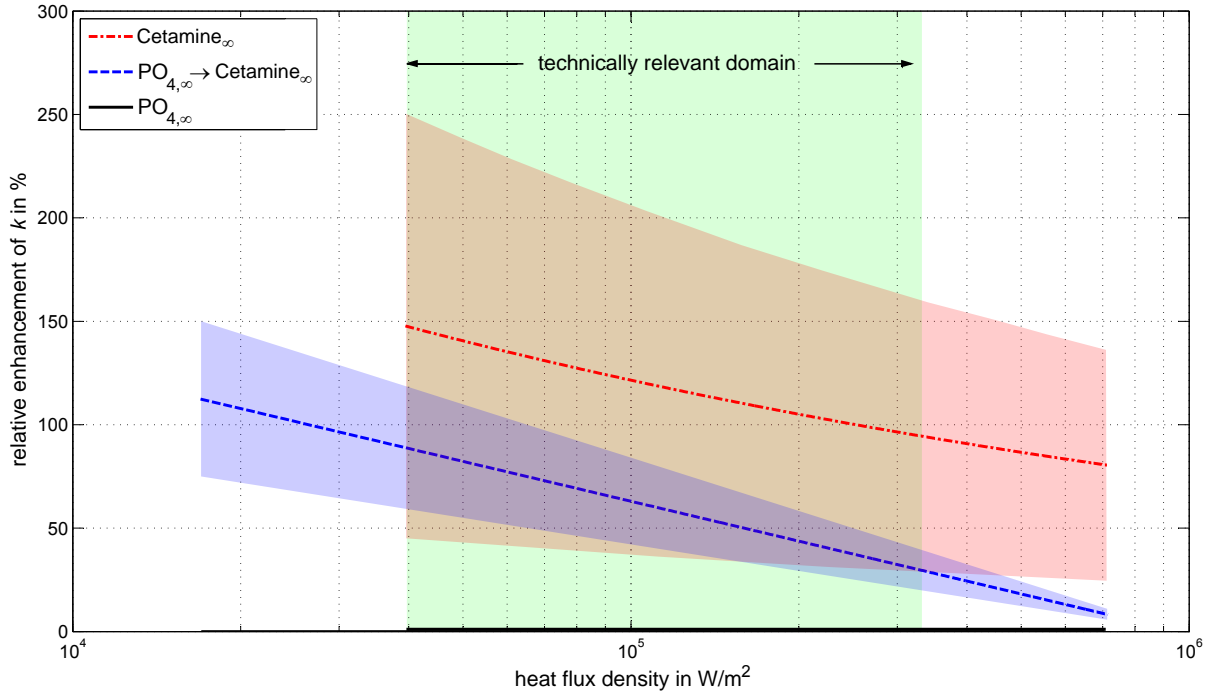


Figure 7.51: Net enhancement of k for *Cetamine* operation relative to the steady state of PO_4 conditioning at $p_s = 15$ bar.

when starting from bare steel surfaces, dispersing processes after treatment switching from $PO_{4,\infty}$ to $PO_{4,\infty} \rightarrow Cetamine_{\infty}$ lead to a loss of available nuclei on the oxide layer surface. This condition leads to an increase of the nucleate boiling exponent and eventually to convective boiling at low heat fluxes. Due to dispersion processes, a part of the potential to enhance the heat transmission during nucleate pool boiling is wasted. After reaching a steady state of the heat transmission coefficient ($PO_{4,\infty} \rightarrow Cetamine_{\infty}$), the nucleate boiling exponent at $p_s = 15$ bar equals the exponent after “infinite” treatment period of formerly metallic-blank specimens.

As predicted from the thermotechnical experiment and verified by CLSM investigations, the oxide layer morphology is comparable for steady state samples under the mentioned conditionings. The oxide layer of *Cetamine* $_{\infty}$ treated samples feature a smaller thickness than after phosphate conditioning, as evident from a comparably smaller decline in the convective heat transport. As there is an oxide layer on the organically treated tube samples, the term ‘corrosion inhibitor’ must be reconsidered. On the one hand, there is an oxide layer on the surface after treatment, so oxidation is not prevented. On the other hand, as the observed layers are compact and firmly adhering passivating layers,

the film-forming amine actually does have an inhibitory effect regarding further anodic dissolution.

The overall net improvement of the heat transmission coefficient k at $p_s = 15 \text{ bar}$ is depicted in the summary figure 7.51. The experimentally verified improvement of k can be expected to enhance the efficiency of different boiler types, from steam converters and fire-tube shell boilers to pressurised-water reactors in nuclear power plants. Film-forming amine operation can be assumed to improve part-load heat transfer in plant components, where low heat fluxes occur, since the most significant enhancements are observed under low- \dot{q} conditions.

7.4.4 Changeover from trisodium phosphate and hydrazine to film-forming amine

Investigations have also been carried out for the $(PO_4 + N_2H_4)_\infty \rightarrow \text{Cetamine}$ treatment. The corresponding data and diagrams are located in the appendix H. The overall improvement of the film-forming amine treatment over the trisodium phosphate and hydrazine treatment is nominally smaller than compared to the trisodium phosphate conditioning. In short, the principal data is summarised in table 7.4.

Table 7.4: *Principal data describing the impact of $(PO_4 + N_2H_4)_\infty \rightarrow \text{Cetamine}$ treatment on the heat transfer at $p_s = 15 \text{ bar}$.*

Quantity	n_0	n_∞	\bar{n}	C_∞	ΔC	τ_{99}
Value	0.54	0.60	0.58	28.4 K^{-1}	4.0 K^{-1}	72.9 h

7.5 Burn-out phenomena

7.5.1 Burn-out I

The boiling crisis 1st kind represents the departure from nucleate boiling. In order to prevent film boiling in shell boilers, the design heat flux densities are limited to $\dot{q} \leq 240 \cdot 10^3 \text{ W/m}^2$. Experimental heat fluxes of more than 10^6 W/m^2 are intentionally exceeding the recommendation by^[39] to gain information on the effect of passivating layers and the film-forming amines on the critical heat flux density.

Table 7.5 lists the investigated tube samples by their name, treatment type and state, and the achieved critical heat flux density. In some cases, the conditions for a burn-out I could not be provided by the electrical gear. These specimens are indicated by *. In this case, the highest generated value of \dot{q}_{max} is stated. For non-pickled bare steel tube samples from St 35 BK, conditioned with organic and inorganic feed water agents, Steinbrecht found the critical heat flux density at $p_s = 2 \text{ bar}$ in the region of $1.40 \cdot 10^3 \text{ W/m}^2 \leq \dot{q}_{crit} \leq 1.55 \cdot 10^3 \text{ W/m}^2$.^[27]

Table 7.5: Results of the burn-out I tests on metallic-blank and steady state tube samples.

Tube name	Type of treatment	Treatment period	$\dot{q}_{crit}, \dot{q}_{max}^*$
A150	<i>Cetamine</i>	0	$1.831 \cdot 10^3 \text{ W/m}^2$
A151	<i>Cetamine</i>	0	$1.814 \cdot 10^3 \text{ W/m}^2$
A159	<i>Cetamine</i>	530 h	$1.670 \cdot 10^3 \text{ W/m}^2^*$
A160	<i>Cetamine</i>	400 h	$1.732 \cdot 10^3 \text{ W/m}^2^*$
A236'	$PO_{4,\infty} \rightarrow \textit{Cetamine}$	450 h	$1.703 \cdot 10^3 \text{ W/m}^2^*$
A222	PO_4	0	$1.840 \cdot 10^3 \text{ W/m}^2$
A231	PO_4	0	$1.774 \cdot 10^3 \text{ W/m}^2$
A237	PO_4	1050 h	$1.808 \cdot 10^3 \text{ W/m}^2$
A204	PO_4	840 h	$1.440 \cdot 10^3 \text{ W/m}^2$

The experimentally obtained values for the critical heat flux density on thermotechnically steady state specimens A159, A160 and A236' cannot be stated, as departure from nucleate boiling could not be achieved. The highest possible electrical current and the respective heat flux density prove insufficient for the mentioned samples.

An imaginable electric bypass via the vessel walls or by the boiler water is excluded as the electrical conductivity of the water is determined as $59 \mu\text{S/cm}$ (lower than for Na_3PO_4

treatment, where a burn-out I is attainable). Compared to the electrical tube resistance of approximately $2 \cdot 10^{-3} \Omega$, a direct resistance between the power supply and the vessel with $R > 2 \cdot 10^6 \Omega$ is assumed sufficient to exclude a bypass. Figure 7.52 shows the results for the listed tubes, including reference starting conditions for the specimen A231 during nucleate boiling at $p_s = 2 \text{ bar}$ and a non-pickled sample A204, which is cleaned with 2-propanol only.

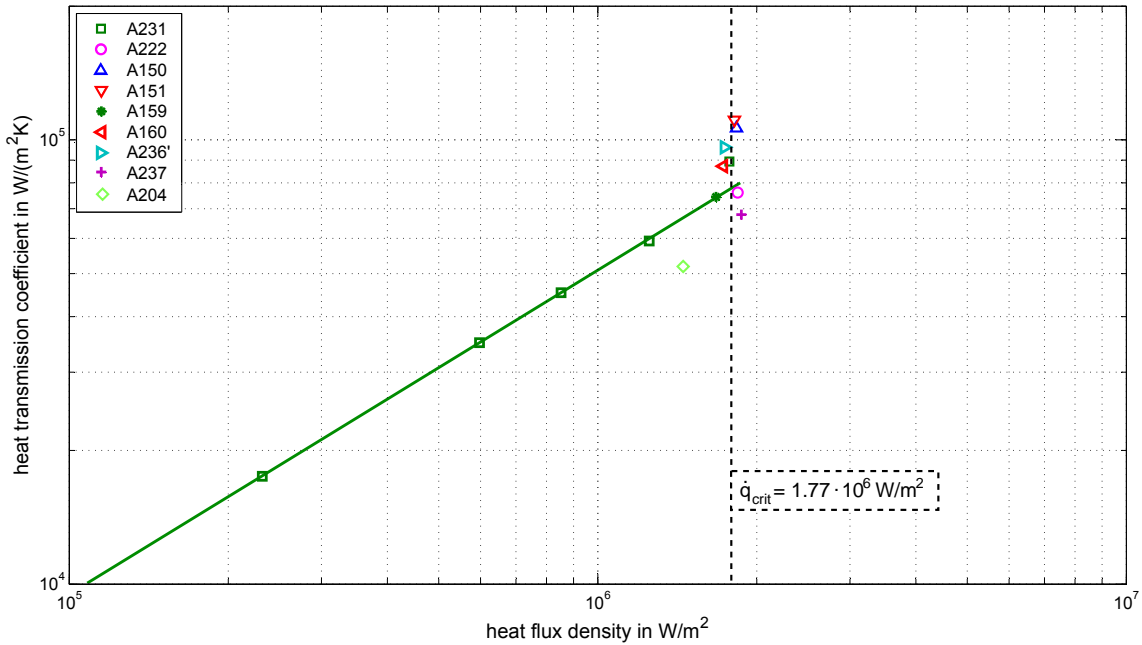


Figure 7.52: Critical heat flux densities and highest attainable values of \dot{q} at $p_s = 2 \text{ bar}$.

With $\dot{q}_{max} = 240 \cdot 10^3 \text{ W}/m^2$ (for bare steel surfaces), all experimentally observed values are exceeding the recommended heat flux density for shell boilers in the literature.^[39] The metallic-blank samples A150, A151, A222, A231 show an average value of $\dot{q}_{crit} = 1.81 \cdot 10^6 \text{ W}/m^2$, which corresponds well with the literature, according to equation 6.1 and using $f = 0.16$. The achieved heat transmission coefficients also comply fairly well with the extended boiling curve of A231. As depicted in figure 7.53 the observed values of \dot{q}_{crit} for the assayed metallic-blank samples are situated in the upper region of the $f = 0.16$ graph calculated via equation 6.1.

These comparably high values are presumably caused by the pretreatment of the tube samples (see section 6.3) apparently resulting in a modified roughness spectrum / nucleation site distribution. The reference, an untreated, 2-propanol-cleaned, sample A204 yields a critical heat flux density of $\dot{q}_{crit} = 1.44 \cdot 10^6 \text{ W}/m^2$, corresponding well with the $f = 0.13$ curve for delivery condition.

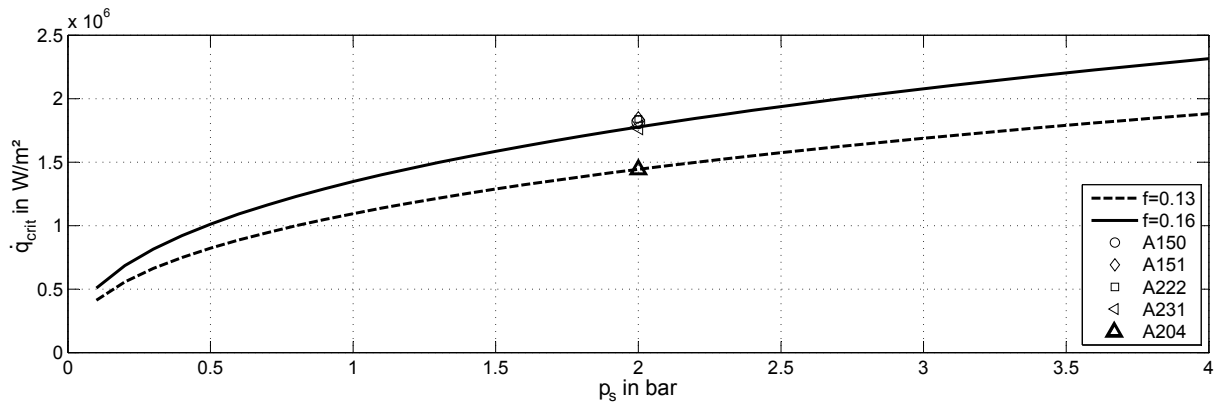


Figure 7.53: Influence of the pretreatment: Experimentally acquired critical heat flux density for etched metallic-blank tubes A150, A151, A222, A231 and sample A204 (2-propanol-flushed) compared with equation 6.1 for $p_s = 2$ bar.

Apparently, the pre-assembly treatment has a major impact on both, the critical heat flux density and the heat transfer coefficient of metallic-blank tube surfaces (see sections 6.3, 7.1.1). There is no indication that the film-forming amine affects the critical heat flux density at $p_s = 2$ bar of metallic-blank or steady state surfaces under typical concentrations. None of the investigated types of water conditioning does affect the departure from nucleate boiling.

The oxide layer developed during the treatment does not influence the critical heat flux density, although a heat transfer impeding in-line resistance is provided by the layer. However, as the surface features sufficiently large cavities for nucleation, the heat can be transferred securely, even after the achievement of a compact passivating layer. The phosphate treated sample A237 indicates no impact of the oxide layer generation on the critical heat flux density compared to metallic-blank conditions. Oxidation processes on the surface have no detectable effect on bubble interaction as critical for departure from nucleate boiling.

After conversion from phosphate to the film-forming amine treatment, the recognised nuclei saturation at elevated heat flux densities does not affect the critical heat flux density.

7.5.2 Burn-out III

The cold start-up tests are started from an ambient temperature of $\vartheta_{ambi} \approx 20$ °C. The measurement is stopped when a system temperature of $\vartheta_{sys} \approx 30$ °C is reached.

As a reference, an inorganically treated test tube is integrated into the following diagrams. This metallic-blank $PO_4 + N_2H_4$ conditioned sample A244 is not sensitive to any nucleation suppression, as it is operated inorganically. A244 represents the reference. As an example, figure 7.54 depicts the development of all relevant physical quantities during cold start-

up on an amine treated specimen ($Cetamine_{\infty}$) for the standard free film-forming amine concentration (see section 6) and a specific thermal load of $\dot{q} = 800 \cdot 10^3 \text{ W/m}^2$. Figure 7.55, in turn, shows the test results of the same tube under hot stand-by conditions (steady state, standard amine concentration, $800 \cdot 10^3 \text{ W/m}^2$). (In the same picture, the data

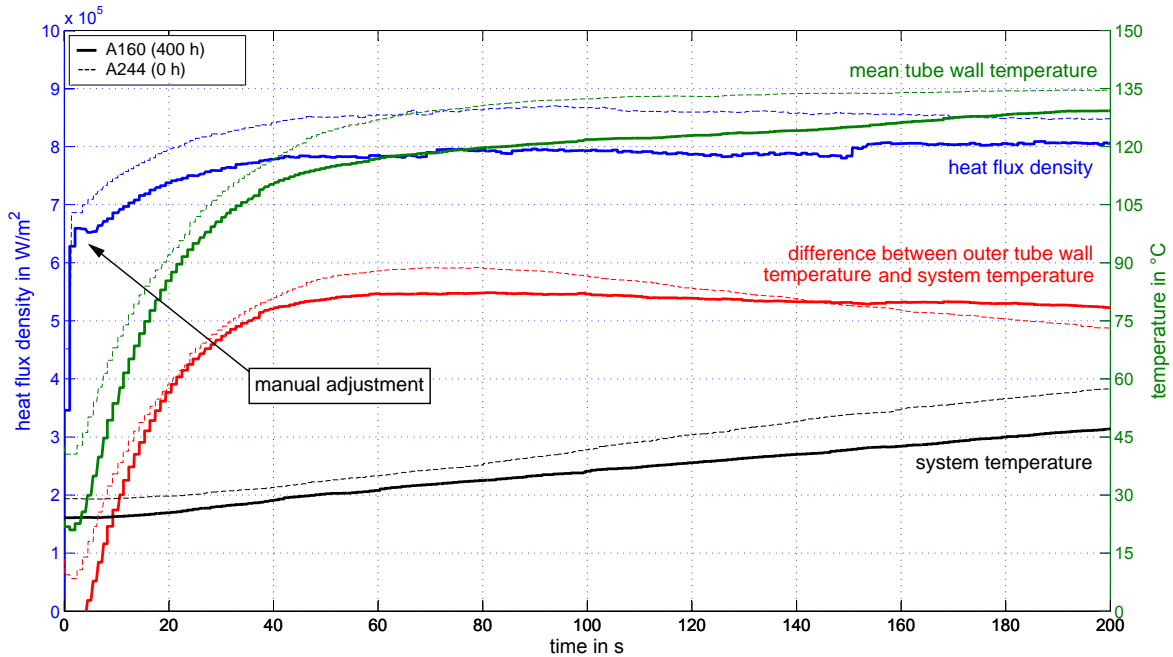


Figure 7.54: *Burn-out III test results for cold start-up conditions for the steady state Cetamine treated tube A160 compared to the $PO_4 + N_2H_4$ reference A244, $\dot{q} = 800 \cdot 10^3 \text{ W/m}^2$ at $p_s = 2 \text{ bar}$.*

acquisition for A244 is cancelled after 150 s due to voltage fluctuations in the local grid, influencing the steadiness of the heating current.)

The temperature trends are very similar to the inorganically conditioned reference tube and do not indicate any critical development. A temperature overswing, as an evidence for a multilayer desorption, cannot be recognised. Further test results under highly overdosed conditions and after switching the treatment can be found in the appendix I.

7.5.3 Conclusion

Neither the surface film-forming during the *Cetamine* treatment nor the oxide layer generation during conventional phosphate treatment affect the critical heat flux density by shifting it to lower values rather than metallic-blank surfaces. If the maximum values that are achievable by the electrical power supply are included, an experimentally verified

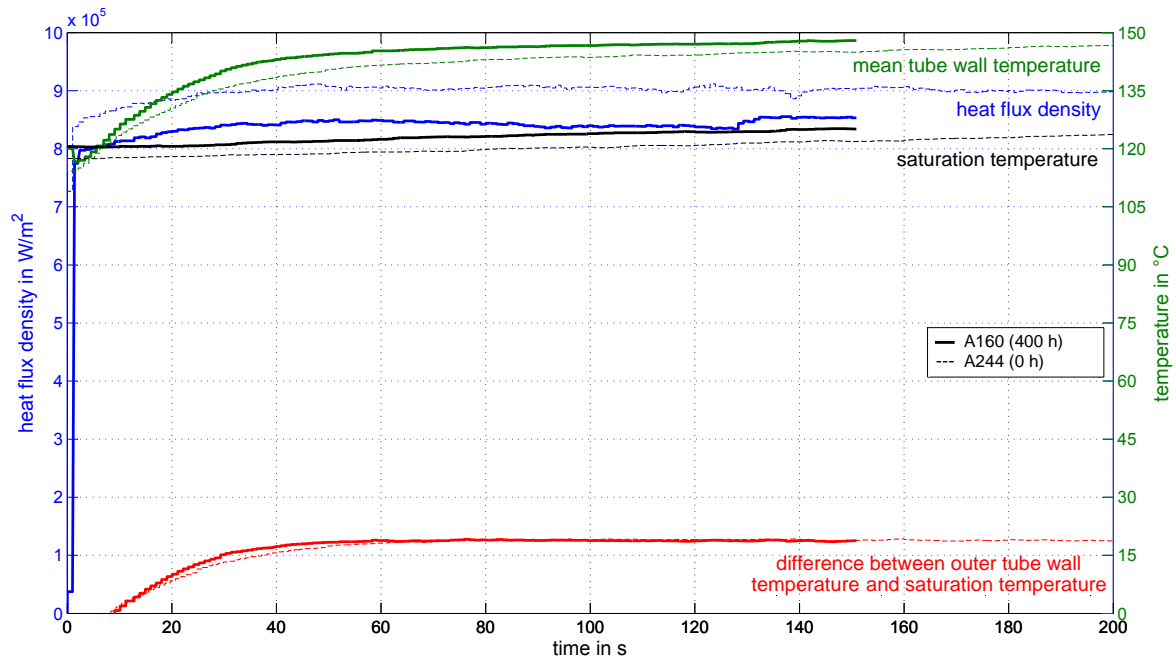


Figure 7.55: *Burn-out III test results for hot stand-by conditions for the steady state Cetamine treated tube A160 compared to the $PO_4 + N_2H_4$ reference A244, $\dot{q} = 800 \cdot 10^3 \text{ W/m}^2$ at $p_s = 2 \text{ bar}$.*

average value of $1.77 \cdot 10^6 \text{ W/m}^2$ for the investigated treatments is considered *safe* for technical applications.

A burn-out III could not be observed for any of the heat flux densities or investigated system conditions. Neither for the standard concentration nor for a 100-fold overdose, a critical behaviour is observable. It is questionable, whether the phenomenon of burn-out III can be reproduced at all by using the applied film-forming amine. As a consequence, the applied organic corrosion inhibitor can be considered safe for technical applications even when the film-forming amine concentrations are considerably exceeding typical values.

8 Conclusion and preview

Profound experimental investigations have been carried out regarding the effect of different feed water conditioning agents on the heat transport during saturated pool boiling, which contribute to the basic understanding of the surface development and boiling behaviour under the influence of typical feed water agents in shell boilers. Therefore, commercial inorganic and organic agents are compared regarding their impact on the heating surface properties at a saturation pressure of 15 *bar*.

A detailed insight is gained into the effect of exemplary inorganic and one organic treatment on the (oxidised) surface properties and critical operation modes. The made cognitions are exclusively secured for the applied products only.

In detail, a modified non-destructive and thermotechnically intended method is presented and proves valid to describe the influence of feed water agents on the heating surface properties, where usually cutting or destruction were necessary to initiate further analyses (SEM, CLSM, polished section, etc.). The described long term observations of the heat transmission behaviour, however, do not necessarily require destructive methods to gain information on the surface properties.

Correspondingly, the presented experimental setup would profit from an in situ determination of the heat flux density during the measurement. Given that, identical heat flux densities could be impressed repeatedly, uninfluenced by any layer development or treatment influence (e.g. surface activity).

The necessary treatment period for surface passivation in this work can be assumed to show a similar tendency *for comparable water quality* in shell boilers. Pressures higher than 15 *bar* presumably result in shorter periods necessary to achieve stationarity in thermotechnical terms. In the case of elevated electrical boiler water conductivities (compared to this work) or the presence of dissolved oxygen (due to missing or incomplete thermal degassing), a correspondingly increased corrosion rate, corrosion product transport and differences in the structure and/or composition of the oxide layer might result.

Regarding the application of the investigated organic film-forming corrosion inhibitor Cetamine[®]V211, the intrinsic property to form films on water and steam touching surfaces, an earlier nucleation (ONB) and a heat transfer enhancement can be assumed to apply in shell boilers, when operating at higher pressures, and also in flow boilers. A model

to estimate the impact of the film-forming amine compared to the trisodium phosphate treatment in a pressurised-water reactor at $p_s = 15 \text{ bar}$ is presented in the appendix J. The model calculates an increased steam mass production of more than 6 % for the organic conditioning.

As a preview, field trials in a typical shell boiler arrangement are suggested to validate the predicted improvement of heat transfer during film-forming amine treatment as based on the experimental data for a *horizontal single tube*.

Although a considerable number of tube samples have been assayed in this work, which show a fairly good agreement, a certain spread regarding the oxide layer properties is still present. Provided that common surface analyses do not obtain sufficient information about these parameters, modified methods have to be established in order to characterise the effect of cavity type and size distribution on the heat transfer behaviour. The nucleate pool boiling at low saturation pressures is especially predestinated to be further investigated regarding this topic and appears most promising in terms of correlating the heat transfer and the heating surface properties.

The use of high-speed video recording and microscopic surface analysis, including an oxide layer thickness and thermal conductivity determination might lead to a quantitative correlation between the treatment type and period, active nucleation site density, bubble interaction and the heat transfer coefficients. The cognitions on the boiling curves exponent and observed deviations from the generally accepted power law, as framed in this work, provide important information on these phenomena.

The interaction of permanent nucleation on the oxide layer development can be investigated during film-forming amine treatment. Especially after switching from a classic inorganic to film-forming amine treatment, where considerable modifications on the surface structure take place, transport and removal processes of corrosion products due to an interaction of nucleation and dispersion are conceivable.

As the feed water quality and contained species determine the type of applied feed water agents by the resulting electrical conductivity, the oxide layer generation, properties and impact on the heat transport can be investigated by means of the presented method. This interrelation is considered important for many industrial shell boiler applications without feed water preparation, i.e. by demineralisation.

In addition, stainless steel specimens, larger tube diameters and typical feed water treatments at elevated pressures present an interesting field of research to the described method. By investigating such system conditions, conclusions seem possible on the effect of feed water conditionings on materials as present in pressurised-water reactors, for instance.

As a comprehensive summary, the following statements represent the major findings of this work:

1. The presented thermotechnical method allows statements on the heating surface structure and its modification during an operation with conditioned water under saturated pool boiling conditions by evaluation of experimentally determined boiling curves in accordance to the generally accepted proportionality $k \sim \dot{q}^n$ (k - heat transmission coefficient, \dot{q} - heat flux density).
2. The level of the heat transfer coefficient during saturated nucleate pool boiling is determined to a large extent by the exponent n of the heat flux density, which verifiably depends on the surface morphology/nuclei size distribution of the heater material.
3. Independently of the investigated feed water treatment, in all cases iron oxide layers are formed on the test samples during operation, which have a significant effect on the heat transmission coefficient.
4. The treatment period necessary to reach a thermotechnical steady state is found between 80 h for the film-forming amine and 430 h after switching from trisodium phosphate to the film-forming amine.
5. During convective pool boiling the heat transmission is dominated by the heat conduction resistance of the oxide layer.
6. During fully developed nucleate pool boiling, the thermal resistance of the oxide layer provides a minor negative effect on the heat transmission coefficient compared to the influence of the surface structure.
7. A special chemical pretreatment of the heating surface provides an improvement of the initial nucleate pool boiling heat transfer reproducibility. In doing so, the use of test samples from an identical fabrication process and material quality is essential. In the beginning but also during operation, the heat transfer coefficients are influenced by a variety of parameters and cannot be predicted precisely without the knowledge of supportive experimental data.
8. The investigated acidic pretreatment determines the boiling curves exponent and thereby the heat transfer coefficient under nucleate pool boiling conditions by providing a modified cavity size distribution compared to the delivery condition of untreated surfaces.
9. The impact of the resulting surface modification increases with a rising saturation pressure.

-
10. The pickling procedure leads to a significant increase of the critical heat flux density at $p_s = 2 \text{ bar}$ compared to non-etched test-samples for a metallic-blank condition.
 11. In turn, the generated oxide layer does not significantly affect the critical heat flux density at $p_s = 2 \text{ bar}$.
 12. From a technical point of view, permanent nucleation does not affect the corresponding heat transfer coefficients during an operation with trisodium phosphate at $p_s = 15 \text{ bar}$ as compared to unheated surfaces.
 13. Hydrazine, as an additional oxygen scavenger and reducing feed water agent during trisodium phosphate conditioning, has a considerable impact on the necessary operation period to reach a thermotechnical steady state as compared to the trisodium phosphate treatment.
 14. After the combined trisodium phosphate and hydrazine treatment, the heating surface features a slightly more homogeneous surface profile compared to the pure trisodium phosphate conditioning.
 15. As caused by the surface tension decrease, an application of the investigated film-forming amine leads to an enhanced nucleate pool boiling heat transfer by activating smaller nuclei. This effect is reflected in a comparably smaller nucleate boiling exponent and decreases with increasing heat flux densities.
 16. Tube surfaces treated with the investigated film-forming corrosion inhibitor feature a comparably smoother surface than inorganically operated ones.
 17. After switching from trisodium phosphate to film-forming amines after reaching a thermotechnical steady state, besides the heat transfer enhancement dispersion processes take place during operation. As caused by this surface modification, the boiling curves exponent increases during the treatment.
 18. A saturation of active nuclei is observable after the changeover from trisodium phosphate to the film-forming amine, which does not measurably affect the critical heat flux density at $p_s = 2 \text{ bar}$.
 19. The critical heat flux density during nucleate pool boiling at $p_s = 2 \text{ bar}$ remains unaffected by the film-forming amine conditioning.
 20. A suppression of nucleation by a multilayer of film-forming amines could neither be observed for cold start-up nor for hot stand-by conditions.

9 Bibliography

- [1] H. Lehmann. *Handbuch der Dampferzeugerpraxis*. Verlag Resch KG, 4th edition, 2000.
- [2] H. Kirsch and S. Pollmann. Ablagerungs- und Korrosionsprodukte im Wasser/Dampf-Kreislauf von Dampferzeuger-Anlagen. *Chemie Ingenieur Technik*, 40(18):897–903, 1968.
- [3] H. Kaesche. *Die Korrosion der Metalle*. Springer-Verlag, 3rd edition, 1990.
- [4] W. Schatt and H. Worch. *Werkstoffwissenschaft*. Deutscher Verlag für Grundstoffindustrie Stuttgart, 8th edition, 1996.
- [5] H. Fischer and K. Hauffe. *Passivierende Filme und Deckschichten - Anlaufschichten*. Springer, 1956.
- [6] A. Rahmel and W. Schwenk. *Korrosion und Korrosionsschutz von Stählen*. Verlag Chemie, 1977.
- [7] W. Tornier. Schäden an Wasserrohr- und Großwasserraumkesseln - Ursachen und Vermeidung. *Technische Überwachung*, page 19, 2001.
- [8] Deutsches Institut für Normung e. V. DIN EN 12953-10 Großwasserraumkessel, Teil 10: Anforderungen an die Speisewasser- und Kesselwasserqualität., 12/2003.
- [9] TRD 611 (Technische Regeln für Dampfkessel): Speisewasser und Kesselwasser von Dampferzeugern der Gruppe IV. Vorschriftensammlung der Staatlichen Gewerbeaufsicht Baden-Württemberg, 2004.
- [10] D. Steinbrecht. Zur Messung von Wärmeübergangskoeffizienten beim Sieden unter den Bedingungen des pool boiling. *Wissenschaftliche Zeitschrift der Technischen Hochschule Otto von Guericke Magdeburg*, 26(1), 1982.
- [11] D. Steinbrecht. *Zu den Ursachen zeitlicher Veränderungen der Wärmeübergangskoeffizienten beim Sieden von Wasser an Stahlheizflächen*. Habilitation, Technische Hochschule Otto von Guericke Magdeburg, 1983.
- [12] D. Frahne. Zum Verhalten von Polyaminen im Wasserdampfkreislauf. Technical report, Steinbeis-Transferzentrum Reutlingen, 2007.
- [13] W. Hater. Einführung in die Technologie der filmbildenden Amine. PPChem Seminar, Heidelberg, 2007.

-
- [14] G. Bohnsack. Korrosionsinhibierung durch das im Helamin enthaltene "filmbildende" Amin. *VGB Kraftwerkstechnik*, 77(10):777–786, 1997.
- [15] W. Hater and D. Olivet. Organische Kesselspeisewasser-Additive auf Basis filmbildender Amine. *VGB PowerTech*, pages 75–79, 2009.
- [16] A. Leyzerovich. *Wet-steam turbines for nuclear power plants*. PennWell Corporation, 2005.
- [17] K. Oertel, I. Goy, and E. Gläser. Vergleich einiger Wasserregime am Sekundärkreislauf des WWER-2. *Energietechnik*, pages 346–349, 1976.
- [18] E. Czempik, K. Schindler, and A. Schümichen. Anwendung von Octadecylamin zur Optimierung des wasserchemischen Regimes des zweiten Kreislaufs von KKW-Blöcken mit WWER-440. *Kernenergie*, 33:360–361, 1990.
- [19] D. Steinbrecht, M. Strümke, and A. Schümichen. Zum Einfluß von Octadecylamin auf den Wärmeübergang beim Blasensieden von Wasser an Stahlheizflächen mit stationärer Magnetitschicht. *Energietechnik*, 34(10), 1984.
- [20] L. Bursik. Once-through Boiler as an Autoclave for Testing an Organic Cycle Treatment Chemical. *PowerPlant Chemistry*, pages 81–85, 2002.
- [21] R. Lier, G. Janssen, and J. Savelkoul. Three Years of Experience with Polyamines in the High Pressure Steam System of a Naphtha Cracker. *PowerPlant Chemistry*, 2008.
- [22] W. Schöntag. Erfahrungen mit dem Einsatz eines organischen Konditionierungsmittels im Heizkraftwerk SÜD der Stadtwerke München. PPChem Seminar, Mannheim, 2000.
- [23] L. Abbasipour and J. Kallweit. Einsatz von Aminen und Polyaminen bei Anwendern in Industrie- und Heizkraftwerken. PPChem Seminar, Heidelberg, 2007.
- [24] R. Turyna. 2 Jahre Konditionierung und Online-Reinigung mit Aminen und Polyaminen in der Tschechischen Republik. PPChem Seminar, Heidelberg, 2007.
- [25] D. Steinbrecht. Sind Amine eine Alternative zu herkömmlichen Konditionierungsmitteln für Wasser-Dampf-Kreisläufe? *VGB Powertech*, 9:120–123, 2003.
- [26] S. Graßmann. Aktuelle Schadensereignisse an Dampfkesselanlagen. Technical report, TÜV Süddeutschland, 2000.
- [27] E. Backhaus and D. Steinbrecht. Erhöhung der Sicherheit bei der Wärmeübertragung beim Sieden von Wasser in Großwasserraumkesseln. Technical report, VGB-Nr. 192, 2002.
- [28] H.D. Baehr and K. Stephan. *Wärme- und Stoffübertragung*. Springer, 6th edition,

- 2008.
- [29] S. Nukiyama. Maximum and minimum values of heat transmitted from metal to boiling water under atmospheric pressure. *Journ. Society Mech. Eng., Japan*, 37:53/54, 367/74, 1934.
 - [30] E. Schlünder and H. Martin. *Einführung in die Wärmeübertragung*. Vieweg, 8th edition, 1995.
 - [31] Verein Deutscher Ingenieure. *VDI-Wärmeatlas*. Springer, Berlin Heidelberg, 2006.
 - [32] D. Steinbrecht. Untersuchung des Wachstums von Schichten auf siedendem Wasser ausgesetzten Verdampferheizflächen. *Energieanwendung*, 32(2), 1983.
 - [33] D. Steinbrecht and M. Strümke. Beeinflussung des Wärmeübergangs beim Sieden von Wasser an Stahlheizflächen durch Magnetitwachstum. *Wissenschaftliche Zeitung der Technischen Hochschule Otto von Guericke Magdeburg*, 28(2), 1984.
 - [34] M. Michejew. *Grundlagen der Wärmeübertragung*. VEB Verlag Technik Berlin, 2nd edition, 1964.
 - [35] Y.-H. Zhao, T. Masuoka, and T. Tsuruta. Theoretical studies no transient pool boiling based on microlayer model. *International Journal of Heat and Mass Transfer*, 45(21):4325–4331, 10 2002.
 - [36] J.C. Chen. Contributions of convection and boiling to convective flow boiling. In *Convective flow boiling: proceedings of Convective Flow Boiling*, 05 1995.
 - [37] X.F Peng, Z. Wang, and D.J. Lee. Dynamic Behaviour of Bubble Interface During Boiling. *J. of Thermal Science*, 11(4):308–319, 2002.
 - [38] M. Zell and J. Straub. Experimentelle Untersuchungen des Wärmeübergangs und seiner Transportmechanismen bei Siedevorgängen unter reduzierter Schwerkraft. Technical report, Technische Universität München, 1985.
 - [39] FDBR. Druckbehälter-Regeln, 1994.
 - [40] L. Chien and R. Webb. A Parametric Study of Nucleate Boiling on Structured Surfaces, Part II: Effect of Pore Diameter and Pore Pitch. *Journal of Heat Transfer*, 120:1049–1055, 1998.
 - [41] G. Lüdenbach, H. Reichel, and D. Küster. Wiederkehrende Prüfkonzepte im Hinblick auf Schädigungen durch dehnungsinduzierte Risskorrosion (DRK). <http://www.vgb.org/werkstofflabor.html>, 2009.
 - [42] Deutsches Institut für Normung e. V. DIN 4760: Gestaltabweichungen - Begriffe, Ordnungssystem., 06/ 1982.
 - [43] D. Steinbrecht and P. Lorenz. Zur Vorausberechnung der Wärmeübergangskoeffizien-

- ten beim Blasensieden von Wasser an Stahlheizflächen. *Energietechnik*, 34(11), 1984.
- [44] A. Bursik. Polyamine/amine treatment - a reasonable alternative for conditioning high pressure cycles with drum boilers. *PowerPlant Chemistry*, 6(9):549–555, 2004.
- [45] H. Kirsch. Deckschichtbildung auf verschiedenen Stahllarten unter den Bedingungen des Hochdruck-Wasser-Dampfkreislaufes in Kraftwerken. *Werkstoffe und Korrosion*, 22(6), 1971.
- [46] A. Bursik. Kreislaufchemie und typische Kesselrohrschäden. In *Chemie im Wasserdampfkreislauf*, October 2009.
- [47] H. Hömig. *Metall+Wasser*. Vulkan-Verlag Essen, 4th edition, 1978.
- [48] G. Bohnsack. *The solubility of magnetite in water and in aqueous solutions of acid and alkali*. Vulkan-Verlag Essen, 1987.
- [49] H. Hömig. *Physikochemische Grundlagen der Speisewasserchemie*. Vulkan-Verlag Essen, 3rd edition, 1963.
- [50] G. Bohnsack. Das System Eisen/Wasser. - Strukturdenken der organischen Chemie angewandt auf ein anorganisches Problem. *Liebigs Ann. Chem.*, pages 1035–1045, 1974.
- [51] G. Lüdenbach. Bedeutung der Deckschichtzerstörung bei rauchgasseitigen und wasser-/dampfseitigen Korrosionsvorgängen. VGB-Seminar "Chemie im Kraftwerk", 6.-9. März 2007, VGB, Essen, 03 2007.
- [52] H.-G. Heitmann. *Chemie und Korrosion in Kraftwerken*. Vulkan-Verlag, Essen, 2000.
- [53] P. Tremaine, D. Schvedov, and L. Trevani. Sodium Phosphate Hideout Mechanisms. Technical report, Memorial University of Newfoundland, Canada, EPRI, 1999.
- [54] E. Riedel and C. Janiak. *Anorganische Chemie*. Gruyter, 2007.
- [55] G. Hetsroni, M. Gurevich, A. Mosyak, R. Rozenblit, and Z. Segal. Boiling enhancement with environmentally acceptable surfactants. *International Journal of Heat and Fluid Flow*, 25:841–848, 2004.
- [56] H. Dörfler. *Grenzflächen und kolloid-disperser Systeme: Physik und Chemie*. Springer, 2002.
- [57] IAPWS. IAPWS-IF97, X Steam Excel 2.6,. <http://www.x-eng.com>.
- [58] G. Manahan. Thermal expansion and conductivity of magnetite flakes from the Oconee-2 steam generator. *Journal of Materials Science*, 25:3424–3428, 1990.
- [59] P.K. Sarma, V. Srinivas, and K.V. Sharma. Correlation for Heat Transfer in Nucleate Boiling on Horizontal Cylindrical Surface. *Heat Transfer Engineering*, pages 449–457, 2009.

- [60] V.V. Yagov. Nucleate boiling heat transfer: possibilities and limitations of theoretical analysis. *Heat and Mass Transfer*, 45(7):881–892, 2009.
- [61] S. Kandlikar. A Theoretical Model to Predict Pool Boiling CHF Incorporating Effects of Contact Angle and Orientation. *Journal of Heat Transfer*, 123:1071–1079, 2001.
- [62] T. Hikibi and M. Ishii. Active nucleation site density in boiling systems. *International Journal of Heat and Mass Transfer*, 46, 2003.
- [63] H. Chung and H. No. A nucleate boiling limitation model for the prediction of pool boiling CHF. *International Journal of Heat and Mass Transfer*, 50:2944–2951, 2007.
- [64] A. Das, P. Das, and P. Saha. Nucleate boiling of water from plain and structured surfaces. *Experimental Thermal and Fluid Science*, 31:967–977, 2007.
- [65] M. Strümke and D. Steinbrecht. Wärmeübergangsmessungen beim pool boiling als Grundlage der Untersuchung des Wachstums und der Eigenschaften von Magnetitschichten. *Energietechnik*, 1984.
- [66] C. Bidwell. Electrical and Thermal Properties of Iron Oxide. *Physical Review*, 10:756–766, 1917.
- [67] C. Clauser and E. Huenges. *Thermal Conductivity of Rocks and Minerals.*, chapter 3-9, pages 105–126. American Geophysical Union, 1995.
- [68] B. Hemingway. Thermodynamic properties for bunsenite, NiO , magnetite, Fe_3O_4 , and hematite, Fe_2O_3 , with comments on selected oxygen buffer reactions. *American Mineralogist*, 75(7-8):781–790, 1990.
- [69] J. Lis and P. Kellard. Measurements of the thermal conductivity of thin films of magnetite. *BRIT. J. APPL. PHYS.*, pages 1117–1123, 1968.
- [70] E. Takegoshi, Y. Hirasawa, and S. Imura. Measurement of thermal properties of iron oxide pellets. *International Journal of Thermophysics*, 5(2):219–228, 1984.
- [71] J. Molgaard and W.W. Smeltzer. Thermal Conductivity of Magnetite and Hematite. *Journal of Applied Physics*, pages 3644–3647, 1971.
- [72] M. Kang. Effect of Tube Inclination on Pool Boiling Heat Transfer. *Journal of Heat Transfer*, 122:67–81, 2000.
- [73] M. Chun and M. Kang. Effects of heat exchanger tube geometries on nucleate pool boiling heat transfer in a scaled in-containment refueling water storage tank. *International Communications in Heat and Mass Transfer*, 23(1):24–34, 1996.
- [74] D. Steinbrecht. Einfluß der Wärmeleitfähigkeit des Heizflächenmaterials auf die Wärmeübergangszahlen beim Blasensieden. *Wissenschaftliche Zeitschrift der Technischen Hochschule Otto von Guericke Magdeburg*, 14:929–930, 1970.

-
- [75] D. Steinbrecht, M. Strümke, and A. Innemann. Einfluß von Octadecylamin auf den Wärmeübergang beim Sieden von Wasser an Stahlheizflächen. *Wissenschaftliche Zeitschrift der Technischen Hochschule Otto von Guericke Magdeburg*, 28(4), 1984.
- [76] H. Frohne, K.-H. Löcherer, and H. Müller. *Moeller Grundlagen der Elektrotechnik*. Vieweg+Teubner, 21st edition, 2008.
- [77] P. Miles, W. Westphal, and A. Hippel. Dielectric spectroscopy of ferromagnetic semiconductors. *Reviews of Modern Physics*, 29(3):279–307, 1957.
- [78] E. Verwey and P. Haayman. Electronic conductivity and transition point of magnetite (Fe_3O_4). *Physica*, 8(9):979–987, 1941.
- [79] J. Grehn and J. Krause. *Metzler Physik*. Schroedel, 4th edition, 2007.
- [80] S. M. Ross. *Statistik für Ingenieure und Naturwissenschaftler*. Spektrum Akademischer Verlag, 2006.
- [81] Technische Vereinigung der Großkraftwerksbetreiber e.V. *VGB-R 513: Innere Reinigung von Wasserrohr-Dampferzeugeranlagen und Rohrleitungen.*, 2006.
- [82] Deutsches Institut für Normung e. V. DIN 10305-1: Steel tubes for precision applications - Technical delivery conditions - Part 1: Seamless cold drawn tubes., 06/2010.
- [83] Technische Vereinigung der Großkraftwerksbetreiber e.V. *VGB-R 450: Richtlinien für die Speisewasser-, Kesselwasser- und Dampfqualität für Kraftwerke / Industriekraftwerke.*, 2006.
- [84] A. Banweg, D. G. Wiltsey, and B. N. Nimry. Carbohydrazide - A Hydrazine Replacement: 10 Years of Utility Experience. *Institute of Power Engineers*, pages 4–7, 2005.
- [85] U. Hansen. Dampferzeugeranlagen. Vorlesungsskript, 2008.
- [86] H. Topp, D. Steinbrecht, W. Hater, and A. de Bache. The Influence of Film-Forming Amines on Heat Transfer during Saturated Pool Boiling. *PowerPlant Chemistry*, (12):388–395, 7/2010.

Appendix

A Computational determination of the heat transmission coefficient

A.1 Iteration procedure and convergence

The procedure of determination of the heat transmission coefficient k uses the heat conduction according to Fourier and yields the following equation:

$$\vartheta_i - \vartheta_o = \frac{\dot{q}_A}{\lambda} \cdot \frac{2r_a}{r_a^2 - r_i^2} \cdot \frac{r_i^2}{4} \left[\left(\frac{r_a}{r_i} \right)^2 - 2 \ln \frac{r_a}{r_i} - 1 \right] \quad (\text{A.1})$$

After subsuming the geometrical terms, the fundamental equations are:

$$\vartheta_i - \vartheta_o = \frac{\dot{q}_A}{\lambda} \cdot K_R \quad (\text{A.2})$$

and:

$$\dot{q} = k \cdot (\vartheta_o - \vartheta_s) \quad (\text{A.3})$$

Solving for k and implementing the reformed equation A.2 yields:

$$k = \frac{\dot{q}}{\left[\vartheta_i - \frac{\dot{q}}{\lambda} \cdot K_R \right] - \vartheta_s} \quad (\text{A.4})$$

Since the heat flux density \dot{q} as well as the heat conductivity λ are functions of the mean tube temperature ϑ_m , an iterative process is used solving for ϑ_o .

Therefore, ϑ_o is guessed in the first step:

$$\vartheta_{guess} = random \quad (\text{A.5})$$

The mean wall temperature is calculated from the inner tube temperature ϑ_i and ϑ_{guess} by:

$$\vartheta_m = \frac{\vartheta_i - \vartheta_{guess}}{\ln \left(\frac{\vartheta_i}{\vartheta_{guess}} \right)} \quad (\text{A.6})$$

The thermal conductivity λ and the specific electrical resistance ξ are also evaluated by using the mentioned guessed temperature via a polynomial correlation. Afterwards their

values are used to determine the heat flux density \dot{q} by implementing the rating equation for electrical resistances:

$$\dot{q} = \frac{\xi(\vartheta_m) \cdot \frac{l}{A_{cross}} \cdot I^2}{A_s} \quad (\text{A.7})$$

Thereby a new outer tube temperature is calculated:

$$\vartheta_o = \vartheta_i - \frac{\dot{q}(\vartheta_m)}{\lambda(\vartheta_m)} \cdot K_R \quad (\text{A.8})$$

with the cross-sectional area A_{cross} and the outer surface A_s of the tube.

The calculated value for ϑ_o is then compared with ϑ_{guess} in regard to an appropriate abort criterion for iteration. In this case, the criterion is

$$abs(\vartheta_o - \vartheta_{guess}) \leq 10^{-9} \text{ K}$$

providing sufficient accuracy.

If this condition is satisfied, the guessed value of ϑ_o represents the desired outer tube temperature. However, since the first ϑ_{guess} is rather unlikely to be sufficiently close to ϑ_o from equation A.8, this loop has to be run repeatedly until the condition is satisfied. If so, this ϑ_o from the final iteration is used to calculate the heat transmission coefficient in equation A.3.

Following schematic A.1 depicts the iterative process for the determination of ϑ_o and k , respectively.

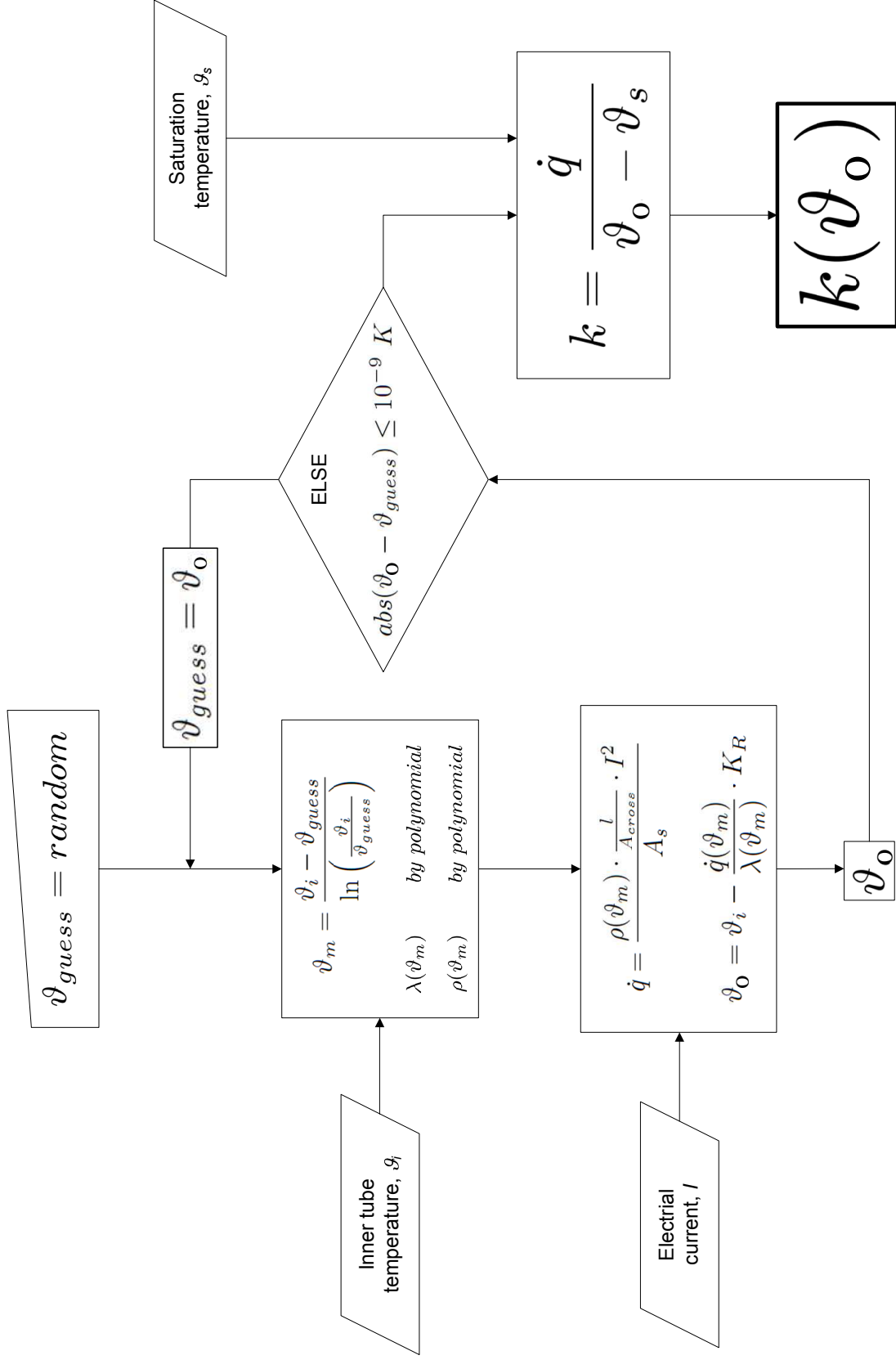


Figure A.1: Schematic of the iteration loop

To demonstrate the applicability and furthermore the reproducibility of the presented algorithm, a random example has been investigated regarding the influence of the initially guessed outer temperature ϑ_{guess} . Considering the fourth measurement at A212 after 42 h of magnetite growth the following physical data have been acquired (see table below). The outer tube temperature was found with $\vartheta_o = 214.26 \text{ }^\circ\text{C}$ using the algorithm for

Measured quantity	Value	Dimension
ϑ_i	221.48	$^\circ\text{C}$
ϑ_s	198.32	$^\circ\text{C}$
I	837.66	A

two different starting values of $\vartheta_{guess} = (100, 220) \text{ }^\circ\text{C}$ (see figure A.2). The described procedure shows good reproducibility as well as stability even after considerably exceeding the threshold (for an initial temperature of $\vartheta_{guess} = 100 \text{ }^\circ\text{C}$). Iteration is demonstrated as an analogous function $\vartheta_o(\textit{iteration step})$ for visualisation matters only.

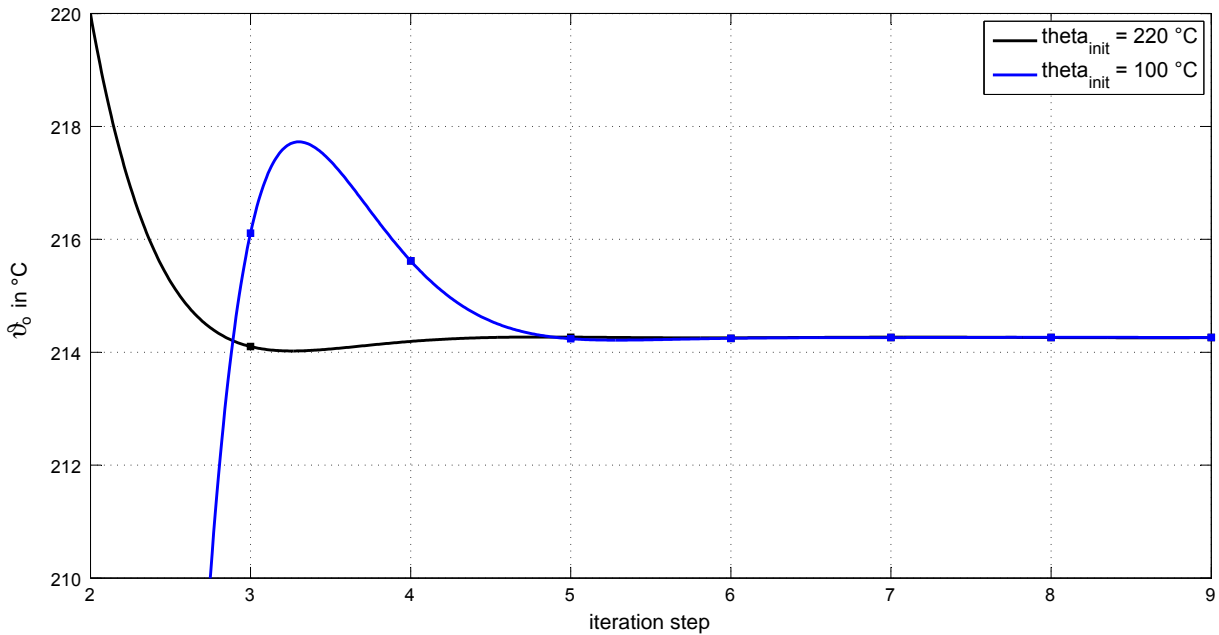


Figure A.2: Influence of the initial ϑ_{guess} on the reproducibility of $\vartheta_o = 214.26 \text{ }^\circ\text{C}$ (depicted as an analogous function).

A.2 Evaluation routine (Matlab-code)

```

function Struktur_Cases=A1_newMethod(name,number,tau)

% Syntax: Struktur_Cases=A1_newMethod(name,number,tau)
% Evaluates the measured data from the .TAB-file 'name', the consecutive
% tube number A'xxx' and the treatment period 'tau'
% Result: diagram k(q), data-structure

% Imports the data set from the respective .TAB-file into vector 'C'
% starting with 3rd row
IMP=importdata(name, '\t', 2);
C=IMP.data;
clear IMP;

% Case distinction with respect to the pressure stage (|Ts(i)-Ts(j)| >=10 K)
Liste_Pressure=TestCase(C,5,10);

% Case distinction of the heat flux density (electric current): Structure
% Assumption: maximum number of 20 operation points / pressure!
Struktur_Cases(20,length(Liste_Pressure))=struct;
for z=1:length(Liste_Pressure)
    Liste_Cases(z).Case=findNewTestCase(Liste_Pressure(z).Case,1,10);
end

% Assignment of the pressure discrete data into the structure
L=size(Liste_Cases);
Laenge=L(1,2);
for n=1:Laenge
    for x=1:length(Liste_Cases(1,n).Case)
        Structure_Cases(x,n).Case=Liste_Cases(1,n).Case(1,x).Case;
    end
end

% Averaging and correction (calibration)
for z=1:length(Liste_Pressure)
    for j=1:GetHeatFluxes(Structure_Cases(:,z))
        Structure_Cases(j,z).Mean=calcMean(Structure_Cases(j,z).Case,[1 2 5]);
        Structure_Cases(j,z).Mean_corr=mean_corr(Structure_Cases(j,z).Mean,
        [1 2 3],[-6 -.8 0]);
    end
end

% Creation of an empty active diagram of double-log scale
figure;
hold;
propertyeditor('on');
set(gca, 'xscale', 'log');
set(gca, 'yscale', 'log');
grid on;

```

```

% Headline generation and formatting
tmp='Boiling conditions for A';
tmp2=' at p_s(abs) = (2, 5, 10, 15) bar after \tau = ';
tmp3=' h';
tmp4=[tmp number tmp2 tau tmp3];
title(tmp4, 'FontSize',16);
xlabel('heat flux density [W/m^2]', 'FontSize',14);
ylabel('heat transmission coefficient [W/(m^2K)]', 'FontSize',14);
box ON;

```

```

% Iteration loop
for z=1:length(List_Pressure) % gets the structures length
    for j=1:GetHeatFluxes(Structure_Cases(:,z))
        TRa_init=190; % guessed initial value of the outer tube temp.
        Ts=abs(Structure_Cases(j,z).Mean_corr(3)); % saturation temp.
        TR=abs(Structure_Cases(j,z).Mean_corr(2)); % inner tube temp.
        I=abs(Structure_Cases(j,z).Mean_corr(1)); % electric current

        % executing the actual loop
        [alpha,q_dot,TRa,TRm]=it_loop(Ts,TR,I,TRa_init);
        a=alpha(1,end); % heat transfer /transmission coefficient
        q=q_dot(1,end); % heat flux density
        T_W=TRa(1,end); % outer tube wall temp.
        TRm=TRm(1,end); % mean tube wall temp.

        % Assignment of the determined values into the result-structure
        Structure_Cases(j,z).alpha=a;
        Structure_Cases(j,z).WSD=q;
        Structure_Cases(j,z).TRa=T_W;
        Structure_Cases(j,z).TRm=TRm;
        vector_q(z,j)=Structure_Cases(j,z).WSD;
        vector_a(z,j)=Structure_Cases(j,z).alpha;
    end

    % Scatter plot: o-marker of 30 pixel^2 area
    scatter(vector_q(z,:),vector_a(z,:),30);
end

```

```

function List_Pressure=TestCase(matrix,column,difference)

```

```

% Syntax: Liste_Pressure=TestCase(matrix,column,difference)
% Divides the data into distinct pressure stages contained in 'matrix'
% Distinction after the respective 'column' (saturation temperature) and
% 'difference'

k=1;
z=1;
for i=2:length(matrix(:,column))
    if abs(matrix(i,column)-matrix(i-1,column))>difference
        List_Pressure(k).Case=matrix(z:i-1,2:7);
        k=k+1;
        z=i;
    end
end
List_Pressure(k).Case=matrix(z:i-1,2:7); % generates structure 'List_Pressure.Case'
% containing data measured at the distinct saturation pressure

```

```

function List_Cases=findNewTestCase(matrix,column,difference)

% List_Cases=findNewTestCase(matrix,column,difference)
% Distinguishes between different heat flux densities/currents in
% the maxtrix column by criterion 'difference'

k=1;
z=1;
for i=2:length(matrix(:,column))
    if abs(matrix(i,column)-matrix(i-1,column))>difference
        List_Cases(k).Case=matrix(z:i-1,1:6);
        k=k+1;
        z=i;
    end
end
List_Cases(k).Case=matrix(z:i-1,1:6);

```

```

function NumberHeatFluxes=GetHeatFluxes(PressureMeasurement)

NumberHeatFluxes=0;
for j=1:length(PressureMeasurement)
    if ~(isempty(PressureMeasurement(j).Case))
        NumberHeatFluxes=NumberHeatFluxes+1;
    end
end

```

```

function mean_value=calcMean(list,vector_columns)

% Syntax: mean_value=calcMean(list,vector_columns)
% Calculates the mean value of a vector column

for i= 1:length(vector_columns)
    mean_value(i)=mean(list(:,vector_columns(i)));
end

```

```

function corr_mean=mean_corr(vector, vector_columns, vector_corr)

% Syntax: corr_mean=mean_corr(vector, vector_columns, vector_corr)
% Calculates the mean value 'corr_mean' of 'vector columns' by addition
% of 'vector_corr' (calibration)

corr_mean=vector;
for i=1:length(vector_columns)
    corr_mean(i)=vector(i)+vector_corr(i);
end

```


B Photometric test calibration

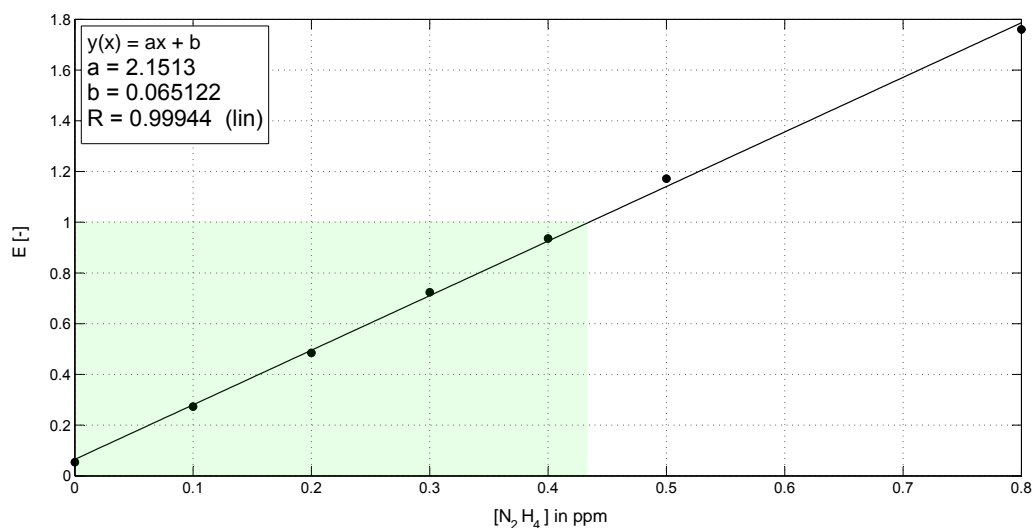


Figure B.1: Calibration curve of the photometric hydrazine test for use with the WTW PhotoLab Spektral NOVA 400 photometer.

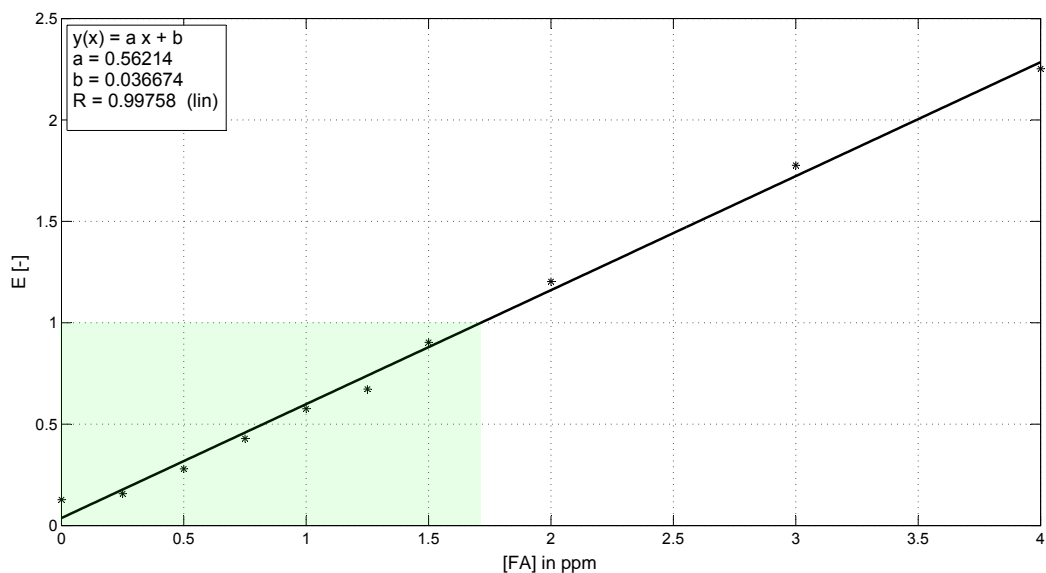


Figure B.2: Calibration curve of the photometric film-forming amine test A18 for use with the WTW PhotoLab Spektral NOVA 400 photometer.

C Nucleate boiling curves from the nucleation site investigations

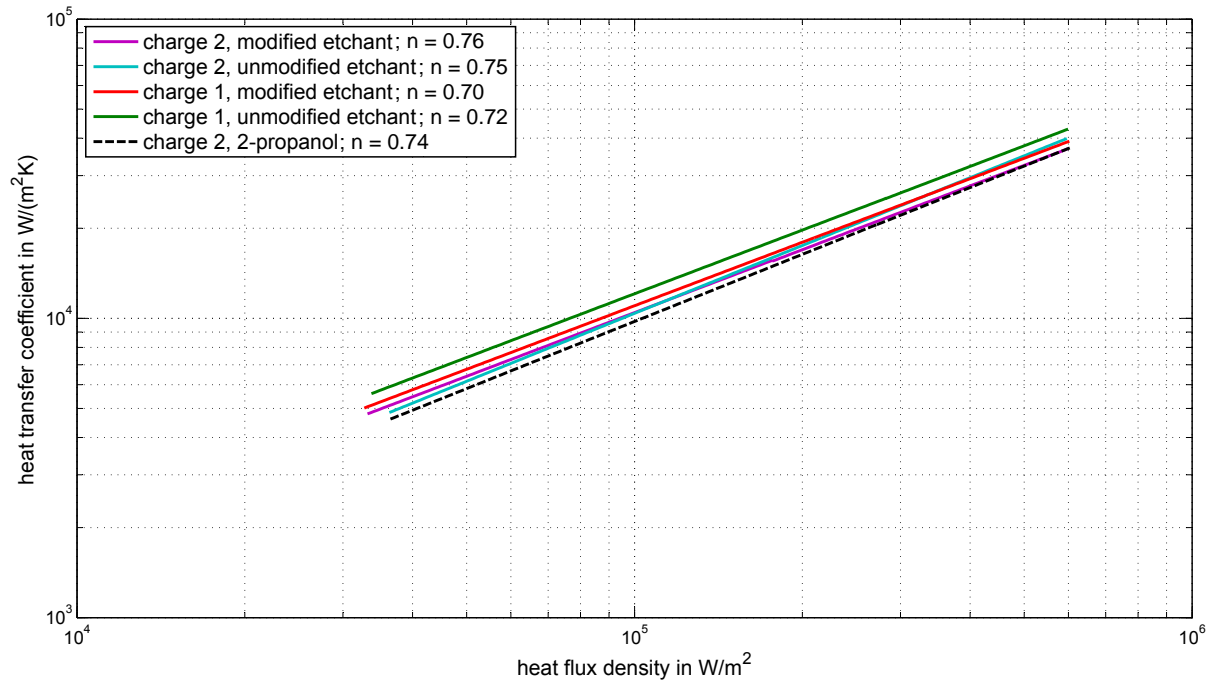


Figure C.1: Comparison of the initial heat transfer behaviour of differently pretreated tube surfaces at $p_s = 2$ bar.

C. Nucleate boiling curves from the nucleation site investigations

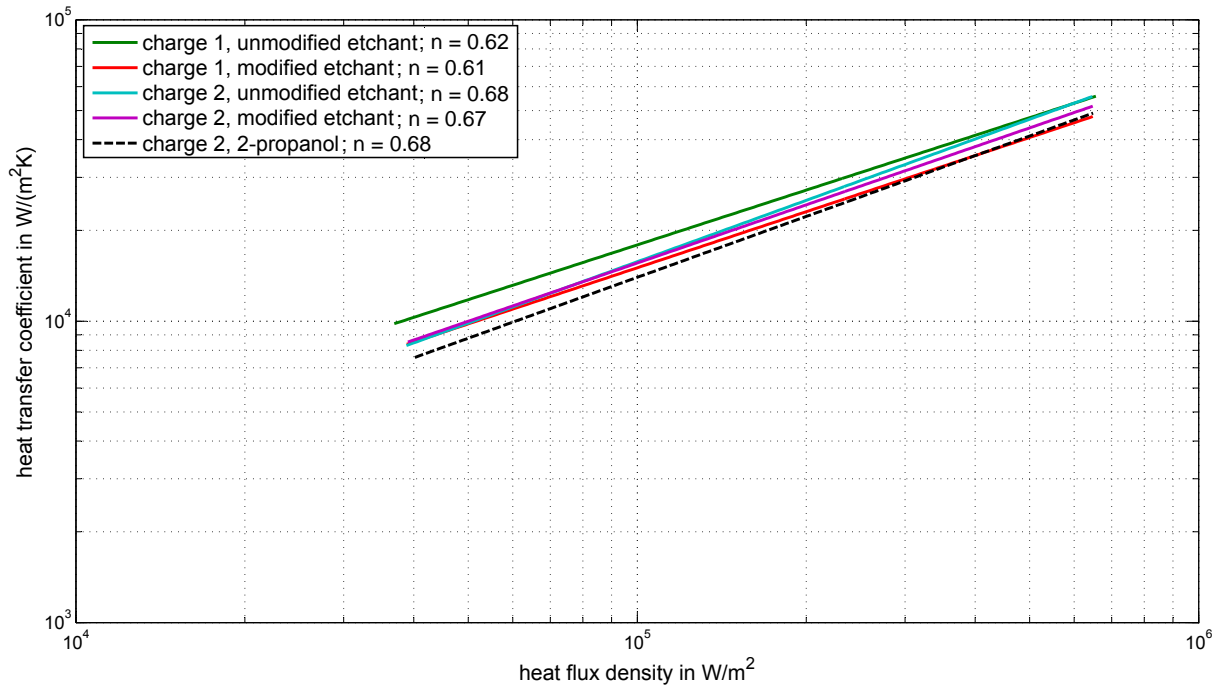


Figure C.2: Comparison of the initial heat transfer behaviour of differently pretreated tube surfaces at $p_s = 5$ bar.

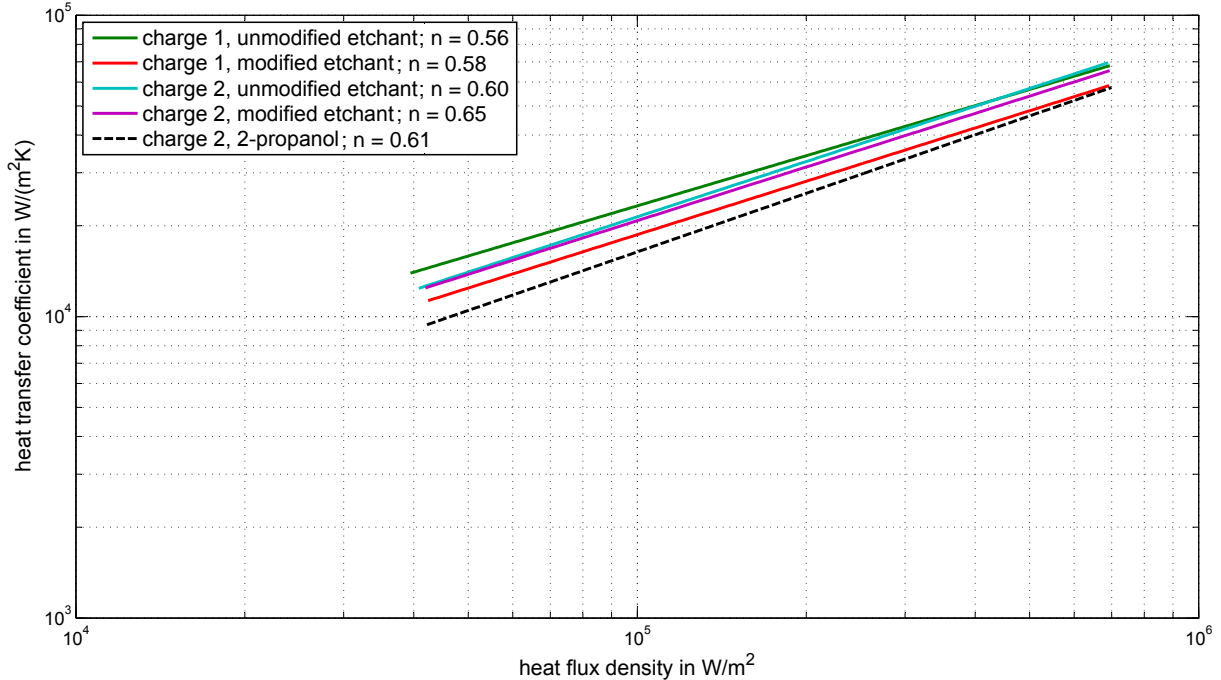


Figure C.3: Comparison of the initial heat transfer behaviour of differently pretreated tube surfaces at $p_s = 10$ bar.

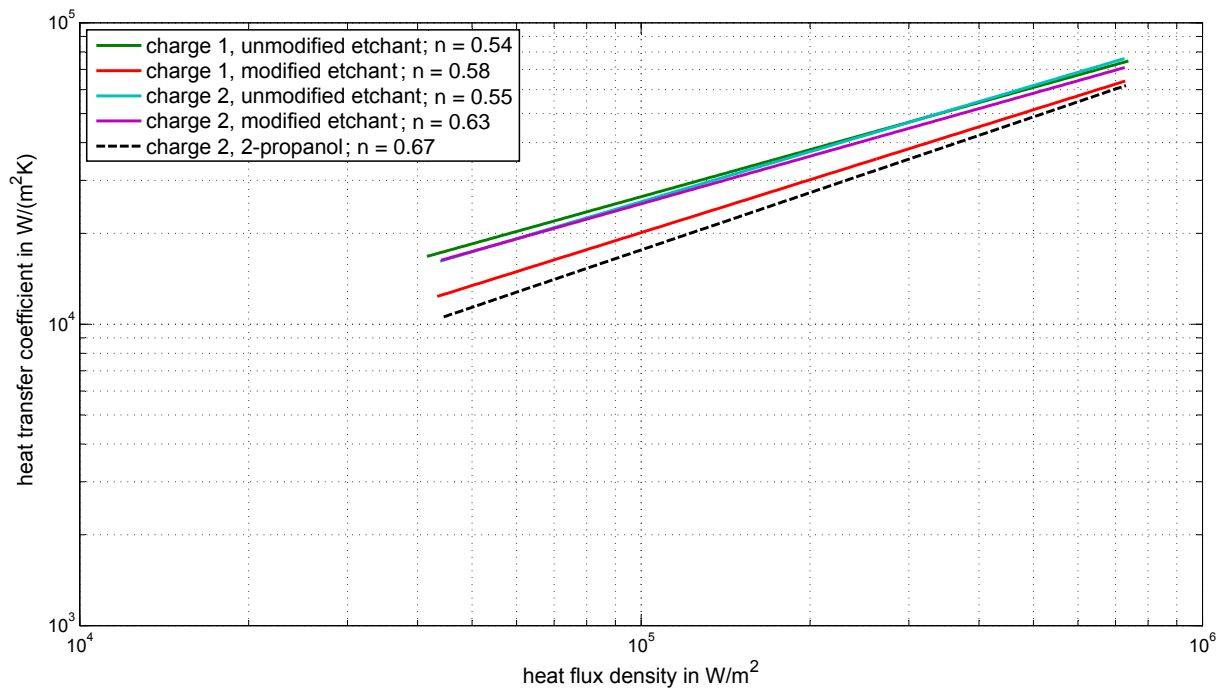


Figure C.4: Comparison of the initial heat transfer behaviour of differently pretreated tube surfaces at $p_s = 15$ bar.

D Organic all-volatile treatment

Two samples are investigated thermotechnically regarding their heat transmission behaviour at $p_s = 15 \text{ bar}$. Although the chemical parameters are complied with (see section 6.4.2), the resulting time response is not reproducible. The following picture demonstrates the development of the individual values of C_{red} during feed water treatment with DEHA and alkalisating amines at $p_s = 15 \text{ bar}$. Reduction is carried out with the mean exponent

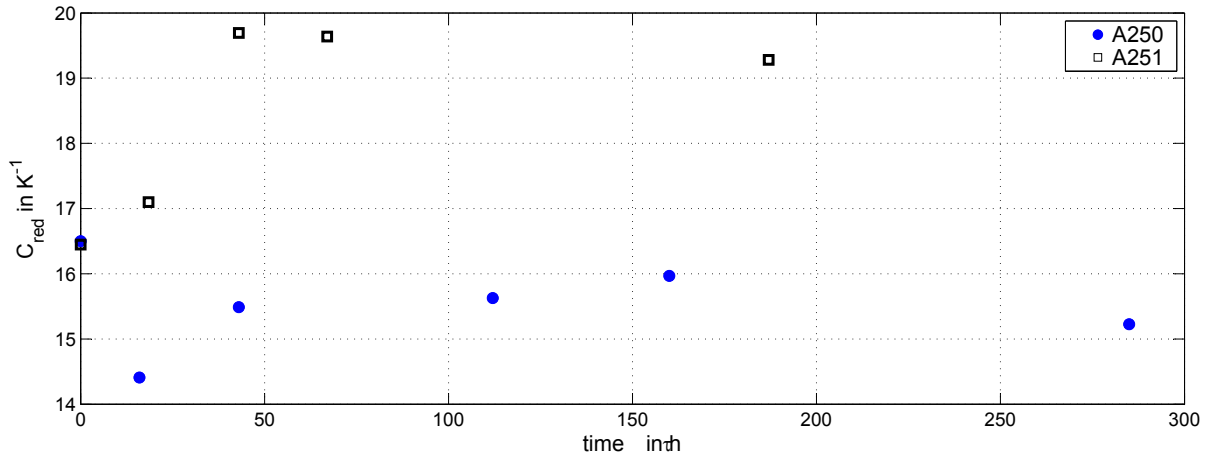


Figure D.1: *Development of C_{red} during organic AVT. Reduction is carried out with $\bar{n} = 0.61$.*

$\bar{n} = 0.61$, obtained by regression of the nucleate boiling data at $p_s = 15 \text{ bar}$ throughout the operational period, as depicted in the following figure.

The value of n remains constant during operation, although the determined heat transmission coefficients show a rather unexpected behaviour. A good reproducibility of the nucleate boiling start conditions is achieved, which is comparable to the trisodium phosphate treatment (see the following figures for more information).

Although the applied alkalisation is expected to lead to the generation of a heat transport impeding oxide layer, both samples show an untypical alternating time response. Implementation of an exponential approach is omitted. The reason for this phenomenon could not be elaborated.

Further tests have not been possible due to a limited time frame. At least three tubes with comparable trends $C_{red}(\tau)$ are demanded in order to make reliable statements on the time response of k .

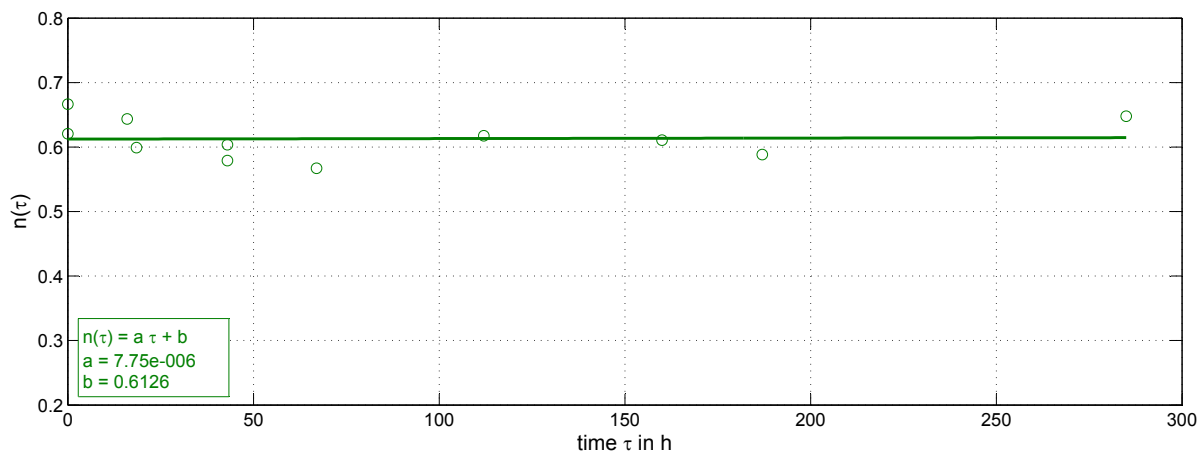


Figure D.2: Development of n during organic AVT at $p_s = 15$ bar.

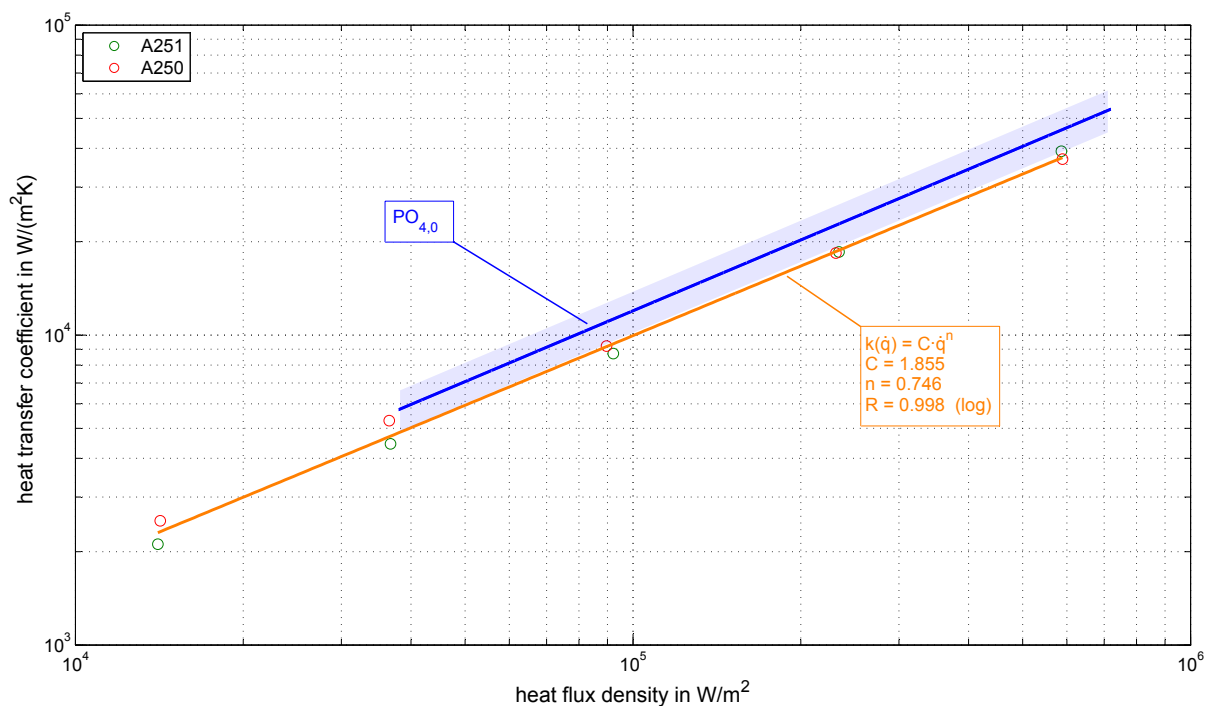


Figure D.3: Initial heat transfer coefficient during organic all-volatile treatment at $p_s = 2$ bar.

Despite lacking reproducibility of the heat time response of C_{red} , the boiling curves exponent as well as the initial heat transmission coefficient is comparable to PO_4 and $PO_4 + N_2H_4$ treatment (start of operation).

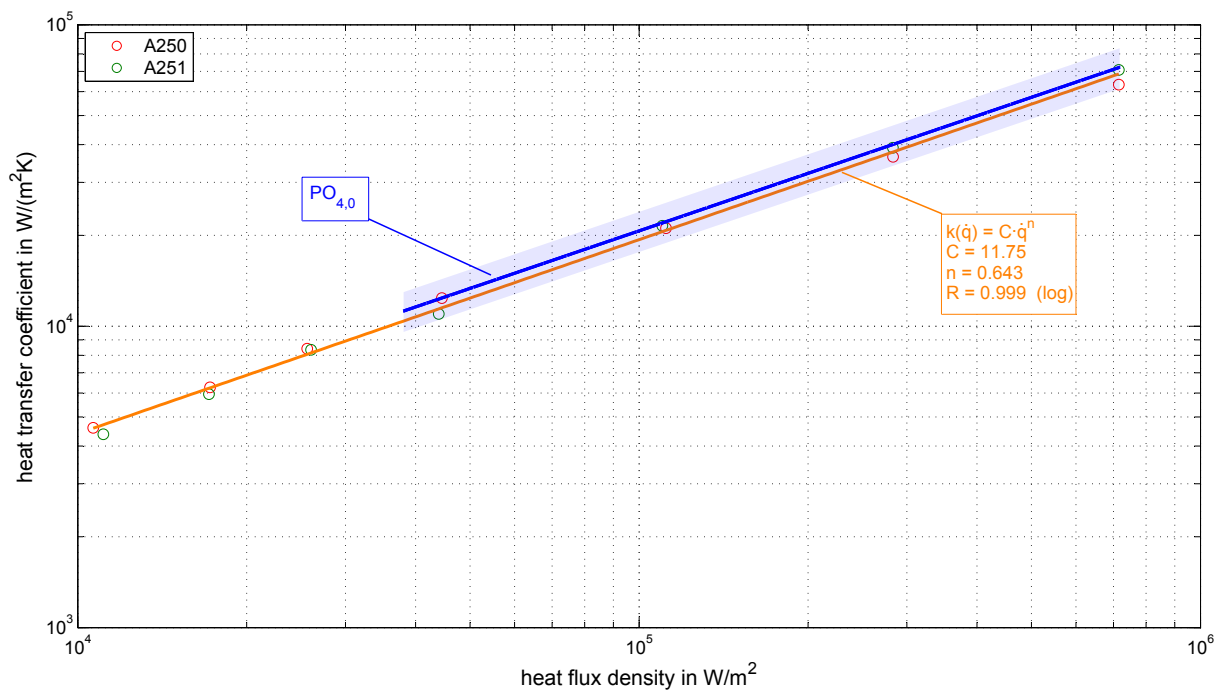
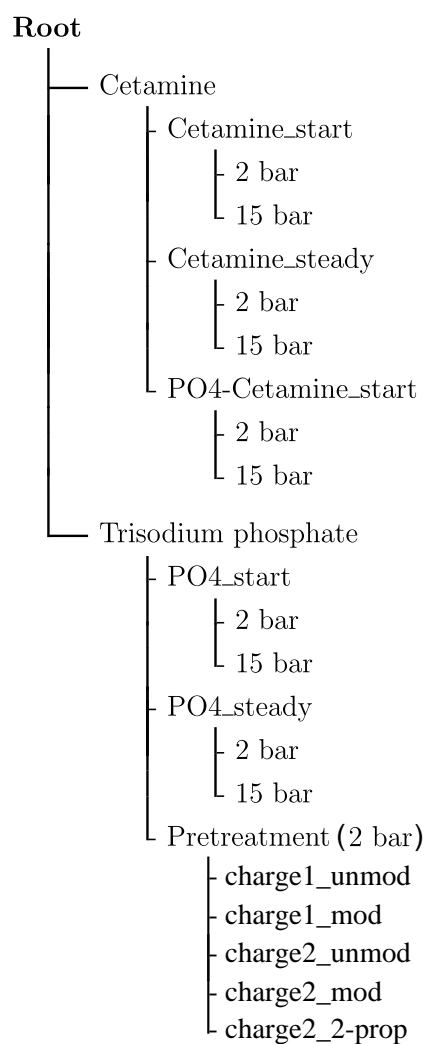


Figure D.4: Initial heat transfer during organic all-volatile treatment at $p_s = 15$ bar.

E Video recordings (Optical data carrier)

The enclosed data carrier contains video recordings, carried out to verify the effect of different pretreatments and chemical conditionings on the active nucleation site density using the described setup. All files are compressed with an MPEG-2 codec at 720 x 576 pixels. Please make sure, the right codec is installed before playback.

Every file is named by the value of amperage that was applied for heating. The following tree of directories helps finding the desired files:



For an overview, the following pages contain freeze-frames obtained from the video recordings at $p_s = 2 \text{ bar}$, $\dot{q} \approx 40 \cdot 10^3 \text{ W/m}^2$ at the same treatment moment.

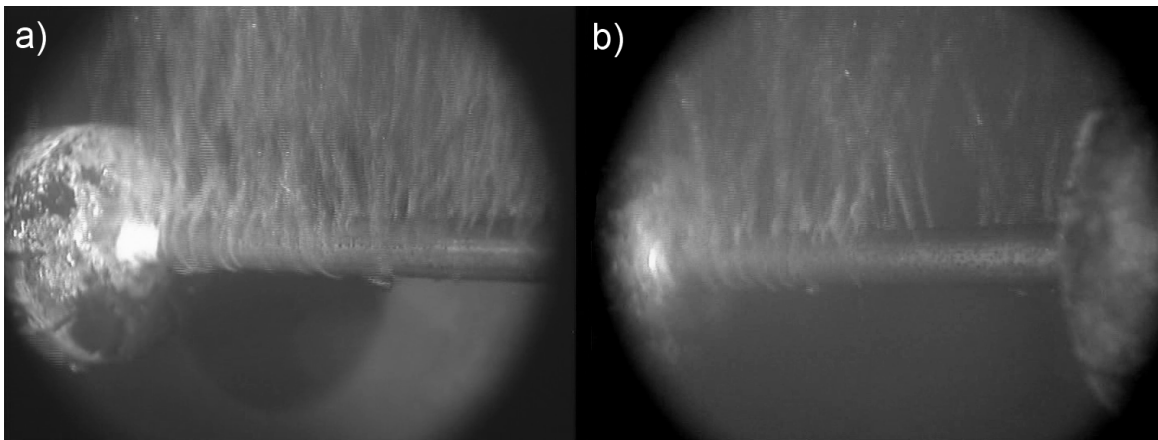


Figure E.1: *Cetamine₀* operation (a) compared to *PO_{4,0}* operation (b) at $p_s = 2 \text{ bar}$ and $\dot{q} \approx 40 \cdot 10^3 \text{ W/m}^2$.

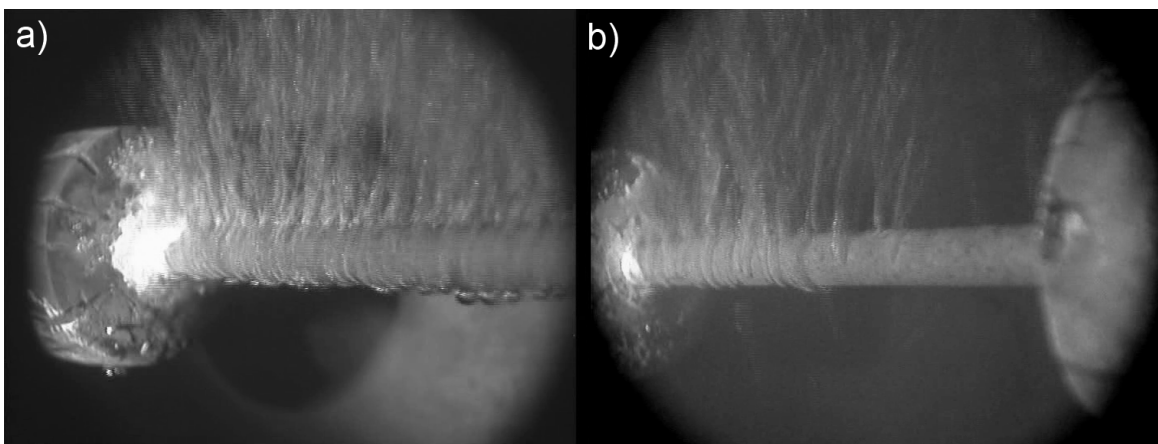


Figure E.2: *Cetamine_∞* operation (a) compared to *PO_{4,∞}* operation (b) at $p_s = 2 \text{ bar}$ and $\dot{q} \approx 40 \cdot 10^3 \text{ W/m}^2$.

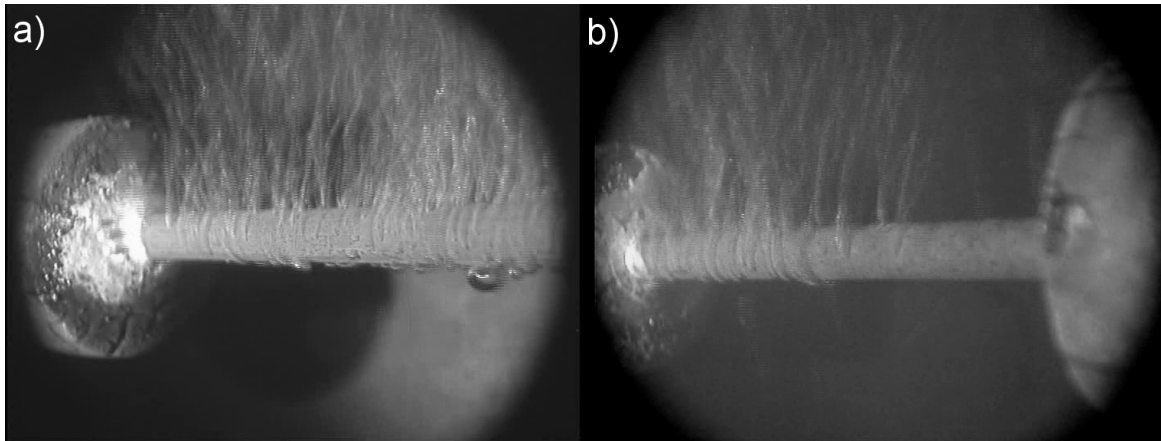


Figure E.3: $PO_{4,\infty} \rightarrow Cetamine_0$ operation (a) compared to $PO_{4,\infty}$ operation (b) at $p_s = 2 \text{ bar}$ and $\dot{q} \approx 40 \cdot 10^3 \text{ W/m}^2$.

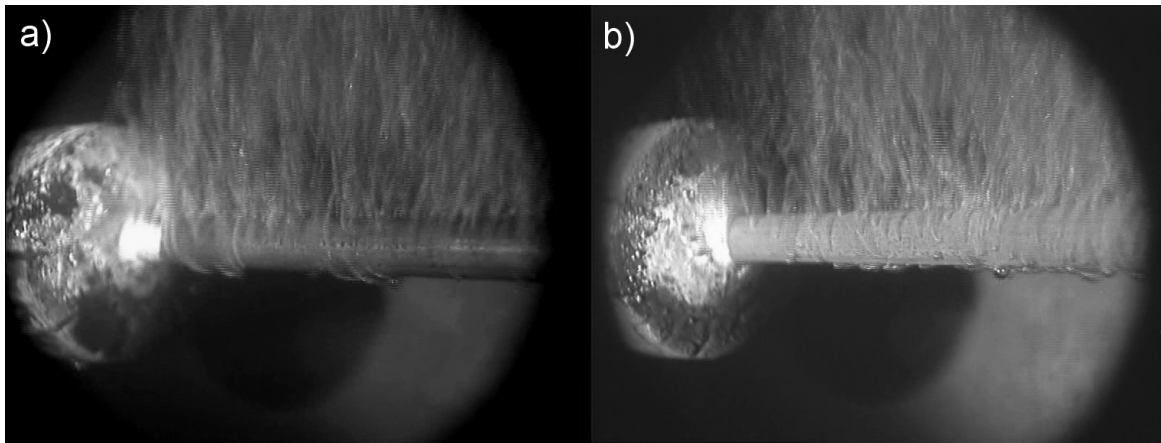


Figure E.4: $Cetamine_0$ operation (a) compared to $PO_{4,\infty} \rightarrow Cetamine_0$ operation (b) at $p_s = 2 \text{ bar}$ and $\dot{q} \approx 40 \cdot 10^3 \text{ W/m}^2$.

F Reduction of the heat transmission coefficients during Cetamine conditioning

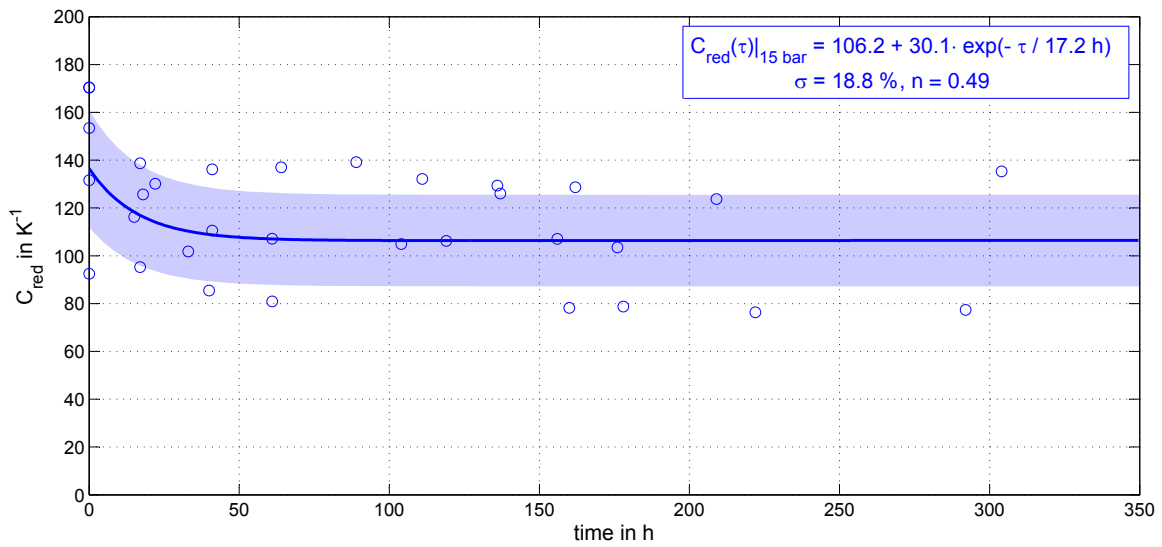


Figure F.1: Time response of C_{red} at $p_s = 15$ bar under Cetamine treatment with $n = 0.49$ for re-calculation of the expected k -values.

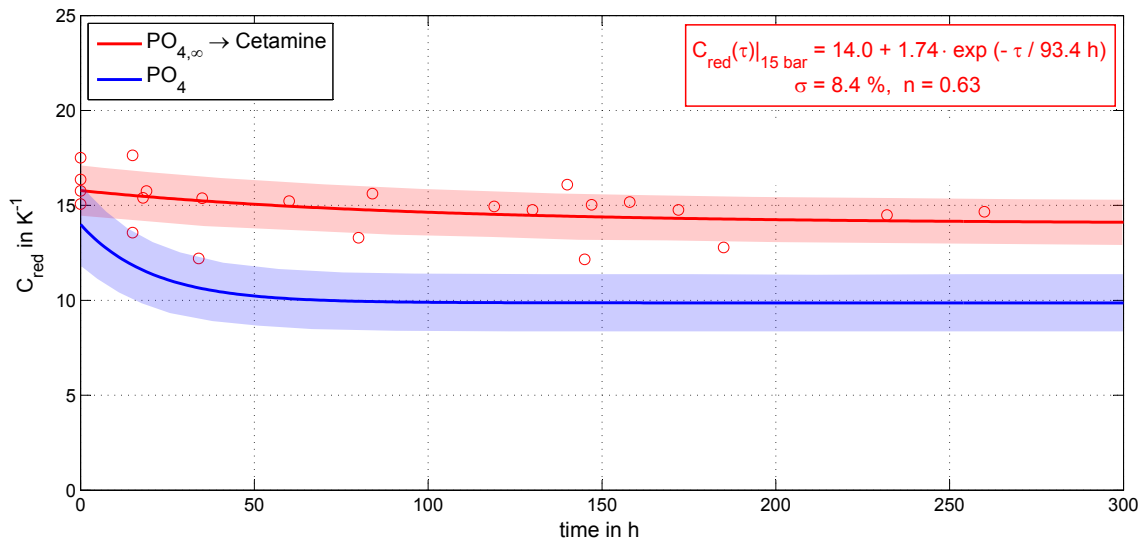


Figure F.2: Time response of C_{red} at $p_s = 15$ bar under $PO_{4,\infty} \rightarrow$ Cetamine treatment with $n = 0.63$ for comparison to the pure PO_4 treatment.

G Selected microsection/CLSM pictures

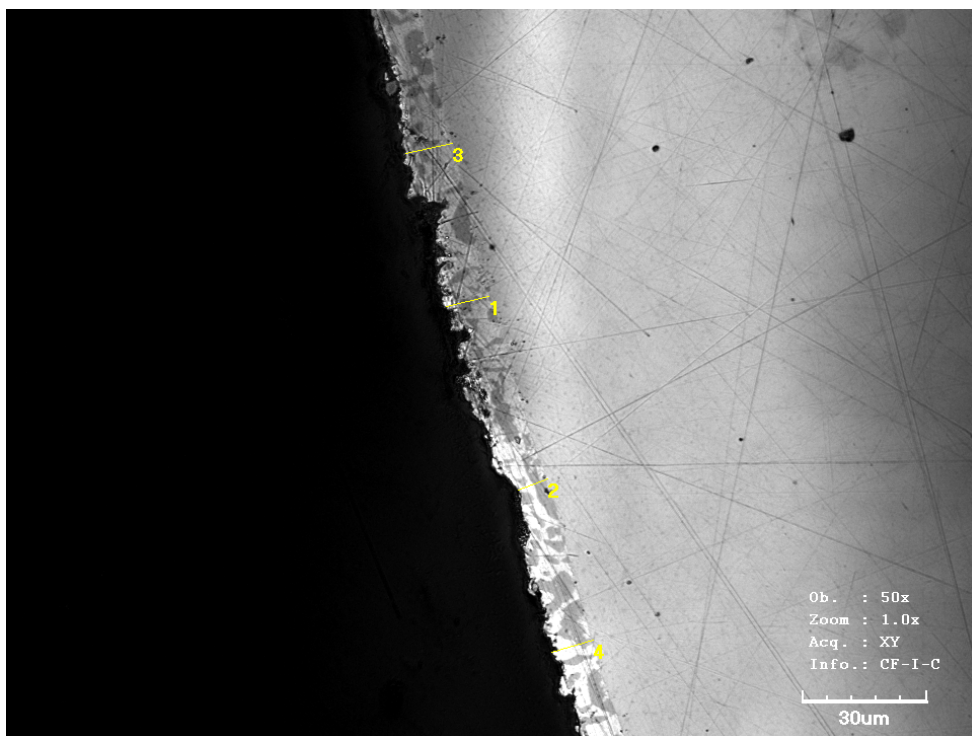
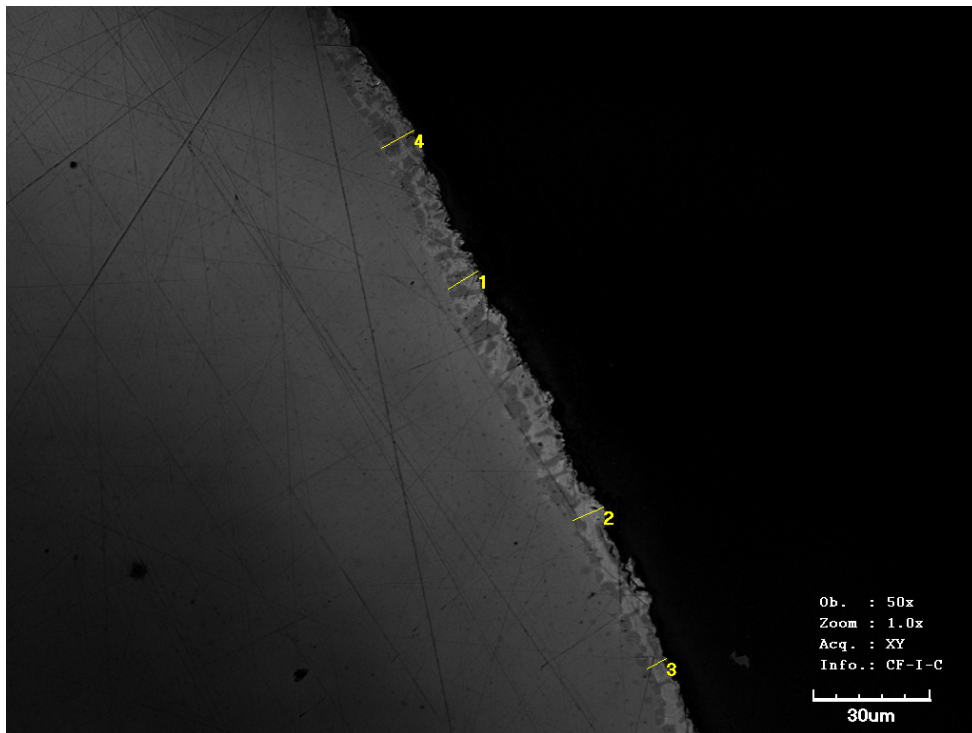


Figure G.1: *CLSM view of two exemplary locations of the oxide layer on a polished PO_4 treated tube sample.*

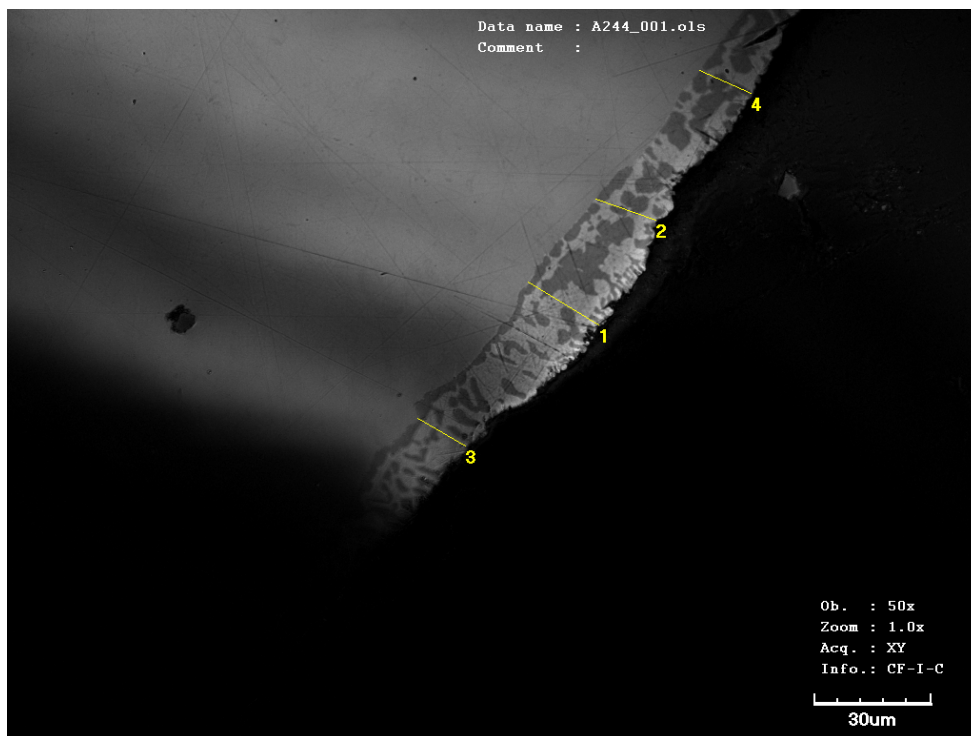
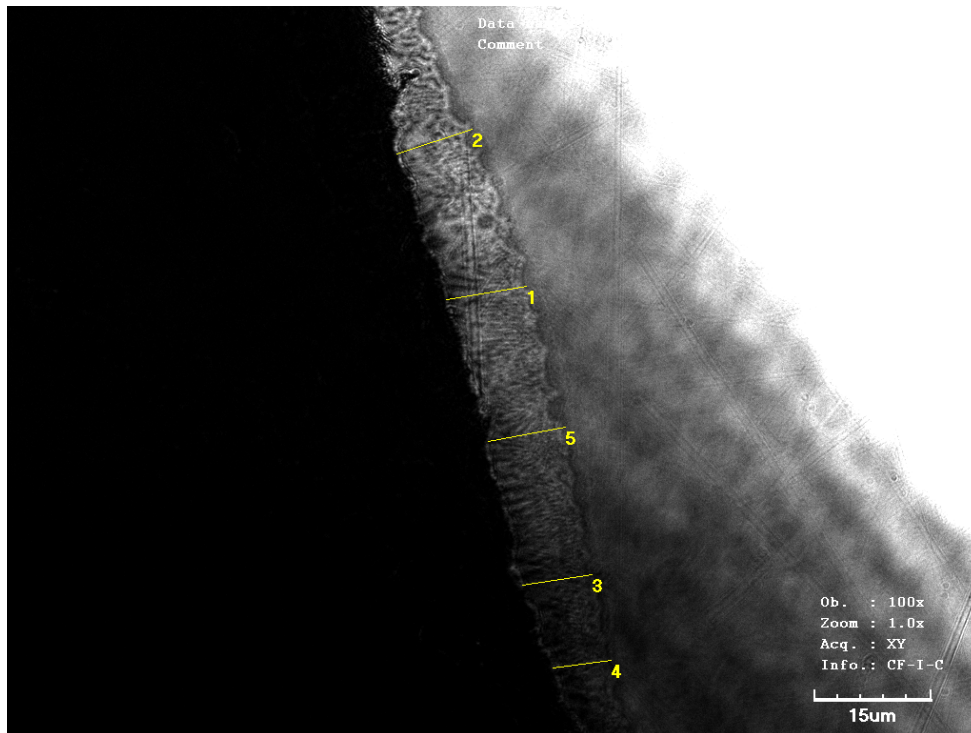


Figure G.2: *CLSM view of two exemplary locations of the oxide layer on a polished $PO_4 + N_2H_4$ treated tube sample.*

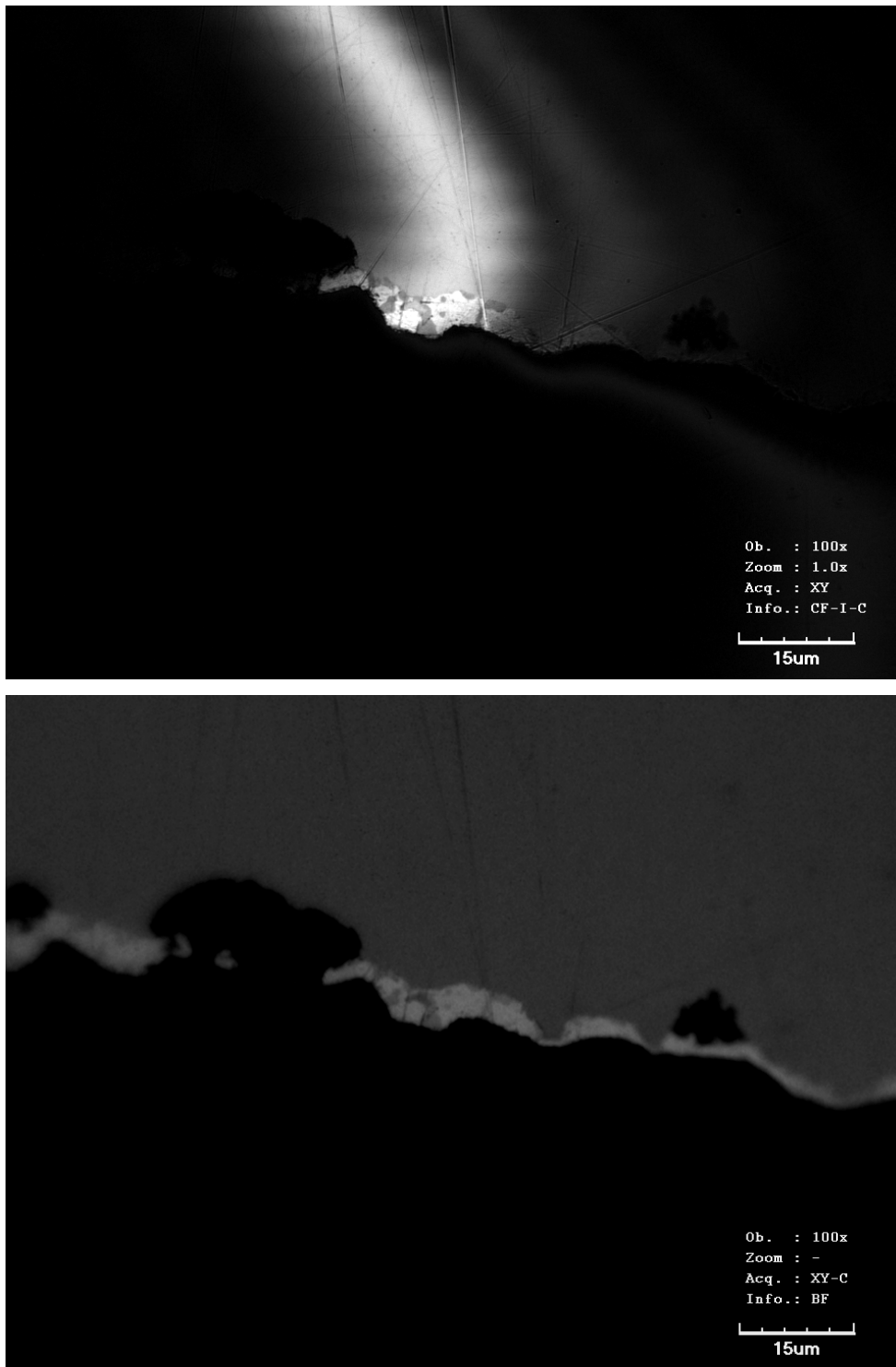


Figure G.3: *CLSM view of two exemplary locations of the oxide layer on a polished Cetamine treated tube sample.*

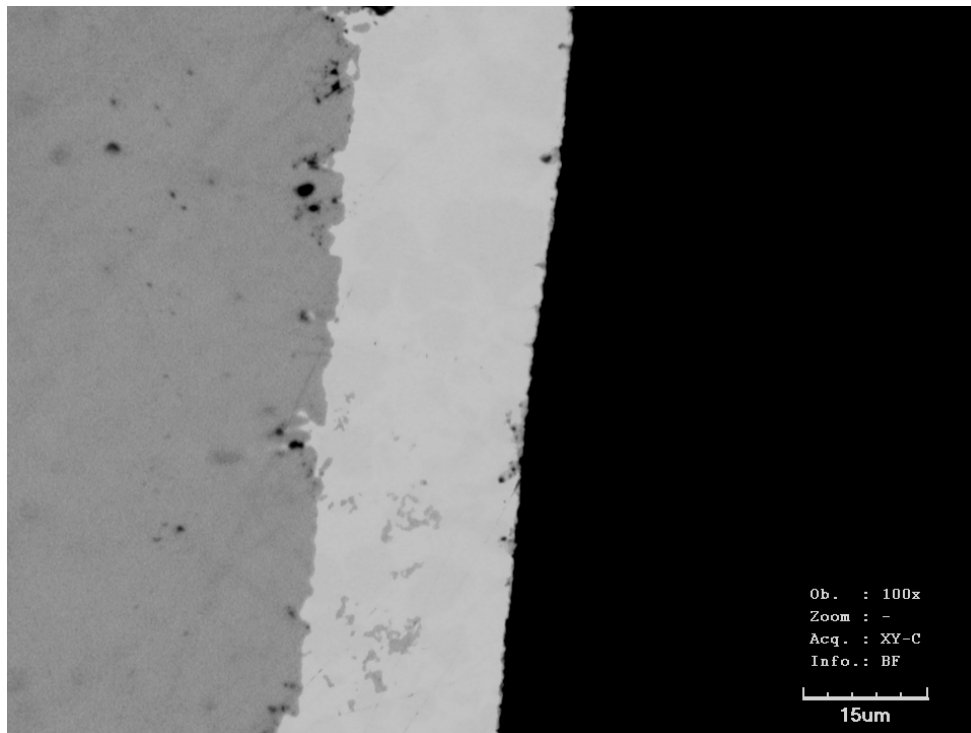
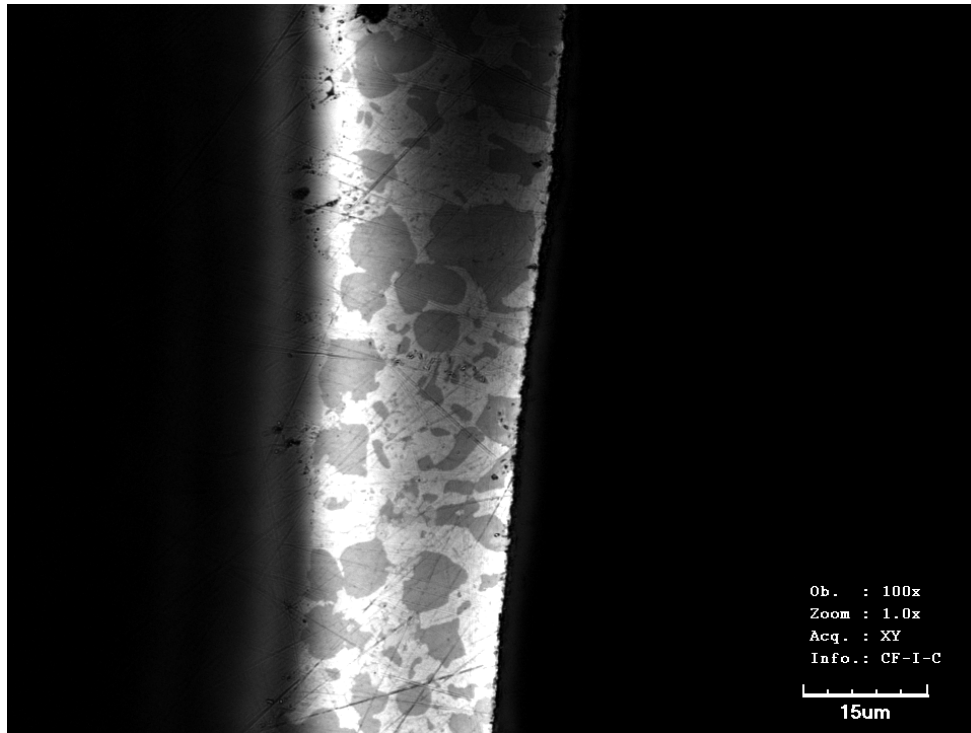


Figure G.4: *CLSM view of two exemplary locations of the oxide layer on a polished $PO_{4,\infty} \rightarrow$ Cetamine treated tube sample.*

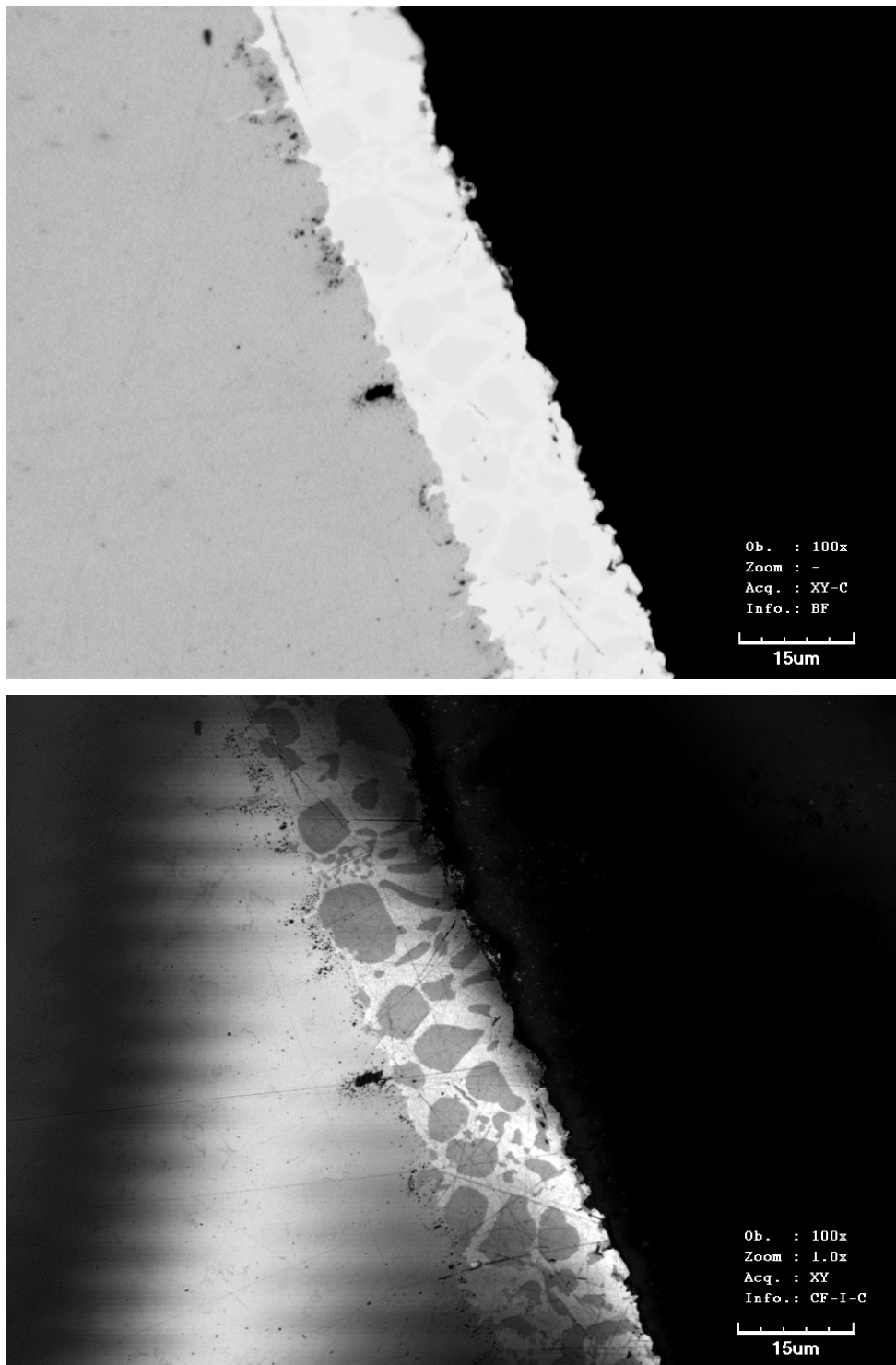


Figure G.5: *CLSM view of two exemplary locations of the oxide layer on a polished $(PO_4 + N_2H_4)_\infty \rightarrow$ Cetamine treated tube sample.*

H Changeover from phosphate and hydrazine treatment to FA

The reduction of the obtained $k(\dot{q})$ pairs requires a closer look at the exponent during treatment. As for the $PO_{4,\infty} \rightarrow Cetamine$ operation, a dispersing effect by the film-forming amine must be expected. However, as the surface roughness is already lower for the hydrazine and phosphate treated samples than for the pure phosphate treated specimens, a less intense modification might result. The following figure H.1 shows the development of n during operation. The data of $n(\tau)$ shows a considerable spreading width. An exponential approach is used for regression, following the exponential decay function used for C_{red} , as the surface processes which influence the decline of C_{red} are assumed to cause the development of n . There is a noticeable increasing trend, supporting the

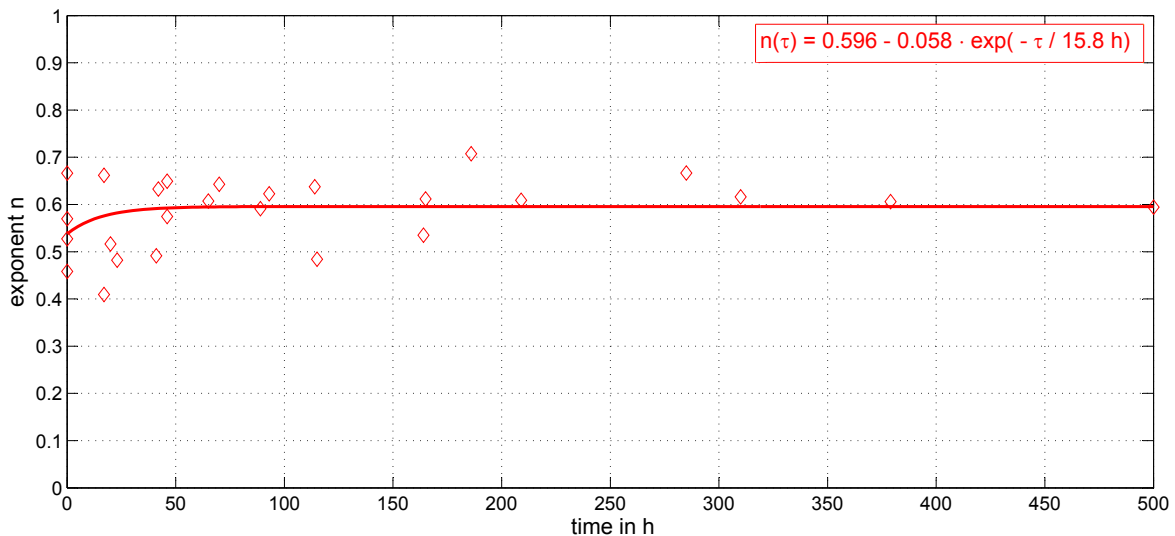


Figure H.1: *Development of $n(\tau)$ at $p_s = 15$ bar under $(PO_4 + N_2H_4)_\infty \rightarrow Cetamine$ treatment.*

made statements for the amine-treatment after generating a closed passivating layer under phosphate conditions. However, the change in n is small as compared to the $PO_{4,\infty} \rightarrow Cetamine$ conditioning. The decline in the resulting C_{red} is also smaller for using a fixed average exponent of $\bar{n} = 0.58$ as depicted in figure H.2

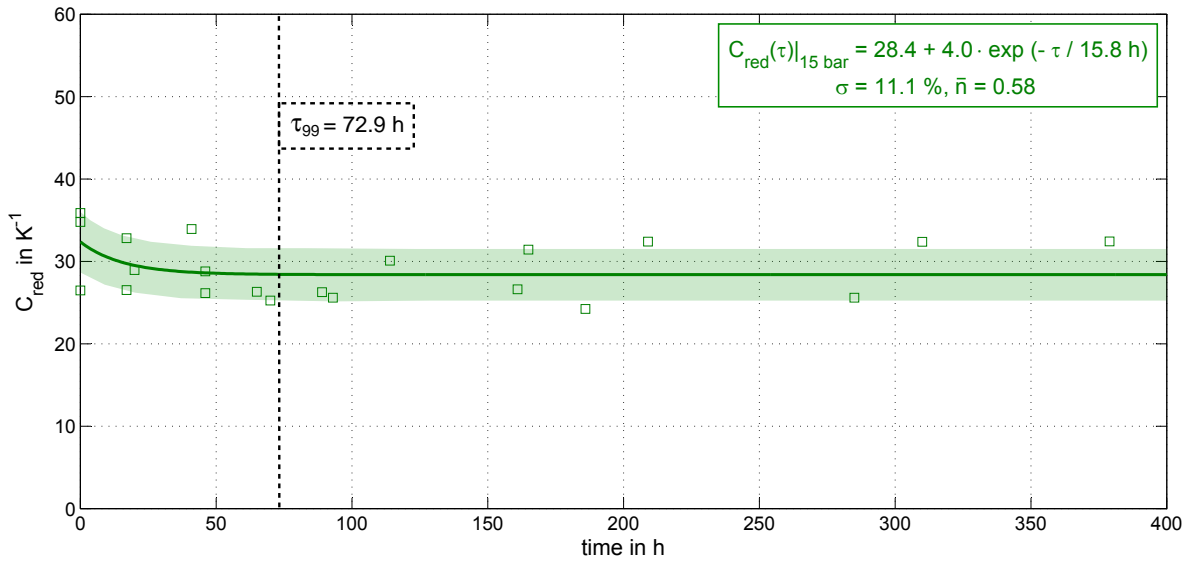


Figure H.2: Time response of C_{red} at $p_s = 15$ bar under $(PO_4 + N_2H_4)_\infty \rightarrow Cetamine$ treatment with $\bar{n} = 0.58$ for comparison to the pure PO_4 treatment.

In the following, the corresponding change in the boiling curves are depicted for the initial (figure H.3) and the steady state (figure H.4) operation at $p_s = 15$ bar compared to the $PO_4 + N_2H_4$ treatment at a steady state of k .

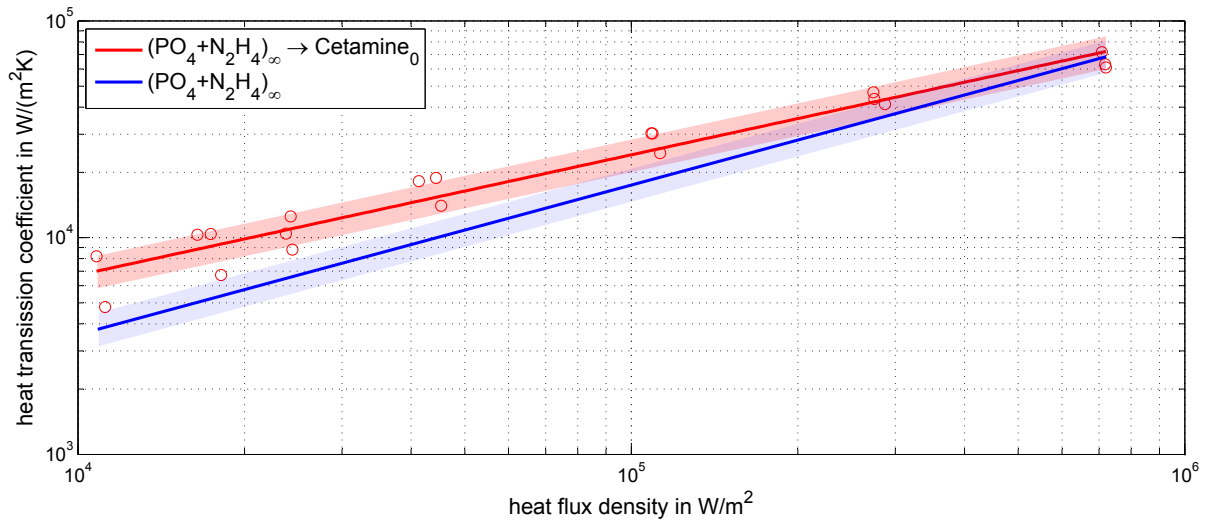


Figure H.3: Boiling curve at $p_s = 15$ bar for $(PO_4 + N_2H_4)_\infty \rightarrow Cetamine_0$ treatment compared to $(PO_4 + N_2H_4)_\infty$.

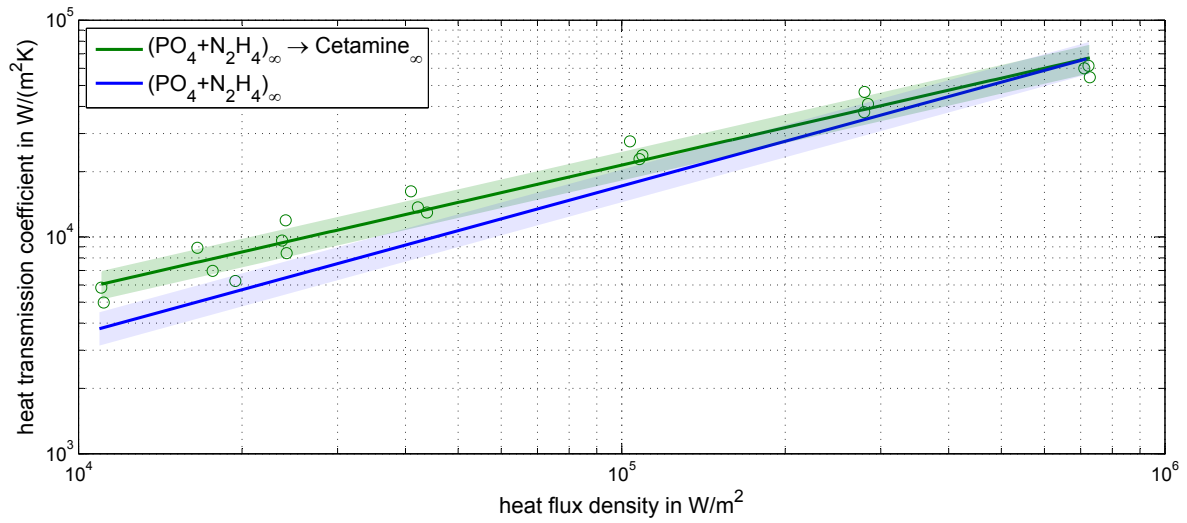


Figure H.4: Boiling curve at $p_s = 15$ bar for $(PO_4 + N_2H_4)_\infty \rightarrow Cetamine_\infty$ treatment compared to $(PO_4 + N_2H_4)_\infty$.

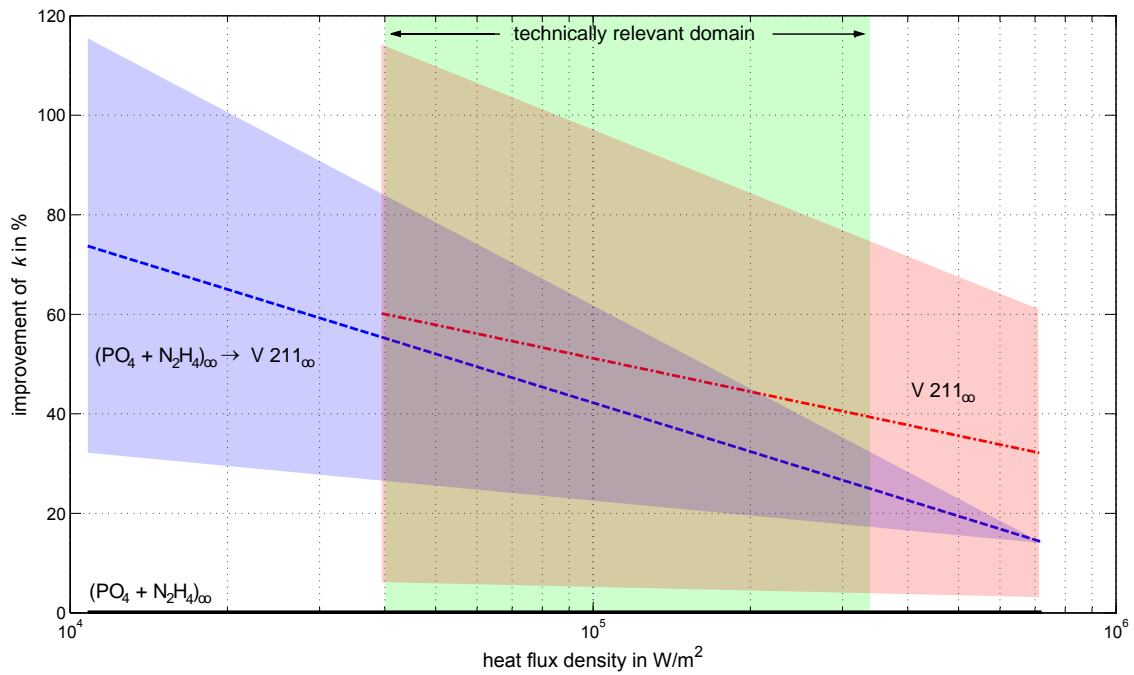


Figure H.5: Net enhancement of k during Cetamine treatment relative to the steady state of $PO_4 + N_2H_4$ conditioning at $p_s = 15$ bar.

I Further burn-out III test results

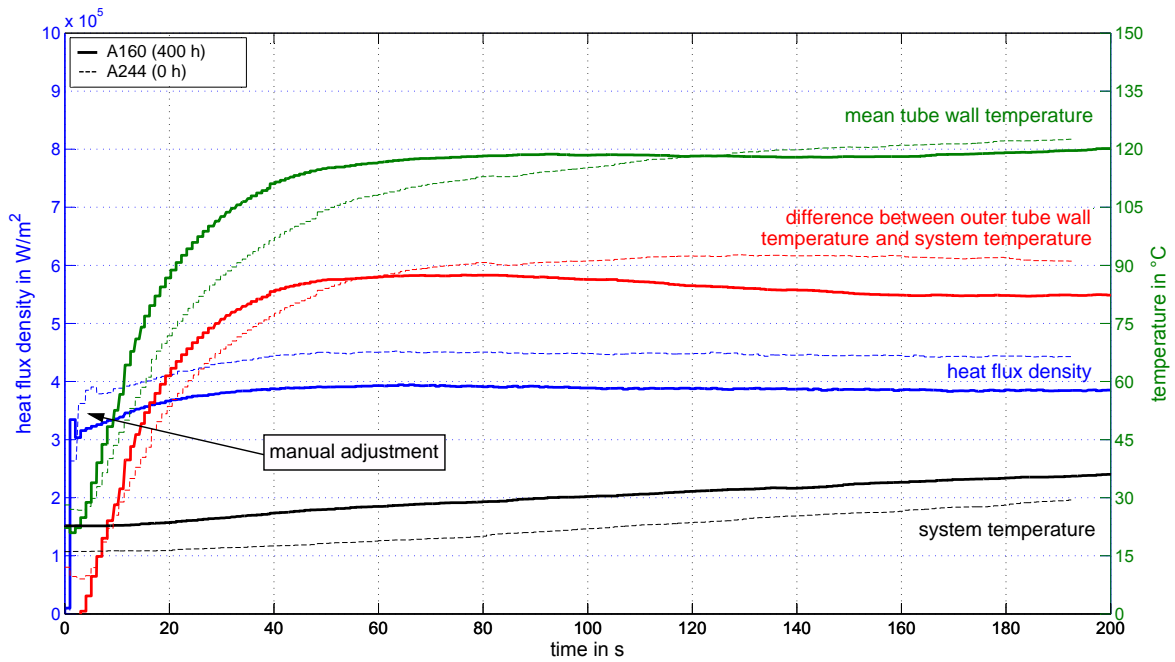


Figure I.1: Burn-out III test results for cold start-up conditions for the steady state Cetamine treated tube A160 compared to the $PO_4 + N_2H_4$ reference A244, $\dot{q} = 400 \cdot 10^3 W/m^2$ at $p_s = 2$ bar.

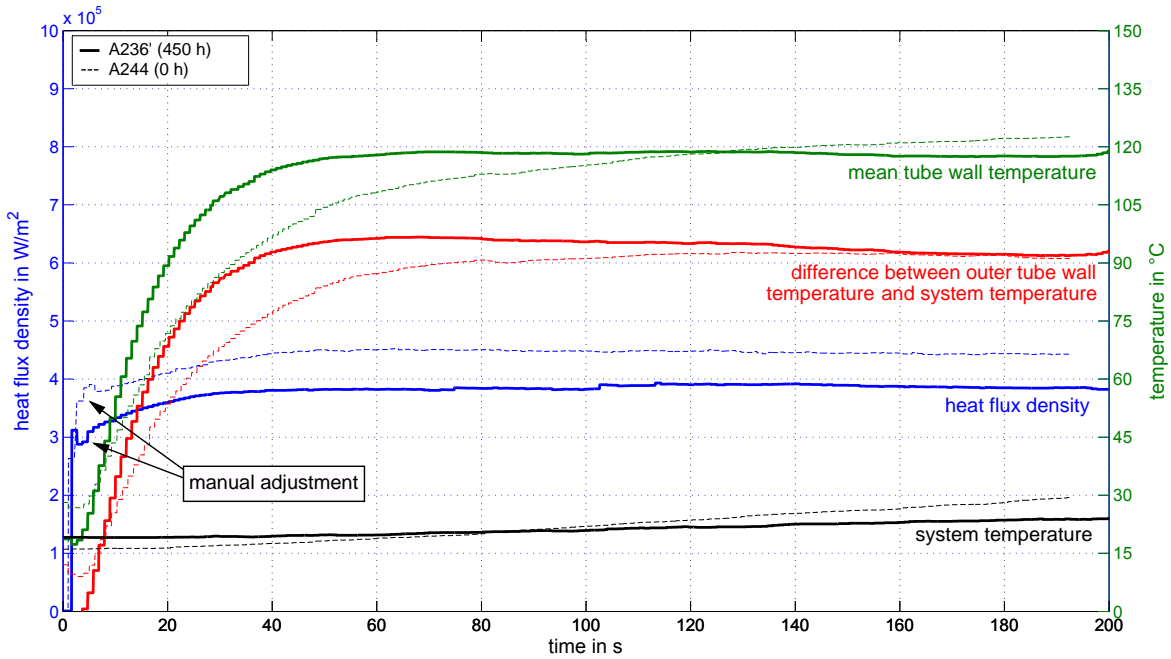


Figure I.2: *Burn-out III test results for cold start-up conditions for the steady state Cetamine treated tube A236' compared to the $PO_4 + N_2H_4$ reference A244, $\dot{q} = 400 \cdot 10^3 W/m^2$ at $p_s = 2$ bar.*

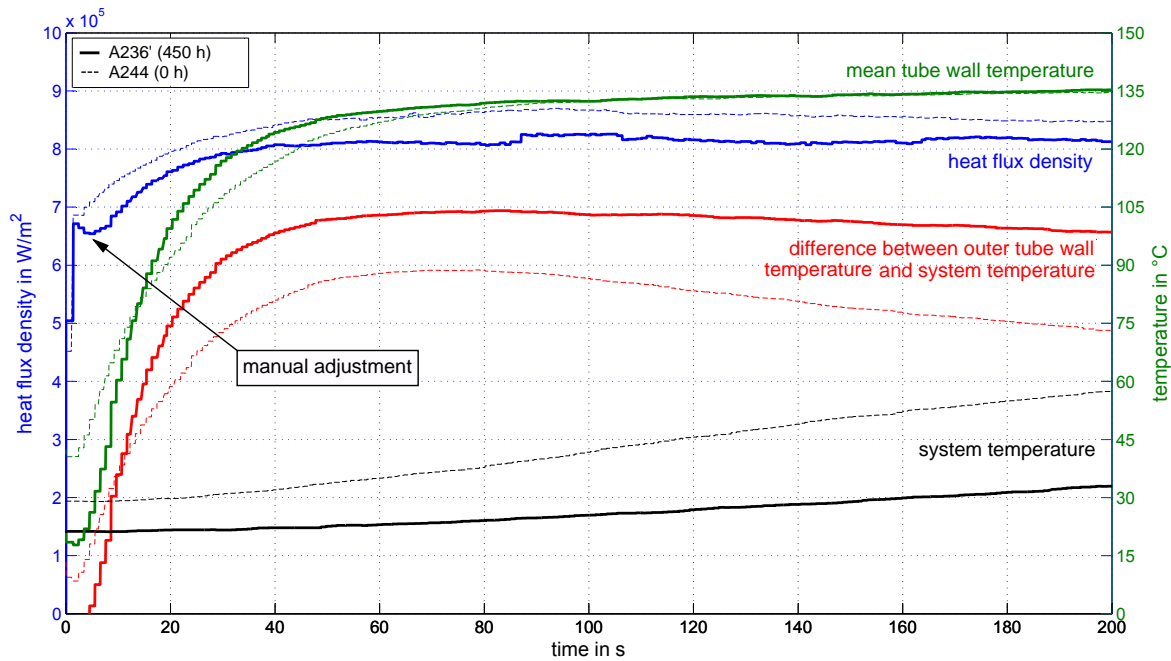


Figure I.3: *Burn-out III test results for cold start-up conditions for the steady state Cetamine treated tube A236' compared to the $PO_4 + N_2H_4$ reference A244, $\dot{q} = 800 \cdot 10^3 W/m^2$ at $p_s = 2$ bar.*

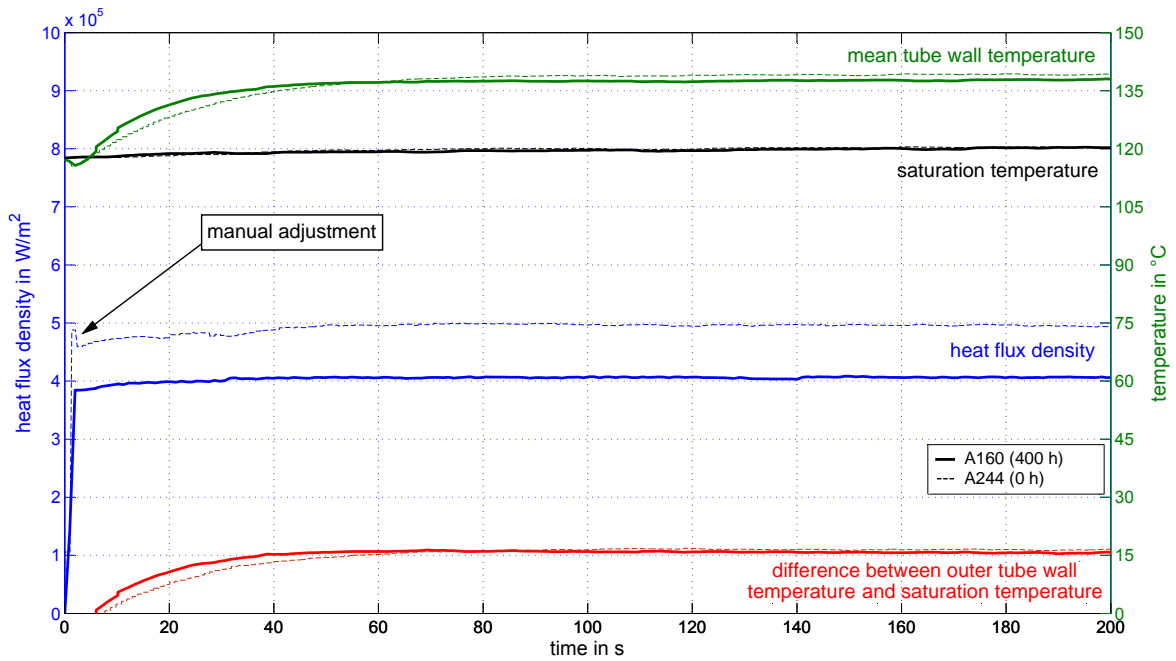


Figure I.4: *Burn-out III test results for hot stand-by conditions for the steady state Cetamine treated tube A160 compared to the $PO_4 + N_2H_4$ reference A244, $\dot{q} = 400 \cdot 10^3$ W/m^2 at $p_s = 2$ bar.*

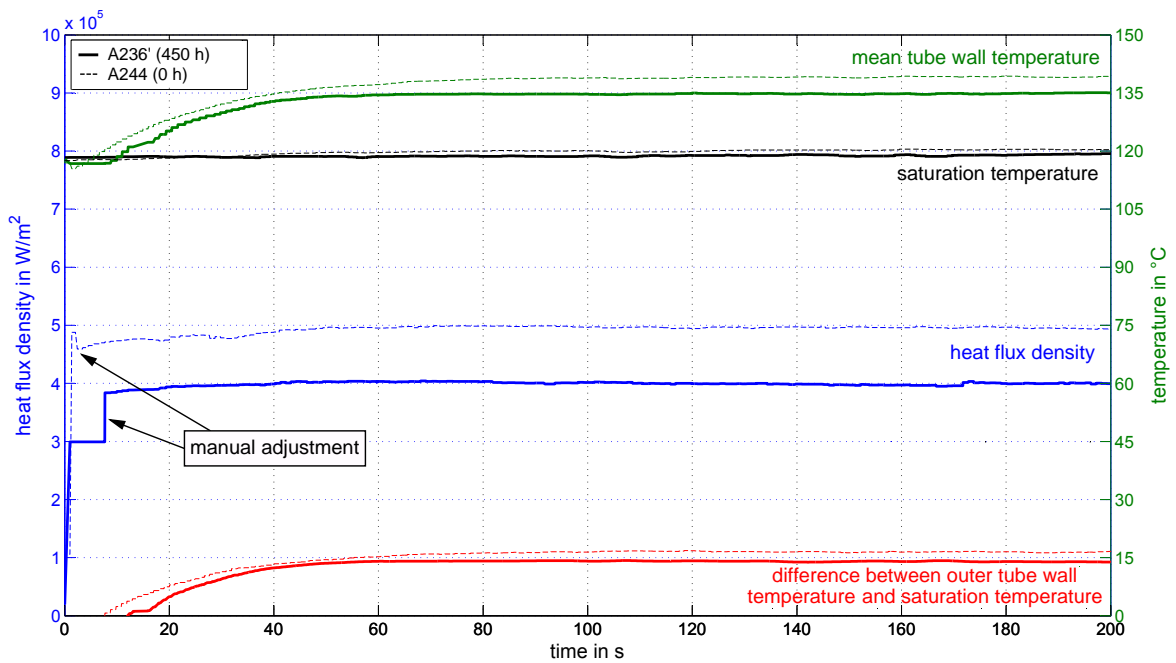


Figure I.5: *Burn-out III test results for hot stand-by conditions for the steady state Cetamine treated tube A236' compared to the $PO_4 + N_2H_4$ reference A244, $\dot{q} = 400 \cdot 10^3$ W/m^2 at $p_s = 2$ bar.*

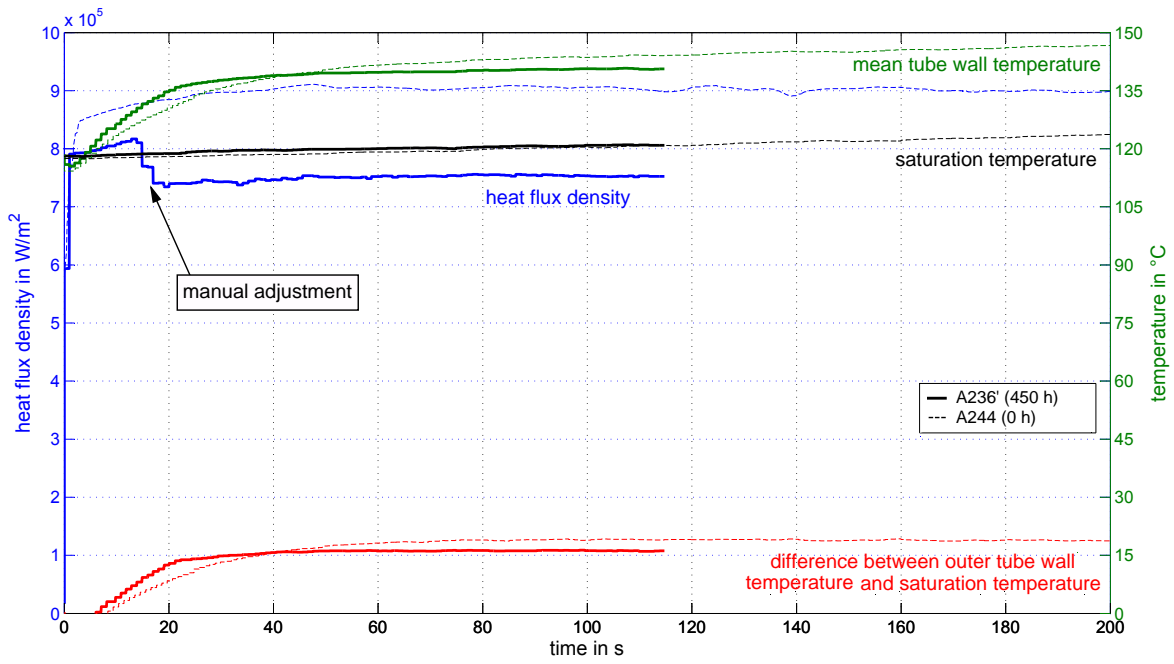


Figure I.6: *Burn-out III test results for hot stand-by conditions for the steady state Cetamine treated tube A236' compared to the $\text{PO}_4 + \text{N}_2\text{H}_4$ reference A244, $\dot{q} = 800 \cdot 10^3 \text{ W/m}^2$ at $p_s = 2 \text{ bar}$.*

J Estimation of the savings potential under film-forming amine treatment

In the following paragraphs, a model⁷ for the improvement of heat transfer in a pressurised-water reactor is described, in the case where the film-forming amine contained in Cetamine®V211 is applied.

In this case, the primary and the secondary loop of the pressurised-water reactor are considered. While in the primary loop water under a certain pressure is heated by nuclear decay to an extent where boiling will not occur, the secondary loop is comparable to a waste heat boiler in a shell boiler arrangement.^[85]

The contaminated highly-energetic water is pumped in pipes through a heat exchanger (steam generator), where a part of its energy is transferred by convection through the pipe walls to (pool) boiling water at the desired saturation pressure in the secondary loop. The water/steam mixture is usually transported by convection to a phase separator. The saturated steam is then expanded in a wet steam turbine set.

In the model, the pressure for the secondary loop is chosen $p_s = 15 \text{ bar}$. Although this is not a typical operating pressure and trisodium phosphate used as a reference is usually not applied in such facilities, the experimental data can be used to recognise tendencies.

The model uses a fixed heat transferring surface, an approximate fixed heat transfer coefficient from the pressurised water to the inner walls of the primary loop of the heat exchanger and enables iterative calculation of the transferred heating power to the boiling water. When trisodium phosphate and the film-forming amine conditions are compared, this can, in turn, directly be translated into steam production.

Figure J.1 demonstrates the boundaries of the model including the chosen parameters.

According to Bošnjaković (1958), the heat exchangers operational characteristic Φ is defined as follows:

$$\Phi = \frac{T_{in} - T_{out}}{T_{in} - T_s}$$

⁷Made available by D. Steinbrecht.

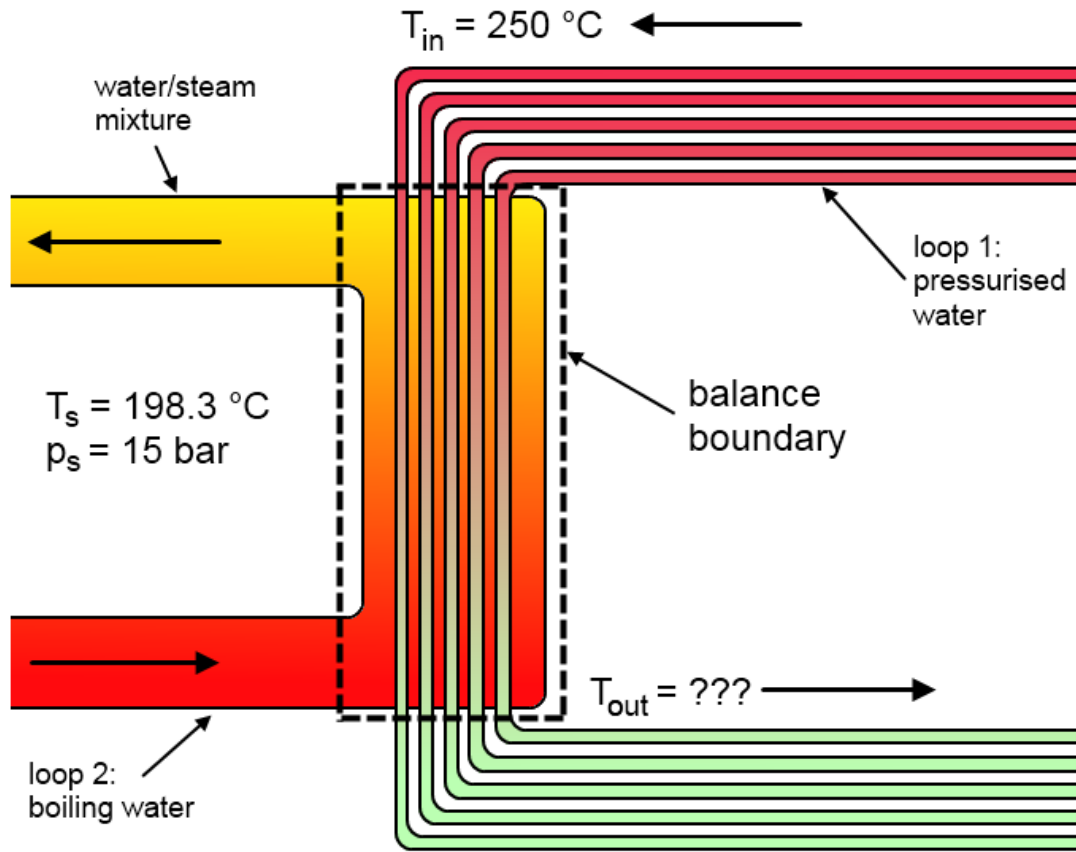


Figure J.1: Model schematic and parameters for the prediction of the effect of film-forming amines in a pressurised-water reactor.

The heat capacity flow \dot{C} can be defined for both investigated loops (1: primary; 2: secondary):

$$\begin{aligned}\dot{C}_1 &= \dot{Q}_1 / (T_{in} - T_{out}) \\ \dot{C}_2 &= \dot{Q}_2 / (T_s - T_s)\end{aligned}$$

Since the liquid temperature in loop 2 remains constant during evaporation, evaporator heat capacity flow is $\dot{C}_2 = \infty$, while the water temperature in loop 1 will decrease between inlet and outlet. In case of $\dot{C}_1 / \dot{C}_2 = 0$, Φ equals for every kind of heat exchanger and type of fluid flow. It becomes:

$$\Phi = 1 - \exp\left(-\frac{k \cdot A}{\dot{C}_1}\right)$$

with the heating surface area A and the summary heat transmission coefficient k_o , which with respect to the outer tube diameter d_o becomes:

$$\frac{1}{k_o} = \frac{1}{k_2} + \frac{d_o}{2\lambda} \ln\left(\frac{d_o}{d_i}\right) + \frac{d_o}{\alpha_1 d_i}$$

Here, k_2 is the heat transmission coefficient between the outer tube wall (loop 2) through the assumed oxide layer after operation under PO_4 conditioning as a reference (in the following case compared to the steady state after *Cetamine* treatment). The inner tube diameter is d_i .

The heating surface is assumed to provide a total area of $A = 5000 \text{ m}^2$, which consists of pipes with the dimension $d_o \times d_i = 20.00 \text{ mm} \times 1.25 \text{ mm}$. The thermal conductivity of the pipe material (stainless steel) is $\lambda = 15 \text{ W}/(\text{m} \cdot \text{K}) = \text{const}$. The inner heat transfer coefficient from the pressurised water to the inner walls (loop 1) is chosen $\alpha_1 = 6000 \text{ W}/(\text{m}^2\text{K}) = \text{const}$ along the heated tube surface. As the model describes the heat transfer during pool boiling (steam generator), the heat capacity flow on the secondary loop is infinite, while the temperature on the primary side will decrease during heat transfer. The inlet temperature of the pressurised water is $T_{in} = 250 \text{ }^\circ\text{C}$. The outlet temperature T_{out} is to be calculated.

First, the value for the outlet temperature T_{out} is guessed as well as the value for the heat transmission coefficient k_2 . According to these values, the transferred heat flux from loop 1 to loop 2 is calculated. Using this heat flux, the heat flux density can be determined via the transferring surface area:

$$\dot{q} = k_o \cdot (\Delta T_m)$$

with the logarithmic mean temperature difference ΔT_m :

$$\Delta T_m = \frac{(T_{in} - T_s) - (T_{out} - T_s)}{\ln \frac{(T_{in} - T_s)}{(T_{out} - T_s)}}$$

The calculated mean heat flux density \dot{q} , which is assumed to be constant along the heated tube surface, is introduced into the power law for infinite trisodium phosphate operation (according to chapter 7.1.3):

$$k_2(\dot{q})|_{PO_4, \infty} = 9.86 \text{ K}^{-1} \cdot \dot{q}^{0.63}$$

as the reference. Calculating the actual heat transmission coefficient k_2 and comparing it to the guessed value yields an iterative approach, repeatedly calculating the outlet temperature for loop 1 until convergence via:

$$T_{out} = T_{in} - \Phi \cdot (T_{in} - T_s)$$

and the heat flux density:

$$\dot{q} = k_o \cdot (T_{in} - T_{out}(guessed))$$

If convergence for $k_2(\dot{q}) \approx k_2(guessed)$ is reached, the temperatures $T_{out}(guessed)$ and T_{out} are compared with respect to the convergence of k_2 . After that, the transferred heat flux is calculated, which, in a steady state operation, equals the steam enthalpy flow that can be directly translated into the steam production \dot{m}_{steam0} at $p_s = 15 \text{ bar}$.

A procedure identical to the described one is carried out using the power law for infinite *Cetamine* treatment (see chapter 7.4):

$$k_2(\dot{q})|_{Cetamine_\infty} = 106.2 \text{ K}^{-1} \cdot \dot{q}^{0.488}$$

This, in turn, calculates the transferred heat flux for the *Cetamine* operation, which can be compared to the trisodium phosphate conditions.

The described procedure yields the following heat fluxes as a result of the different treatment type:

$$\dot{Q}(Cetamine) = 464.56 \cdot 10^6 \text{ W}; \quad T_{out} = 212.8 \text{ }^\circ\text{C}$$

$$\dot{Q}(PO_4) = 437.32 \cdot 10^6 \text{ W}; \quad T_{out} = 215.0 \text{ }^\circ\text{C}$$

$$\Delta\dot{Q} = 27.24 \cdot 10^6 \text{ W}; \quad \Delta T_{out} = 2.2 \text{ K}$$

As a consequence of *Cetamine* treatment, the outlet temperature of the pressurised water in the primary loop is decreased by 2.2 K, which results in an improvement of the transferred heat flux (steam production, respectively) of

$$\Delta\dot{Q} \hat{=} \Delta\dot{m}_{steam} = 6.23 \%$$

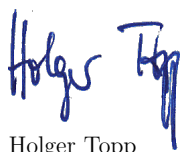
compared to trisodium phosphate treatment. The overall heat transmission coefficient benefits from the enhanced heat transfer on the boiling water side using the film-forming amine.

Since the improvement of heat transfer under *Cetamine* conditioning is a result of the surface tension decrease and given that the surface tension between the boiling water and its saturated steam decreases with rising pressure, the effect can be assumed smaller for real pressures in a pressurised-water reactor. However, the effect of the film-forming amine conditioning is likely to apply also under realistic operation.

Selbständigkeitserklärung

Ich versichere hiermit an Eides statt, dass ich die vorliegende Arbeit selbständig angefertigt und ohne fremde Hilfe verfasst habe, keine außer die von mir angegebenen Hilfsmittel und Quellen dazu verwendet habe und die den benutzten Werken inhaltlich und wörtlich entnommenen Stellen als solche kenntlich gemacht habe.

Rostock, 14. September 2010

A handwritten signature in blue ink that reads "Holger Topp". The signature is written in a cursive style with a large 'H' and 'T'.

Holger Topp

Publications

1. H. Topp, D. Steinbrecht, W. Hater, A. de Bache: "The Influence of Film-Forming Amines on Heat Transfer during Saturated Pool Boiling", PPChem, 2010, 12(7), pages 388 - 395
2. H. Topp, D. Steinbrecht, W. Hater, A. de Bache: „Einfluss filmbildender Amine auf den Wärmeübergang beim gesättigten Behältersieden“, VGB PowerTech, 2010 (submitted)
3. H. Topp, D. Steinbrecht, W. Hater, P. Blériot: “Amélioration du rendement thermique d’un générateur de vapeur par un traitement à l’aide d’amines filmantes” Journées Information Eaux (Proceedings), Poitiers, 2010

Conference presentations

1. H. Topp, D. Steinbrecht: „Zum Wärmeübergang beim Sieden von Wasser an Stahlheizflächen“, VDI Thermodynamik- Kolloquium, Rostock, 2007
2. H. Topp, D. Steinbrecht: „Wirkung organischer Konditionierungsmittel auf den Wärmeübergang beim Sieden von Wasser an Stahlheizflächen“, PPChem Seminar: Organische Konditionierungsmittel für den Wasserdampfkreislauf, Heidelberg, 2007
3. H. Topp, D. Steinbrecht, W. Hater, C. zum Kolk, A. de Bache: „Verhalten von filmbildenden Aminen in Dampfkesselanlagen“, PPChem Seminar: Chemie im Wasserdampfkreislauf, Stuttgart, 2009
4. H. Topp, D. Steinbrecht, W. Hater, A. de Bache, C. zum Kolk: „Verhalten von filmbildenden Aminen in Dampfkesselanlagen“, VGB Sitzung des Arbeitskreises „Industrie- und Heizkraftwerke, BHKW“, Berlin, 2009
5. H. Topp, D. Steinbrecht, W. Hater, C. zum Kolk, A. de Bache: „Verhalten von filmbildenden Aminen in Dampfkesselanlagen“, VGB Konferenz: Chemie im Kraftwerk, Dresden, 2009
6. H. Topp, D. Steinbrecht: „Wärmetechnische Charakterisierung der Wechselwirkung filmbildender Amine mit der Wärmeübertragerfläche in Großwasserraumkesseln“, Cetamine Symposium, Essen, 2010
7. H. Topp, D. Steinbrecht, W. Hater, P. Blériot: “Amélioration du rendement thermique d’un générateur de vapeur par un traitement à l’aide d’amines filmantes”, Journées Information Eaux, Poitiers, 2010 (scheduled)